Imperial College London
Department of Physics
Space and Atmospheric Physics Group

Flux Ropes at the Earth's Magnetopause: an Investigation with the Magnetospheric Multiscale Mission

Sadie L. Robertson

March 2022

Submitted in fulfilment of the requirements for the degree of
Doctor of Philosophy

Declarations

I declare that the work presented in this thesis is my own, unless explicitly stated and referenced otherwise.

- *Sadie L. Robertson, March 2022*

The work presented in Chapter 6 of this thesis has been published in a peer-reviewed journal article:

Robertson, S. L., Eastwood, J. P., Stawarz, J. E., Hietala, H., Phan, T. D., Lavraud, B., et al. (2021). Electron trapping in magnetic mirror structures at the edge of magnetopause flux ropes. *Journal of Geophysical Research: Space Physics*, 126, e2021JA029182. https://doi.org/10.1029/2021JA029182

Abstract

Magnetic reconnection is a fundamental plasma physics process and takes place in space plasma environments throughout the solar system. During the process, magnetic field lines break and reconnect, allowing different plasma populations to mix and releasing energy stored in the magnetic field, which heats and accelerates particles. This change in magnetic field topology allows the production of helical magnetic field structures known as flux ropes. Here, we use data from NASA's Magnetospheric Multiscale (MMS) mission to investigate the properties of magnetopause flux ropes, how they relate to the ongoing reconnection, and how they could facilitate energy transfer during magnetic reconnection.

This thesis presents a statistical survey of flux ropes associated with encounters of the magnetopause electron diffusion region (EDR), which is the central location where magnetic reconnection takes place. We find that the 245 identified EDR-associated flux ropes are smaller and have less flux content than previously reported, and that their properties vary with proximity to the EDR. This suggests that we are studying a distinct set of flux ropes that are potentially newly formed by the EDR.

The evolution and dynamics of the flux ropes are investigated by applying a force-free flux rope model. We find that the flux ropes generally show good agreement with the model, potentially being more force-free when they have larger radii and stronger axial fields. We also investigate the flux rope topology, finding that most flux ropes have an open topology and that closed topology observations are potentially correlated with a negative IMF B_Y component.

Finally, two case studies of electron trapping in magnetic mirror structures on the edge of magnetopause flux ropes are presented. These observations present a unique acceleration mechanism for flux ropes, and therefore magnetic reconnection more generally, highlighting the importance of such substructure for energy transfer during reconnection.

Acknowledgements

I would like to thank my supervisor, Jonathan, for his guidance and support throughout both my PhD and masters studies. I would also like to thank Julia for always being there to answer my questions. It has been a pleasure to work with both of you. Thank you to all the other members of SPAT who I have discussed this work with, particularly Marina and Ralf for their feedback during my progress reviews.

My PhD experience wouldn't have been as enjoyable without the people I shared it with; thanks to all the lovely members of SPAT who provided welcome distractions, including SPAT football, bouldering and lots of pub trips. Special mention goes to my pre-pandemic office mates, Earn and Pete, who kept up the regular coffee breaks even across continents.

Biggest thank you goes to my family for always believing in me, and to Leon for encouraging me throughout.

Contents

List of Tables

List of Figures

Chapter 1

Introduction

This thesis investigates twisted magnetic field structures known as flux ropes in the context of the Earth's plasma environment. Flux ropes are a key feature of magnetic reconnection, which is a fundamental plasma physics process observed in laboratory plasma physics experiments and throughout space plasma environments. It is one of the dominant process coupling the solar wind, the continuous stream of plasma emitted by the Sun, and the Earth's magnetosphere, the bubble of influence of the Earth's dipole field, driving space weather events. The process rearranges the magnetic field topology of the plasma involved, as well as releasing energy stored in the magnetic field to heat and accelerate the plasma. Flux ropes are formed during the reconnection process and are thought to facilitate this energy transfer.

In this chapter, we will introduce the topics above alongside the space plasma physics theory required to understand them. Section 1.1 introduces space plasma physics and its fundamental concepts, including single-particle motion, magnetohydrodynamics and the frozen-in flux theorem. This section also introduces magnetic reconnection theory and models. Section 1.2 discusses magnetic reconnection in the Earth's magnetosphere, introducing the solar wind, the magnetosphere and how they are coupled. This section also details the key research areas for magnetic reconnection in the magnetosphere, such as the electron diffusion region (EDR) and particle energisation. Section 1.3 introduces

flux ropes and their observations in the magnetosphere. In Section 1.4, we will then discuss the open questions in these research areas and how this thesis works to address them.

1.1 Space Plasmas

Plasma is the fourth state of matter, alongside solids, liquids and gasses. Unlike its counterparts, plasma is rarely observed on Earth, with only phenomena such as flames and lightning bolts reaching high enough temperatures. However, this isn't the case for the rest of the universe; over 99% of the observable matter in the universe is in the plasma state (Baumjohann and Treumann, 1996). The Sun is a hot ball of dense plasma, from which streams the solar wind, a cooler, lower density plasma that fills the solar system. In this section, we introduce the fundamental concepts used to define and describe such space plasmas and their dynamics, as necessary for the understanding of the work presented in this thesis.

A plasma is an ionised gas consisting of approximately equal numbers of ions and electrons such that it can be defined as quasineutral. This means that macroscopic plasma properties, such as temperature and density, vary on scales much larger than those on which charge separation in the plasma occurs. This characteristic plasma length scale is given by the Debye length,

$$\lambda_D = \sqrt{\frac{\epsilon_0 k_B T_e}{n_e e^2}}, \tag{1.1}$$

where T_e and n_e are the temperature and number density of the electrons in the plasma, e is the charge of an electron, ϵ_0 is the permittivity of free space and k_B is the Boltzmann constant. The Debye length defines an ion's sphere of influence on the surrounding charged particles in the plasma.

The long-range electromagnetic forces present in a plasma means that it acts with

collective behaviour, where the charged particles in the plasma influence and interact with each other. For these interactions to take place, it is required that there are enough particles present inside a Debye sphere, with radius λ_D. This is characterised by the plasma parameter, $\Lambda = n_e {\lambda_D}^3$, and the criteria that $\Lambda \gg 1$.

A plasma must have sufficiently few neutral particles such that they do not affect the plasma's collective behaviour, i.e. it must be approximately collisionless. If the plasma's quasineutrality is disturbed, the more mobile electrons will be accelerated more easily by the resulting electric fields and will move to restore the previous equilibrium. Their inertia results in oscillations about this equilibrium, defined by the electron plasma frequency,

$$\omega_{pe} = \sqrt{\frac{n_e e^2}{m_e \epsilon_0}}, \tag{1.2}$$

where m_e is the electron mass. For the plasma to be considered collisionless, the plasma frequency must be much greater than the time between electron-neutral collisions.

To understand how a plasma behaves, we must have a framework for how the particles and fields interact with each other. This relationship is defined by Maxwell's equations:

$$\nabla \cdot \mathbf{E} = \frac{\rho}{\epsilon_0}, \qquad \text{(Poisson's equation)} \tag{1.3}$$

$$\nabla \times \mathbf{E} = -\frac{\partial \mathbf{B}}{\partial t}, \qquad \text{(Faraday's law)} \tag{1.4}$$

$$\nabla \cdot \mathbf{B} = 0, \qquad \text{(Gauss's law of magnetic fields)} \tag{1.5}$$

$$\nabla \times \mathbf{B} = \mu_0 \mathbf{j} + \mu_0 \epsilon_0 \frac{\partial \mathbf{E}}{\partial t}, \qquad \text{(Ampère's law)} \tag{1.6}$$

where $\mathbf{E}$ and $\mathbf{B}$ are the vector electric and magnetic fields, ρ is the density of charged particles, $\mathbf{j}$ is the vector current density and μ_0 is the permeability of free space. These

equations can be combined with the Lorentz force law,

$$m\frac{d\mathbf{v}}{dt} = q(\mathbf{E} + \mathbf{v} \times \mathbf{B}) \tag{1.7}$$

where m, q and $\mathbf{v}$ are the particle mass, charge and vector velocity, respectively, to give a full picture of how changes in the plasma properties influence the fields and vice versa. Solving these equations completely is often infeasible and simplified models are often used, as described in the following subsections.

1.1.1 Single Particle Motion

We can gain insight into how particles behave in a plasma by neglecting the effect of the particles on the fields and simply considering how a particle responds to constant fields. The Lorentz force law (Equation 1.7) tells us that a charged particle moving in a constant magnetic field will experience a force perpendicular to the magnetic field, causing it to gyrate at a constant velocity, $v_\perp$, around the field with gyrofrequency and gyroradius:

$$\omega_g = \frac{qB}{m}, \tag{1.8}$$

$$r_g = \frac{mv_\perp}{|q|B}. \tag{1.9}$$

Applying this to both electrons and ions, we find that electrons gyrate more quickly and with a smaller radius than ions. The charge dependence of the gyrofrequency results in ions and electrons gyrating around the field in opposite directions.

Non-uniformities in the magnetic field, the addition of an electric field, or the presence of additional external forces, will all act to alter this idealised gyromotion. Some examples of the resulting particle drifts are as follows:

- The addition of an electric field results in a particle drift in the direction perpendicular to the magnetic field.
- The addition of a magnetic field gradient results in a particle drift in the direction perpendicular to both the magnetic field and its gradient, in opposing directions for ions and electrons.
- The addition of an external force results in a drift perpendicular to both the force and the magnetic field, in opposing directions for ions and electrons.

Due to their charge and mass dependence, some of these drifts result in associated currents.

1.1.2 Kinetic Theory and Magnetohydrodynamics

Kinetic theory takes an opposing approach to single-particle motion by considering the plasma as a collection of interacting particles and describing them using six-dimensional velocity phase-space distributions, $f(\mathbf{x}, \mathbf{v}, t)$, where $\mathbf{x}$ and $\mathbf{v}$ are the location and velocity in phase space at time, t. In this description, the Vlasov equation describes the variation of the distribution functions for a collisionless plasma:

$$\frac{\partial f}{\partial t} + \mathbf{v} \cdot \nabla_{\mathbf{x}} f + \frac{q}{m}(\mathbf{E} + \mathbf{v} \times \mathbf{B}) \cdot \nabla_{\mathbf{v}} f = 0. \tag{1.10}$$

This non-linear partial differential equation is often infeasible to solve completely. Instead, it is possible to describe the plasma by taking moments of the distribution function by integrating over velocity space to define plasma bulk variables that depend on space and time. The first two moments of the distribution function, the number density, n, and plasma bulk velocity, $\mathbf{u}$, are computed as follows:

$$n = \int f(\mathbf{v}) d^3v, \tag{1.11}$$

$$\mathbf{u} = \frac{1}{n} \int \mathbf{v} f(\mathbf{v}) d^3v. \tag{1.12}$$

Taking the third and fourth moments gives the plasma pressure and heat tensors.

By taking moments of the Vlasov equations, we find the fluid variables for the plasma, therefore developing a macroscopic fluid description of the plasma. These, combined with Maxwell's equations, create a fusion of fluid dynamics and electrodynamics known as magnetohydrodynamics (MHD), which is widely used to describe space plasmas.

Single fluid ideal MHD treats the plasma as a single conducting fluid with equal numbers of ions and electrons, $n_i = n_e = n$, bulk velocity, $\mathbf{u}$, and mass density, $\rho = n_i m_i + n_e m_e \approx n m_i$. It is also assumed that the plasma bulk properties vary on slow/large scales, displacement currents can be neglected and that the plasma is in thermal equilibrium such that the pressure is scalar and can be determined by the ideal gas law ($P = nk_BT$). The first and second moments of the Vlasov equation lead to the mass and momentum equations, respectively:

$$\frac{\partial \rho}{\partial t} + \nabla \cdot (\rho \mathbf{u}) = 0, \tag{1.13}$$

$$\rho \left[\frac{\partial \mathbf{u}}{\partial t} + (\mathbf{u} \cdot \nabla) \mathbf{u} \right] = -\nabla P + \mathbf{j} \times \mathbf{B}, \tag{1.14}$$

where $\mathbf{j}$ is the current density.

Each time we take a higher-order moment of the Vlasov equation, a higher-order plasma term is introduced; in the case of the momentum equation (Equation 1.14), we have introduced the current density. We therefore cannot simply continue to take moments in order to find a complete plasma description. To close the system of equations, we must

introduce a simplified Ohm's law:

$$\mathbf{E} + \mathbf{v} \times \mathbf{B} = \eta \mathbf{j}. \tag{1.15}$$

where η is the plasma resistivity. This equation gives an expression for the current density, $\mathbf{j}$, therefore closing the system of equations. The $\eta\mathbf{j}$ term describes the resistive process taking place in the plasma. When $\eta = 0$ we have ideal MHD, where the resistivity is neglected. Otherwise, this plasma description is known as resistive MHD. The generalised version of this equation, the generalised Ohm's law, introduces further non-ideal effects and is discussed in Section 1.1.4. For completeness, we must also include the energy equation,

$$\frac{\partial}{\partial t}\left(\frac{P}{\rho^\gamma}\right) + \mathbf{u} \cdot \left(\frac{P}{\rho^\gamma}\right) = 0, \tag{1.16}$$

where γ is the ratio of specific heats, typically $\frac{5}{3}$.

Plasma Beta

The momentum equation (Equation 1.14) informs us on the forces present in the plasma; there is a contribution from the thermal pressure and a $\mathbf{j} \times \mathbf{B}$ term. Substituting Ampère's law (Equation 1.6) into this $\mathbf{j} \times \mathbf{B}$ force term and applying some vector algebra, we find that

$$\mathbf{j} \times \mathbf{B} = -\nabla\left(\frac{B^2}{2\mu_0}\right) + \frac{1}{\mu_0}\nabla \cdot (\mathbf{BB}). \tag{1.17}$$

The terms on the right-hand side correspond to the divergence of the magnetic pressure, devined as $P_B = B^2/2\mu_0$ and a magnetic tension force term, where $\mathbf{BB}/\mu_0$ is the magnetic stress tensor.

We can take the ratio of the thermal and plasma pressures to define a useful plasma parameter know as the plasma beta,

$$\beta = \frac{P}{P_B} = \frac{nk_BT}{B^2/2\mu_0}. \tag{1.18}$$

The plasma beta can tell us if the plasma or the magnetic field dominate the dynamics of a given plasma. For an anisotropic plasma, the thermal pressure splits into parallel and perpendicular components for which we can define corresponding plasma betas

$$\beta_\parallel = \frac{2\mu_0 P_\parallel}{B^2},\ \beta_\perp = \frac{2\mu_0 P_\perp}{B^2}. \tag{1.19}$$

1.1.3 Frozen-in Flux Theorem

A consequence of ideal MHD is the frozen-in flux theorem. First proposed by Alfvén (1942), and therefore also known as Alfvén's theorem, it states that the magnetic field is frozen into the plasma and must move with the plasma. The theorem is derived by combining Faraday's law (Equation 1.4), Ohm's law (Equation 1.15) and Ampère's law (Equation 1.6) to get the magnetic induction equation:

$$\frac{\partial \mathbf{B}}{\partial t} = \nabla \times (\mathbf{u} \times \mathbf{B}) + \eta \nabla^2 \mathbf{B}, \tag{1.20}$$

where $\eta = \frac{1}{\sigma\mu_0}$, and σ is the plasma conductivity. The two terms on the right-hand side of the equation determine how the magnetic field evolves in the plasma; the first term gives the contribution from the convection of the plasma and the second from the diffusion of the magnetic field. The magnetic Reynolds number takes the ratio of the convective and diffusive terms, approximating the characteristic length-scales as L, to give:

$$R_M \sim \frac{uL}{\eta} = \mu_0 \sigma L u. \tag{1.21}$$

For ideal MHD, we assume resistivity to be negligible and work in the large R_M limit, where convection dominates, resulting in the frozen-in flux theorem.

One important consequence of the frozen-in flux theorem is that two distinct plasma populations are unable to mix as they are tied to field lines that are unable to cross each other. Many space plasmas can be considered ideal and are therefore unable to mix in this way, leading to the formation of planetary magnetospheres which are discussed in more detail in Section 1.2.1. At the boundaries between frozen-in fields, current sheets form and the magnetic Reynolds number can become small, leading to non-ideal plasma effects, such as diffusion of the magnetic field and magnetic reconnection. The following subsection introduces the generalised Ohm's law, which describes these non-ideal plasma effects.

1.1.4 Generalised Ohm's Law

Generalised Ohm's law is derived by considering the electron and ion equations of motion in the plasma separately, leading to the equation:

$$\mathbf{E} + \mathbf{v} \times \mathbf{B} = \eta \mathbf{j} + \frac{1}{ne}\mathbf{j} \times \mathbf{B} - \frac{1}{ne}\nabla \cdot \mathbf{P_e} + \frac{m_e}{ne^2}\frac{\partial \mathbf{j}}{\partial t}, \tag{1.22}$$

where $\mathbf{P_e}$ is the electron pressure tensor. As introduced when discussing ideal MHD, the terms on the right hand side of this equation introduce the non-ideal properties of the plasma. The first term on the right hand side is the resistive term discussed in Section 1.1.2. The second term is the Hall term, which describes the differences in ion and electron motion. The third term is a result of gradients in the electron pressure and the final term comes from the electron inertia.

Each of these non-ideal terms become comparable to the ideal MHD electric field ($\mathbf{E} = -\mathbf{v} \times \mathbf{B}$) on different characteristic plasma length scales which determine when they can or cannot be neglected. It can be shown using dimensional analysis that the Hall and

electron pressure terms become important on scales proportional to the ion inertial length, $d_i = c/\omega_{pi}$, where c is the speed of light. The electron inertia term becomes important on scales proportional to the electron inertial length, $d_e = c/\omega_{pe}$. The electron plasma frequency, ω_{pe}, is given by Equation 1.2, and the ion plasma frequency, ω_{pi}, is given by the same equation with m_e replaced by m_i.

When we have a purely ideal MHD magnetic field (i.e. the terms on the right hand side of Equation 1.22 = 0) the frozen-in flux theorem (Section 1.1.3) applies and both ions and electrons are frozen-in to the magnetic field. On scales on which the Hall term becomes important, ions can decouple from the magnetic field, whereas electrons remain frozen-in. As the scale sizes become smaller and further terms become important, electrons then also decouple from the magnetic field. Such decoupling of the particles from the plasma takes place during a process called magnetic reconnection, which is introduced in the following section.

1.1.5 Magnetic Reconnection

Magnetic reconnection is a fundamental plasma physics process that takes place when the idealised MHD description of the plasma, described in the previous subsection, breaks down. The process takes place between opposing magnetic fields, which form a current sheet as a consequence of Ampère's Law (Equation 1.6). When the thickness of this current sheet becomes comparable to the gyroscale of the ions in the plasma, the fluid description of the plasma becomes invalid and diffusive processes in the plasma become significant (i.e. the Reynolds number, R_M (Equation 6.1), becomes small), allowing the violation of the frozen-in flux theorem. In this diffusion region, the opposing fields break and reconnect, allowing the mixing of the plasma populations associated with each of the fields.

Figure 1.1 shows a simple diagram of how the magnetic fields rearrange during the reconnection process. Plasmas inflowing from the top and bottom of the diagram,

following the blue arrows, have opposing magnetic fields (black arrows), forming a current sheet along the dashed blue line. At the centre of the diagram, reconnection takes place at the X-point, where the opposing fields break and reconnect to form the new bent field lines. The plasma on these new bent field lines is then accelerated away from the reconnection site due to magnetic tension in the newly bent field lines and the energy released from the magnetic field during the process. The process results in a change in the topology of the magnetic field; the inflowing field lines originally have the same connectivity at both ends, however, the newly formed field lines are now connected to both inflowing plasma sources.

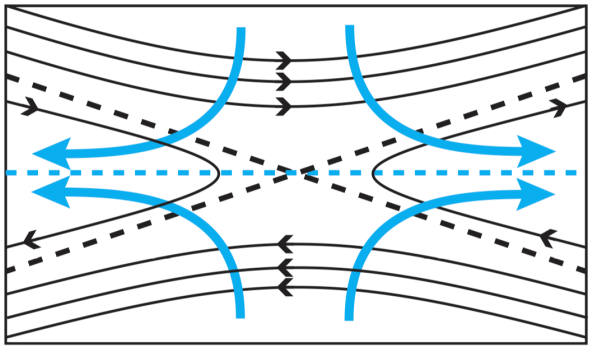

Figure 1.1: Diagram showing a simple magnetic reconnection geometry. Arrowed black lines show the magnetic field and arrowed blue lines show the plasma motion. Black dashed lines show the magnetic reconnection separatrices and the blue dashed line shows the current sheet. *Figure from Figure 1 of Eastwood et al. (2013).*

Reconnection Models

The concept of magnetic reconnection in was first postulated by Giovanelli (1947) who suggested solar flares originate at magnetic nulls on the solar surface. Dungey (1953) further developed the idea as a production mechanism for energetic particles observed in the Earth's magnetosphere. Sweet (1958) and Parker (1957) proposed the first theoretical description of reconnection. They proposed a two-dimensional steady-state model using resistive-MHD which relied upon aspect ratios and conservation of energy fluxes in and out of a central diffusion region. This model gives reconnection exhaust velocities on the

order of the Alfvén speed, defined as

$$V_A = \frac{B}{\sqrt{\mu_0 \rho}}, \tag{1.23}$$

where ρ is the mass density of the plasma.

The Sweet-Parker model for reconnection was found to apply well to dense plasmas and explosive reconnection events, such as in solar flares, however, the model requires a long and thin diffusion region which produces a reconnection rate that was too slow for some observed phenomena. The model also requires all of the expelled plasma to pass through the diffusion region. Petschek (1964) addressed these issues by introducing a new model including a diffusion region with a smaller width-to-height aspect ratio and slow-mode shocks at the boundaries of the exhausts which in-flowing plasma can pass through to enter the exhausts. These modifications increased the reconnection rate meaning this model could explain the so-called 'fast' reconnection rates that are observed in space plasmas. However, the shocks required are not commonly observed and simulations are only able to recreate such reconnection if strong anomalous resistivity is employed (Malyshkin et al., 2005).

Both the Sweet-Parker and Petschek reconnection models are resistive-MHD models requiring collisions in the plasma. However, collisionless space plasmas, such as the solar wind and in the magnetosphere, can still undergo reconnection. Developing a model for such collisionless reconnection required a theory beyond MHD in which smaller-scale particle motion within the plasma is considered. This important development in reconnection theory was proposed by Sonnerup (1979) who suggested that ions and electrons decouple from the magnetic field on different scales in the diffusion region. As discussed in Section 1.1.4, from the generalised Ohm's law we find that non-ideal terms become significant on varying scales which results in the heavier ions decoupling from the magnetic field before the electrons due to their differing gyromotion. This results in a smaller electron diffusion region embedded within a larger ion diffusion region. The differential

motion of the particle species in these regions creates a current system which results in the quadrupolar magnetic field seen in Figure 1.2 (b). Mandt et al. (1994) demonstrated that the inclusion of these non-ideal terms in Ohm's law would make reconnection fast enough to describe the reconnection rates observed in space.

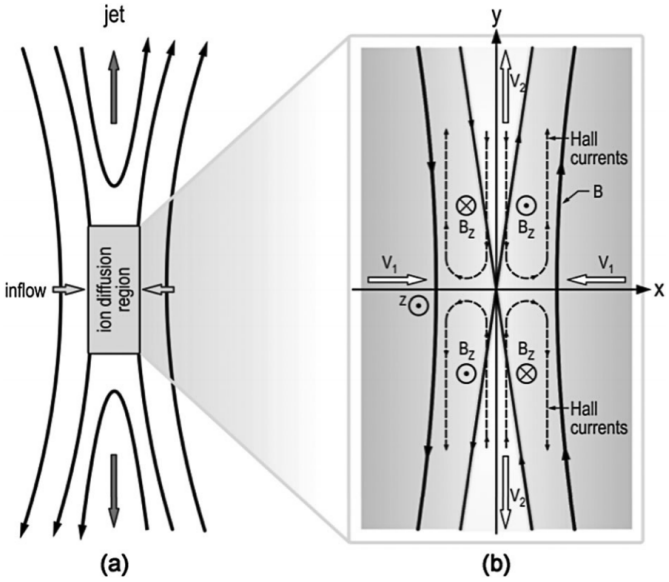

Figure 1.2: Magnetic reconnection geometry as proposed by (a) Petschek (1964) and (b) Sonnerup (1979). (b) shows the quadrupolar Hall field produced by the differential motion of electrons and ions in the diffusion region. *Figure from Figure 2 of Burch et al. (2016a).*

1.2 Magnetic Reconnection in the Earth's Magnetosphere

The Sun continually emits a stream of collisionless plasma known as the solar wind. This plasma fills the solar system, creating the region known as the heliosphere. The solar wind interacts with all magnetised bodies in its path; at magnetised planets, it impacts the planet's magnetic field. As discussed in Section 1.1.3, as both the solar wind and the plasma contained on the planet's magnetic field are collisionless, the frozen-in flux theorem prevents the mixing of the two plasma populations, resulting in a protective bubble being formed around the planet, called a magnetosphere and defined as the region

over which the planet's magnetic field dominates.

As discussed in Section 1.1.5, magnetic reconnection can take place between two plasmas with opposing magnetic fields. Under certain conditions, magnetic reconnection can take place between the solar wind and the plasma contained within a planetary magnetosphere, allowing the solar wind plasma to enter the magnetosphere. This can have great influence on the structure and dynamics of the magnetosphere, such as at Earth where it can drive space weather events that are hazardous to infrastructure both in space and on Earth. In this section, we introduce and discuss this interaction between the solar wind and the Earth's magnetosphere.

1.2.1 The Solar Wind

The solar wind is a highly conducting, collisionless plasma made up of mostly protons, electrons and alpha particles. As such, it follows much of the ideal MHD description discussed in the previous section. It obeys the frozen-in flux theorem with the stream of emitted plasma rotating with the Sun's period ($\sim$ 24.5 days) and dragging the magnetic field radially outwards, resulting in a spiral magnetic field structure propagating throughout the heliosphere known as the Parker spiral (Parker, 1957). Figure 1.3 shows the structure of the Parker spiral out to the location of the Earth's orbit, at 1 astronomical unit (AU), where the interplanetary magnetic (IMF) field is at $\sim 45^\circ$ to the radial direction.

Figure 1.3 also highlights some of the more complex aspects of the IMF. The radial direction, or the polarity, of the IMF differs depending on the hemisphere of the Sun that the plasma originated from, forming the heliospheric current sheet (HCS) between the two regions of plasma according to Ampère's law (Equation 1.6). The Sun's rotational axis is tilted with respect to its magnetic dipole, resulting in an offset of the HCS from the ecliptic plane. This leads to a reversal in the IMF polarity approximately twice per rotation of the Sun at 1 AU. The different polarity field lines are indicated by the red and

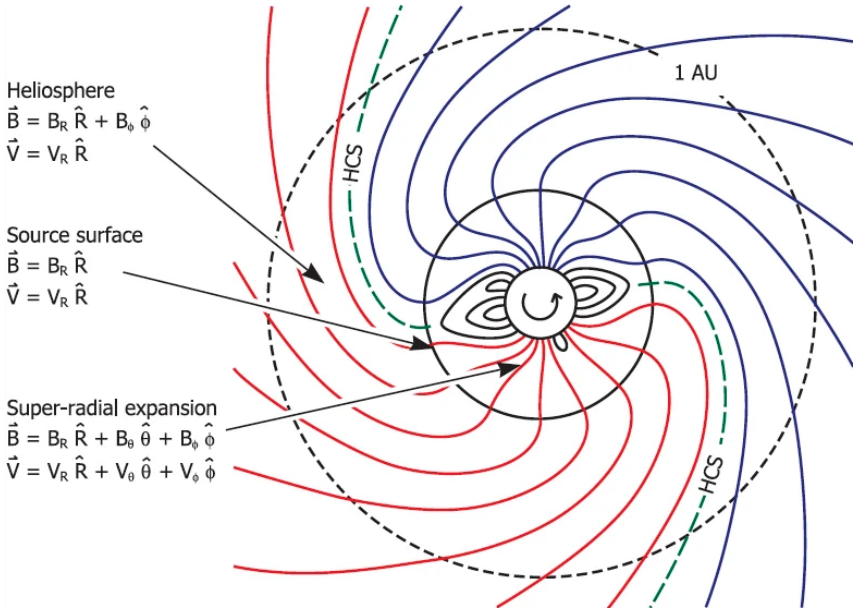

Figure 1.3: Diagram of the Parker spiral which forms as the Sun continually emits plasma as it rotates. *Figure from Figure 1 of Owens and Forsyth (2013).*

blue lines in Figure 1.3, and the HCS is shown by the dashed green line.

The complex evolution of the solar wind is also indicated in Figure 1.3. The solar wind is formed by the expansion of the extremely hot solar corona, which cools and expands, accelerating to reach supersonic speeds. Two streams of solar wind plasma have been identified; slow solar wind ($< 400\ kms^{-1}$), originating in the streamer belt around the solar equator and typically observed in the ecliptic plane, and fast solar wind ($> 600\ kms^{-1}$), originating from coronal holes. Many more stable and transient structures, such as co-rotating interaction regions (CIRs) and coronal mass ejections (CMEs), add further complexity to this picture, resulting in highly variable solar wind conditions at Earth (see Owens and Forsyth, 2013, for more detail). However, at Earth, we typically observe solar wind with velocities of 300 - 400 kms^{-1}, electron density of $\sim$ 5 cm^{-3}, electron temperature of $\sim$ 10^5 K, and an IMF magnitude of the order of 5 nT (Baumjohann and Treumann, 1996).

1.2.2 The Earth's Magnetosphere

The Earth has a magnetic field generated by dynamo action in its conducting core. At large distances from the planet's surface, this can be approximated by a dipole field with an inclination of $\sim$ 10° to the rotational axis. When the solar wind impacts this dipole, the plasma is unable to penetrate the field lines due to the frozen-in flux theorem and a boundary between the solar wind and Earth's magnetic field is formed, which is known as the magnetopause and defines the region known as the magnetosphere. The location of this boundary is determined by the pressure balance between the solar wind dynamic pressure ($P_{sw} = \rho_{sw} v_{sw}^2$, where ρ_{sw} and v_{sw} are the solar wind mass density and velocity), and the sum of the thermal and plasma pressures of the Earth's dipole field (see Section 1.1.2), and therefore varies with the solar wind and magnetospheric conditions.

Figure 1.4 shows a diagram of the Earth's magnetosphere in which the solar wind is moving from left to right towards the Earth. Where the solar wind meets the magnetosphere, a bow shock is formed as the solar wind plasma rapidly decelerates from supersonic speeds. In this diagram, the IMF is pointing southward resulting in it directly opposing the Earth's magnetic field at the subsolar point. This means that, under the typical solar wind conditions, magnetic reconnection can take place in this region, marked with an X on the diagram. On the nightside of the Earth, the Earth's magnetic field is elongated by the propagation of the solar wind, forming the magnetotail with opposing magnetic fields in the northern and southern hemispheres. Again, magnetic reconnection can take place between these opposing fields in the tail and is marked with an X on the diagram. In this figure, the geocentric solar magnetospheric (GSM) coordinate system is used, where X-axis points sunward and the X, Z-plane contains the Earth's dipole. In the following discussion, this coordinate system can be assumed unless otherwise noted.

This process of magnetic reconnection in the subsolar region and magnetotail forms part of a cycle of plasma convection at Earth known as the Dungey cycle, after it was first proposed by Dungey (1961). Figure 1.5 shows the process in greater detail. Originally

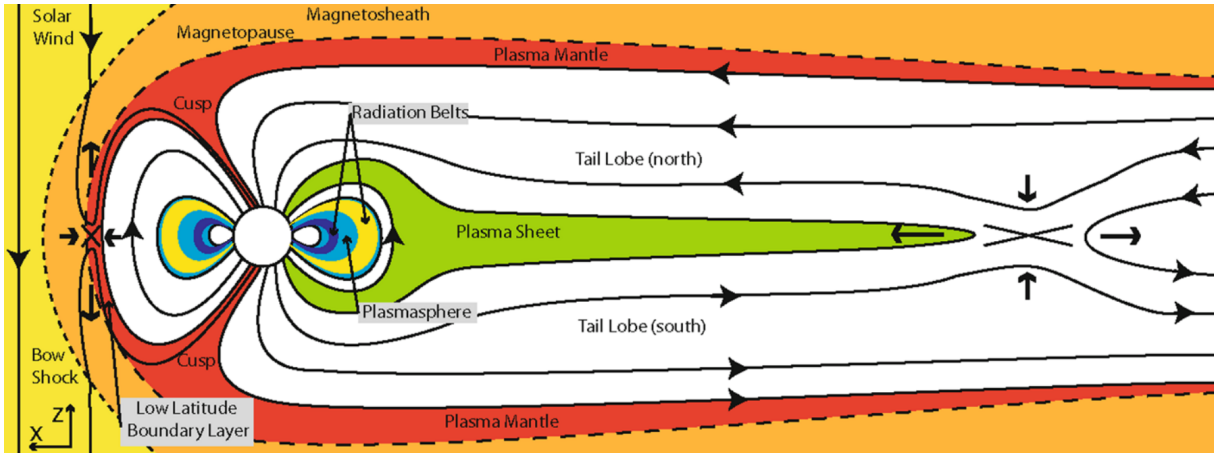

Figure 1.4: Diagram of the Earth's magnetosphere under southward IMF. Locations marked with an X show where magnetic reconnection is taking place. The geocentric solar magnetospheric (GSM) coordinate system is used, where X-axis points sunward and the X, Z-plane contains the Earth's dipole. *Figure from Figure 1 of Eastwood et al. (2015).*

closed solar wind field lines (blue) and closed magnetospheric field lines (red) undergo reconnection to produce newly open magnetic field lines (purple) which are connected to the magnetosphere at one end and the solar wind at the other. These open field lines are dragged over the magnetopause by the motion of the solar wind and subsequently increase the magnetic flux in the tail lobes. Magnetic reconnection between these opposing open fields in the tail completes the cycle by allowing the release of this buildup of magnetic flux as plasmoids and return flow to Earth.

1.2.3 Magnetopause Reconnection

Observational evidence for magnetic reconnection in the Earth's magnetosphere was first provided by Paschmann et al. (1979) who observed accelerated plasma flows across rotational discontinuities on the Earth's magnetopause using the ISEE spacecraft. Figure 1.6 shows these observations; in the righthand plot we observe plasma flow speeds up to $\sim 500\ kms^{-1}$ as the magnetic field rotates, corresponding to a magnetopause crossing (labelled MP). Since then, reconnection has been extensively studied in-situ in the Earth's magnetosphere by multiple spacecraft missions (e.g. Cluster (Escoubet et al.,

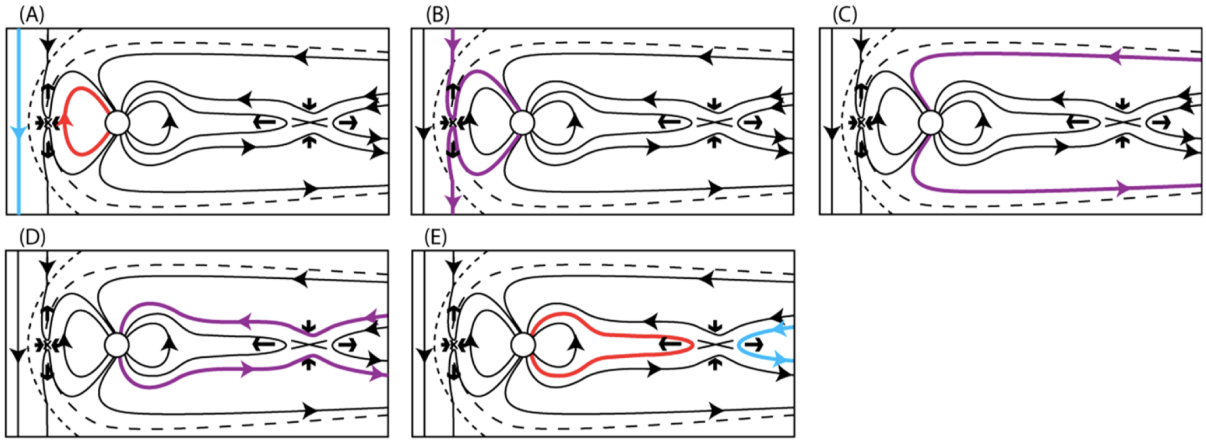

Figure 1.5: Diagram of the Dungey cycle. The light blue solar wind and red magnetospheric field lines in (A) reconnect to form the purple field lines in (B). These are then dragged anti-sunward into the magnetotail (C). This process repeats, causing a build-up of flux in the tail which eventually reconnects (D). This results in the release of a plasmoid, shown by the blue field lines in (E). *Figure from Figure 8 of Eastwood et al. (2015).*

2001a), THEMIS (Angelopoulos, 2009), MMS (Burch et al., 2016a)), allowing us to form an understanding of the nature of reconnection on large scales. When the pictures of reconnection we have been considering are extended into three-dimensions, the X-point becomes an X-line along which reconnection takes place. Magnetic reconnection X-lines have been observed to extend continuously across the magnetopause under southward IMF (Phan et al., 2000) and have been observed in the cusps of the magnetosphere under northward IMF (Phan et al., 2003).

Dungey (1961) presented an anti-parallel reconnection model, which suggests that reconnection should take place where magnetic fields directly oppose each other. On the magnetopause, under purely southward IMF, this leads to an X-line which is a locus of points approximately along the equator. However, it was shown by Crooker (1979) that two separate reconnection lines in different hemispheres can form when the IMF has a significant GSM B_Y component. This theory was opposed by a component reconnection model which states that reconnection can take place when components of the two magnetic fields oppose each other, removing the need for strictly anti-parallel fields (Sonnerup, 1974). The X-line is determined by maximising the anti-parallel components of the merging magnetic fields; the X-line location and orientation are at and normal to these

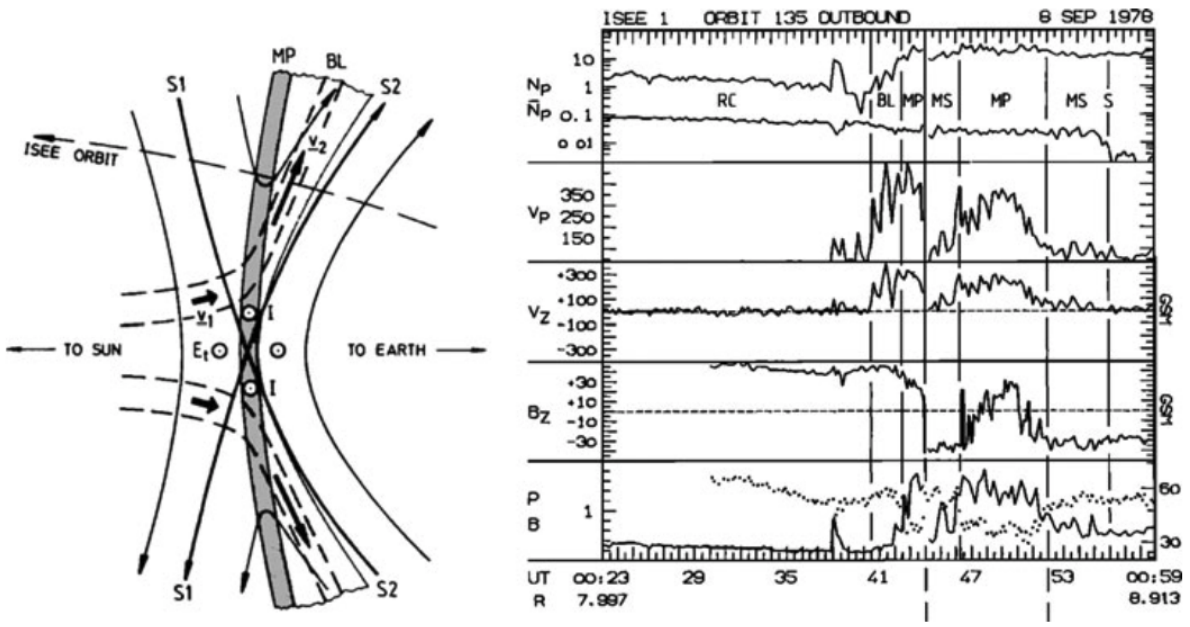

Figure 1.6: First in-situ observational evidence for magnetic reconnection as reported by Paschmann et al. (1979). Plasma flow speeds of plasma flow speeds up to $\sim 500\ kms^{-1}$ are observed as the magnetic field rotates, corresponding to a magnetopause crossing (labelled MP). *Figure from Figure 2 of Paschmann et al. (2014).*

points. This results in a tilted X-line which extends continuously across the dayside magnetopause, regardless of the magnitude of the IMF B_Y component. In fact, the ratio of the B_Y and B_Z components determine the extent of the tilt of the X-line. Figure 1.7 shows a diagram of the expected X-line locations according to the antiparallel and component reconnection theories for IMF with a negative B_Z and significant B_Y components.

Determining the dominant mechanism for reconnection proved important as each has different implications for energy transfer into the magnetosphere; during component reconnection the field lines are less sharply bent, resulting in lower plasma acceleration and less energy transfer (Trattner et al., 2007a). More recent studies of the cusps of the magnetosphere were used by Trattner et al. (2007a) to show that both reconnection mechanisms can occur depending on the conditions of the solar wind. This led to the development of the maximum magnetic shear model (Trattner et al., 2012) which predicts component reconnection during dominant B_Y conditions (typical of the IMF at Earth) and anti-parallel reconnection during dominant B_Z conditions.

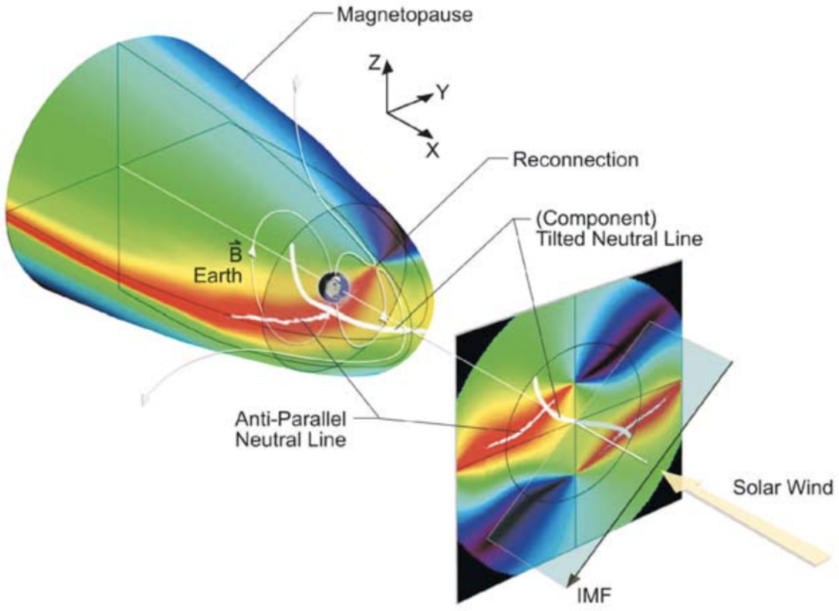

Figure 1.7: Diagram of the magnetosphere and its projection into the 2-D plane for IMF clock angle 234° (i.e. significant B_Y component). X-lines for both reconnection scenarios are shown. Anti-parallel reconnection results in two disjointed X-lines in the red regions: where the shear is maximised at 180°. Component reconnection results in the tilted X-line which passes through the subsolar point (the central point of the 2-D projection). *Figure from Figure 1 of Trattner et al. (2007b).*

1.2.4 The Electron Diffusion Region (EDR)

Magnetopause reconnection diffusion regions have been observed and investigated, and are characterised by out-of-plane Hall magnetic fields, as discussed in Section 1.1.5. Øieroset et al. (2001) presented the first measurements of the Hall magnetic field inside the diffusion region using the Wind spacecraft in the Earth's magnetotail. Mozer et al. (2002) presented a magnetopause diffusion region encounter using the Polar spacecraft and Vaivads et al. (2004) presented multi-spacecraft measurements of the diffusion region using the Cluster spacecraft.

Observations of the electron diffusion region (EDR) proved more challenging; taking the ratio of the scale sizes of the two regions, $d_i/d_e = \sqrt{m_i/m_e}$, we find the EDR to be ~ 43 times smaller than the ion diffusion region. Some EDR encounters were reported using the Cluster and Geotail spacecraft (e.g. Chen et al., 2008; Nagai et al., 2011), how-

ever the resolution of the measurements were not sufficient to study the electron-scale physics of the EDR. Burch et al. (2016b) presented the first electron-scale measurements of magnetic reconnection using data from the Magnetospheric Multiscale (MMS) mission, identifying an EDR encounter on 16th October 2015 at around 13:07:00 UT. Here, we discuss these observations as an example of an EDR encounter and its properties. These observations are made possible by the data collected by MMS, the first mission of its kind that is able to resolve electron-scale dynamics in the magnetosphere. MMS data is the primary data source for the work presented in this thesis; Section 2.1 presents the mission and its capabilities in greater detail.

Figure 1.8 (A-J), from Burch et al. (2016b), shows a 2-minute time series data interval around this EDR observation. Figure 1.8 (K) shows a simulation of magnetic reconnection under similar boundary conditions with an over-plot of the inferred trajectory of MMS. In Figure 1.8 (A-J) the magnetopause crossings are shown by the vertical dashed blue lines. These crossings are identified by the change in particle energy, shown in panels (B) and (C), and the corresponding variations in the magnetic field. As discussed in the previous sections, we can identify the magnetosphere as the low-density region with a strong and steady northward magnetic field, such as at the beginning of the interval. Using these boundary crossings we can build a picture of the motion of the spacecraft, as can be seen in (K). In the interval shown, the spacecraft first crosses the magnetopause from the magnetosphere into the magnetosheath, where it observes a southward-directed reconnection jet. It then partially crosses the magnetopause before returning back to the magnetosheath. During this crossing the spacecraft observes a reconnection jet reversal at the same time the reconnecting magnetic field (B_L) drops close to zero, suggesting an encounter with the diffusion region (the red bar between panels (D) and (E) in Figure 1.8). This is further confirmed by the presence of intense currents, which the simulation predicts will be localised to the diffusion region, and an enhancement of the reconnection electric field (E_M). This leads to a positive $\mathbf{j} \cdot \mathbf{E}'$, where $\mathbf{E}' = \mathbf{E} + \mathbf{v_e} \times \mathbf{B}$, which shows that energy is being dissipated (Zenitani et al., 2011).

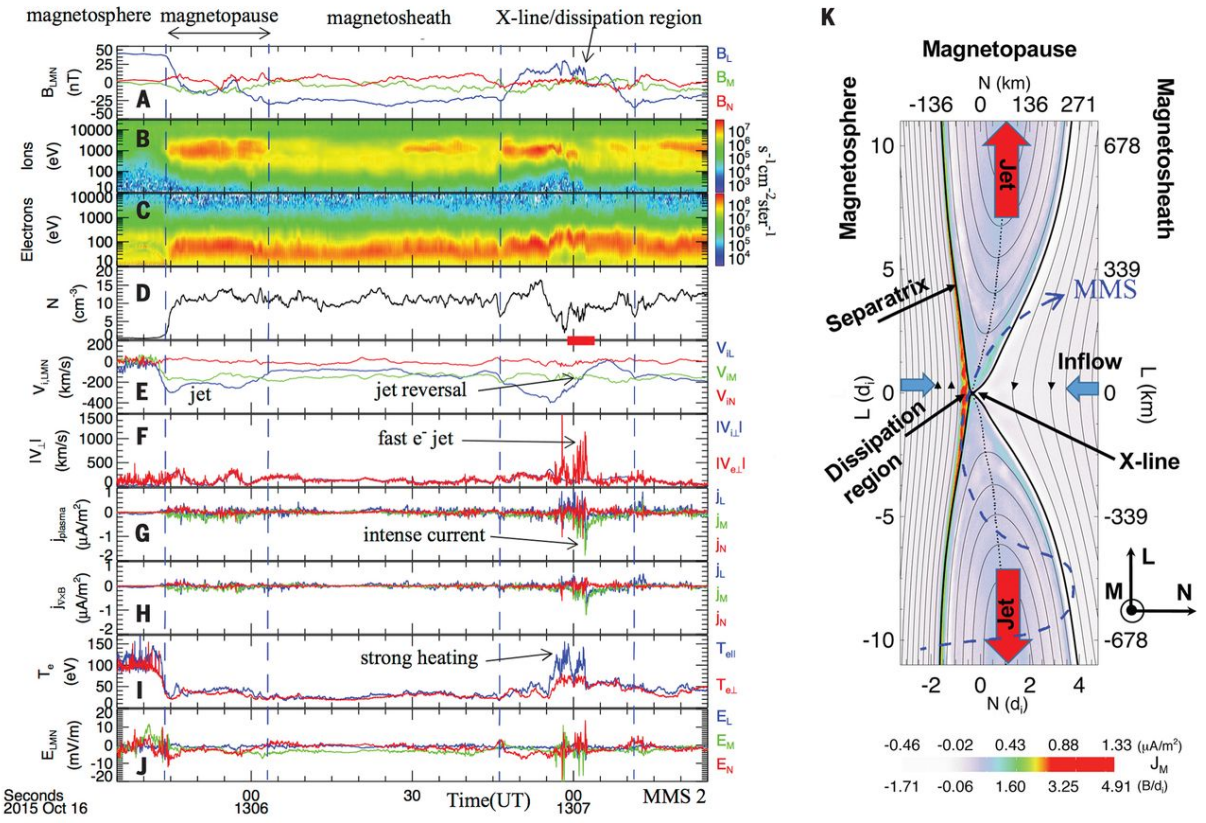

Figure 1.8: (A) - (J) show time series of MMS data for the diffusion region encounter presented by Burch et al. (2016b). The panels show: (A) the magnetic field components; (B) & (C) the ion and electron energy spectrograms; (D) the number density; (E) the ion velocity; (F) the ion and electron velocity magnitude perpendicular to the magnetic field; (G) & (H) the current density as measured and calculated by the curlometer technique; (I) the electron temperature; (J) the electric field. (K) shows a magnetic reconnection simulation of a similar event, with an over-plot of the inferred spacecraft trajectory. A LMN reconnection coordinate system is used in which where L is the direction of the reconnecting component of the magnetic field and N is the magnetopause normal. The red bar between panels (D) and (E) highlights the diffusion region encounter. *From Burch, J. L., et al. 'Electron-scale measurements of magnetic reconnection in space.' Science 352.6290 (2016): aaf2939. Reprinted with permission from AAAS.*

Evidence for the direct observation of the EDR comes from the electron velocity space distributions. Simulations by Hesse et al. (2014) predicted that inside the EDR when electrons decouple from the magnetic field, becoming demagnetised, they should have crescent-shaped distributions in the velocity plane perpendicular to the magnetic field. This first EDR observation by Burch et al. (2016b) confirmed this to be the case. It has been suggested that these crescent-shaped distributions are due to particles meandering near the magnetic field reversal (Lapenta et al., 2017).

1.2.5 Particle Heating and Acceleration

During magnetic reconnection, energy stored in the magnetic field is converted into kinetic and thermal energy of the particles in the plasma; populations of particles can be accelerated to above the thermal background level of the plasma (Phan et al., 2013, 2014). The acceleration of electrons to high energies is of wide importance in solar, astrophysical and laboratory plasmas (e.g. Hudson and Ryan, 1995; Blandford and Ostriker, 1978; Modena et al., 1995), and has been observed in many plasma environments. In the magnetosphere, Øieroset et al. (2002) provided the first measurement of such high-energy electrons in the magnetotail reconnection diffusion region, observing electron energies up to 300 keV and very little response form the ions. Further magnetotail observations by Taylor et al. (2006) found electron beams of energy up to 400 keV. Multiple different mechanisms have been proposed for particle energisation during magnetic reconnection to explain these high energy particle observations, however, it is not yet known which are viable or dominant.

Many acceleration mechanisms revolve around acceleration by the electric fields present in magnetic reconnection. From the Lorentz force law (Equation 1.7), we find that a magnetic field does no work on the particle and results only in the gyration of the particle around the magnetic field, and therefore an electric field is required for particle acceleration. Acceleration by the Hall electric field, produced by charge separation in the diffusion region during reconnection (see Figure 1.2), was originally proposed as an acceleration mechanism (Shay et al., 1998). However, Taylor et al. (2006) suggested that Hall acceleration was not of great enough magnitude to explain the high energy electrons beams that they observed. Hoshino (2005) proposed a 'surfing' mechanism in which a polarization electric field produced across the reconnection current sheet can trap electrons in a potential well, where they are then accelerated. Similarly, Egedal et al. (2005) suggested that electric fields that are produced parallel to the magnetic field during reconnection could trap and accelerate particles. These theories highlight a key

theme of acceleration mechanisms: the need to trap particles in a region to then allow their subsequent acceleration.

An alternative acceleration mechanism that does not require acceleration by electric fields was proposed by Drake et al. (2006a). In this mechanism, particles are instead trapped on the magnetic field lines in magnetic islands, which are closed loops of magnetic field produced during reconnection and are discussed in greater detail in the following section. The electrons are accelerated by a process similar to Fermi acceleration, where particles gain energy as they bounce between the ends of the contracting magnetic islands. This mechanism was demonstrated using a particle-in-cell (PIC) simulation, as can be seen in Figure 1.9. Drake et al. (2012) showed that this mechanism produced acceleration which is consistent with the electron energy spectra observed throughout the heliosphere. Chen et al. (2007) provided the first simultaneous observations of energetic electrons and magnetic islands produced during reconnection. They found that the electron fluxes peaked at sites of compressed density within the islands. However, the acceleration mechanism was not confirmed.

Fu et al. (2011) investigated electron acceleration in the dipolarisation front during magnetotail reconnection. This is the leading edge of the newly reconnected field lines moving towards the Earth in the magnetotail. They suggested that two processes were responsible for the acceleration in the reconnection outflow jets: betatron and Fermi acceleration. Betatron acceleration results from the conservation of the first adiabatic of the plasma which is associated with a particle's gyromotion and known as the magnetic moment ($\mu_m = \frac{mv_\perp^2}{2B}$). This conservation means that an increase in the magnetic field strength results in an increase in the perpendicular particle velocity. They determined that Fermi acceleration dominates in a decaying flux pileup region (where the magnetic field is enhanced around the dipolarisation region) whereas betatron dominates inside a growing flux pileup region. A further study by Fu et al. (2013) proposed that unsteady reconnection causes electron acceleration. The study found that betatron acceleration was responsible for at least half of the energy gain in the peak observed fluxes.

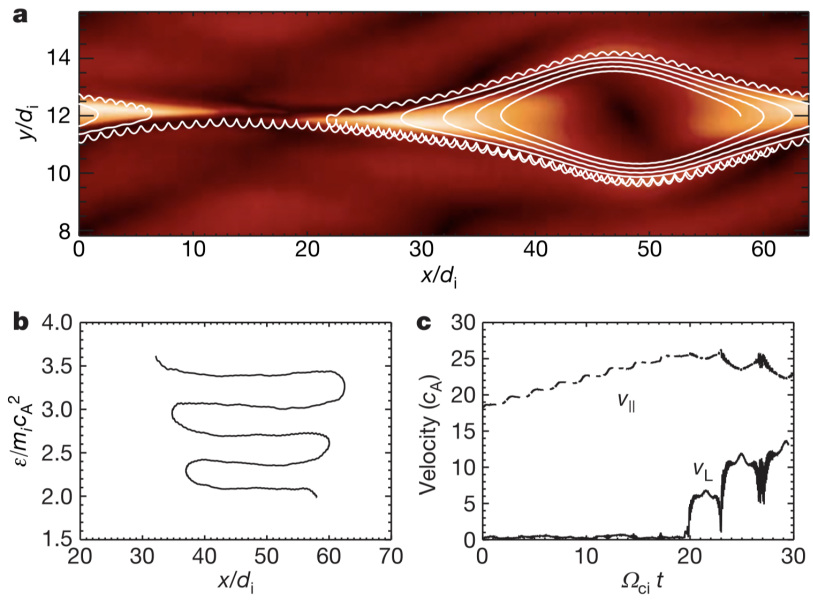

Figure 1.9: Diagram of the Fermi acceleration mechanism inside a contracting island as proposed by Drake et al. (2006a). (a) shows the motion of an electron through the island, where it is gyrating around and moving along the magnetic field lines. (b) shows the energy gain of the particle as a function of its position. (c) shows the change the the electron's parallel ($v_{||}$) and gyration (v_L) velocities as it is accelerated. *Figure from Figure 2 of Drake et al. (2006a).*

1.3 Magnetic Flux Ropes in the Earth's Magnetosphere

In Section 1.2, we have discussed magnetic reconnection as a largely steady-state process, however, this is not generally true. Magnetic reconnection varies depending on the incoming plasma conditions; magnetopause reconnection depends on the variable incoming solar wind conditions as discussed in Section 1.2.1. During such transient reconnection, we commonly observe bipolar magnetic field signatures known as magnetic islands in two dimensions and becoming helical magnetic field structures known as flux ropes in three dimensions. Flux ropes are observed in almost all environments in which we observe magnetic reconnection, highlighting the inherently time-variable nature of the process. Flux ropes are observed on the Sun and in the solar wind (Liu et al., 2020), in planetary magnetospheres, including the Earth, Mercury, Mars and Saturn (Russell and Elphic,

1978; DiBraccio et al., 2015; Briggs et al., 2011; Jasinski et al., 2016), and in ionospheres, such as at Jupiter's moon, Titan (Martin et al., 2020). Flux ropes are also observed in magnetic reconnection simulations (e.g. Drake et al., 2006b; Daughton et al., 2011b).

At the magnetopause, flux transfer events (FTEs) are observed as bipolar signatures in the component of the magnetic field normal to the magnetopause and typically consist of helical magnetic field structures known as flux ropes. FTEs were first identified by Russell and Elphic (1978) in ISEE magnetometer data, as shown in Figure 1.10. They suggested that they could be an integral feature of reconnection. FTEs are typically observed to have a size of 1 to a few Earth radii (R_E) (Sonnerup et al., 2004) and have flux contents ranging between $1 - 10$ MWb (Rijnbeek et al., 1984). FTEs produced near the subsolar point have been observed to travel poleward over the magnetosphere (Berchem and Russell, 1984), facilitating the transport of magnetic flux from the magnetopause into the magnetotail as part of the Dungey cycle (Section 1.2.2) and potentially being responsible for 13% of the open flux in the polar cap (Fear et al., 2017). In this section, we will discuss magnetopause flux ropes and their importance in the study of magnetic reconnection.

1.3.1 Magnetopause Flux Ropes

Flux ropes on the magnetopause are identified by a bipolar signature in the component of the magnetic field normal to the magnetopause along with a corresponding increase in magnetic field strength due to the increase in axial field strength at the core of the flux rope. Eastwood et al. (2016) presented MMS observations of two flux ropes on 16 October 2015 at 13:04:05 UT, as can be seen in Figure 1.11. Here, the geocentric solar ecliptic (GSE) coordinate system is used, which is similar to GSM; the X-axis also points towards the Sun, however, the Z-axis is now defined as perpendicular to the plane of the Earth's orbit around the Sun. In this coordinate system, the normal to the magnetopause is $\sim \quad B_X$ near the subsolar point. These flux ropes are observed in a reconnection

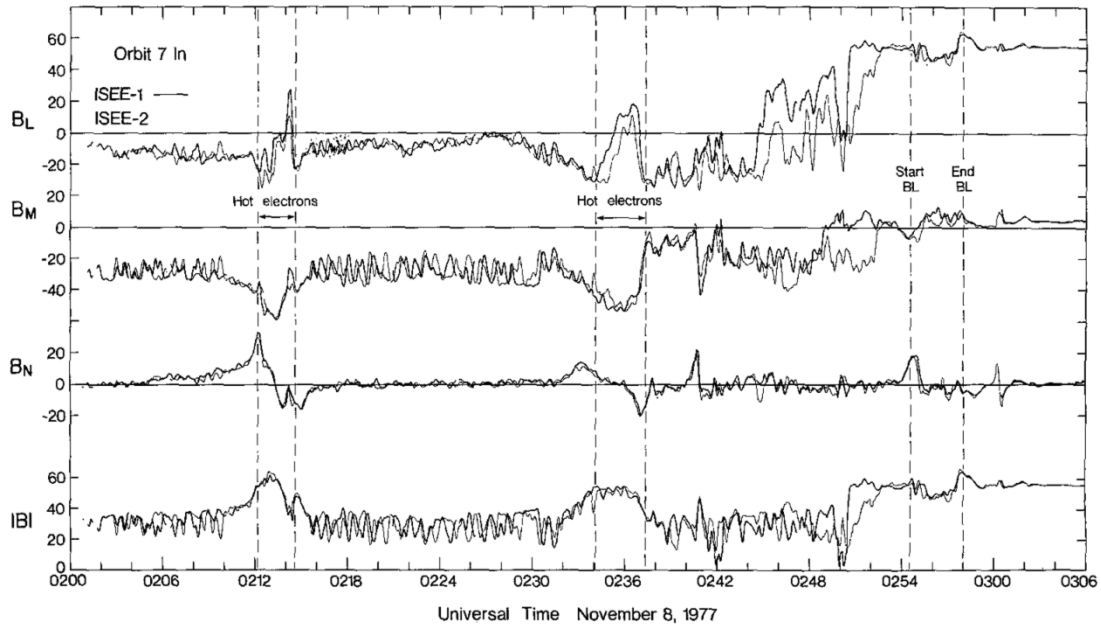

Figure 1.10: FTE observations by Russell and Elphic (1978) during an ISEE magnetopause encounter. Two FTEs are identified by bipolar B_N signatures and corresponding increases in $|\mathbf{B}|$. *Figure from Figure 9 of Russell and Elphic (1978).*

outflow jet, shortly before an encounter with the EDR, and are moving southward over the spacecraft (the plasma has negative v_Z, see panel (g)). Using this and the magnetic field observations, the two negative to positive B_X bipolar signatures (panel (c)) can be used to sketch the path of the spacecraft through the structures, as can be seen in Figure 1.11 (q).

Eastwood et al. (2016) found these flux ropes to be small-scale with diameters on the order of ion-scales ($\sim 7\ d_i$) and to have small flux contents ($\sim 22\ kWb$), orders of magnitude smaller than previously reported values. They concluded that these flux ropes represent a new class of FTE which is generated by secondary reconnection (multiple X-lines) at the magnetopause. The following section discusses this and other proposed flux rope formation mechanisms.

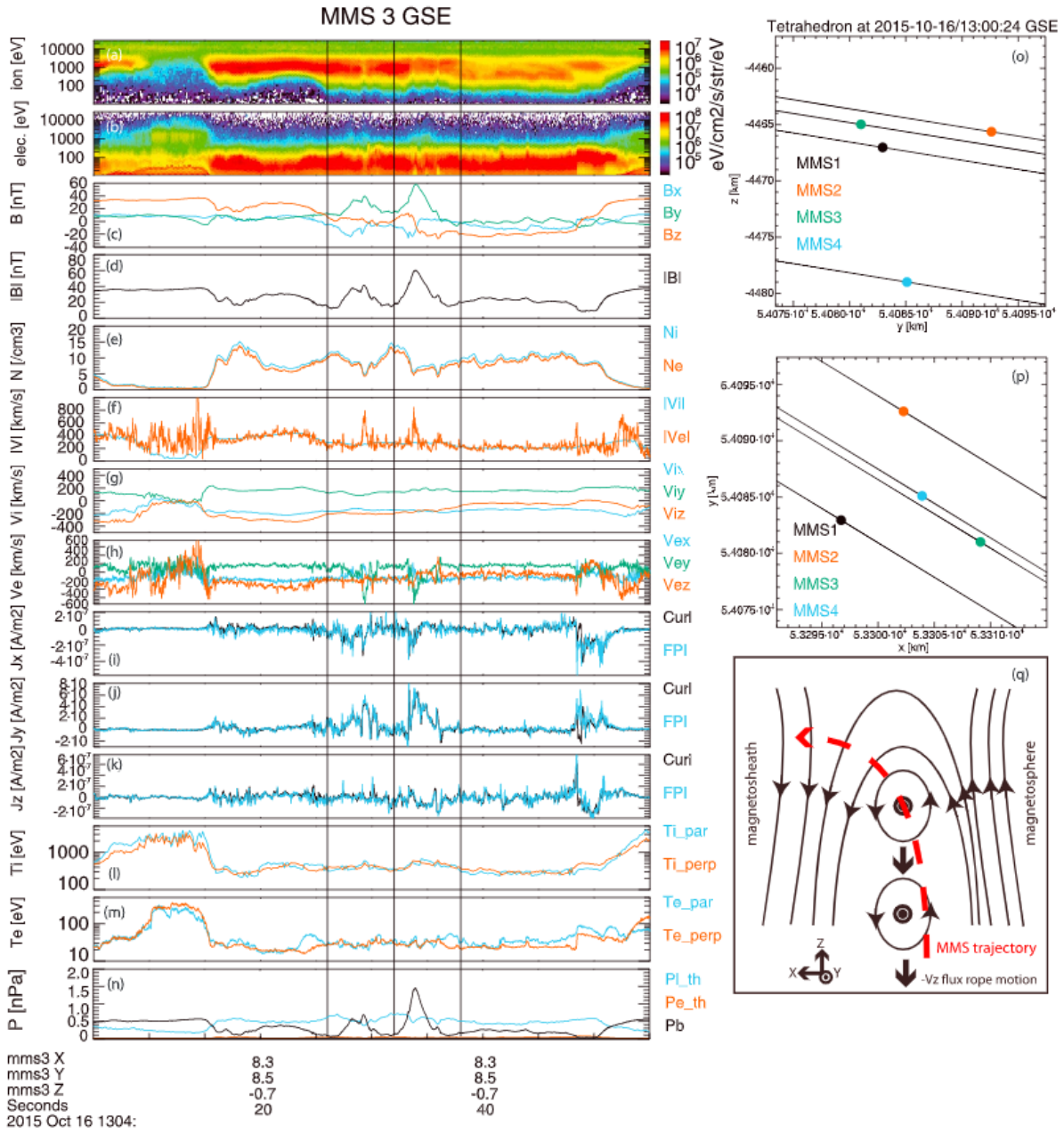

Figure 1.11: (a) - (n) show time series of MMS data for the flux rope observations presented by Eastwood et al. (2016) in GSE coordinates. The panels show: (a) & (b) the ion and electron energy spectrograms; (c) & (d) the magnetic field components and magnitude; (e) & (f) the number densities and velocities; (g) & (h) the ion and electron velocities; (i), (j) & (k) the component current densities as measured and calculated using the curlometer technique; (l) & (m) the ion and electron temperatures; (n) the ion, electron thermal and magnetic pressures. (o) and (p) show the MMS tetrahedron formation during the measurements. (q) shows a diagram of the spacecraft trajectory through the structures. *Figure from Figure 1 of Eastwood et al. (2016).*

1.3.2 Flux Rope Formation Mechanisms

There are multiple proposed methods for FTE formation during magnetic reconnection, mostly requiring the reconnection to be non-steady-state or adding complexity to the picture of a single predictable magnetopause X-line. Each mechanism results in a different field configuration for the FTE as described below:

1. The bursty reconnection model (Russell and Elphic, 1978) suggests FTEs can be produced by spatially and temporally limited bursts of reconnection on the dayside magnetosphere. This results in two flux ropes with limited azimuthal extents; the two flux ropes join at a kink creating a hole in the magnetopause and resulting in an 'elbow'-shaped flux rope, an example of which can be seen in Figure 1.12 (a) and (b).

2. The single X-line model (Scholer, 1988; Southwood et al., 1988) suggests temporal variations in reconnection can lead to the formation of FTEs as bulges in the magnetopause (Figure 1.12 (e) and (f)).

3. The multiple X-line model suggests FTEs can be formed between multiple X-lines during a reconnection event (Lee and Fu, 1985). This results in extended flux ropes formed between consecutive X-lines. An example of an FTE resulting from two X-lines can be seen in Figure 1.12 (c) and (d).

It is important to note that despite all these mechanisms resulting in FTEs with a characteristic magnetopause bipolar signature, only the bursty and multiple X-line models result in FTEs containing flux ropes.

There have been observations of FTEs that are consistent with the single X-line formation mechanism (mechanism 1 above, e.g. Dunlop et al., 2005) and the bursty reconnection mechanism (mechanism 2 above, e.g. Varsani et al., 2014). However, the multiple X-line formation mechanism has been most widely identified (e.g. Hasegawa et al., 2010; Øieroset et al., 2011), with MMS allowing for the identification of ion-scale flux ropes

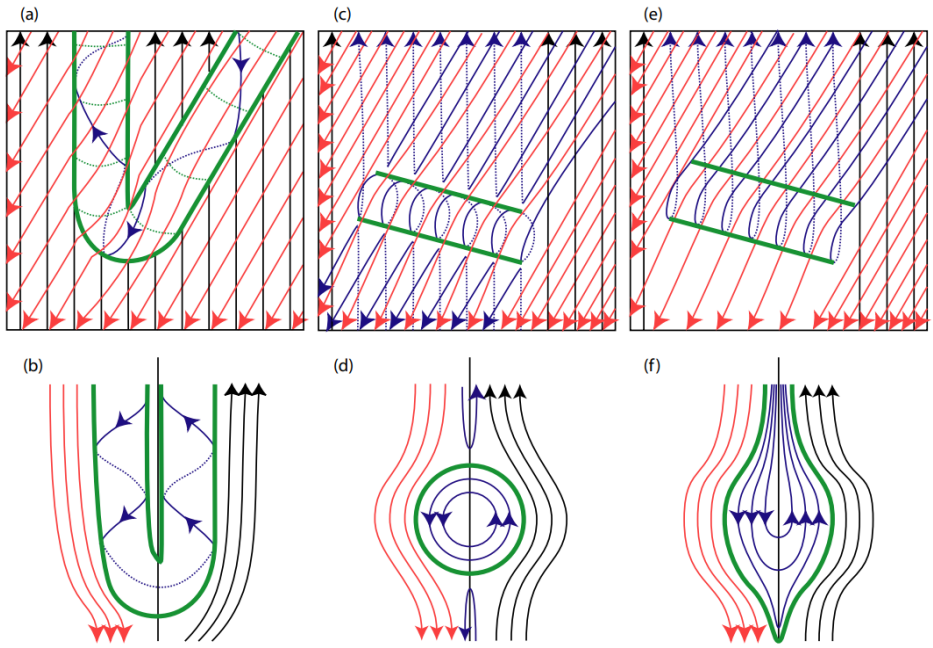

Figure 1.12: Diagram of different FTE models with a 150° magnetosheath field clock angle. Magnetosheath field lines are shown in red and magnetospheric field lines in black. Blue field lines represent 'open' reconnected field lines. The boundaries of the FTEs are shown in green. (a) and (b) illustrate the bursty reconnection formation model proposed by Russell and Elphic (1978). (c) and (d) illustrate the multiple X-line model proposed by Lee and Fu (1985). (e) and (f) illustrate the single X-line model proposed by Scholer (1988) and Southwood et al. (1988). *Figure from Figure 1 of Fear et al. (2008).*

produced by this mechanism (Eastwood et al., 2016, as discussed in the previous subsection). Hwang et al. (2018) introduced a new aspect to this FTE generation mechanism; they observed a series of ion-scale flux ropes formed between two X-lines that were unstable due to the tearing instability. The tearing instability (Furth et al., 1963) leads to the formation of magnetic islands, suggesting that it could be responsible for the flux ropes observed in this study. Such small, ion-scale magnetic islands are also observed in simulations; Drake et al. (2006b) observed secondary islands formed during reconnection using a full particle-in-cell simulation. They found that the ambient guide field controls whether reconnection remains steady or becomes bursty, with a stronger guide field (i.e. component reconnection) producing longer, unstable X-lines which produce secondary islands.

1.3.3 Topology, Substructure and Evolution

FTEs have been observed to contain a mixture of both magnetospheric and magnetosheath plasma (Thomsen et al., 1987), showing that the magnetic field lines they contain can be connected to both regions, and reinforcing the requirement for reconnection in their formation. The connectivity of the flux ropes (i.e. the plasma source at the end of a magnetic field line) is closely related to the topology of the flux rope, which can be defined as open (with one end connected to the magnetosphere and the other to the magnetosheath) or closed (with both ends either connected to the magnetosphere or magnetosheath). Fu et al. (2013) observed an FTE in which all potential flux rope topologies were observed, suggesting that FTEs can contain interesting substructure. This is further reinforced by Owen et al. (2001) who observed FTE substructure on the order of the Cluster spacecraft separation of $\sim$ 600 km. The topology and substructure of the flux rope can help determine their formation mechanism; Varsani et al. (2014) used observations of cold plasma in the core of the FTE and antiparallel electrons at the edge to determine a bursty reconnection formation mechanism.

Once they are formed, FTEs are observed to move poleward over the magnetosphere (Berchem and Russell, 1984). This has been confirmed using remote sensing techniques to observe ionospheric signatures of FTEs (e.g. Milan et al., 2000). FTEs observed in the magnetospheric cusps have greater diameters than those observed at the magnetopause (Fermo et al., 2011; Akhavan-Tafti et al., 2018), suggesting they grow in size during this poleward motion (Rijnbeek et al., 1984). One mechanism proposed for this FTE growth is FTE coalescence; in simulations, magnetic islands produced by reconnection are observed to merge together via subsequent reconnection to produce larger magnetic islands (Daughton et al., 2011b). The observation of reconnection at the centre of FTEs (Øieroset et al., 2016; Fargette et al., 2020) could be due to reconnection between two flux ropes, potentially verifying this coalescence theory.

The evolutionary state of flux ropes has been investigated by identifying the forces

acting on the flux rope (e.g. Zhao et al., 2016). For a flux rope that is in steady-state and not evolving, we would expect to observe balanced forces on the plasma contained by the flux rope. Such force-free flux rope models have been developed and applied to flux ropes in the magnetosphere, and have been found to be consistent with observations (Eastwood et al., 2012a). However, non-force-free flux ropes have also been observed (Teh et al., 2017). This has consequences for potential flux rope particle acceleration mechanisms; Drake et al. (2006a) suggested that contracting islands can accelerate electrons via a Fermi-like acceleration process. This would require a non-force-free flux rope with forces on the contained plasma acting to contract the flux rope.

1.4 Open Questions on Magnetopause Reconnection and Flux Ropes

One of the main open questions in the study of magnetic reconnection is how energy is transferred from the magnetic energy stored in the magnetic field to the kinetic and thermal energy of the ejected plasma (Yamada et al., 2018). There are multiple proposed mechanisms, as discussed in Section 1.2.5, however, there is no consensus on which operate under which conditions and where each process is dominant. There is also the potential for some yet-undiscovered mechanism to be taking place. Understanding this energy transfer process will not only develop our understanding of this fundamental plasma physics process but has direct implications for our space weather resilience. As discussed in Section 1.2, magnetic reconnection couples the solar wind and magnetosphere and is one of the main drivers of magnetospheric dynamics. The energy transferred in the process also drives space weather events, impacting satellites in space and infrastructure on Earth.

Flux ropes are a fundamental feature of magnetic reconnection and are produced when the process is transient in nature. As such, they are an integral feature of the

process and have implications for how reconnection can transfer energy. Flux ropes have been suggested as a location for electron acceleration (Drake et al., 2006a) and have been observed to contain high energy particles (Chen et al., 2007). There is still a lot that is not fully understood about flux ropes, such as if they can be formed within the electron diffusion region (EDR) or further downstream in the reconnection exhaust, their role in flux transport in the Dungey cycle and how they evolve and interact once they are formed.

In this thesis, we will use Magnetospheric Multiscale (MMS) mission data to investigate flux ropes, their relationship to the EDR and their role in particle acceleration. The MMS misson and the data analysis techniques employed are introduced in the following section. Chapter 3 presents a survey of flux ropes observed on days on which the EDR was also encountered by MMS as reported by Webster et al. (2018). The size and flux content of the flux ropes are investigated, as well as the relationship of the flux ropes to the respective EDR encounters, with the aim of addressing if the flux ropes are produced by the EDR and how they relate to the ongoing reconnection. Chapters 4 and 5 continue to investigate these 245 EDR-associated flux ropes, looking at their force-free nature and topology, respectively, and exploring potential flux rope formation mechanisms and subsequent evolution. Chapter 6 presents two observations of a new potential electron acceleration mechanism for magnetic reconnection in which electrons are trapped in magnetic mirror structures on the edge of magnetopause flux ropes. Finally, Chapter 7 concludes the thesis, summarising it's findings and the directions for future research.

Chapter 2

Instrumentation and Methodology

2.1 The Magnetospheric Multiscale Mission

The Magnetospheric Multiscale (MMS) mission is a flagship NASA mission which was launched in March 2015 and aims to advance our understanding of magnetic reconnection in the Earth's magnetosphere. MMS is a multi-spacecraft mission consisting of four probes each containing the same instrumentation, allowing the separation of spatial and temporal evolution of observed structures via the application of multispacecraft analysis techniques (see Section 2.3). These instruments can measure the thermal electron and ion 3D distributions at 30 ms and 150 ms time resolution, respectively, at spacecraft separations down to a few kilometers. This allows magnetic reconnection to be examined down to electron scales for the first time. The mission's statement is to *'Understand the microphysics of magnetic reconnection by determining the kinetic processes occurring in the electron diffusion region that are responsible for collisionless magnetic reconnection, especially how reconnection is initiated.'* - Burch et al. (2016a).

The MMS mission instrumentation is divided into 3 groups which are discussed below: the Hot Plasma Suite (Section 2.1.1), the Energetic Particle Detector (EPD, Section 2.1.2), and the FIELDS Suite (Section 2.1.3). These groups contain multiple instruments, as illustrated in Figure 2.1. In this thesis, we primarily use particle data

from the Fast Plasma Investigation (FPI, part of the Hot Plasma Suite) and magnetic field data from the FIELDS suite; these instruments will receive a particular focus in the following discussion. Section 2.1.4 describes the orbits, spacecraft separation and data sampling techniques employed by the mission.

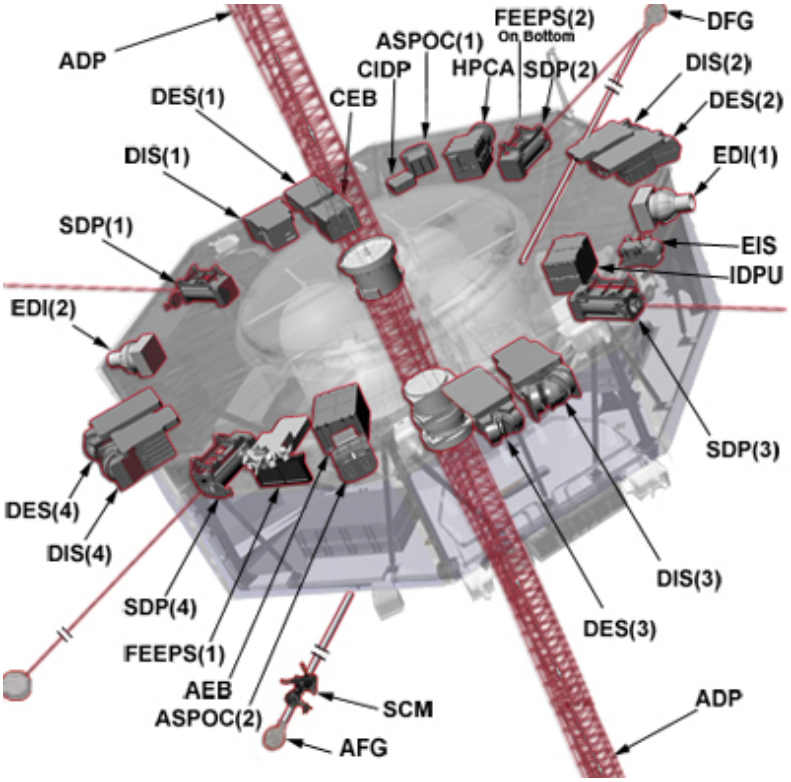

Figure 2.1: MMS instrumentation. *Figure from the official NASA website (NASA et al., 2021).*

2.1.1 Hot Plasma Suite

The Hot Plasma Suite consists of two instruments: the Fast Plasma Investigation (FPI) and the Hot Plasma Composition Analyser (HPCA). FPI is an electrostatic analyser which measures the directional flux of magnetospheric particles (Pollock et al., 2016). Particles enter the instrument through a narrow opening with a specified angular field of view and are electrostatically deflected by 90°. Only particles of specific energy per charge values will be deflected by the correct amount to be detected by the instrument's sensors; the

voltage applied between the deflector walls is varied to sample different particle energies. The direction and speed of these particles are measured to create a velocity distribution from which higher order plasma moments can be calculated. Each MMS spacecraft has four dual 180° electron (DES) and ion (DIS) electrostatic analysers which are located in the spin plane of the spacecraft and combine to provide a full-sky view of the plasma. They can measure 32 different energies ranging between 10 eV - 30 keV. The electron flux can be measured every 30 ms and ions every 150 ms giving a measurement rate 100 times greater than has been previously achieved. The accuracy of FPI's ion and electron measurements means it is able to directly resolve the current density, a measurement which has often been unreliable in previous missions. As well as this, the current density can be calculated using the curlometer technique (Section 2.3.2) to verify measurements.

HPCA measures the composition of the plasma that MMS encounters, again using an electrostatic analyser with an added time of fight measurement (Young et al., 2016). Using this time, the mass, and therefore type, of the particle can be measured. Each spacecraft has one detector which spins with the spacecraft and scans the sky every 20 s.

2.1.2 Energetic Particle Detector (EPD)

The Energetic Particle Detector (EPD) consists of two instruments: The Fly's Eye Energetic Particle Sensor (FEEPS) and the Energetic Ion Spectrometer (EIS) (Mauk et al., 2016). Together these instruments measure the energy, angle, and composition of incoming ions present in the plasma environment of the solar wind and magnetosphere. FEEPS consists of a solid-state silicon detector which produces a current when hit by a particle, allowing the energy of the particle to be measured. There are two instruments per spacecraft which measure instantaneous full-sky distributions ranging from 25 keV to > 0.5 MeV for electrons and 25 keV to > 0.5 MeV for ions. EIS measures ion mass in a similar way to HPCA (Section 2.1.1) and can measure energies ranging from 20 keV to > 0.5 MeV. The measurements of the two instruments are combined to produce a full-sky

ion distribution.

2.1.3 FIELDS Suite

The FIELDS instrument suite provides measurements of the vector magnetic and electric fields (Torbert et al., 2016). The suite consists of multiple instruments; there are both analog and digital fluxgate magnetometers (AFG and DFG, respectively), the electron drift instrument (EDI), spin-plane and axial double probes (SDP and ADP) and a search coil magnetometer (SCM), which are coordinated using the central electronics box (CEB).

The fluxgate magnetometers work by inducing a magnetic field in a ring core of permeable material using a driving coil of wire wrapped around the core which will then symmetrically desaturate when the inducing current is removed if there is no background magnetic field. In the presence of a background field, the permeable material desaturates unevenly, allowing the background field to be measured. Three axis sensors are combined to measure the full vector magnetic field. The magnetometers are mounted at the end of 5 m booms and can measure fields up to $\sim$ 500 nT in low range and up to $\sim$ 8200/10500 nT (AFG/DFG) for high range measurement modes, with a timing accuracy $>$ 0.1 ms and at frequencies up to 6 kHz. Together the two instruments provide full redundancy.

ADP and SDP measure the electric field using the double probe technique where the voltage difference is measured between two electrodes in order to determine the electric field; the voltage of the electrodes changes according to the plasma environment such that the net current on the sphere is zero, and the electric field can then be calculated as the gradient of these measured potentials. SDP consists of four electrodes placed at the end of 60 m booms in the spin plane of the spacecraft and ADP consists of two sensors in the spin axis of the spacecraft located on $\sim$ 15 m booms. Together the instruments measure the 3D electric field with an accuracy of 0.5 mV/m up to frequencies of 100 kHz.

SCM measures the fluctuations of the magnetic field in 3D using a coil wrapped

around a ferromagnetic material and measuring the resulting voltage. It can measure fluctuations in the range of 1 Hz - 6 kHz, meaning most plasma fluctuations of intrest can be detected.

Finally, EDI measures the electric and magnetic fields geometrically by firing electrons into the plasma, which then undergo an $\mathbf{E} \times \mathbf{B}$ drift according to the ambient conditions and can be detected back at the spacecraft after completing a single gyration. EDI operates at a rate of 10 samples per second and can be combined with the previously described measurements to increase the overall accuracy of the FIELDS suite.

2.1.4 Orbits and Data Selection

The MMS orbits are designed to optimally sample magnetic reconnection at both the magnetopause and in the magnetotail, $\sim 12\ R_E$ and $\sim 25\ R_E$ from Earth, respectively. Sampling these regions requires two different orbits, meaning the mission has been separated into different phases: Phase 1 samples the magnetopause and Phase 2 samples the the magnetotail. The orbits are designed by placing the apogee, where the dwell time is maximised as the spacecraft velocity decreases, in these two regions. These orbits have a perigee $\times$ apogee of $1.2 \times 12\ R_E$ for Phase 1 and $1.2 \times 25\ R_E$ for Phase 2. In Phase 1 the orbits remain within $\pm\ 25°$ of the ecliptic plane to target the subsolar region where electron diffusion region (EDR) encounters are more likely.

In this thesis we use data from the magnetopause-focused phase of the mission, with orbits as shown in Figure 2.2. The predicted spacecraft orbits for Phase 1 of the mission are shown in green, with predicted magnetopause crossings in red. Phase 1a is shown in the first column and will take $\sim$ 6 months to complete. Phase 1b is shown in the second column and has fewer predicted magnetopause encounters as it will take $\sim$ 4 months to complete.

During the mission, the spacecraft separation can be adjusted to allow sampling over the range of predicted diffusion region sizes; the thickness $\times$ width of the magne-

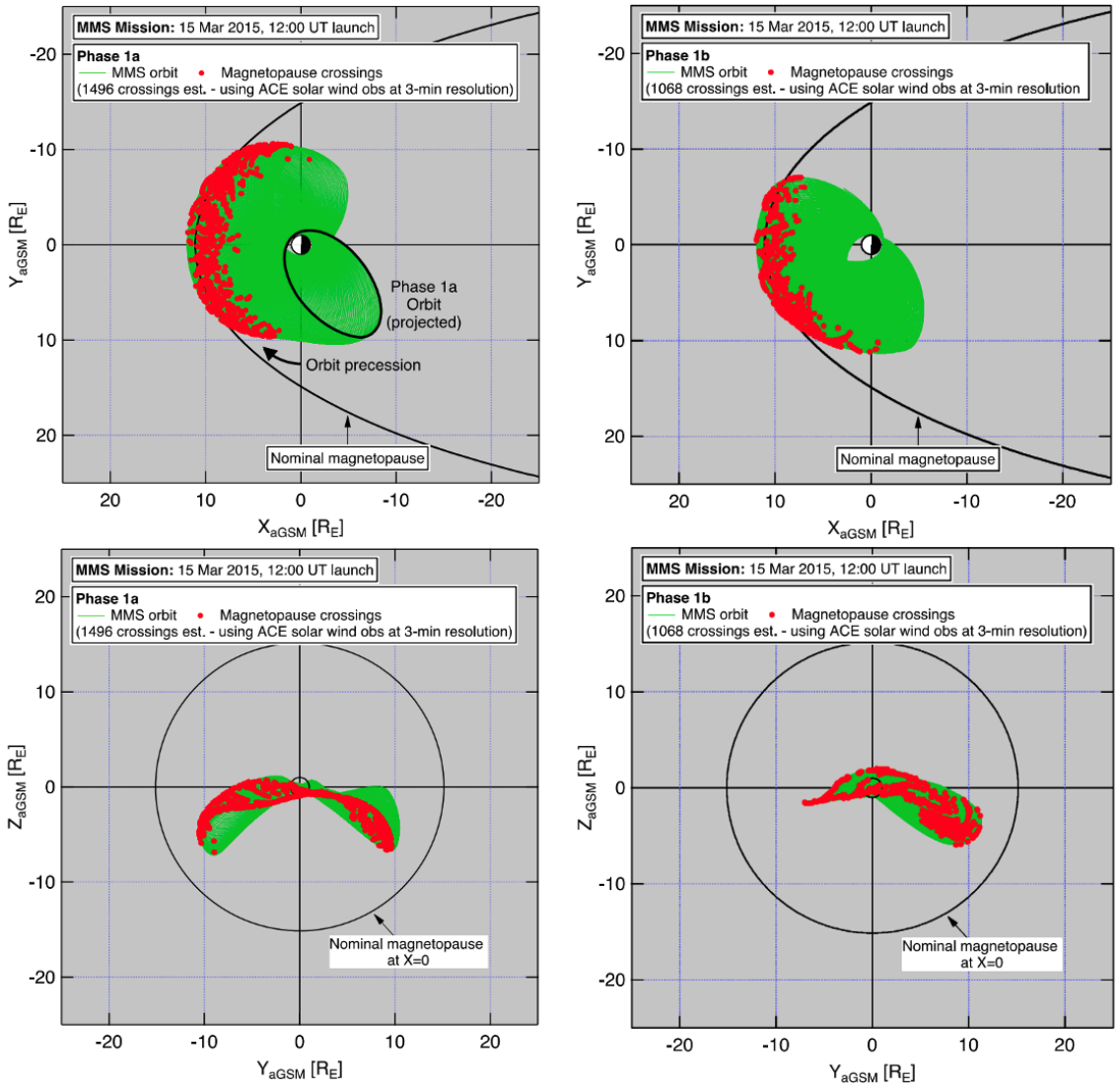

Figure 2.2: MMS Phase 1 orbits targeting magnetopause reconnection. The top panels show the orbits in the GSM X-Y plane and the bottom panels show the orbits in the GSM Y-Z plane. The black curves in the top panels and circles in the bottom panels show the average position for the magnetopause boundary. In the top panels, the black oval and subsequent green overlayed ovals show the precession of the MMS orbits. The red dots show the predicted magnetopause encounters. *Figure 1 and 2 of Fuselier et al. (2016).*

topause diffusion region has been predicted to be as small as 1 × 10 km or as large as 30 × 300 km (Fuselier et al., 2016). The separation is varied from 10 - 160 km. If the diffusion region size is on the order of the smaller scales, then the minimum spacecraft separation targets sequential encounters of the diffusion region. If the diffusion region is on the order of the larger estimates, the minimum separation instead allows simultane-

ous measurements within the diffusion region, however this means that the probability of encountering the region is reduced. During the first two months of each phase the separation was adjusted every 15 days and the measurements analysed to identify an optimum separation for the remainder of the phase.

The instruments discussed above have been designed to collect data at unprecedented rates. However, the retrieval of this data is limited by low transmission rates to the ground. This is addressed by only a small percentage of the data being transmitted in the highest resolution burst mode. Burst data selections are made by scientists monitoring the data for interesting features such as magnetopause crossings (Phan et al., 2016).

2.2 Minimum Variance Analysis (MVA)

Minimum variance analysis (MVA) is a commonly used tool in spacecraft data analysis and is used to identify the normal to one-dimensional transition layers in a plasma, such as a current sheet or wavefront (Sonnerup and Scheible, 1998). As a spacecraft moves through a structure measuring the vector magnetic field, MVA identifies the component of the field that varies least; this is the normal to the 1D transition which is assumed to be constant. Mathematically, the 1D layer is expressed as $\partial/\partial x = 0$, $\partial/\partial y = 0$, with the normal to this layer along the z-axis for which $\nabla \cdot \mathbf{B} = \partial B_z/\partial z = 0$.

The minimum magnetic field component is identified by finding the unit normal vector, $\hat{\mathbf{N}}$, which minimises the standard deviation of the magnetic field values from their mean values, given by the equation

$$\sigma^2 = \frac{1}{S}\sum_{i=1}^{S} |(\mathbf{B_i} - \langle \mathbf{B} \rangle) \cdot \hat{\mathbf{N}}|^2 \tag{2.1}$$

where $\langle \mathbf{B} \rangle = \frac{1}{S}\sum_{i=1}^{S} \mathbf{B_i}$ and S is the number of magnetic field measurements. This minimisation is achieved through solving the eigenvalue equation for the covariance matrix of the magnetic field components, $\mathbf{M}$, which is defined by

$$M_{\mu\rho} = \langle B_\mu B_\rho \rangle - \langle B_\mu \rangle \langle B_\rho \rangle. \tag{2.2}$$

Solving the eigenvalue equation also identifies the maximum and intermediate variance components, which together make an orthogonal coordinate system.

2.3 Multi-Spacecraft Analysis Techniques

Many of the space plasma phenomena presented in the introduction to this thesis (Section 1) are three dimensional and highly time-variable. As such, a single spacecraft trajectory through a structure is often insufficient to determine how it is evolving and to separate spatial and temporal variations. This led to development of multi-spacecraft missions; initially 2 spacecraft missons, such as ISEE-1 and -2 (Russell, 1978), before 4 spacecraft missions such as Cluster (Escoubet et al., 2001b) and MMS (Section 2.1), which are able to determine field gradients present in the plasma.

The development of such missions, led to the development of multi-spacecraft analysis techniques in order to fully exploit the data (see Paschmann and Schwartz, 2000). Below we present commonly used multi-spacecraft analysis techniques, including gradient analysis methods (Section 2.3.1), the curlometer technique (Section 2.3.2) and timing analysis (Section 2.3.3).

2.3.1 Gradient Analysis Methods

Multi-point spacecraft measurements can be used to determine local spatial gradients in the plasma. Such analysis requires the assumption that measurements are made simultaneously by the spacecraft, and that there are no gradients present on scales smaller than the spacecraft separation. Assuming a cartesian coordinate system, for a given quantity measured at a reference spacecraft 1, Q_1, we can Taylor expand about this spacecraft 1 measurement to first order to find

$$Q_n \approx Q_1 + \frac{\partial Q}{\partial x}(x_n - x_1) + \frac{\partial Q}{\partial y}(y_n - y_1) + \frac{\partial Q}{\partial z}(z_n - z_1), \tag{2.3}$$

where $n = 2, 3, 4$ for the non-reference spacecraft (Shuster et al., 2019). Writing this as a system of equations for all n, we find

$$\begin{bmatrix} (x_2 - x_1) & (y_2 - y_1) & (z_2 - z_1) \\ (x_3 - x_1) & (y_3 - y_1) & (z_3 - z_1) \\ (x_4 - x_1) & (y_4 - y_1) & (z_4 - z_1) \end{bmatrix} \cdot \begin{bmatrix} \frac{\partial Q}{\partial x} \\ \frac{\partial Q}{\partial y} \\ \frac{\partial Q}{\partial z} \end{bmatrix} = \begin{bmatrix} Q_2 - Q_1 \\ Q_3 - Q_1 \\ Q_4 - Q_1 \end{bmatrix}, \tag{2.4}$$

which can be solved to give an estimate for ∇Q. More advanced techniques overconstrain this quantity by using all combinations of spacecraft separations (i.e. using different reference spacecraft) and then use minimisation techniques to find an estimate (see Harvey, 1998, for more details).

2.3.2 The Curlometer Technique

The curlometer technique uses the measured magnetic fields at each of the four spacecraft, which together form the vertices of a tetrahedron, to estimate the current density using Ampere's law (Equation 1.6). In regions where the displacement current ($\mu_0 \epsilon_0 \partial \mathbf{E}/\partial t$) can be neglected, Ampère's law becomes $\mu_0 \mathbf{j} = \nabla \times \mathbf{B}$. Using the integral form of this equation, we find that the current density can be estimated using

$$\mu_0 \mathbf{j}_{av} \cdot (\mathbf{r}_i \times \mathbf{r}_j) = \Delta \mathbf{B}_i \cdot \mathbf{r}_j - \Delta \mathbf{B}_j \cdot \mathbf{r}_i \tag{2.5}$$

where $\mathbf{j}_{av}$ is the average current density measured over the tetrahedron and $\mathbf{r}_i$ and $\Delta \mathbf{B}_i$ are the differences in position vectors and magnetic field vectors between a chosen reference spacecraft and another spacecraft, labelled i. This equation allows us to determine the component of $\mathbf{j}_{av}$ in the direction perpendicular to the plane made by the reference spacecraft and two other spacecraft, i and j. If, for example, spacecraft 1 is chosen as the

reference spacecraft, there are then 3 combinations of the other three spacecraft to chose for i and j, allowing for the full determination of $\mathbf{j}_{av}$. There is also a third combination of the three non-reference spacecraft which can be used to calculate a third redundant current density component.

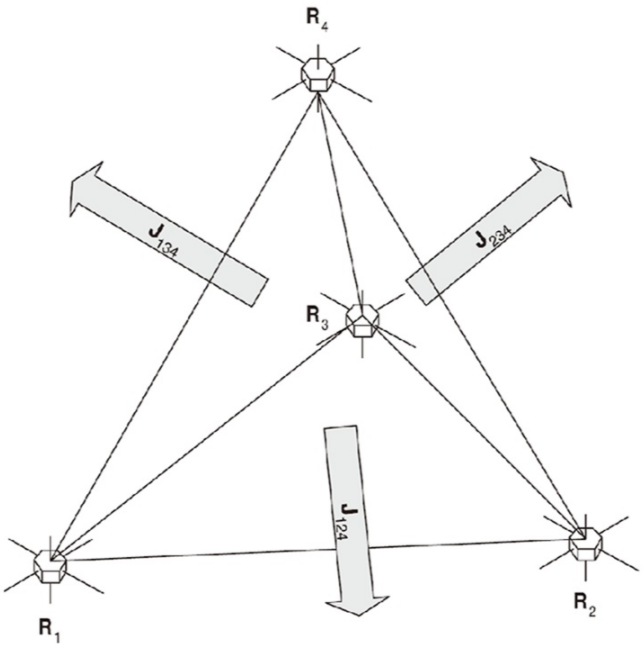

Figure 2.3: Diagram of current estimates determined by the curlometer technique. *Figure 1 of Dunlop et al. (2021).*

2.3.3 Timing Analysis

Timing analysis can be used to determine the normal vector, $\hat{\mathbf{n}}$, and normal speed, V, of a planar discontinuity observed by multiple spacecraft, such as a current sheet. The method requires that four spacecraft observe the same boundary at different times. Assuming this, we find that

$$(\mathbf{r_i} - \mathbf{r_1}) \cdot \hat{\mathbf{n}} = V(t_i - t_1), \tag{2.6}$$

where $\mathbf{r_i}$ and t_i are the spacecraft locations and boundary observation times, respectively, with $i = 2, 3, 4$ for each of the spacecraft, with spacecraft 1 being arbitrarily chosen as

the reference spacecraft. This system of equations can be solved to find $\hat{\mathbf{n}}/V$, giving the normal to the boundary and its speed along this normal direction.

2.4 Force-Free Flux Rope Model

Flux ropes are helical magnetic field structures. When modelled as force-free ($\mathbf{j} \times \mathbf{B} = \mathbf{0}$), we find flux ropes have a simple structure in cylindrical coordinates which varies in the θ and z directions only:

$$B_\theta = B_0 H J_1(\alpha r), \tag{2.7a}$$

$$B_z = B_0 J_0(\alpha r), \tag{2.7b}$$

$$B_r = 0, \tag{2.7c}$$

where B_0 is the peak core field, H is the helicity/handedness of the flux rope ($H = \pm 1$), J_0 and J_1 are Bessel functions and α is a constant. This solution is obtained using the Lundquist (1950) constant-α solution and looks like a cylindrically symmetric helix. Figure 2.4 shows an example of this force-free flux rope magnetic field arrangement, where the axial component, B_z, is labelled B_A and the azimuthal component, B_θ, is labelled B_T.

Flux ropes on the magnetopause can often be modelled as force-free (Xiao et al., 2004). The above model can be fit to spacecraft flux rope observations using minimum variance analysis, as described in Section 2.2. If a spacecraft passes through the centre of such a force-free flux rope, which is invariant along its axis, the minimum variance direction will be identified along the spacecraft trajectory as there will be zero magnetic field in this direction (the spacecraft is always travelling along the B_r direction). In this case, the maximum variance direction would be perpendicular to the spacecraft path and exhibit a bipolar signature with zero field at the centre of the flux rope. The intermediate direction would point along the axis of the flux rope and peak at its centre. Figure 2.4

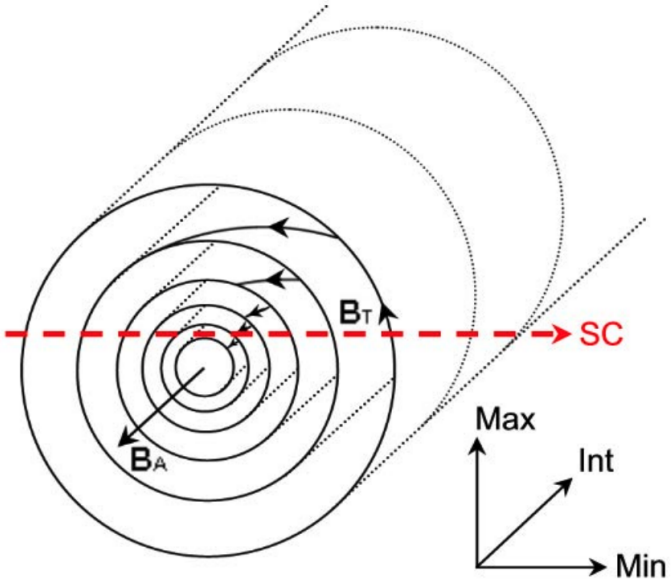

Figure 2.4: Example of a force-free flux rope. MVA coordinates are identified for the spacecraft path through the flux rope in red. *Figure 1 of Henderson et al. (2006).*

shows how MVA would identify a similar coordinate system for a spacecraft trajectory that does not pass through the centre of the flux rope, with the axial component being directed along the intermediate direction and the minimum and maximum directions both containing bipolar field signatures.

Chapter 3

A Survey of Flux Ropes Associated with Electron Diffusion Region (EDR) Encounters

3.1 Introduction

Flux ropes are produced by magnetic reconnection and are commonly observed in the magnetosphere (Russell and Elphic, 1978). They are important for the transfer of flux in the Dungey cycle; flux ropes produced during magnetopause reconnection transfer flux into the magnetotail as they move poleward over the magnetosphere (Fear et al., 2017). Flux ropes and plasmoids produced in the magnetotail are responsible for flux unloading from the tail (Hones Jr., 1984). As such, many previous studies of flux ropes have looked to quantify their properties with this in mind, evaluating their radius, core magnetic field strength and flux content. It has been suggested that flux ropes could be responsible for up to 13% of the open flux in the polar cap (Fear et al., 2017). In such studies, magnetopause flux transfer events (FTEs) are often the focus and simple cylindrical or force-free flux rope models are often assumed to calculate their properties (e.g. Eastwood et al. (2012b)). Magnetospause FTEs are observed to have a size of 1 to a few Earth

radii (R_E) (Sonnerup et al., 2004) and have flux contents ranging between 1 - 10 MWb (Rijnbeek et al., 1984). However, the increased data resolution of recent missions, such as the Magnetospheric Multiscale (MMS) mission, has allowed the observation of small-scale flux ropes of diameter $\sim$ 5 - 11 d_i (e.g. Eastwood et al., 2016; Hwang et al., 2018).

Wang et al. (2005) presents a survey of FTEs observed in the high latitude magnetopause and low latitude flanks by the Cluster mission between 2001 and 2003. Fermo et al. (2011) studies this database of flux ropes further, calculating the diameter of the flux ropes by multiplying the FTE velocity and the observation time length, assuming the spacecraft passes through the centre of the flux rope, i.e. that the impact parameter (IP), which is the fractional distance of the closest approach of the spacecraft to the centre of the flux rope, is zero. Figure 3.1 shows the resulting distribution of flux rope diameters, along with an exponential fit to the tail of the data. The distribution has a mean flux rope diameter of 5280 km. Akhavan-Tafti et al. (2018) studied 55 flux ropes observed during Phase 1a of the MMS mission when the spacecraft were observing the subsolar magnetopause region. This study fits a force-free flux rope model to the flux ropes and only includes flux ropes with an IP < 0.5, as estimated by the force-free model. When the IP was assumed to be zero, they found the flux rope diameter distribution to follow a similar exponential tail distribution with a mean diameter of 690 km, as can be seen in Figure 3.2. When the force-free flux rope model is used to find the flux rope diameter, the mean flux rope diameter to increases to 1670 km. Flux rope coalescence is used to explain the difference in the flux rope diameter observations between these two studies; it is proposed that flux ropes coalesce as they move over the magnetopause, resulting in larger flux ropes with greater flux content being observed at higher latitude (Daughton et al., 2011b). Akhavan-Tafti et al. (2018) also calculates the flux content of the flux ropes using the force-free fit model parameters and finds the mean flux content to be 100 ± 30 kWb.

The formation of flux ropes requires magnetic reconnection to change the topology of the magnetic field, allowing the formation of their helical magnetic field signatures.

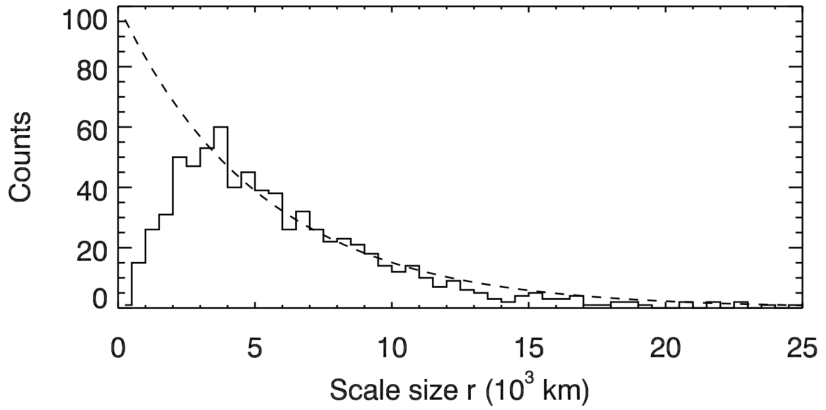

Figure 3.1: Distribution of the diameters of 1098 flux ropes observed by Cluster with an exponential fit to the tail of the distribution. *Figure 7 of Fermo et al. (2011).*

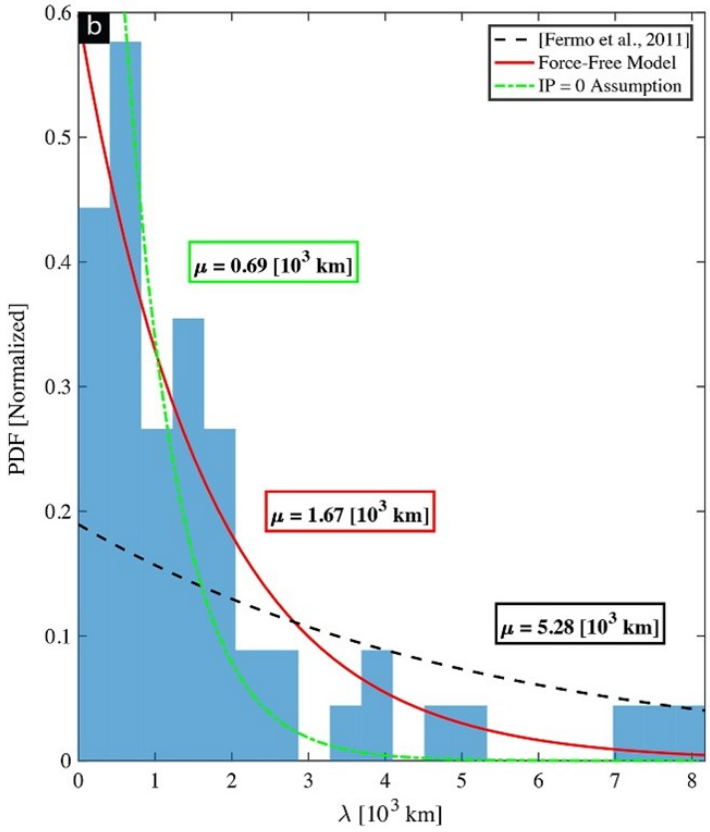

Figure 3.2: Distribution of the diameters of 55 flux ropes observed by MMS. The black curve shows the exponential tail fit from the Fermo et al. (2011) distribution presented in Figure 3.1. The red and green curves are exponential fits for the diameter from a force-free fit model and assuming the IP = 0. *Adapted from Figure 4 of Akhavan-Tafti et al. (2018).*

There are multiple proposed FTE formation mechanisms, all requiring differing ongoing reconnection conditions, these include bursty or patchy reconnection, leading to bulges

in the magnetic field which can display a bipolar magnetic field structure (Russell and Elphic, 1978; Scholer, 1988; Southwood et al., 1988), or multiple X-line models which allow the formation of twisted flux rope structures (Lee and Fu, 1985). There have been many reported observations of flux ropes near ongoing reconnection (e.g. Hasegawa et al., 2010; Hwang et al., 2018), supporting the necessity of magnetic reconnection for their formation.

Recently, simulations and observations have suggested that small-scale flux ropes can be produced inside the electron diffusion region (EDR), and that they grow as they are ejected from this region (Chen et al., 2021). Studies have suggested that the tearing instability could be responsible for the formation of multiple X-lines and therefore flux ropes (Daughton et al., 2011b). Despite such case studies and simulations suggesting links between the EDR and flux ropes, a statistical study into this relationship is yet to be conducted.

In this chapter, we investigate EDR-associated flux ropes and quantify their statistical properties. We address how EDR-associated flux ropes differ from previously-reported magnetopause flux ropes (e.g. in studies by Fermo et al., 2011; Akhavan-Tafti et al., 2018), and discuss how this could influence flux rope formation theories, such as the multiple X-line model (Lee and Fu, 1985) and the tearing instability (Daughton et al., 2011b). We aim to show that the flux ropes studied have distinct properties which link them to the EDR, whilst exploring and developing this EDR-flux rope relationship.

The chapter is structured as follows. Section 3.2 presents 32 magnetopause EDR encounters over 28 days of MMS observations, as reported by Webster et al. (2018). In Section 3.3, we present the 245 flux ropes are investigated in this study, detailing how they are identified and how minimum variance analysis (MVA) is used in the selection process. In Section 3.4, we present the statistical findings for the flux rope properties, including their size, core magnetic field strength and flux content, and discuss how these compare to previous studies. In Section 3.5.1, we present how flux rope observations and properties vary with the time between the flux rope and EDR observations. In Section 3.5.2, we

investigate how the number of flux ropes observed surrounding each EDR varies with the properties of the EDR, and in Section 3.5.3 we investigate how the flux rope properties vary with the EDR properties. Section 3.6 presents the conclusions of the flux rope EDR survey.

3.2 EDR Observations

During Phase 1 of the Magnetospheric Mulitscale (MMS) mission, the spacecraft surveyed the dayside magnetosphere to investigate magnetic reconnection, with the aim of encountering the electron diffusion region (EDR). The first EDR encounter was reported by Burch et al. (2016b), which describes the characteristic features of the EDR to be agyrotropic, crescent-shaped electron phase space distributions (PSDs) normal to the magnetic field vector. Further studies highlighted another feature of EDR observations to be a bipolar signature in the normal electric field component which is balanced by the electron pressure tensor divergence (e.g. Fuselier et al., 2017).

Webster et al. (2018) presents 32 EDR encounters over 28 observation days during Phase 1 of the MMS mission. The EDRs were identified by initially identifying conditions typical of ongoing magnetopause magnetic reconnection, including hot electrons, low magnetic field strength, DC or fluctuating electric field, ion jet reversals, and large positive current density in the y GSM direction. The electron PSDs were then investigated for the presence of the characteristic EDR agyrotropic crescent-shaped features. Fewer than 1 in 15 of the originally selected events showed these EDR features.

Webster et al. (2018) computes many of the widely studied EDR properties which are presented in Tables 1 and 2 of the paper and are reproduced here in Tables 3.1 and 3.2. These properties are used for EDR-flux rope relationship investigations in Sections 3.5.2 and 3.5.3.

tag	date/time [UTC]	sep. [km]	x $[R_E]$	y $[R_E]$	z $[R_E]$	B_{min} [nT]	$\mathbf{j}.\mathbf{E}'_{av}$ $[nWm^{-3}]$	$\mathbf{j}.\mathbf{E}'_{max}$ $[nWm^{-3}]$	$\mathbf{j}.\mathbf{E}'_{int}$ $[nWm^{-3}]$
A01	19/09/2015-07:43:00	71.57	6.346	5.399	-2.982	10.14	0.057	6.05	12.7
A02	16/10/2015-10:33:00	13.87	9.231	6.092	-4.403	2.42	0.244	2.42	6.66
A03	16/10/2015-13:07:00	13.78	8.31	7.078	-4.800	2.24	0.117	22.57	26.24
A04	22/10/2015-06:05:00	16.93	9.637	3.481	-1.961	3.95	-0.342	7.47	16.93
A05	01/11/2015-15:08:00	14.58	7.814	6.202	-3.470	19.49	0.217	4.15	8.95
A06	12/11/2015-07:19:00	15.82	11.507	2.302	-1.776	3.75	0.002	0.97	0
A07	06/12/2015-23:38:00	19.23	8.516	-3.916	-0.810	19.76	0.563	10.13	23.88
A08	08/12/2015-11:20:00	15.3	10.233	1.288	-1.364	14.76	0.163	8.31	18.01
A09	09/12/2015-01:06:00	17.34	9.922	-3.671	-0.928	9.85	-0.422	1.07	0
A10	14/12/2015-01:17:00	16.97	10.131	-4.163	-1.191	4.49	0.577	7.13	15.16
A11	07/01/2016-09:36:00	41.75	8.888	-1.968	-0.733	8.03	0.759	6.78	32.95
A12	10/01/2016-09:13:00	40.84	8.808	-2.395	-0.775	9.94	0.924	13.98	55.33
A13	07/02/2016-20:23:00	15.99	3.874	-9.325	-5.720	3.06	0.055	0.38	0
B14	22/10/2016-12:58:00	8.87	6.406	7.700	-4.706	3.81	0.848	11.92	61.31
B15	02/11/2016-14:46:00	8.18	7.241	8.812	-3.543	8.67	-0.089	1.09	0
B16	06/11/2016-08:40:00	11.76	7.943	4.113	-2.826	28.89	0.445	8.12	20.52
B17	12/11/2016-17:48:00	7.35	6.624	9.165	-1.104	6.1	-0.213	5.12	6.24
B18	13/11/2016-09:10:00	11.38	8.958	4.563	-2.625	18.57	0.206	18.28	48.2
B19	18/11/2016-12:08:00	4.88	9.596	6.460	-2.509	3.21	0.043	1.02	0
B20	23/11/2016-07:49:00	6.43	9.613	3.232	-1.604	5.93	0.445	7.35	19.47
B21	23/11/2016-07:49:00	6.43	9.613	3.232	-1.604	22.24	3.13	32.32	124.23
B22	23/11/2016-07:50:00	6.42	9.62	3.245	-1.608	19.9	0.733	8.57	26.44
B23	28/11/2016-15:47:00	6.32	8.884	7.184	-0.440	12.99	0.077	1.63	0.63
B24	11/12/2016-04:41:00	6.89	9.489	-0.056	-0.448	8.03	0.342	2.07	2.2
B25	19/12/2016-14:15:00	8.42	10.204	4.170	0.934	5.52	0.146	2.33	2.33
B26	02/01/2017-02:58:00	9.96	9.647	-3.007	-0.649	4.3	0.375	2.37	21.98
B27	11/01/2017-04:22:00	8.17	10.809	-3.713	-0.154	5.14	0.416	8.53	25.98
B28	20/01/2017-12:32:00	6.47	9.634	-0.461	1.967	6.01	1.48	8.31	78.36
B29	22/01/2017-10:15:00	5.75	10.744	-2.138	1.766	2.35	0.414	4.13	20.23
B30	22/01/2017-10:15:00	5.74	10.75	-2.148	1.764	4.53	0.214	3.39	5.4
B31	22/01/2017-10:47:00	5.86	10.519	-1.790	1.837	11.43	0.179	1.98	1.38
B32	27/01/2017-12:05:00	6.05	9.27	-1.370	1.964	2.95	0.447	7.51	62.75

Table 3.1: EDR data table from Webster et al. (2018), with columns from left to right: EDR tag; date and time in UTC; spacecraft separation; spacecraft location x-, y-, and z-components in GSM coordinates; minimum magnetic field magnitude; $\mathbf{j}.\mathbf{E}'$ average, maximum and integrated, across the EDR observation.

3.3 Flux Rope Identification

Flux ropes have unique helical magnetic fields which can be used to identify them in spacecraft data. In a magnetic field time-series in which a spacecraft has passed through a flux rope, we would typically expect to observe a bipolar signature in one magnetic field component, corresponding to the twisted azimuthal component of the flux rope, and an enhancement in another component, corresponding to the increase in axial magnetic field

tag	max ρ_e [km]	max ρ_i [km]	av. n_e $[cm^{-3}]$	max $E_{\|\|}$ $[mVm^{-1}]$	av. T_e [ratio]	min $\frac{T_{e\|\|}}{T_{e\perp}}$ [eV]	max $\frac{T_{e\|\|}}{T_{e\perp}}$ [ratio]	av. $\sqrt{Q_e}$ [index]	max $\sqrt{Q_e}$ [index]	av. $\|\mathbf{j}\|$ $[\mu Am^{-2}]$	max j_y $[\mu Am^{-2}]$	max $\|\mathbf{j}\|$ $[\mu Am^{-2}]$
A01	6.83	1374.9	22.93	16.45	46.4	0.87	2.01	0.017	0.06	0.79	1.84	2.73
A02	8.72	1703.8	13.55	7.8	36.6	0.84	2	0.017	0.052	0.56	0.9	1.2
A03	11.59	2401.1	6.92	105.94	66.1	0.92	2.22	0.03	0.09	0.63	1.52	1.85
A04	9.35	509.9	15.17	48.06	51.8	0.66	1.83	0.018	0.069	0.75	2.46	2.74
A05	4.25	112	9.12	29.44	53.2	0.68	2.01	0.023	0.072	0.71	1.48	1.98
A06	8.67	570.8	5.84	2.82	45.8	0.9	1.75	0.018	0.086	0.24	0.75	1.06
A07	5.74	108.3	9.16	109.77	111.9	0.58	2.81	0.022	0.066	0.69	1.61	2.82
A08	4.83	174.6	5.12	60.68	86.1	0.97	4.43	0.026	0.084	0.44	2.15	2.43
A09	6.1	619.2	8.03	20.91	64.2	0.95	2.46	0.019	0.051	0.37	0.84	1.11
A10	9.46	846.1	5.09	63.73	103.1	0.93	2.8	0.031	0.095	0.49	1.68	1.73
A11	7.24	348.7	21.41	3.3	67	1.05	1.81	0.017	0.047	0.64	1.93	2.18
A12	6.67	386.4	14.74	51.93	73.1	0.69	2.39	0.022	0.066	0.83	3.13	3.75
A13	10.72	2327.4	8.49	7.66	56.5	0.79	1.48	0.016	0.057	0.18	0.19	0.52
B14	6.21	331.3	25.49	52.27	27.1	0.9	2.8	0.019	0.055	0.85	2.17	2.81
B15	6.16	159.7	9.83	16.38	46.9	0.89	1.65	0.016	0.036	0.28	0.6	0.9
B16	3	133.1	13.7	44.14	58.7	1.54	2.97	0.037	0.075	0.96	1.82	2.4
B17	10.98	432.7	5.04	38.55	133.5	0.77	1.97	0.014	0.048	0.34	0.7	0.96
B18	5.61	341.7	9.4	36.17	88.9	0.81	1.51	0.011	0.05	0.48	1.98	2.92
B19	8.4	474.8	15.45	5.1	42.7	0.99	2.93	0.016	0.05	0.54	1.38	1.47
B20	8.16	413.9	11.61	8.83	67.8	0.71	3.49	0.024	0.121	0.73	1.56	2.23
B21	4.25	106.9	8.78	133.36	94.5	1.19	3.78	0.031	0.089	1.36	2.77	2.96
B22	4.66	110	9.05	33.59	86.6	0.88	3.55	0.031	0.078	1.04	2.3	2.59
B23	4.8	150.6	16.94	11.82	45	1.04	3.1	0.015	0.036	0.33	0.46	1.8
B24	7.79	400	13.1	2.85	77.7	0.73	1.99	0.01	0.026	0.35	0.74	0.9
B25	7.9	669.9	11.12	27.59	61.6	0.95	3.06	0.016	0.05	0.42	0.84	1
B26	8.5	761	12.71	8.24	57.2	0.65	1.55	0.012	0.026	0.37	0.78	0.89
B27	9.1	488.5	13.16	5.07	67.1	0.85	1.33	0.01	0.055	0.33	0.95	1.66
B28	9.27	485.1	16.51	97.06	90.2	0.97	2.62	0.015	0.051	0.72	1.25	1.96
B29	13.7	1006.4	10.78	19.7	70.4	0.58	2.36	0.018	0.043	0.45	1.63	1.82
B30	9.99	475.9	9.79	10.19	72.7	0.94	2.26	0.017	0.044	0.47	1.17	1.29
B31	7.48	391.9	9.59	16.16	92.1	0.82	1.38	0.011	0.036	0.44	0.97	1.17
B32	13.22	1054.9	7.27	12.65	95.1	0.9	62.75	0.015	0.046	0.47	1.23	1.49

Table 3.2: EDR data table from Webster et al. (2018), with columns from left to right: maximum electron and ion gyroradii; average electron density; maximum parallel electric field; average electron temperature; minimum and maximum ratio of electron parallel to perpendicular temperature; average and maximum electron agyrotropy; average current density magnitude; maximum y component of current density; maximum current density magnitude.

strength at the centre of the flux rope. On the magnetopause, where flux ropes tend to be produced by reconnection at the subsolar point, we expect to see flux ropes moving in the $\sim$ z GSE direction over the spacecraft as they are embedded in the reconnection outflows, and to be orientated with their axial direction pointing along the magnetopause in approximately the same direction as the reconnection X-line. Therefore, would expect the azimuthal bipolar component of the flux rope to be normal to the magnetopause in $\sim$ x GSE and the core field to be in $\sim$ y GSE direction.

In this study, we survey all of the MMS burst resolution data from the days on which EDR observations were reported by Webster et al. (2018). This data is from Phase 1

of the MMS mission when the spacecraft were surveying the dayside subsolar region of the magnetopause. We would therefore expect typical flux rope signatures to be as described in the previous paragraph. When probing the data, we looked for overall magnetic field strength enhancements and corresponding bipolar signatures, predominantly in the y GSE component. No quantitative limit was set on the the required size of the peak, allowing a wide selection of bipolar features to be selected as candidates for further investigation; this was to allow the identification of flux ropes observed further from the subsolar point or under non-typical conditions.

The MMS Science Data Centre (SDC) quick-look plots were first investigated for flux ropes. From this preliminary investigation, we found flux rope observation time lengths to be on the order of a few seconds. To allow for uniform identification of the flux ropes, we created 1-minute interval plots for all the recorded burst mode data for each of the Webster et al. (2018) EDR observation days. This resulted in 2622 plots showing $\sim$ 44 hours of MMS burst data. An example of one of these plots used for flux rope identification is shown in Figure 3.3.

Surveying these plots resulted in 491 flux rope candidates, giving an observation rate of 1 flux rope candidate per every 5.34 minutes of burst mode data. Once flux rope candidates were identified from these plots, the precise start and end times of the flux rope candidates were collected, and minimum variance analysis (MVA) was applied to the flux rope intervals (see Section 2.2). If the spacecraft passed through the flux rope close to the central axis, MVA should rotate the flux rope into an optimum coordinate system in which one MVA component picks out the bipolar signature of the flux rope and another picks out the axial direction. These two components should be the maximum and intermediate MVA components, however, which one is which depends on the spacecraft trajectory through the flux rope. This rotation puts the flux rope in a coordinate system suitable for further analysis and allows us to be confident in the axial field strength of the flux. An example of MVA being successfully applied to one of the candidate flux ropes is shown in Figure 3.4 (a), where the flux rope axial component is identified as the MVA

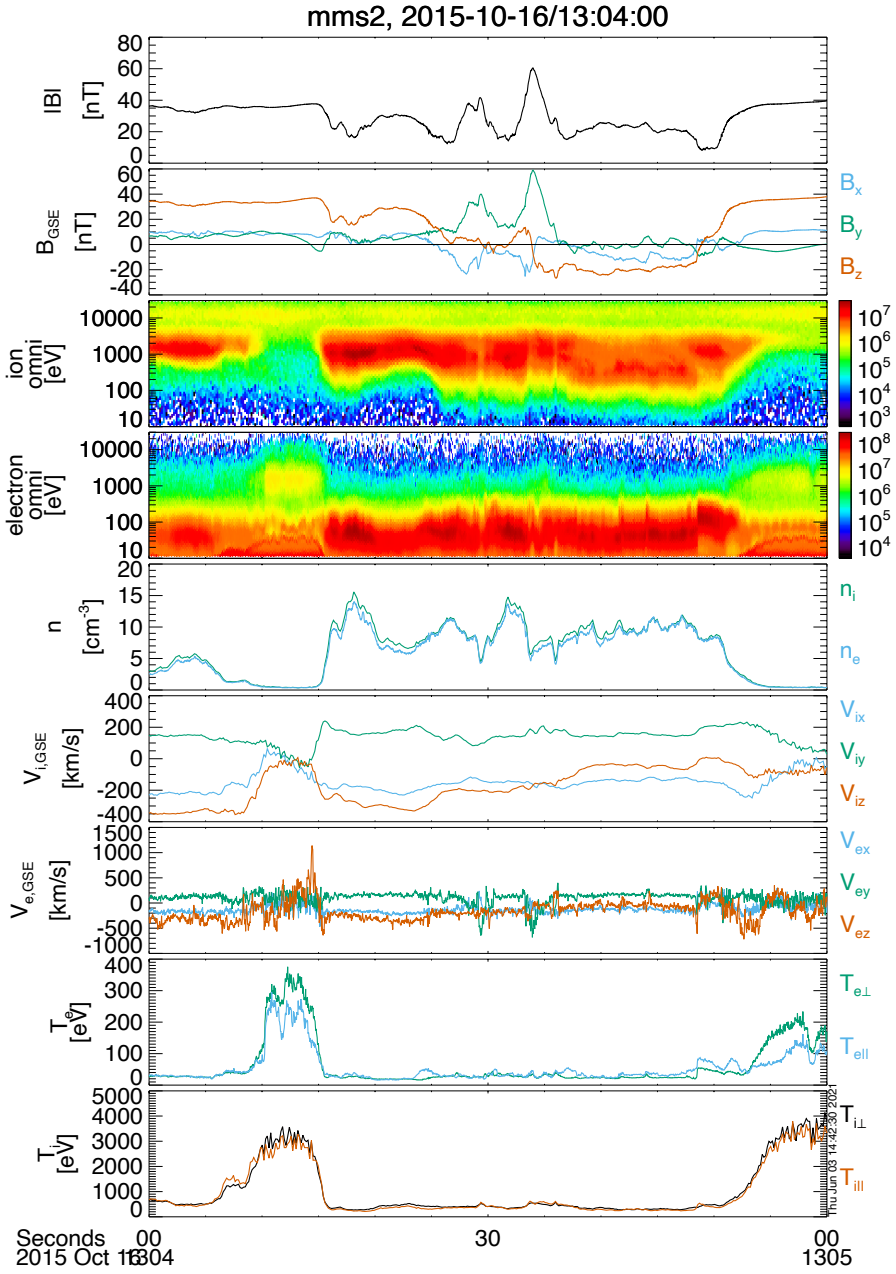

Figure 3.3: An example 1-minute plot of MMS burst-mode data used to identify flux ropes. The two peaks in the centre of the first panel of the plot show the characteristic flux rope magnetic field enhancements. The second panel shows corresponding bipolar features in the y GSE and z GSE magnetic field components. Subsequent panels show the ion and electron energy spectra, the ion and electron densities, the ion velocity, the electron velocity, the electron temperature and the ion temperature.

intermediate component.

Applying MVA to the flux ropes should make the flux rope structure become

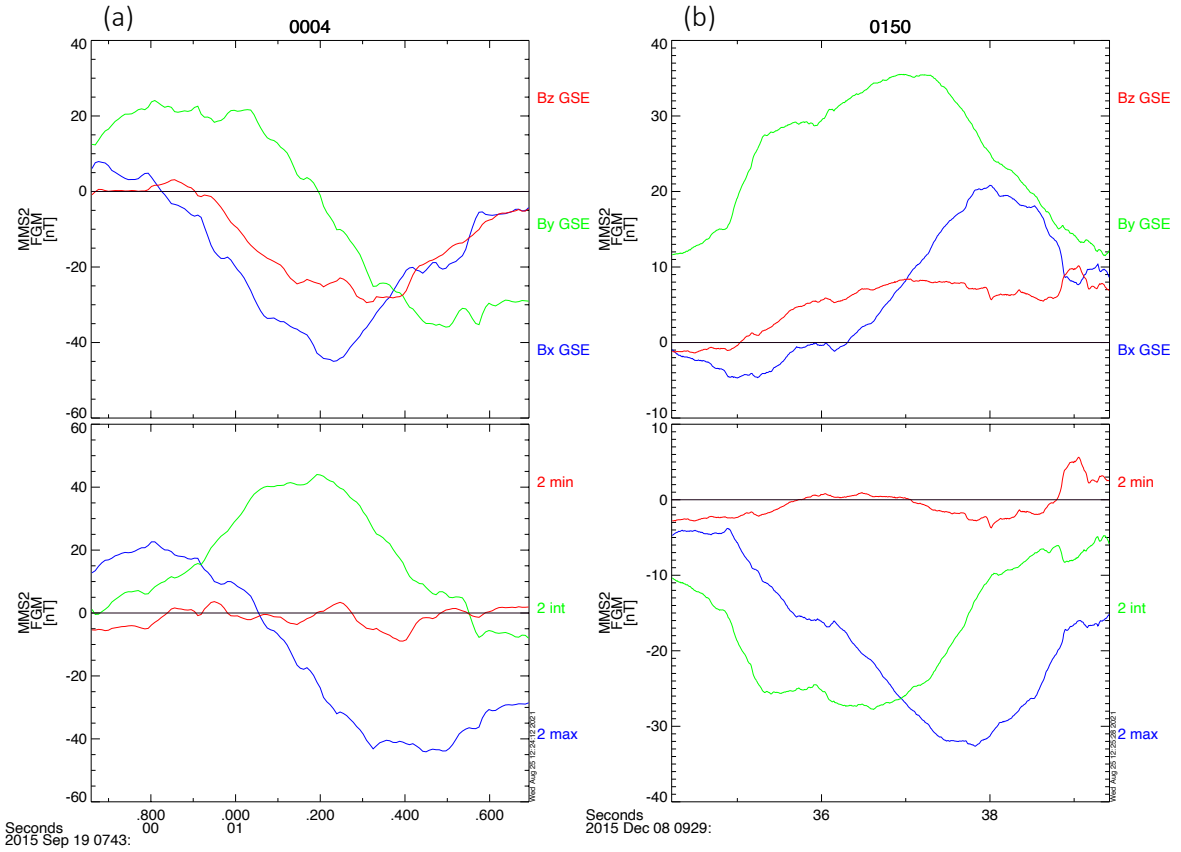

Figure 3.4: Two examples of MVA applied to flux rope candidates, where the upper panels show the field arrangement in GSE coordinates and the lower panels show the field arrangement in MVA coordinates. (a) shows an example where the MVA rotation has made the flux rope structure clearer by identifying a bipolar feature in the maximum variation component, a peak in the intermediate and a near-zero minimum component. (b) shows an example where the MVA rotation has removed the flux rope structure that was apparent in GSE coordinates.

clearer. However, this assumes the flux rope structure is idealised and that the spacecraft pass close to the central axis of the flux rope. This is not always the case for flux ropes in this study; upon closer inspection of the 491 flux rope candidates, it was found that 259 (52.7%) had a clear flux rope structure in the original GSE coordinate system and 245 (49.9%) had a clear flux rope structure in the MVA coordinate system, where a clear structure was defined as the typical bipolar signature in one field component centred on an overall magnetic field magnitude increase, as can be seen in Figure 3.4 (a). 91 flux ropes that had a clear structure in GSE did not have a clear structure once rotated into the MVA coordinate system. An example of one of these flux ropes and its MVA rotation

can be seen in Figure 3.4 (b). This suggests that an MVA rotation does not always result in an optimised coordinate system for analysing flux ropes. This could be due to the flux ropes themselves being non-ideal or the spacecraft trajectory not being close enough to the central axis. In this study we require a well-defined coordinate system in which to analyse the flux ropes, therefore, in the following analysis, we include only the 245 flux ropes which have clear flux rope structure when rotated into MVA coordinates. A full list of these flux ropes is included in Appendix A.

3.4 Flux Rope Statistics

In this Section, we analyse 245 magnetopause flux ropes identified in MMS burst mode data on the same day as EDR observations reported by Webster et al. 2018. All of these flux ropes have a well-defined MVA coordinate system. The extracted flux rope data used for the following analysis is included in full in Appendix A. When analysing this data, we have excluded extreme outliers where the lower and upper limits are defined by $Q1 - 3 \times IQR$ and $Q3 + 3 \times IQR$, respectively, where $Q1$ and $Q3$ refer to quartiles 1 and 3 of the data, respectively, and IQR refers to the interquartile range $(Q3 - Q1)$. Candidates falling outside this range were visually inspected and found to have distinct characteristics such as ongoing reconnection at their centre, as in Øieroset et al. (2016).

The radii of the flux ropes were calculated by multiplying the observation time by the average ion velocity over the observation period (an estimate for the flux rope speed). The distributions of these radius values are shown in Figure 3.5. Figure 3.5 (a) shows this distribution in km units, whereas Figure 3.5 (b) scales this distribution by the average ion inertial length for the observation, d_i. In Figure 3.5 (a), a vertical marker shows the average ion inertial length for the data, in Figure 3.5 (b) the vertical marker shows where $d_i = 1$. These distributions have a mean flux rope radius of 237.37 km and 4.11 d_i, respectively.

Previous studies have fit an exponential tail to the flux rope radius distribution

and have not considered the drop-off of small radius flux rope observations. This could be due to artificial small-scale cut-offs in the observations due to limited spacecraft data resolution. Using MMS, we are able to observe plasma dynamics down to electron scales, so are able to resolve small-scale flux ropes without concern. In these flux rope radius distributions, we observe a drop-off in radius observations below a flux rope radius of $\sim 1\ d_i$, suggesting that flux ropes are ion-scale features. Because of this confidence in our distribution observations at small scales, we have fit a skewed distribution to the data to capture the full distribution, rather than just the tail.

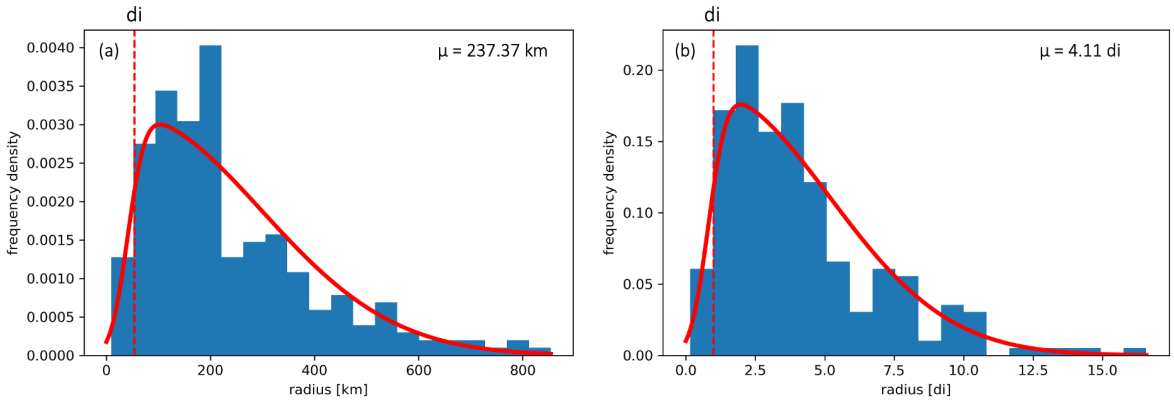

Figure 3.5: Distribution of the radii of 245 flux ropes observed by MMS. (a) shows the radius distribution in km units and (b) shows the distribution normalised by d_i calculated for each flux rope. Vertical lines indicate the average calculated d_i and $d_i = 1$ for (a) and (b), respectively. The red curves show the skewed fits for each of the distributions.

The axial field strength of the flux rope was calculated by finding the maximum value of the axial magnetic field component over the flux rope, as identified by the MVA analysis. This was then used along with the calculated flux rope radius to calculate the flux content of the flux ropes. The formula, $flux = 0.4158 J_1(2.40482) \times (2\pi r^2 B)$, where J_1 is the first Bessel function, r is the flux rope radius, and B is the axial field strength of the flux rope, was used to estimate the flux content. This assumes the flux rope is cylindrical and force-free (Eastwood et al., 2012b). The distributions for the axial field component and flux content of the flux ropes can be seen in Figure 3.6. We find the flux ropes to have a mean axial field strength of 38.27 nT and a mean flux content of 3.39 kWb. Here, we have again fit a skewed distribution to the axial field strength, and

an exponential distribution for the flux content.

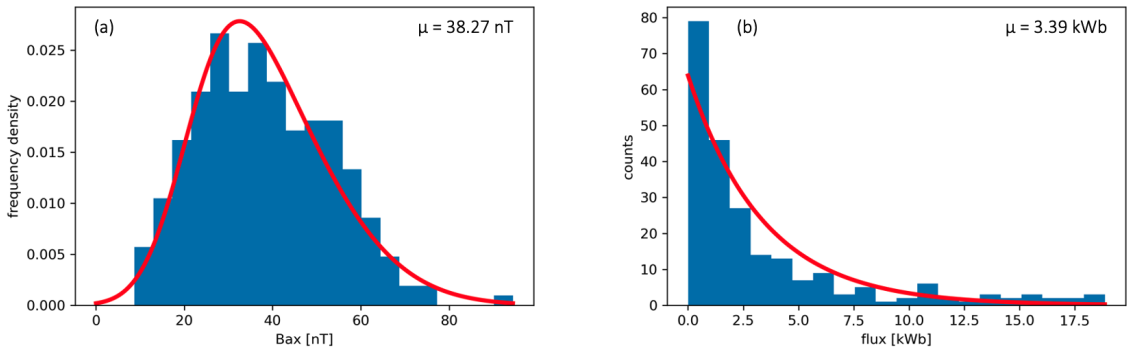

Figure 3.6: (a) distribution of the axial field strengths observed for each flux rope. The red curve shows the skewed distribution fit. (b) distribution of the calculated flux content of the flux ropes. The red curve shows an exponential distribution fit.

We find that the flux ropes in this study have smaller radii than previously reported in flux rope surveys. Fermo et al. (2011) found flux ropes observed by Cluster to have a mean radius of 2640 km and Akhavan-Tafti et al. (2018) found a survey of magnetopause flux ropes with MMS to have a mean radius of 345 km, when assuming the flux rope impact parameter = 0, as we have in this study. The mean radius of the flux ropes in our study was found to be 237 km. This is an order of magnitude smaller than the flux ropes observed by Fermo et al. (2011), and 31% smaller than the flux ropes presented by Akhavan-Tafti et al. (2018).

There is a clear difference between the flux rope and FTE radius observations using MMS and Cluster. This has previously been explained by the different spacecraft orbits and therefore different observation regions; the Fermo et al. (2011) Cluster study surveys FTEs at the high latitude magnetopause and low latitude flanks and observes larger flux rope radii, whereas this study, and Akhavan-Tafti et al. (2018), survey the subsolar magnetopause region where smaller radii are observed. This difference is consistent with the flux rope coalescence theory which suggests flux ropes are formed by reconnection, typically in the subsolar region, and then coalesce as they move over the magnetopause (Daughton et al., 2011c), growing in size. This suggests that the spacecraft are sampling different subsets of flux ropes/FTEs; the MMS studies could be sampling newly formed

flux ropes that are less likely to have coalesced, and the Cluster study could be observing flux ropes that are more likely to have undergone coalescence. Furthermore, this could be reinforced by the smaller flux rope radii observed in our study compared to those observed by Akhavan-Tafti et al. (2018). In this study, we focus on flux ropes observed near EDR encounters, which could mean we are observing a greater number of 'younger' flux ropes than the general population of subsolar magnetopause flux ropes surveyed by Akhavan-Tafti et al. (2018). This relationship, along with other flux rope EDR relationships, is investigated further in the following section.

In this study, we have found the flux rope radius distributions to follow skewed distributions. For the distribution in km units, we find the peak of the distribution to be just greater than the average calculated d_i for the flux ropes. When this radius is scaled into d_i units for each of the flux ropes, we similarly find the peak to be located at just greater than 1 d_i. For both distributions, we do observe a small population of flux ropes with radius < 1 d_i, but the distributions have a cut off at ~ 1 d_i. The MMS spacecraft are capable of resolving electron-scale dynamics, suggesting that this is not an artificial cut-off due to the resolution of the data. This, therefore, suggests that flux ropes tend to be observed at ions scales, and are less likely to be observed below ions scales. The smaller size of the flux ropes will act to decrease their observation likelihood, however, we would not expect this to lead to a visible cut-off as we see in this distribution.

The smaller flux rope radii found in this study result in much smaller calculated flux contents, due to the r^2 dependence of the calculation. In this study, we find the average flux content to be 3.39 kWb, whereas Akhavan-Tafti et al. (2018) found the average flux rope flux content to be 100 ± 30 kWb. This reinforces the previous discussion which suggests we are sampling a distinct set of flux ropes that are potentially newly formed by the EDR.

3.5 Flux Rope EDR Relationships

3.5.1 Time to EDR

For each of the flux ropes, the time between the flux rope observation and the EDR observation was calculated. For most days, there was only one EDR observation, however, on 16/10/2015 and 23/11/2016 the EDR was observed 2 and 3 times, respectively. In these cases, the time to the closest EDR was identified. The distribution of these time to EDR values are plotted in Figure 3.7, where (a) shows a time span of 24 hrs, (b) 1.5 hrs and (c) 20 minutes. From Figure 3.7 (a) we can see that flux ropes are much more likely to be observed close to the EDR with a clear peak in the 0 - 2 hours bar. Figures 3.7 (b) and (c) investigate this peak close to zero further, with (c) showing that 31% of flux ropes are observed within 20 of the EDR.

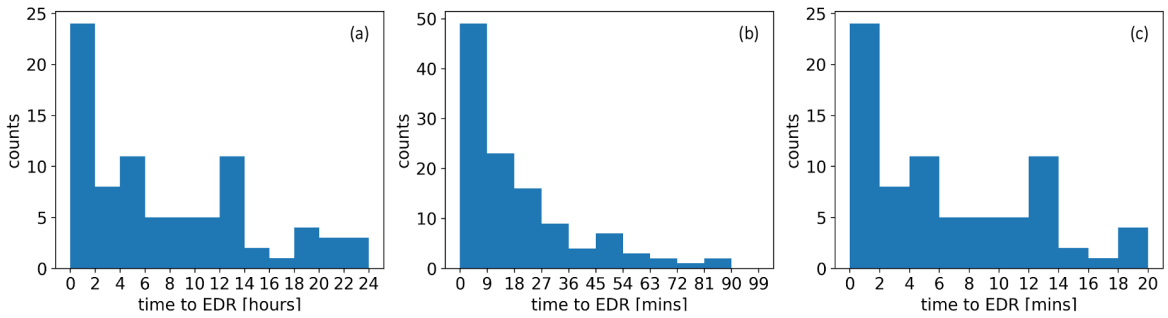

Figure 3.7: Histograms showing the time between flux rope and EDR observations (time to EDR) for varying time ranges: (a) 0 - 24 hours, (b) 0 - 100 minutes and (c) 0 - 20 minutes.

Figure 3.8 investigates if the properties of the flux ropes vary with the time between the flux rope and EDR observations. Figures 3.8 (a), (c) and (e) show scatter plots of the time to the EDR observation against the flux rope radius, axial magnetic field strength and flux content, as calculated in the previous section. The plots are split into 7 vertical bins which are then averaged to aid the identification of any trends in the data. Figure 3.8 (b), (d) and (f) show the same data represented as heat maps. All of these plots show an increase in the spread of the data as the time to the EDR increases, and potentially

greater radius, axial magnetic field strength and flux content values with a smaller spread at smaller times to the EDR.

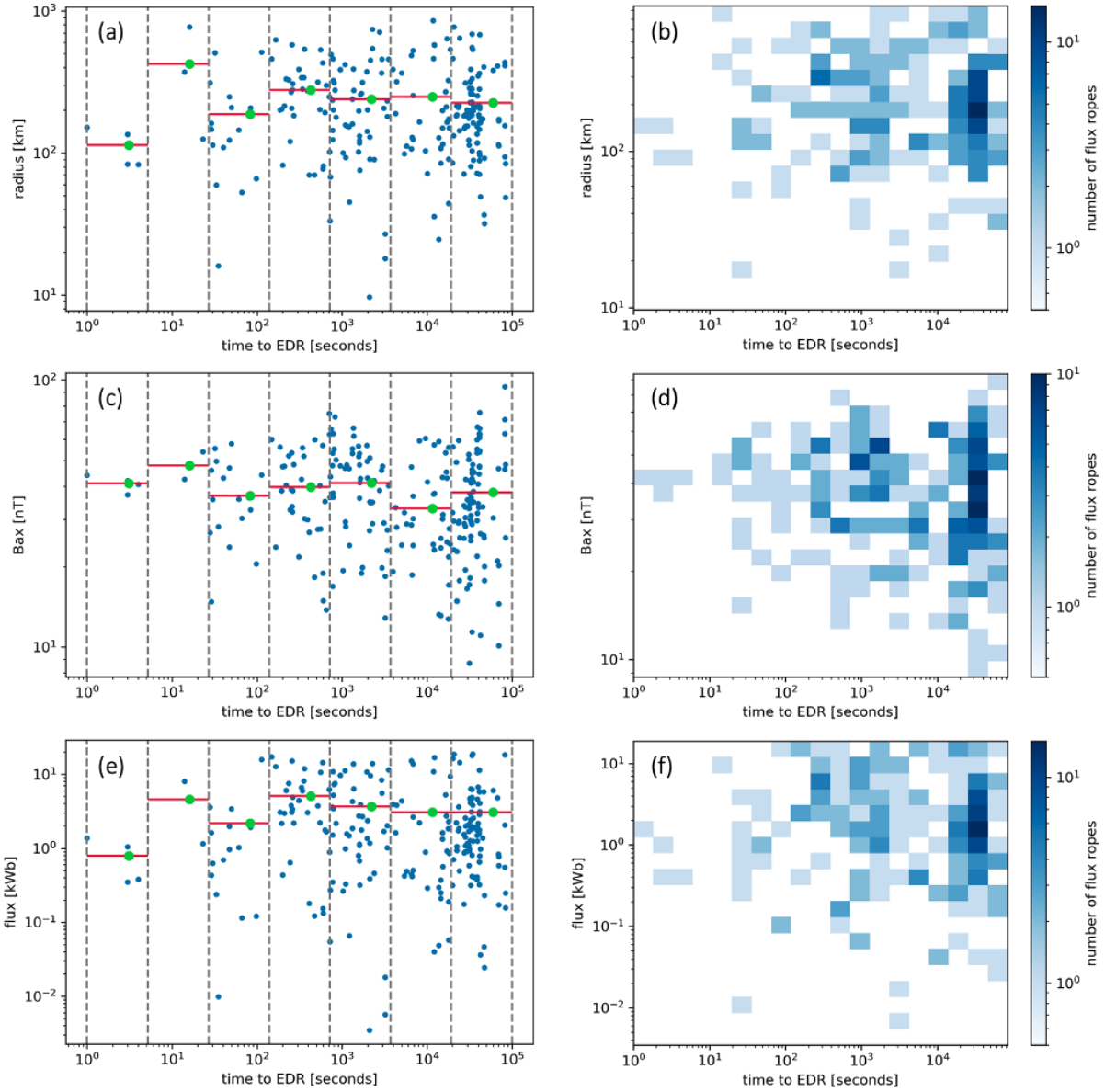

Figure 3.8: (a), (c) and (e), show scatter plots of the time between flux rope and EDR observations (time to EDR) and the flux rope radius, axial magnetic field strength and flux content, respectively. Green points and red lines indicate the running averages of the data. (b), (d) and (f) show the same data represented on a heat map.

To investigate this further, we split the flux ropes into 2 subsets: flux ropes observed within t minutes of and EDR and flux ropes observed more than t minutes from an EDR. We then plot and compare the cumulative distributions for these two subsets for the

flux rope radius, axial magnetic field strength and flux content for varying values of t. Figure 3.9 (a), (c) and (d) show cumulative distribution comparisons for the radius, axial magnetic field strength and flux content at $t = 70$, 40 and 50 minutes, respectively. In all of these plots, the distribution in blue for the flux ropes observed within t minutes of the EDR is shifted to the right highlighting higher values.

To determine the statistical significance of the differences between these distributions we employ the Kolmogorov–Smirnov (KS) test (Massey, 1951) which can determine if two data sets are sampled from the same underlying distribution. The test returns a p-value and KS statistic which are plotted for varying t for each of the flux rope properties in Figure 3.9 (b), (d) and (e). If the KS statistic is small or the p-value is high, then we cannot reject the hypothesis that the distributions of the two samples are the same i.e. the two data sets are sampled from the same underlying distribution.

Focusing on using the p-value to determine the outcomes, for the radius distributions from 90 - 160 minutes we have low p-values of < 0.15 so we can say the samples come from different underlying distributions with a 15% confidence interval. The axial magnetic field strengths have more striking differences with the flux ropes observed closer to the EDR (blue line) having greater axial magnetic field strength. Between 30 - 80 minutes the p-values give a confidence interval of below 5%, dropping to ~ 1 at 40 minutes, which corresponds to the distributions shown in Figure 3.9 (c). This plot shows that flux ropes observed within 40 minutes of an EDR observation have $\sim$ 5 - 10 nT greater axial magnetic field strength than those observed more than 40 minutes from an EDR observation. The axial magnetic field strength and radius are combined to calculate the flux content of the flux ropes. Comparing these distributions results in similarly high confidence intervals for different underlying distributions; between 50 - 160 minutes we have p-values < 0.075, showing that flux ropes observed closer to the EDR have greater flux content, at a cut off of $t = 50$ minutes flux ropes have $\sim$ 1 - 2 kWb greater flux content.

From the distribution analysis and the KS test results we can conclude that flux

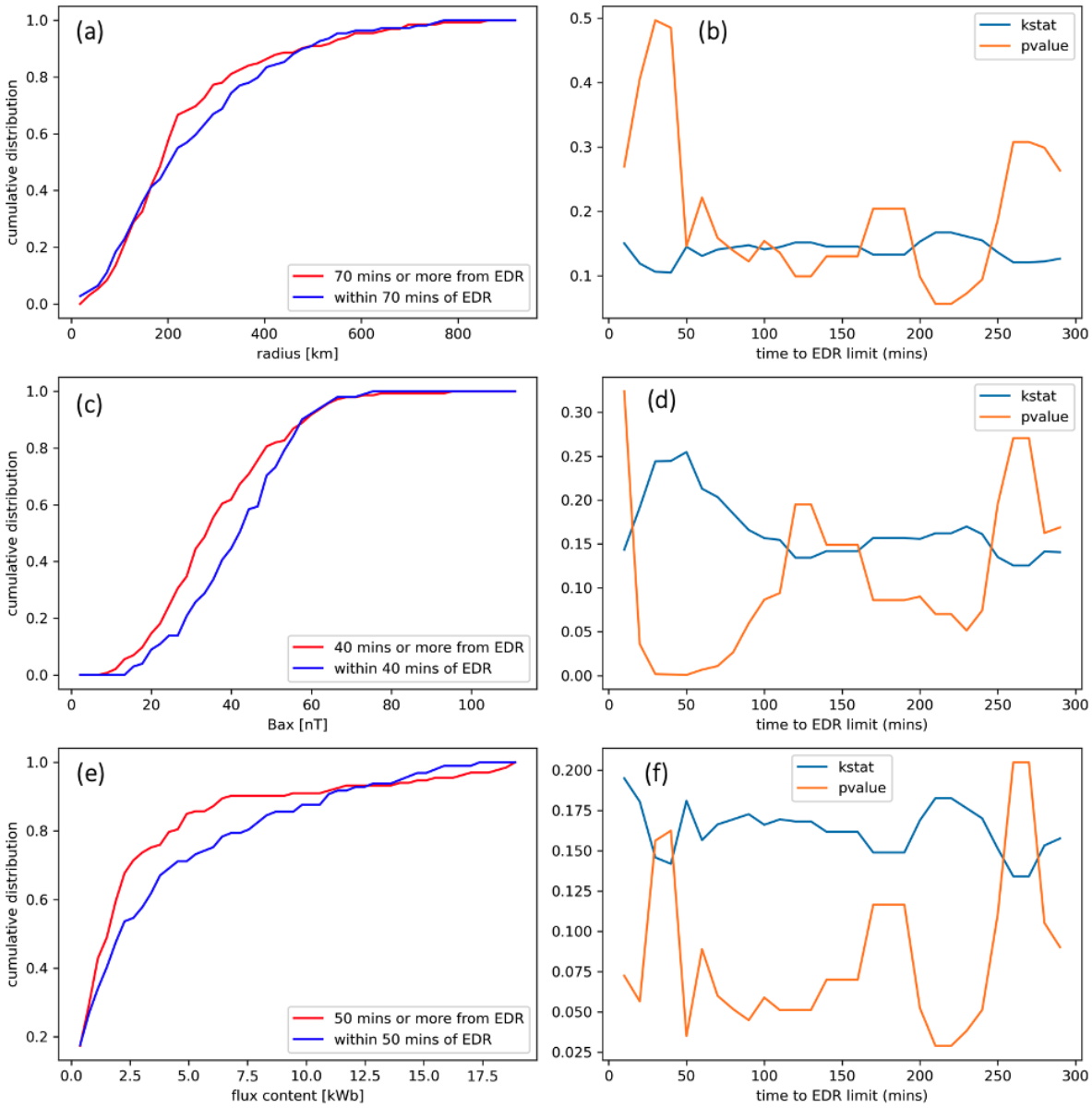

Figure 3.9: (a), (c) and (e), show cumulative distributions for the flux rope radius, axial magnetic field strength and flux content, respectively. The blue distributions correspond to flux ropes observed within t minutes of an EDR and the red distribution corresponds to flux ropes observed more than t minutes from an EDR, where t = 70, 40 and 50 minutes for plots (a), (c) and (e), respectively. (b), (d) and (f) show the KS test results for comparing these cumulative distributions for the flux rope radius, axial magnetic field strength and flux content, respectively, for various t. The blue line shows the KS statistic and the orange line shows the p-value.

ropes observed within $\sim$ 1 hour of an EDR observation tend to have greater axial magnetic field strength (5 - 10 nT greater) and larger flux content ($\sim$ 1 - 2 kWb greater). There is

potentially a trend towards a larger radius closer to the EDR, however, this is focused to the middle of the cumulative distribution and is less statistically conclusive. These results suggest that the flux ropes observed closer to EDR encounters have different properties, potentially forming a distinct subset of flux ropes. These differences could be due to these flux ropes being recently formed by the EDR. If so, this would suggest that newly formed flux ropes have stronger axial magnetic fields and therefore greater flux content.

These observations may appear inconsistent with the flux rope coalescence theory which suggests that flux ropes coalesce, becoming larger and having greater flux content, as they move away from the reconnection location where they are formed (Daughton et al., 2011c). This theory was used to explain the much larger flux rope radii observed at the high latitude magnetopause and cusps by Fermo et al. (2011) compared to the smaller radii observed at the subsolar magnetopause by Akhavan-Tafti et al. (2018). We suggest that our results are not necessarily in conflict with these coalescence observations and theory; our results reinforce that we expect to see small flux ropes in the subsolar region which is consistent with coalescence theory on the scale of the magnetopause. The differences we are observing are differences in subsets of these subsolar region flux ropes where different physics may be at play, prior to their evolution over the magnetopause where they may then undergo coalescence.

In this study, flux ropes observed far from EDR observations could be close to an EDR that the spacecraft didn't happen to observe. This means that the subset of flux ropes defined as being t minutes or more from an EDR observation may contain flux ropes that are within t minutes of an unobserved EDR. This would work to diminish any differences between these subsets of flux ropes, meaning any differences observed in this study may in reality be more pronounced than they appear.

3.5.2 Number of Flux Ropes Produced

In this section, we investigate what controls the number of flux ropes observed near each EDR. Figure 3.10 (a) plots the locations of each of the EDR observations in the y-z GSE plane, where the points are colour-coded by observation date and their size is proportional to the number of flux ropes observed on the EDR encounter day. The plot shows us how the spacecraft orbit varies, leading to a variation in the location of the magnetopause encounters and therefore the EDR encounters. All Phase 1a and the majority of Phase 1b encounters have negative z GSE coordinate, meaning we would expect to mostly be to the south of the X-line and embedded in southward-directed reconnection exhausts. Figure 3.10 (b) limits this plot to flux ropes observed within 20 minutes of an EDR encounter. In this plot, we observe that the red points are generally smaller than the blue, suggesting that we were more likely to observe more flux ropes closer to the EDR during Phase 1a of the mission. We also observe that all of these larger points are when z GSE is negative, so this could also be a factor influencing the number of flux ropes observed surrounding an EDR, however, the z GSE positive sample size is small in this study which may be leading to this observation.

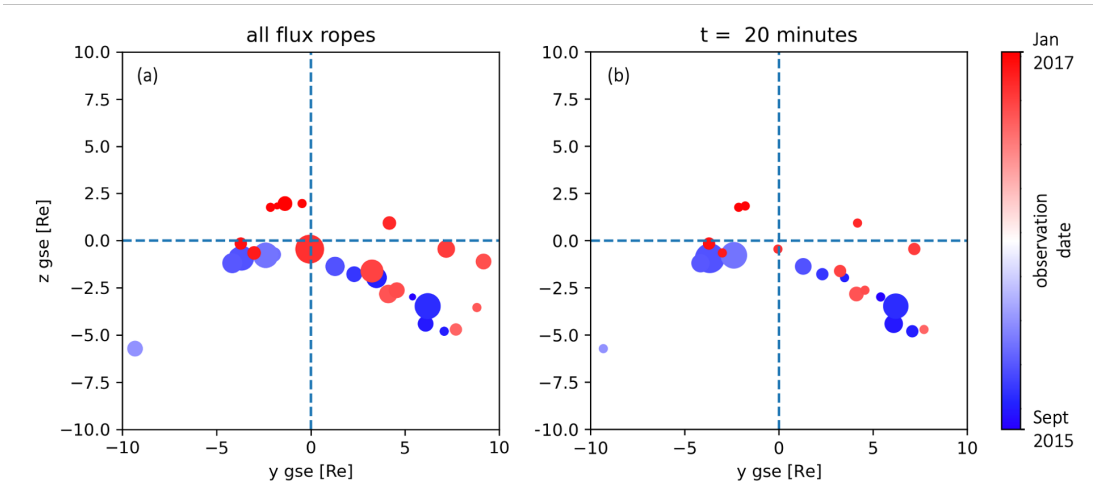

Figure 3.10: Plots showing the location of the EDR observation in the z-y GSE plane, with the size of the points being proportional to the number of flux ropes observed (a) on the same day of the EDR observation (all flux ropes included) and (b) within 20 minutes of the EDR observation (t = 20 minutes). The points are coloured according to the observation date.

The EDR parameters presented in Tables 3.1 and 3.2 were investigated to identify any potential correlations with the number of flux ropes observed to be associated with each EDR. The plasma beta was also investigated and calculated for each of the EDRs using the formula $\beta = (2\mu_0 n k_b T)/B^2$, where μ_0 is the permeability of free space, n is the average electron density at the EDR, k_b is the Boltzmann constant, T is the average electron temperature observed at the EDR and B is the minimum magnetic field strength observed at the EDR (Webster et al. (2018) did not define an average magnetic field strength value). Scatter plots of the EDR parameters against the number of flux ropes observed were made, and the plots showing correlations are presented in Figure 3.11. The following potential relationships are observed:

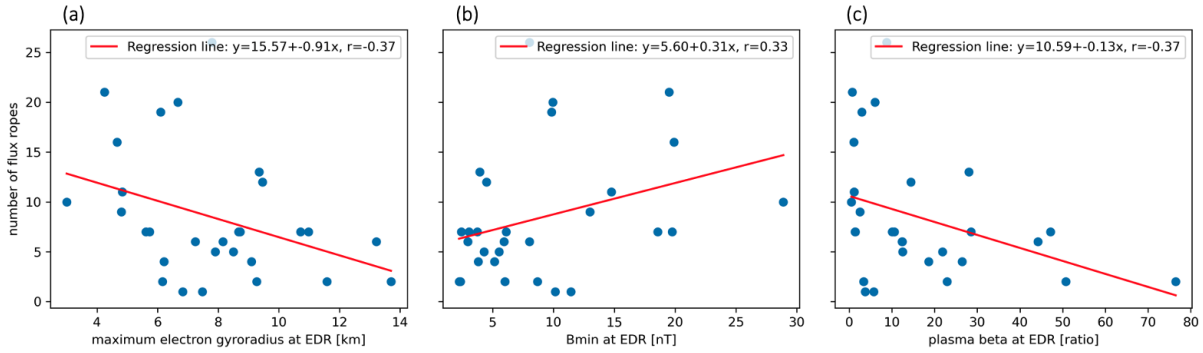

Figure 3.11: Scatter plots of (a) maximum electron gyroradius, (b) minimum magnetic field strength and (c) plasma beta observed at the EDR against the number of flux ropes observed surrounding the EDR.

- The maximum electron gyroradius observed at the EDR appears to limit the number of flux ropes observed by the EDR; all EDRs observed with a large number of flux ropes are observed at a small minimum electron gyroradius at the EDR. (See Figure 3.11 (a), r = -0.37).

- The plasma beta at the EDR also limits the number of flux ropes observed, with only large numbers of flux ropes being observed at EDRs with low plasma beta, as can be seen in Figure 3.11 (c) (r = -0.37).

- There is a slight correlation shown in Figure 3.11 (b), which suggests that more flux ropes could be produced for larger minimum magnetic field strength observed at the EDR ($r = 0.33$).

The minimum magnetic field strength observed at the EDR gives a measure for the guide field of the ongoing reconnection: the greater the minimum magnetic field observed, the stronger the guide field present. The correlation in Figure 3.11 (b) suggests that more flux ropes could be produced when the guide field is stronger. One of the criteria for the initial identification of ongoing reconnection, before the EDRs were then identified, was a dip in magnetic field strength, meaning that our observations could be skewed to small guide field EDRs. This relationship could become clearer if the study was expanded to investigate EDRs with greater minimum magnetic field values.

3.5.3 EDR and Flux Rope Property relationships

The properties of the flux ropes, including their radius, core magnetic field strength and flux content, were investigated with respect to the EDR variables listed in Tables 3.1 and 3.2, and the calculated plasma beta, as described in the previous section. Scatter plots were made to identify any correlations present, with only flux ropes observed within 15 minutes of the EDR included so that it is more likely that the flux rope proprieties can be associated with the given EDR. In these plots, the following potential correlations (with $r > 0.35$) are observed and are shown in Figure 3.12:

- The maximum $|\mathbf{j}|$ and j_y component of the current density positively correlates with the observed axial magnetic field strength of the flux ropes (Figure 3.12 (a) and (b), $r = 0.46$ and $r = 0.44$, respectively).

- $\mathbf{j}.\mathbf{E}'$ maximum, average and integrated over the EDR positively correlates with the observed axial magnetic field strength of the flux ropes (Figure 3.12 (c), (d) and (e), $r = 0.40$, 0.5 and 0.42, respectively).

- The average electron temperature observed at the EDR correlates positively with the axial magnetic field strength of the flux ropes (Figure 3.12 (f), $r = 0.46$).

- The maximum parallel electric field observed at the EDR correlates positively with the axial magnetic field strength of the flux rope (Figure 3.12 (g), $r = 0.40$).

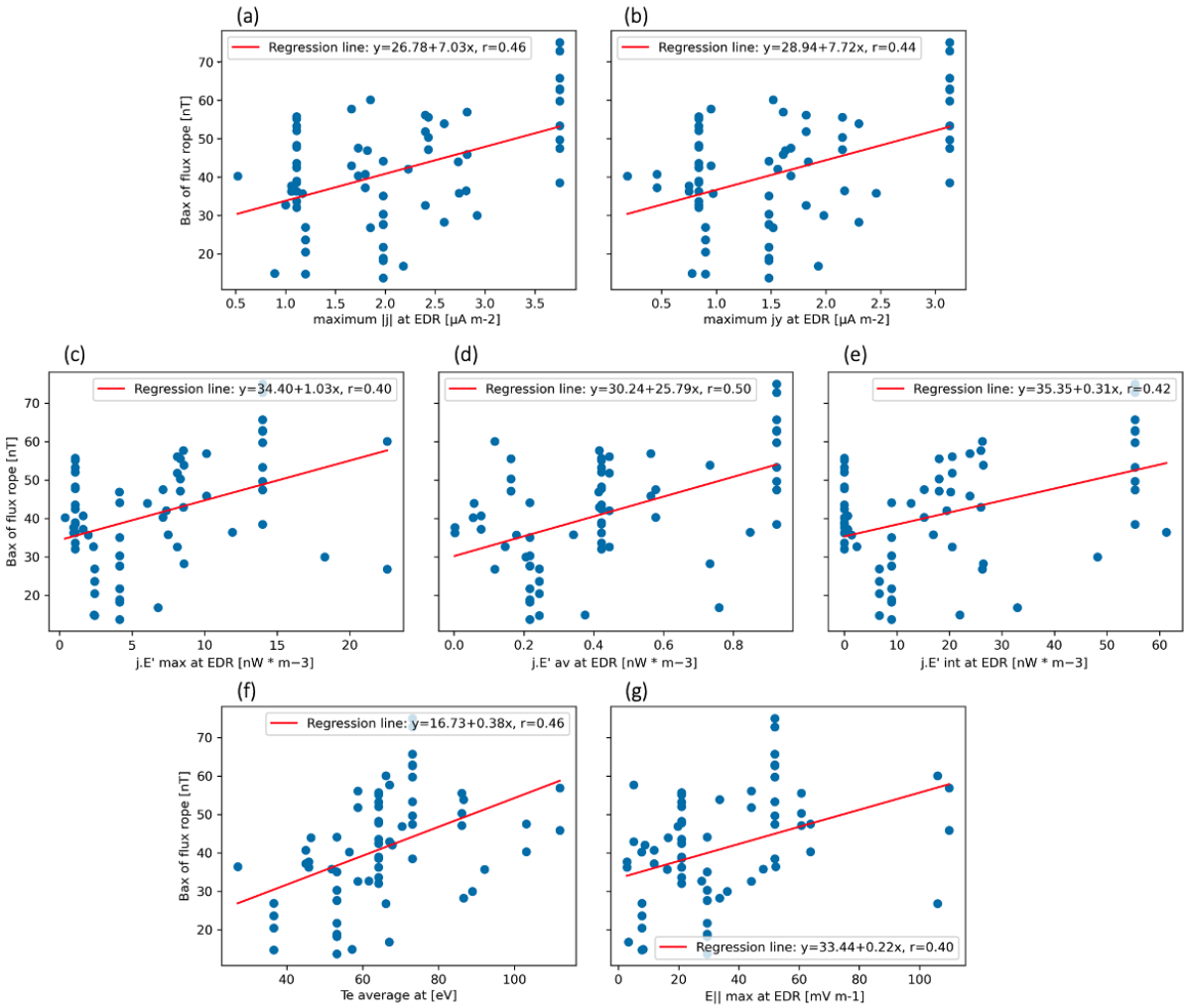

Figure 3.12: Scatter plots of EDR variables: minimum magnetic field magnitude ((a), (b) and (c), respectively) and plasma beta ((d), (e) and (f)), against flux rope variables (axial magnetic field strength, radius and flux content). The red lines show the linear regression fits for the data.

Correlations are only observed between the EDR properties and the axial magnetic field strength of the flux ropes, suggesting that this flux rope property is most likely to be effected by external plasma conditions. The positive correlations of the axial magnetic field

strength with the $\mathbf{j}\cdot\mathbf{E}'$ terms observed at the EDR suggests that when more energy is being transferred by a given EDR, flux ropes with stronger axial fields are observed surrounding it. It is also possible that these observed correlations are not direct correlations; for example a stronger guide field could lead to both an increase in the EDR properties and the increase in axial magnetic field strength of the flux ropes, as reported by Karimabadi et al. (1999).

3.6 Conclusions

In this chapter, we have presented a survey of flux ropes observed by MMS near magnetopause EDR encounters reported by Webster et al. (2018). 491 potential flux rope candidates were identified in 1-minute resolution data plots on days on which the EDRs were encountered, giving a resolution of 1 flux rope candidate per every 5.34 minutes of burst mode data. 49.9%, or 245, of these flux ropes had clear flux rope structure in MVA coordinates and were therefore used for subsequent analysis in the chapter.

The flux ropes presented in this survey have an average radius of 237 km, which is smaller than has been presented in previous studies (e.g. Akhavan-Tafti et al. (2018) found an average flux rope radius of 345 km). The smaller observed flux rope radii resulted in smaller calculated flux rope flux contents, with the average flux content found to be 3.39 kWb. This value is significantly smaller than reported in previous studies; Akhavan-Tafti et al. (2018) found an average flux rope flux content of 100 ± 30 kWb. These differences suggest that we are sampling a distinct set of flux ropes that are potentially newly formed by the EDR.

The flux rope radii distribution followed a skewed distribution with a cut off at ~ 1 d_i and a peak at just greater than 1 d_i. Previous studies have only fit an exponential tail distribution to radius distributions due to a potential artificial cut-off in observations at small scales due to the limited data resolution of spacecraft observations. In this study, we are confident that the MMS data resolution and our selection criteria would allow the

identification of flux ropes down to the electron scales, and are therefore confident in the cut-off at ion scales which we observe in our data. However, this does conflict with our suggestion that the flux ropes could be formed by the EDR which would suggest formation on electron-scales. Further investigation, via observational case studies or simulations, is required to determine if the flux ropes are formed inside the EDR itself or in the vicinity of the EDR due to other processes.

We found that flux ropes were more likely to be observed closer to the EDR, and that the properties of flux ropes varied the closer to the EDR that they were observed. Flux ropes observed closer to the EDR were found to have greater axial magnetic field strength and therefore greater flux content. This observation is in conflict with the theory of coalescence (Daughton et al., 2011c) which suggests that flux ropes interact and coalesce as they evolve, becoming larger and having greater flux content. We suggest that this coalescence could be taking place on larger scales further from the EDR, meaning different physics could be at play and influencing the flux ropes that we are observing close to the EDR.

We identified potential relationships between flux rope and EDR properties. We found the number of flux ropes observed surrounding an EDR to be limited by the maximum electron gyroradius and plasma beta at the EDR. We also found more flux ropes to be observed for stronger minimum magnetic field strength observed at the EDR. These relationships further support that flux ropes can be associated to and influenced by the EDR.

Chapter 4

Are Flux Ropes Force-Free?

4.1 Introduction

Flux transfer events (FTEs), often containing flux ropes, are a feature of magnetic reconnection and highlight the process's dynamic and variable nature, being produced when the ongoing reconnection is not steady-state (Russell and Elphic, 1978). As well as this, flux ropes themselves have been suggested to be dynamic in nature, with previous observations suggesting that they grow as they move away from the reconnection site and are convected across the magnetopause (e.g. Rijnbeek et al., 1984, using the ISEE 1 and 2 spacecraft). Global MHD simulations have also observed such FTE motion and growth (e.g. Raeder, 2006).

If a flux rope is evolving, we would expect to see forces acting on the plasma contained by the flux rope, such as magnetic pressure and tension. However, if the flux rope is in steady-state configuration, we would expect the forces on the flux rope to be balanced (i.e. $\mathbf{j} \times \mathbf{B} = 0$, where $\mathbf{j}$ is the current vector and $\mathbf{B}$ is the magnetic field vector). Such force-free flux ropes have a characteristic field arrangement which can be defined by a force-free flux rope model (e.g. Burlaga, 1988), characterised by a cylindrical symmetry about the axis of the flux rope. Flux ropes with magnetic fields consistent with this geometry have been observed on the subsolar magnetopause and in the distant

tail magnetopause (Eastwood et al., 2012a, 2016). Flux ropes have also been observed with non-force free structures (e.g. Teh et al., 2017). Recent observations have exploited multi-spacecraft missions to calculate spatial gradients and analyse the balance of forces acting on the plasma to determine if an FTE is in a force-free state (Zhao et al., 2016).

These observations suggest that flux ropes are dynamic in nature and can be observed in either a force-free or non-force-free state as they move over the magnetopause. It remains unclear what dictates whether an observed flux rope is force-free or not, and how this fits in with flux rope evolution theories, such as flux rope coalescence. Coalescence suggests that flux ropes are formed initially by reconnection and can coalesce as they move over the magnetopause, resulting in larger flux ropes with greater flux content (Daughton et al., 2011b). This coalescence process is dynamic in nature, requiring magnetic reconnection to take place between merging flux ropes under non-force-free conditions. Flux rope particle acceleration mechanisms also require flux ropes to be non-force-free: the Drake et al. (2006a) mechanism requires flux ropes to be contracting in order to accelerate electrons.

As well as using a force-free flux rope model to assess if a flux rope is force-free, we can also use the model output to investigate further flux rope properties, such as the helicity of the flux rope. This is the direction in which the flux rope magnetic field twists, i.e. the handedness of the flux rope. The helicity of a flux rope can be either positive or negative, indicating the direction the flux rope twists around its axis. The helicity of flux ropes has been extensively studied in coronal mass ejection (CME) magnetic clouds (e.g. Palmerio et al., 2018) and in planetary magnetospheres (e.g. Martin et al., 2020). At Earth, the helicity of flux ropes has been found to be controlled by the sign of the IMF B_Y component (Kieokaew et al., 2020), with positive helicity flux ropes mostly being preceded by positive IMF B_Y. This observation supports the multiple X-line FTE formation mechanism (Lee and Fu, 1985; Raeder, 2006), which results in flux ropes with opposing helicity for positive and negative IMF B_Y.

In this chapter, we apply a force-free flux rope model to the EDR-associated flux

ropes presented in Chapter 3, which found such flux ropes to have distinct properties, suggesting that they could be newly formed by the EDR. We assess how force-free these flux ropes are using the error on their force-free model fits. The chapter aims to investigate if the flux ropes are force-free and how their force-free nature relates to their properties. These observations are used to investigate flux rope formation and evolution theories. For example, if coalescence is taking place we would expect to observe non-force-free flux ropes (Daughton et al., 2011b).

The chapter is structured as follows. In Section 4.2, we introduce the force-free flux rope model used and how it is applied to the flux ropes. Section 4.3, discusses how we quantify a good force-free fit and investigates the factors that influence this. Section 4.4 discusses the findings of the model outputs, including the flux rope parameter distributions and the helicity. In Section 4.5, the conclusions of this force-free flux rope model analysis are presented.

4.2 Force-Free Flux Rope Model

A force-free flux rope model assumes that the forces acting on the flux rope plasma are balanced and sum to zero. Mathematically, this is expressed as $\mathbf{j} \times \mathbf{B} = 0$, where $\mathbf{j}$ is the current vector and $\mathbf{B}$ is the magnetic field vector. The terms usually on the right-hand side of this equation, corresponding to magnetic pressure and tension (see Section 1.1.2), are equal and opposite, therefore cancel each other. Applying this force-free assumption to the twisted magnetic field structure of a flux rope results in a cylindrically symmetric field structure with purely tangential fields at the edges, a purely axial field at the centre and intermediate orientations in between. The details of the force-free flux rope model used in this section are discussed in greater detail in Section 2.4.

The force-free flux rope model described in Section 2.4 was fit to the 245 flux ropes which had clear flux rope structure in MVA coordinates, as described in Section 3.3. First, the flux rope is rotated into MVA coordinates, identifying the axial and azimuthal flux

rope field components. Then, multiple force-free flux ropes are fit to the data by varying the core magnetic field strength and the impact parameter (IP, the fractional distance of the closest approach of the spacecraft to the center of the flux rope, see Figure 4.8), which are together know as the fit input parameters. The core field is looped from 0.1 nT to 1.5 times the maximum observed magnetic field strength for the flux rope observation and the IP is looped from 0 to 0.5. For each fit, the root mean squared (RMS) error between the observed and model fit magnetic field components are calculated. As the variables are looped over, the fit input parameters for the fit with the smallest RMS value are retained. Once the loops are completed and the fit parameters which give the smallest RMS value, i.e. the best force-free fit, have been identified, they are used to calculate further force-free fit parameters, such as the flux rope radius, axial orientation and helicity. This data is included in Appendix A. An example of one of these best fits can be seen in Figure 4.1.

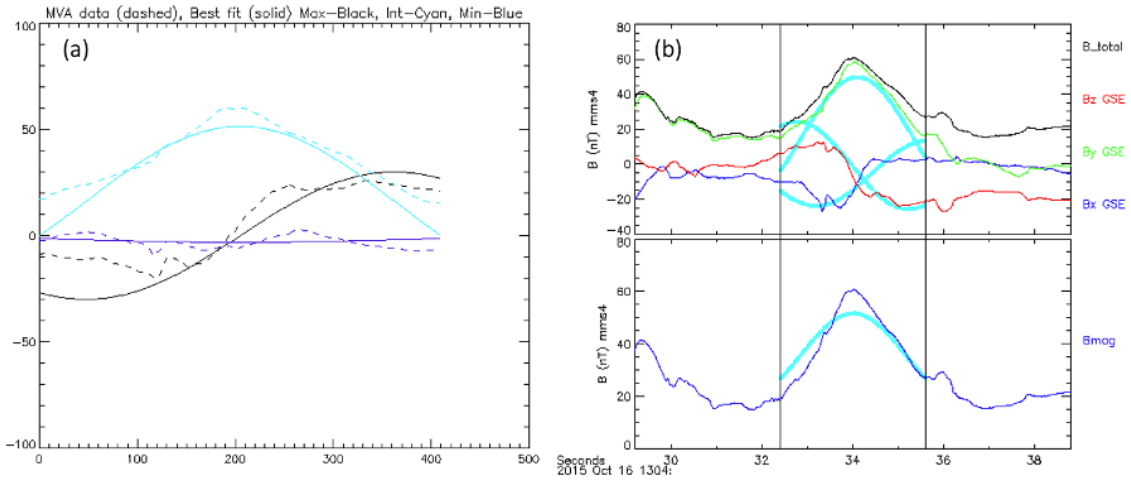

Figure 4.1: Example of a force-free flux rope fit. (a) shows the flux rope observation (dashed lines) and fit (solid lines) in the rotated MVA coordinate system. (b) shows the flux rope observation and fit (thick cyan lines) in the original GSE coordinate system.

4.3 Force-Free Model Error

The root mean squared (RMS) error for the flux rope model can be used as a proxy measure for how force-free a given flux rope is; flux ropes that are more force-free would be expected to have a smaller RMS error, whereas flux ropes in a non-force-free configuration would be expected to have a larger RMS error. For the flux ropes in this study, we have RMS errors ranging from a few to tens of nT (RMS error in units of nT as a measure of magnetic field goodness of fit). Figure 4.2 plots (a) the time between the flux rope and EDR observation, (b) the force-free fit model radius, (c) the force-free fit closest approach (the IP) and (d) the force-free fit axial magnetic field strength against these RMS errors. From (d) it is clear that the RMS error scales with the axial magnetic field strength of the flux rope; there is a strong positive correlation showing that flux ropes with a stronger axial magnetic field have greater RMS error. This is not unexpected as the same percentage error on a greater magnetic field strength will result in a larger RMS error in nT units. This effect could be masking potential correlations in the other scatter plots; to remove it we scale the RMS error of each force-free fit by the fit's axial magnetic field strength, resulting in the plots shown in Figure 4.3. In these plots, distribution outliers become clear. Through a visual inspection of fits with RMS scaled values greater than 1, we decide that this is a reasonable cut-off for defining a failed force-free fit. An example of one of these fits with RMS scaled = 2.60 can be seen in Figure 4.4. Using this cut-off, we find 7 (2.9%) force-free fits have failed and remove them from further analysis.

Removing the failed force-free fits from the data, we replot the RMS scaled error scatters in Figures 4.5 and 4.6, which show the plots for all flux ropes and flux ropes observed within 15 minutes of the EDR, respectively. Figures 4.5 and 4.6 (c) show no correlation between the closest approach (or IP) and the RMS scaled error. Figures 4.5 and 4.6 (d) show weak negative correlations, suggesting that having a stronger axial magnetic field may improve the force-free fit. Figures 4.5 and 4.6 (b), also show a weak negative correlation, suggesting having a greater radius improves the force-free fit.

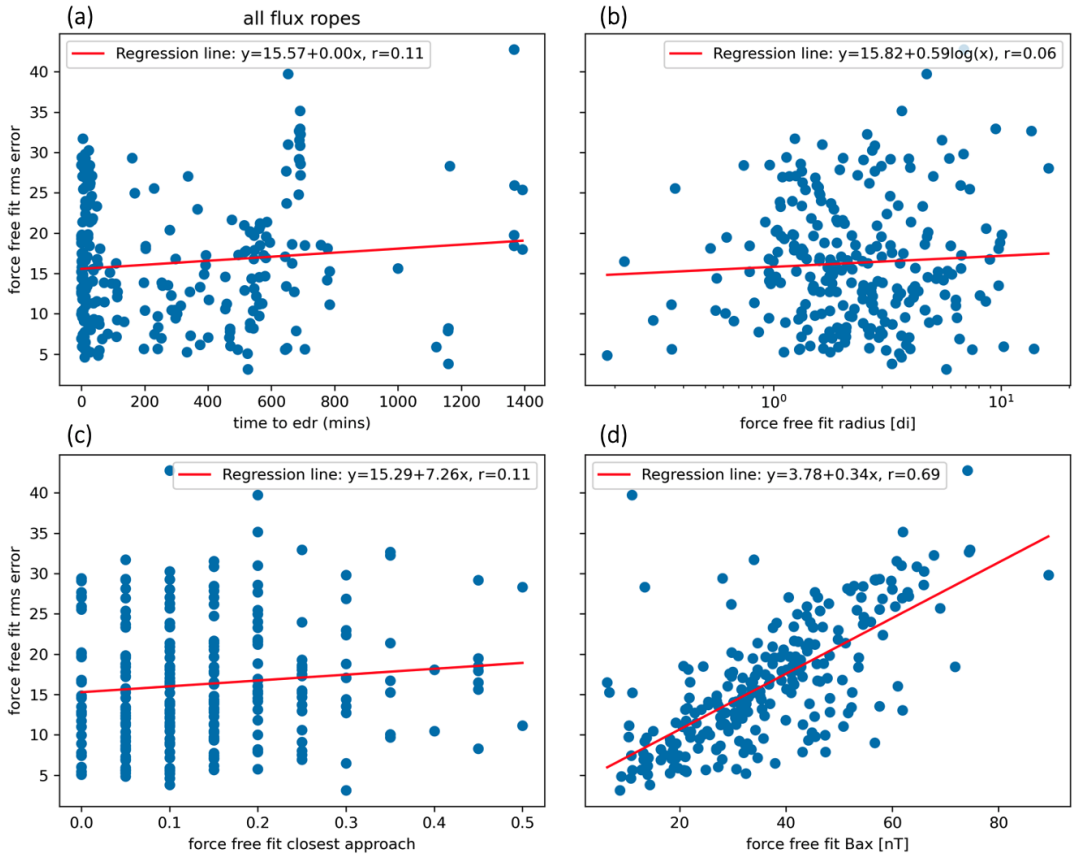

Figure 4.2: Force-free fit RMS error scatter plots for all flux ropes. (a) shows the time between the flux rope and EDR observation, (b) the force-free fit radius, (c) the force-free fit impact parameter (closest approach), and (d) the force-free fit axial magnetic field, against the RMS error of the force-free fit.

These correlations become stronger as the time to the EDR is limited in Figure 4.6, despite the time to EDR plots in Figures 4.5 and 4.6 (a) showing no correlation. This suggests that being close to the EDR does not directly affect the force-free fit, but relationships that do affect the force-free fit could be enhanced closer to the EDR.

These observations suggest that flux ropes with larger radii and stronger axial magnetic fields have better force-fit fits and are therefore potentially more likely to be in a force-free state than flux ropes with smaller radii and weaker axial magnetic fields. If we combine this with the results from Chapter 3, where it was found that flux ropes with stronger core fields, and potentially those with larger radii, were more likely to be observed closer to the EDR, these results could suggest that flux ropes observed closer to the EDR may be more likely to be force-free.

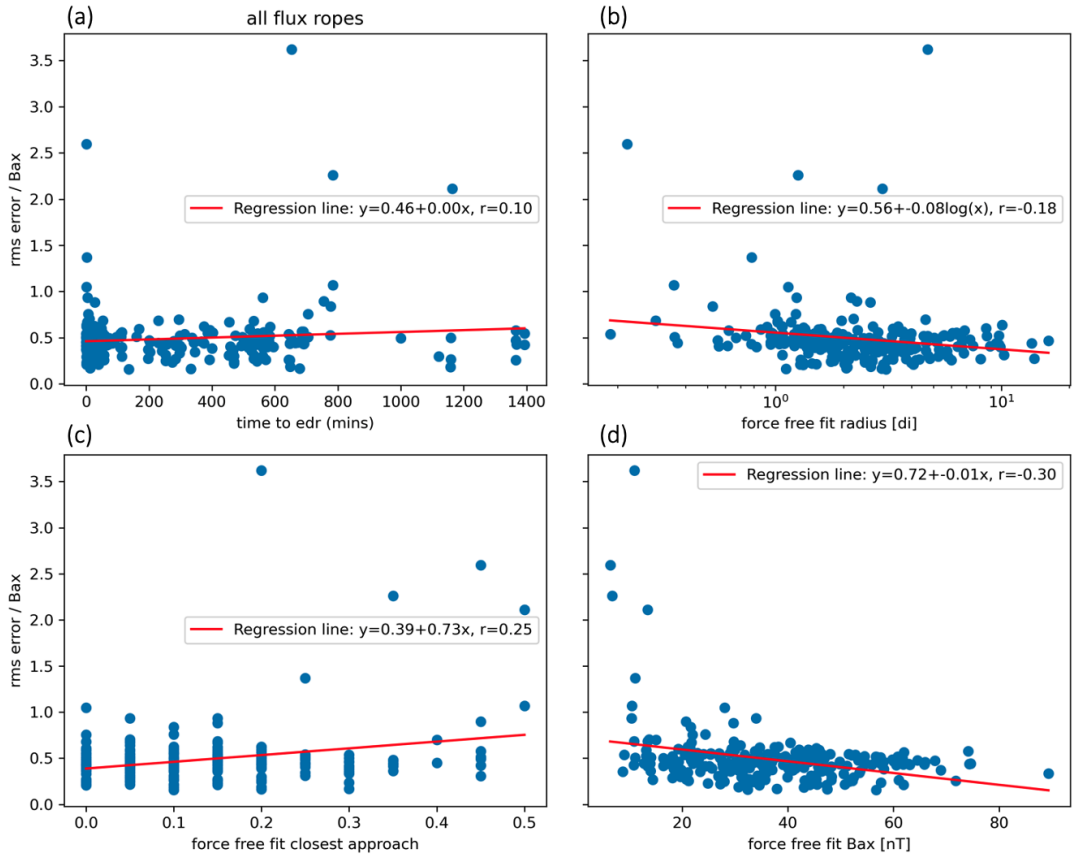

Figure 4.3: Force-free fit RMS error, now scaled by B_{ax}, scatter plots for all flux ropes. (a) shows the time between the flux rope and EDR observation, (b) the force-free fit radius, (c) the force-free fit impact parameter (closest approach), and (d) the force-free fit axial magnetic field, against the RMS error scaled by the axial field strength of the force-free fit.

As discussed in the previous chapter, our population of flux ropes are smaller and have stronger axial field strengths than presented in previous studies, which suggests that we could be sampling a subset of flux ropes that have been recently formed by the EDR. These observations of flux ropes potentially being more force-free closer to the EDR could only apply to this subset of flux ropes and not to the general population of magnetopause flux ropes, as we could mostly be observing flux ropes at the beginning of their evolution before they are convected over the magnetopause. The fact that the majority of flux ropes presented in this study have good force-free fits could suggest that flux ropes tend to be formed in a force-free state by the EDR.

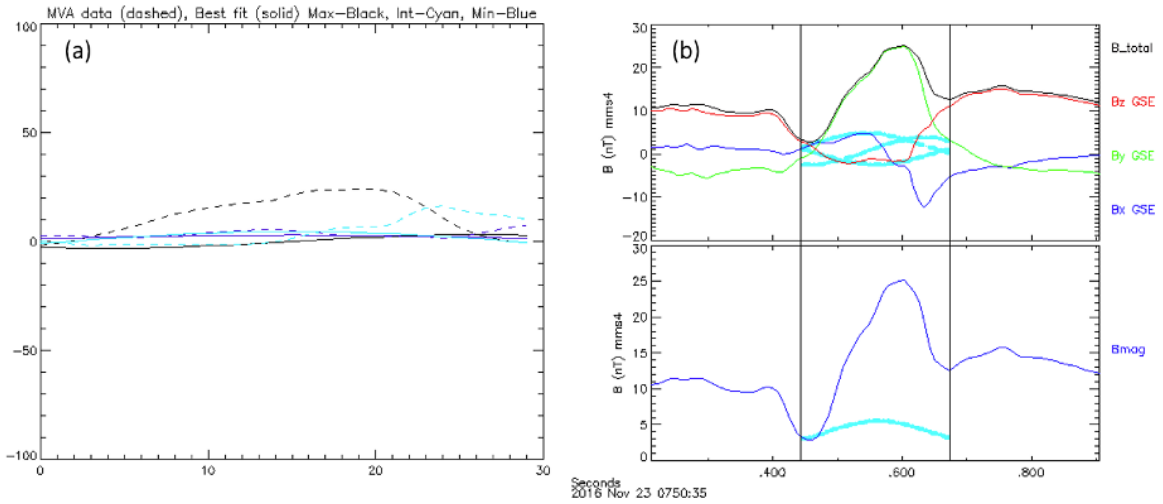

Figure 4.4: Example of a failed force-free flux rope fit. (a) shows the flux rope observation (dashed lines) and fit (solid lines) in the rotated MVA coordinate system. (b) shows the flux rope observation and fit (thick cyan lines) in the original GSE coordinate system.

4.4 Force-Free Model Statistics

Once the force-free flux rope model is applied to the flux ropes, we can then extract and analyse the model output. We find that the model gives an average flux rope axial magnetic field strength of 36.31 nT, comparable to the 38.27 nT found by taking the maximum value of the MVA axial field component in the previous chapter. The model gives an average flux rope radius of 153.23 km or 2.73 d_i, 35% and 34% smaller, respectively than the averages of 237.37 km and 4.11 d_i found by averaging the ion velocity and multiplying by the length of the observation duration, as detailed in the previous chapter. These differences translate into the flux rope flux content estimates, where the equation: $flux = 0.4158 J_1(2.40482) \times (2\pi r^2 B)$, where J_1 is the first Bessel function, r is the flux rope radius, and B is the axial field strength of the flux rope, is again used to calculate the flux content. The force-free fit model estimate gives an average flux content of 1.28 kWb, $\sim$ 49% smaller than the previous estimate of 3.39 kWb. These values are summarised in Table 4.1.

We investigate these differences further by comparing the distributions for the flux rope radii, axial magnetic field strength and flux content for the force-free model outputs

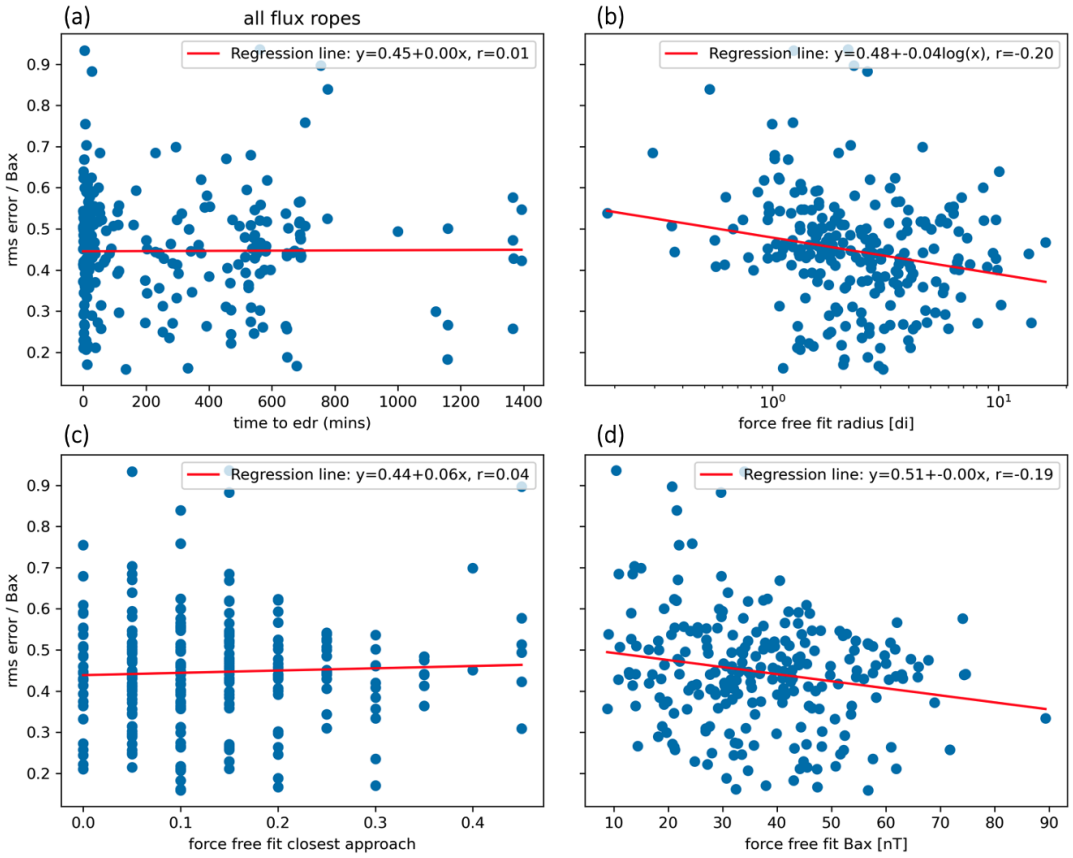

Figure 4.5: Force-free fit RMS error (scaled by the axial field strength) scatter plots, with flux ropes with scaled error $>$ 1 removed. (a) shows the time between the flux rope and EDR observation, (b) the force-free fit radius, (c) the force-free fit impact parameter (closest approach), and (d) the force-free fit axial magnetic field, against the RMS error of the force-free fit.

	radius		**B_{ax}**	**flux content**
	[km]	[d_i]	[nT]	[kWb]
simple estimate	237.37	4.11	38.27	3.39
force-free fit estimate	153.23	2.73	36.31	1.28

Table 4.1: Mean average values for the radius in km and d_i units, the axial magnetic field strength and the flux content for simple estimates from the previous chapter and the force-free fit model.

and the simple estimates used in the previous chapter, as can be seen in Figure 4.7. The force-free fit model radius and axial magnetic field distributions fit well to skewed distributions, as observed for the simple estimates. The radius distributions are narrower with shorter distribution tails for the force-free fit model, however the two distributions peak

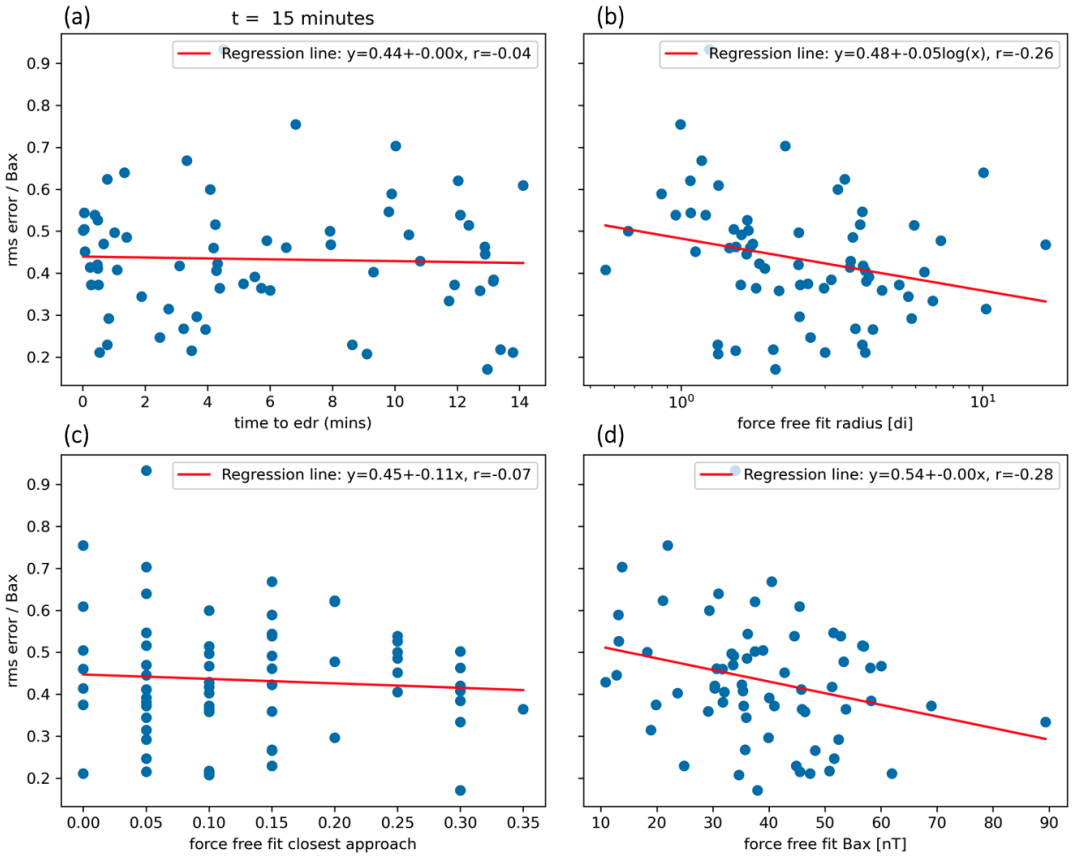

Figure 4.6: Force-free fit RMS error (scaled by the axial field strength) scatter plots, with flux ropes with scaled error > 1 removed and limited to flux ropes observed within 15 minutes of an EDR encounter. (a) shows the time between the flux rope and EDR observation, (b) the force-free fit radius, (c) the force-free fit impact parameter (closest approach), and (d) the force-free fit axial magnetic field, against the RMS error of the force-free fit.

at similar values, with the force-free fit peak being at an only slightly lower value. These observations are true for the radius distributions in both km and d_i units (Figure 4.7 (a) and (b), respectively). The distributions for the axial magnetic field strength are comparable, peaking at $\sim$ 35 nT. The radii differences again translate into the flux content distributions, which both follow exponential distributions with the simple estimate having a longer tail.

As the flux ropes tend to have a good force-free fit, as shown by RMS values in the previous section, we could expect the force-free fit radius estimate to be closer to the true value of the flux rope radius. This is because the force-free fit model takes into account

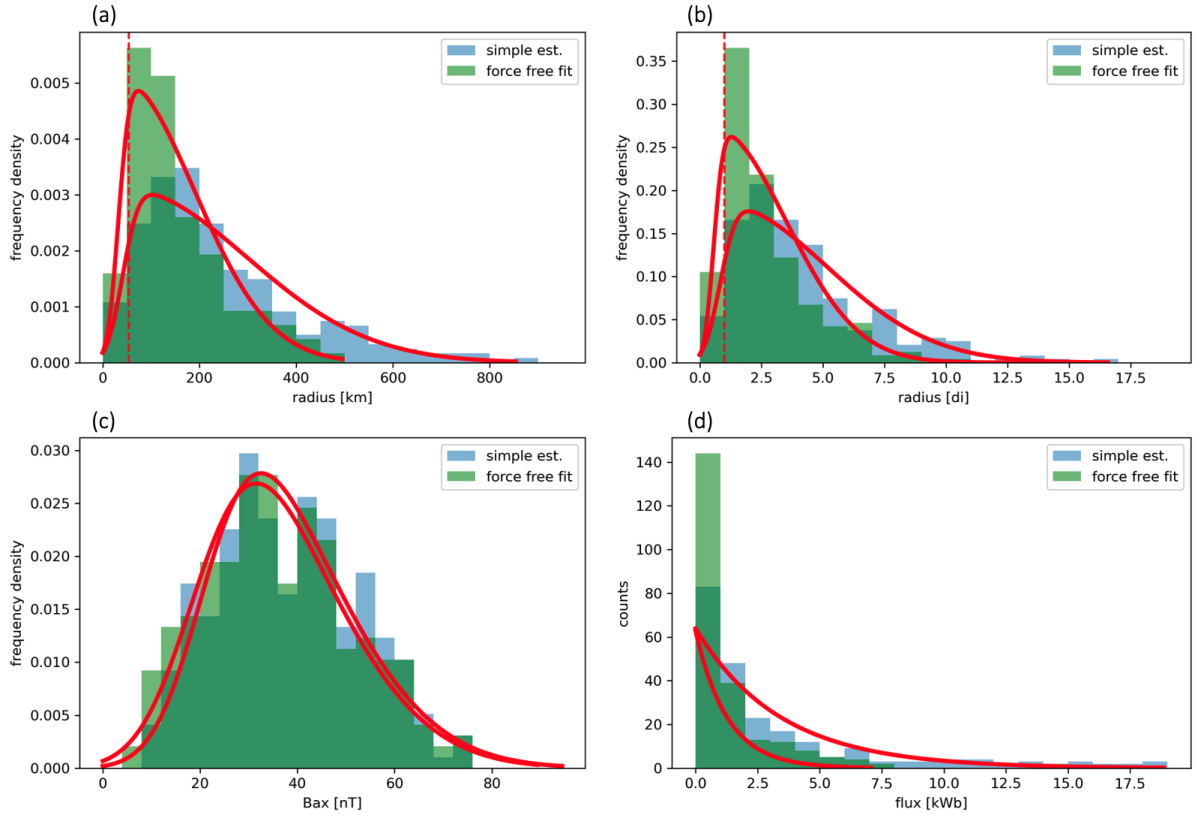

Figure 4.7: Distribution comparison plots for the simple estimates from the previous chapter (blue) and force-free fit estimates (green), with skewed ((a), (b) & (c)) and exponential (d) distribution fits in red. (a) & (b) show radius distributions in km and d_i units, respectively, with vertical dashed lines indicating the location of 1 d_i. (b) shows the axial magnetic field strength, and (c) the flux content.

the impact parameter for the flux rope observation, and therefore does not require the assumption that the observation passes through the centre of the flux rope. This means we would expect a larger radius estimate from the force-free fit model, as shown in Figure 4.8. However, this is not what we observe; we see a smaller average flux rope radius estimate from the force-free fit.

4.4.1 Flux Rope Helicity

For the flux ropes included in this study, we found that 164 (66.9%) flux ropes have positive helicity and 81 (33.1%) have negative helicity. We investigate if the helicity has any dependence on the time between the flux rope observation and the EDR observation. The flux ropes are split into positive and negative helicity subsets and their time to EDR

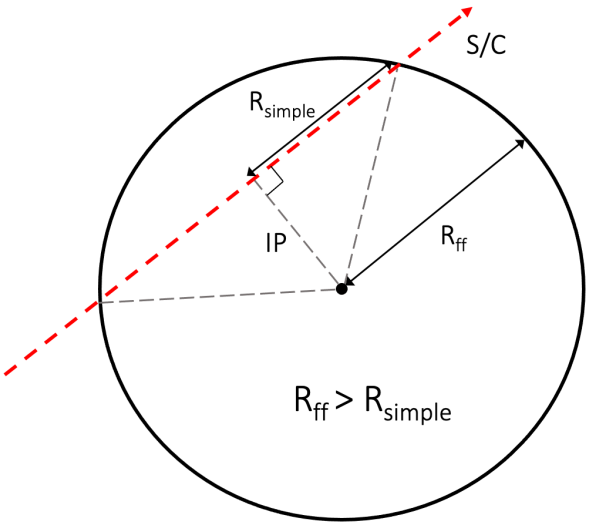

Figure 4.8: Diagram showing how the impact parameter affects the flux rope radius estimate. The red dashed line shows the path of the spacecraft through the flux rope. R_{simple} shows the simple radius estimate which assumes the spacecraft crosses the diameter of the flux rope. R_{ff} shows the force-free fit radius estimate which is able to factor in the impact parameter (labelled IP) of the spacecraft trajectory, resulting in a larger radius estimate.

normalised distributions are compared, as can be seen in Figure 4.9. We observe that positive helicity flux ropes are more likely to be observed close to the EDR. Figure 4.10 investigates this relationship further by comparing the time to EDR cumulative distribution for positive and negative helicity flux ropes. This plot reinforces the observation that more positive helicity flux ropes are observed closer to the EDR.

We also investigate the location of the observed flux rope helicities. Figure 4.11 plots the observed EDR location, where the points are colour-coded according to the proportion of positive (red) and negative (blue) helicity flux ropes surrounding the given EDR and the size of the points are proportional to the number of flux ropes observed surrounding the EDR; (a) is for all flux ropes, (b) shows flux ropes observed within 60 minutes of the EDR and (c) shows flux ropes observed within 15 minutes of an EDR. These plots suggest that the majority of negative helicity flux ropes are observed in the bottom right quadrant of the plot, where the y GSE coordinate is positive and the z GSE coordinate is negative. However, the observations are generally skewed to this quadrant,

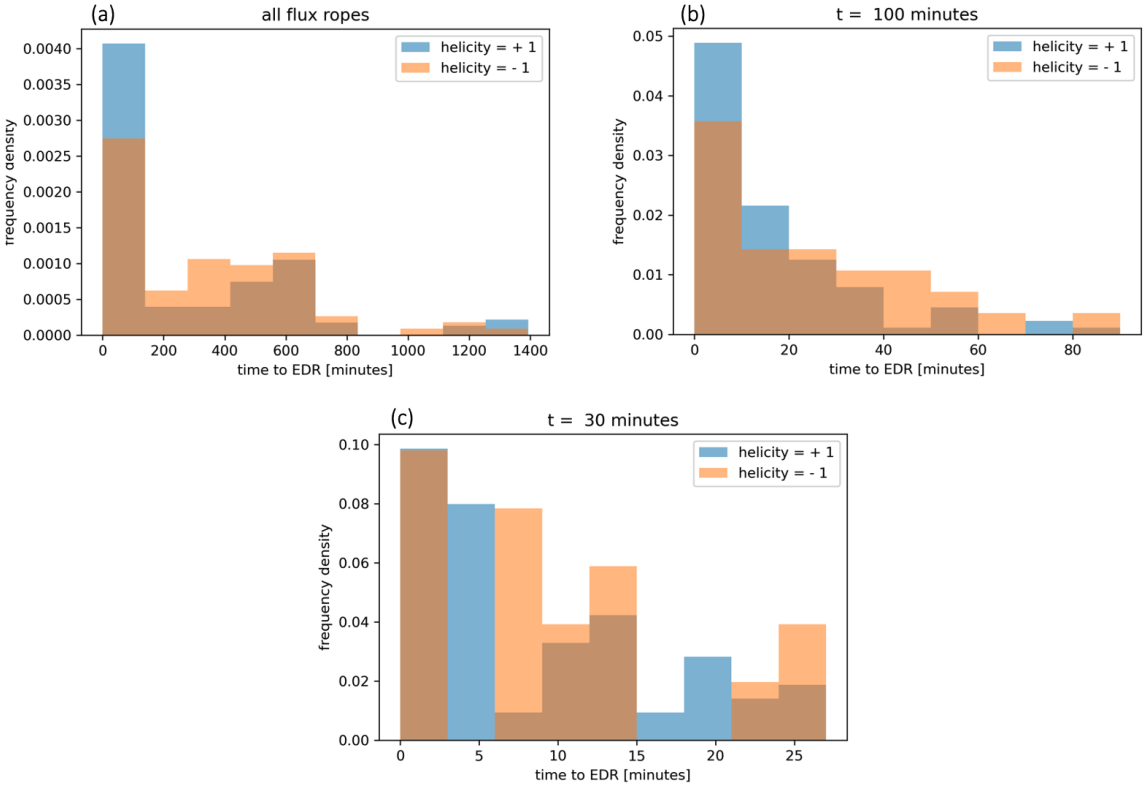

Figure 4.9: Time to EDR distribution comparisons for positive (blue) and negative (orange) flux rope helicity, for (a) all flux ropes, (b) flux ropes observed within 100 minutes of an EDR, and (c) within 30 minutes of an EDR.

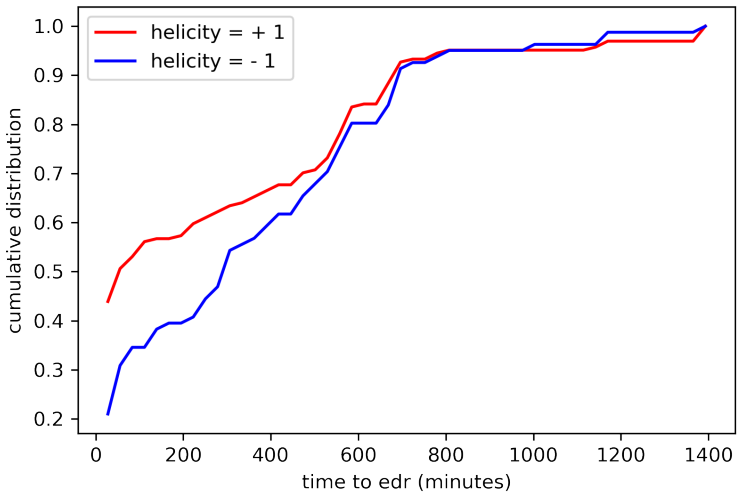

Figure 4.10: Comparison of time to EDR cumulative distributions for positive (red) and negative (blue) helicities

which may also skew this observation.

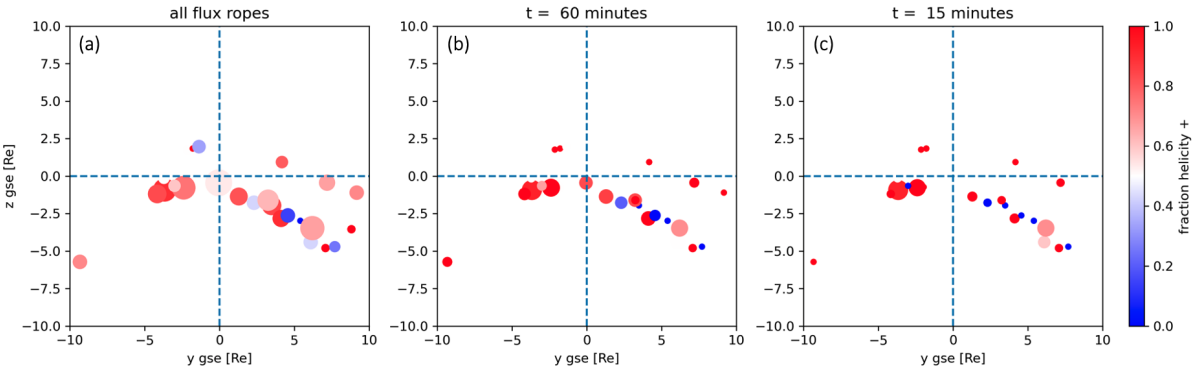

Figure 4.11: Location of EDRs and their corresponding observed flux rope helicities. Points are coloured according to the fraction of flux ropes with positive helicity, where red = 1 means all flux ropes have positive helicity and blue = 0 means all flux ropes have negative helicity. The size of the points is proportional to the number of flux ropes observed surrounding each EDR, with (a) showing all flux ropes, (b) showing flux ropes observed within 60 minutes of the EDR, and (c) showing flux ropes observed within 15 minutes of the EDR.

In this study, we have not considered solar wind conditions, so cannot directly comment on if these observations are consistent with positive IMF B_Y leading to positive helicity flux ropes, as suggested by Kieokaew et al. (2020). However, we can qualitatively investigate this relationship. According to the maximum magnetic shear model (see Section 1.2.3, Figure 1.7), we would expect the reconnection X-line, and therefore the EDR, to be located in the quadrant with positive y GSE and negative z GSE when the IMF has a significant negative B_Y component. This is the quadrant in which we observe the majority of the negative helicity flux ropes, which is consistent with Kieokaew et al. (2020). However, we do also observe many positive helicity flux ropes in this quadrant, suggesting both helicities can be produced by reconnection occurring in this quadrant, potentially conflicting with these observations. Furthermore, our observation of a greater proportion of positive helicity flux ropes closer to the EDR suggests that there could be more complicated helicity-EDR relationships at play.

4.5 Conclusions

In this chapter, we have presented an investigation into the force-free nature of the EDR-associated flux ropes presented in Chapter 3. A force-free flux rope model was applied to the flux ropes, which assumes $\mathbf{j} \times \mathbf{B} = 0$, where $\mathbf{j}$ is the current vector and $\mathbf{B}$ is the magnetic field vector. Under this assumption, the flux rope is in an ideal, cylindrically symmetric configuration and is assumed not to be evolving. For each flux rope, the model parameters were varied and the best fit was identified by minimising the RMS error of the force-free magnetic field fit. This best-fit RMS error was scaled by the axial magnetic field strength of the flux rope and used as a measure for how force-free each flux rope was, with more force-free flux ropes having a better agreement with the force-free fit model and therefore smaller RMS errors. Using the criteria for a good fit as $RMS/B_{ax} < 1$, only 7 (2.9%) of flux ropes were categorised as not being force-free.

When investigating the RMS error of the flux ropes, it was observed that flux ropes with a greater radius and stronger axial field strength have smaller RMS errors, suggesting that they are more force-free. The findings of the previous chapter suggest that flux ropes observed closer to the EDR tend to have stronger axial fields. Combining these observations suggests that flux ropes observed closer to the EDR could be more force-free. This may indicate that the EDR produces flux ropes in a force-free state and that flux rope coalescence is unlikely to take place close to the EDR.

When comparing the output flux rope parameters from the force-free fit model to the simple estimates calculated in the previous chapter, we found that the force-free model gives smaller flux rope radii. The main difference between the two estimates is that the force-free model factors in the impact parameter and as such does not require the assumption that the spacecraft passes through the centre of the flux rope. Considering this, we would expect the force-free model to predict larger radii than the simple estimates, however we find that the force-free model suggests smaller flux rope radii than the simple estimate. This highlights that there are unidentified factors influencing the differences

between the predictions, other than the impact parameter. Further work is required to determine what these factors may be; multi-spacecraft analysis of individual flux rope case studies could help to identify why we observe these differences.

The flux rope helicity was also investigated. The majority of flux ropes (66.9%) were observed to have positive helicity. When these are limited to within 15 minutes of the EDR, we find that the majority of negative helicity flux ropes are observed in the quadrant with positive y GSE and negative z GSE; this is where we would expect reconnection to take place when the IMF has significant negative B_Y component, and therefore corresponding negative helicity observations are consistent with Kieokaew et al. (2020). However, we also observe many positive helicity flux ropes in this quadrant, and observe more positive helicity flux ropes closer to the EDR, suggesting that more complex EDR-helicity relationships may be at play.

Chapter 5

Flux Rope Topology

5.1 Introduction

Magnetic reconnection produces a change in magnetic field topology. At the magnetopause, magnetic field lines originally connected only to the solar wind or only to the magnetosphere reconnect to produce field lines connected to the solar wind at one and the magnetosphere at the other. Unlike the reconnected field lines which have known topologies under steady-state reconnection conditions, flux ropes produced during reconnection can have varying topologies, with either end of the contained magnetic field lines being able to connect to either region; field lines can be open, meaning they are connected to the magnetosheath at one end and the solar wind at the other, or closed, meaning they are connected to either the magnetosheath or solar wind at both ends. This results in four potential field line topologies which can be identified using the particle pitch angle distributions, as is illustrated in Figure 5.1. In (a) we observe a field-aligned ($0-90°$) population of magnetospheric electrons (> 1 keV), anti-field-aligned and accelerated (from ~ 100 eV to $200-700$ eV) field-aligned magnetosheath electrons. From this, we can infer that the magnetospheric electrons are escaping from the magnetosphere into the magnetosheath and the magnetosheath electrons are entering the magnetosphere and being reflected and accelerated. As the magnetospheric particles are field-aligned we can deter-

mine that the flux rope is connected to the southern hemisphere. The topology of this configuration can be seen in Figure 5.1 (a′). Figure 5.1 (b′) shows a similar configuration, however, the flux rope is now connected to the northern hemisphere. In a similar manner, we are able to deduce the closed flux rope topologies in Figure 5.1 (c) and (d). In (c) we observe almost isotropic magnetospheric electrons and counter-streaming magnetosheath electrons, suggesting the flux rope is connected to the magnetosphere at both ends. In (d) we observe a lower flux of magnetospheric electrons and heated magnetosheath electrons suggesting the flux rope is connected to the magnetosheath at both ends.

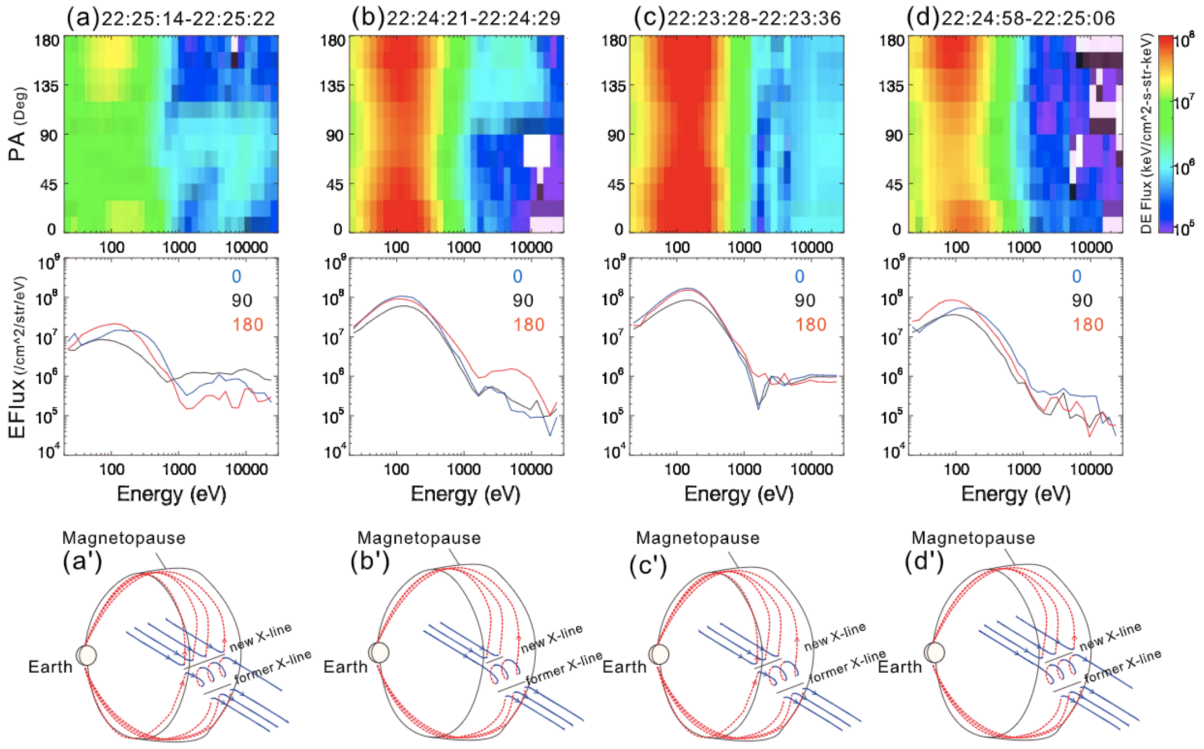

Figure 5.1: Diagram displaying how different flux rope topologies can be inferred from the electron pitch angle energy distributions measured inside the structure. (a) and (b) show open field topologies, where the flux rope is connected to the magnetosphere at one end and the magnetosheath at the other. (c) and (d) show closed topologies, where the flux rope is connected to the magnetosphere and magnetosheath at both ends. *Figure from Figure 2 of Pu et al. (2013).*

There have been numerous observations of complex flux rope topology and substructure; Thomsen et al. (1987) provided the first study of the particle distributions within an FTE and found that FTEs contain a mixture of both magnetospheric and mag-

netosheath electrons, suggesting that the flux rope field lines are connected to both regions. Owen et al. (2001) studied the electron substructure of FTEs using Cluster-PEACE measurements. They observed differences in FTE signatures between the 4 Cluster spacecraft, suggesting substructure on the order of the spacecraft separation ($\sim$ 600 km). Varsani et al. (2014) observed an FTE with multiple layers of plasma, including cold plasma inside the core with a thin layer of antiparallel electrons at the edge. Further small-scale substructure has been observed, including filamentary currents in ion-scale magnetopause flux ropes (Eastwood et al., 2016) and electron vortices in magnetotail flux ropes (Stawarz et al., 2018). These complex substructures are often attributed to the topology and connectivity of the flux rope. Pu et al. (2013) observed all 4 possible topologies inside a single FTE, as shown in Figure 5.1. Owen et al. (2001) observed trapping of magnetospheric electrons on newly-opened FTE field lines. Øieroset et al. (2011) also observed an open magnetic field topology inside an FTE which was situated between two active reconnection X-lines. Ongoing reconnection at the centre of an FTE has been observed (Øieroset et al., 2016), resulting in two distinct topologies through the FTE (Fargette et al., 2020).

The topology of the flux ropes is also important for understanding the larger-scale flux transport implications of the flux ropes. Russell and Elphic (1978) postulated that FTEs observed on the magnetopause move poleward, transferring magnetic flux into the magnetotail. This poleward FTE motion was observed by Berchem and Russell (1984). For flux transfer to be effective, the flux rope must be connected to the magnetosphere. The topology of the flux ropes also has implications for the flux rope formation mechanisms. The multiple X-line formation model, proposed by Lee and Fu (1985) and suggested by multiple observations (e.g. Hasegawa et al., 2010), results in open flux ropes which are connected to the magnetosphere at one end. Russell and Qi (2020) conducted a statistical survey of magnetopause flux ropes and found that $\sim$ 50% of flux ropes contained magnetospheric electrons, suggesting $\sim$ 50% of flux ropes are connected to the magnetosphere and the remaining $\sim$ 50% to the magnetosheath. They conclude that the

flux ropes must be produced in pairs, which then reconnect (as observed by Øieroset et al. (2016)), to account for these observations. Hwang et al. (2021) investigated a case study of an FTE consisting of two merging and reconnecting flux tubes and highlighted how such interactions can impact the large-scale FTE structure and dynamics. Using a global MHD simulation, Mejnertsen et al. (2021) found that non-local reconnection can lead to a change in the topology of flux ropes as they move over the magnetopause.

Despite these multiple case studies suggesting varying and complex flux rope topology, the relationship between flux rope topology and the ongoing reconnection which produces them is yet to be fully understood; for example, does magnetic reconnection of a particular nature lead to the production of flux ropes of a particular topology? Understanding these relationships could help evaluate the significance of flux ropes as an indicator for time-varying or bursty reconnection and their role in energy and flux transport in the magnetosphere.

In this chapter, we classify the topology of the EDR-associated flux ropes presented in Chapter 3, with the aim of investigating how the topology relates to the EDR, ongoing reconnection and flux rope properties. In the following section, we discuss how the topology of the flux ropes is classified and present the initial statistical results. Section 5.3 investigates how the topology is related to the EDR observations. Section 5.4 investigates the relationship between the topology and other flux rope properties. In Section 5.5, the conclusions of this investigation are presented.

5.2 Topology Classification

The flux rope topology was investigated using the electron pitch angle distributions (PADs) from the MMS FPI instrument (Section 2.1.1). For consistency with previous chapters, the 245 flux ropes with well-defined MVA coordinate systems were investigated. Overview plots for each flux rope were made, examples of which can be seen in Figures 5.2 and 5.3. The PADs are presented over 4 panels ((e) – (h)) which show the

Topology class	0 closed magnetosheath	1 open southern	2 open northern	3 closed magnetosphere
high E electrons? (> 1 keV)	none	0°	180°	bidirectional

Table 5.1: Flux rope topology definitions used in this study.

average distribution over all energy ranges and for low (< 100 eV), mid (100 eV – 1 keV) and high (> 1 keV) energy ranges, respectively. The low and mid energy ranges show the presence of magnetosheath electron populations, which can be accelerated up to hundreds of eVs. The high energy range shows magnetospheric electrons which are observed at energies > 1 keV. The presence of these particle populations can also be seen in the omnidirectional energy flux (Figures 5.2 and 5.3 (d)). The presence or absence of such electrons allows us to determine which electron populations are present inside the flux rope, and therefore classify the flux rope's potential topology, as illustrated in Figure 5.1. A closed magnetosheath topology (defined as topology 0, corresponding to Figure 5.1 (d)), where field lines are connected to the magnetosheath on both ends, will show no significant high energy magnetospheric electrons. An example of a flux rope observation with topology 0 can be seen in Figure 5.2. An open magnetosheath topology (defined as topology 1), where field lines are connected to the magnetosheath in the southern hemisphere and the magnetosphere at the other, will have a significant high energy electron population along the field lines streaming away from the magnetosphere, in this case at 0°. An example of a flux rope with topology 1, with a high energy electron population at 0°, can be seen in Figure 5.3. This same open topology can also be connected to the magnetosphere in the northern hemisphere, leading to anti-parallel streaming electrons at 180°, defined as topology 2. A closed magnetospheric topology (defined as topology 3), where field lines are connected to the magnetosphere at both ends, will have significant high energy electron populations at both 0°and 180°. These topology classes are summarised in Table 5.1.

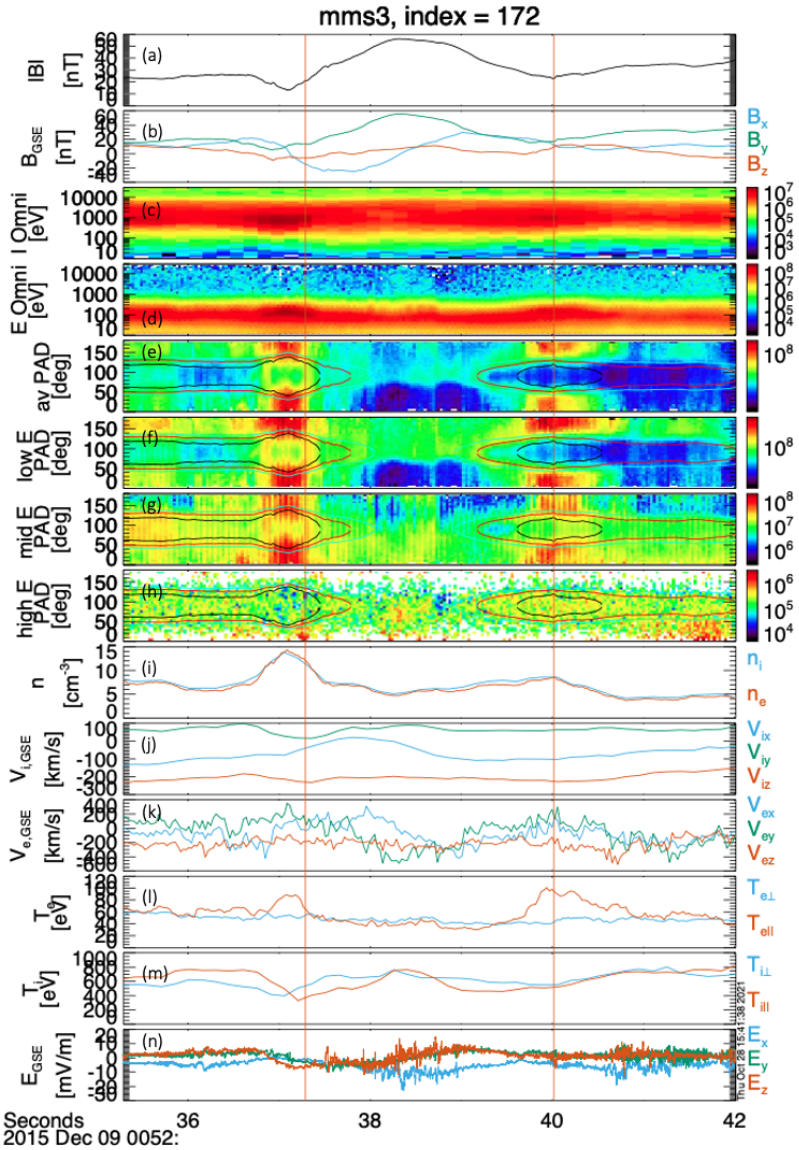

Figure 5.2: Example of a topology 0 flux rope burst mode data plot. The flux rope is closed to the magnetosheath, identified by the lack of high energy (> 1 keV) magnetospheric electrons in panels (d) and (h).

The PADs were visually inspected to identify the topology of each of the flux ropes. It is noted that in some cases the topology was not consistent for the full duration of the flux rope and the flux rope was identified as having a 'patchy' topology. We were unable to determine a topology for 5 of the flux ropes which had no clear trend to their PADs.

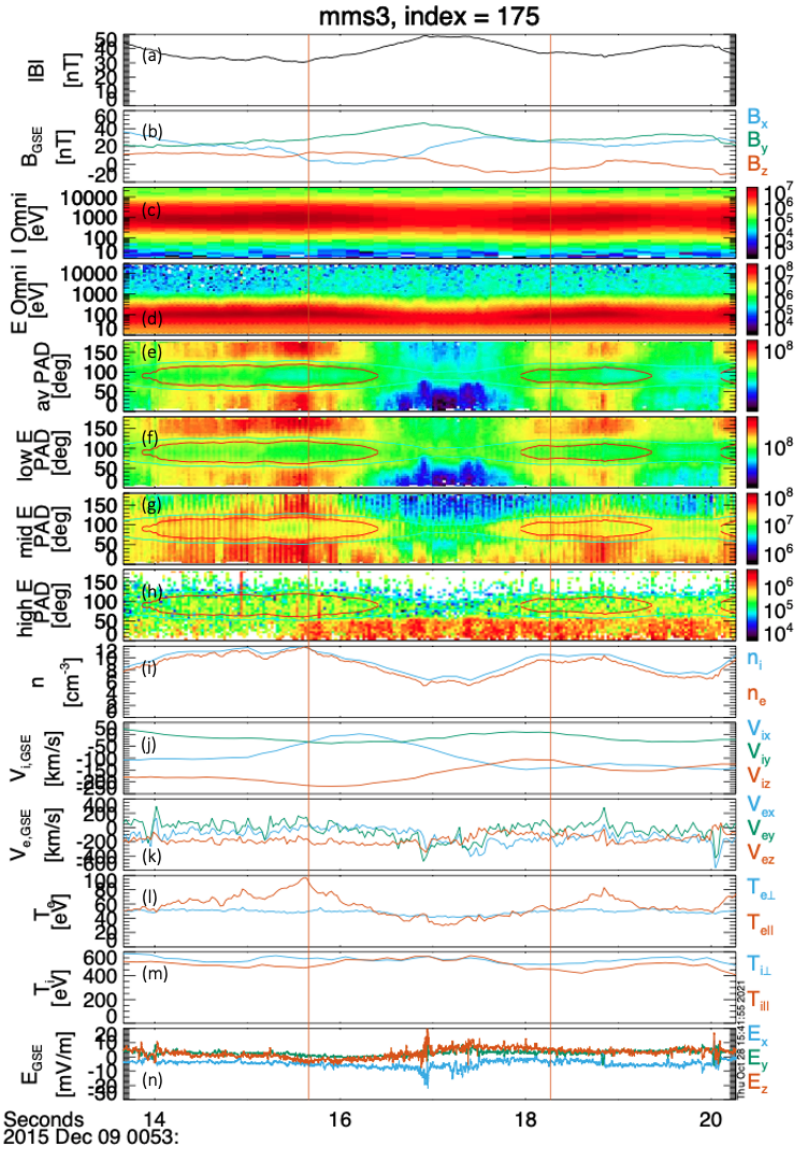

Figure 5.3: Example of a topology 1 flux rope burst mode data plot. The flux rope is connected to the southern hemisphere at one end and open to the magnetosheath at the other, identified by the parallel streaming high energy magnetospheric electrons in panel (h).

5.2.1 Topology Statistics

We found 157 (64.1%) flux ropes to have topology 0 and 63 (25.7%) to have topology 1. We observed only 4 (1.6%) flux ropes with topology 2 and 16 (6.5%) with topology 3. We were unable to identify the topology of 5 of the flux ropes (2.1%). These results are summarised in Table 5.2. The identified topology of each flux rope is listed in Appendix A.

Topology 1, with a 0° high energy electron population, corresponds to the field

Topology	0	1	2	3
count	157	63	4	16
percentage	64.1	25.7	1.6	6.5

Table 5.2: Topology counts and percentages, as defined in Table 5.1

lines being connected to the southern hemisphere at one end and the magnetosheath at the other and is consistent with an open flux rope embedded in a southward reconnection jet produced by the Lee and Fu (1985) multiple X-line model. The dominance of these topology 1 observations over topology 2 observations, where the flux rope is open but connected to the northern hemisphere, is likely due to the dominance of MMS magnetopause crossings being south of the reconnection X-line (Paschmann et al., 2018). To confirm this, further investigation of the large-scale features of the reconnection outflows in which the flux ropes are embedded would be required.

Despite the observations of flux ropes with topology 1 supporting the multiple X-line flux rope formation model, this mechanism alone cannot account for the observations of flux ropes with topology 0. Russell and Qi (2020) explain the presence of flux ropes containing magnetosheath electrons by suggesting that flux ropes are created in pairs with open topologies, connected to opposite hemispheres (one topology 1 flux rope and one topology 2). These pairs become entangled and undergo magnetic reconnection; this is consistent with observations by Øieroset et al. (2019), where reconnection is observed between flux ropes embedded in converging reconnection jets on the magnetopause, and Hwang et al. (2021), where reconnection is observed between interlinked flux tubes inside an FTE. This reconnection results in a pair of flux ropes that are closed, with one connected to the magnetosheath and one to the magnetosphere (topology 0 and 3, respectively). We observe 64.1% of flux ropes to have topology 0, but only 6.5% to have topology 3. For our results to be consistent with the Russell and Qi (2020) pair formation model, where equal numbers of these topologies are expected, the lack of topology 3 flux ropes would need to be accounted for.

One factor to consider for this study is the time scales required for electrons to

populate or evacuate flux rope field lines which have recently changed topology and connectivity. Hwang et al. (2021) estimated that it takes $\sim$ 5 s (2 s) for 1 keV (10 keV) electrons to travel 5 R_E along closed magnetopause field lines. Taking these estimated particle velocities and using the time between the flux rope observation and the EDR as an estimate for the age of the flux rope, we find that the majority of flux ropes will be populated with electrons according to their connectivity, therefore justifying our definition and classifications of the flux rope topologies. However, there is still a chance that flux ropes could be undergoing a change in connectivity at the time of observation, reducing the accuracy of our topology classifications Mejnertsen et al. (e.g. 2021).

Our topology observations are not consistent with previous theories for flux rope topology based on their formation mechanisms. There are many possible explanations for this; for example, there may be multiple flux rope formation mechanisms at play, or different mechanisms could be dominant under different conditions. In the following sections, we investigate how the flux rope topology relates to the properties of the flux rope itself and the associated EDR's properties to try to understand the reasons for our observations.

5.3 Topology EDR Dependence

Firstly, we investigate how the flux rope topology varies with the time between the flux rope and EDR observations. Figure 5.4 shows a plot for the cumulative percentage of each flux rope topology observed within 0 to 60 minutes of the EDR observation as well as the number of flux ropes being included for each time. Initially, for 0 - 5 minutes, up to 70% of the flux ropes have topology 0, and there are approximately equal numbers of topology 1 and 3 flux ropes ($\sim$ 17%) and small numbers of topology 2 flux ropes ($\sim$ 3%). The percentage of topology 0 and 3 flux ropes then drops to $\sim$ 50% and $\sim$ 5% at 5 minutes and the percentage of topology 0 flux ropes increases to $\sim$ 40%. Over this period the number of flux ropes included in the percentage calculation approximately doubles from 20 to 40

flux ropes. At around 10 minutes there is a drop in the percentage of topology 1 flux ropes and a corresponding increase in the percentage of topology 0 flux ropes of $\sim 7\%$. For the remainder of the plot, the percentages remain approximately constant with only the percentage of topology 1 falling steadily and the percentage of topology 0 showing a corresponding increase.

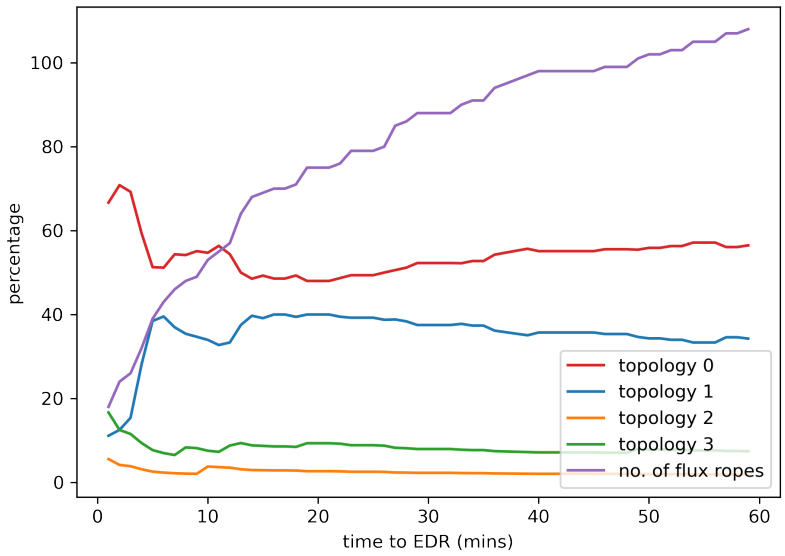

Figure 5.4: Percentages of each observed topology with varying time to EDR limits. The red line shows topology 0, the blue, topology 1, the orange, topology 2 and the green, topology 3. The purple line shows the number of flux ropes included in the percentage calculation at the given time to EDR limit.

These results suggest that we observe a greater percentage of topology 0 flux ropes closer to the EDR. This may in turn suggest that flux ropes can be formed as topology 0, unlike in the previously discussed theories which imply flux ropes are produced only as topology 1 and 2. At around 15 minutes from the EDR, the percentage of each topology approximately levels out. This could give the time at which the effects of the EDR on the topology of the flux ropes becomes unimportant, and is similar to the time to EDR limits we have used previously to ensure flux ropes are related to the observed EDR.

We also investigate how the flux rope topology varies with the location of the EDR. Figure 5.5 shows a bar chart for the number of flux ropes of each topology observed at

each EDR; (a) is for all flux ropes, (b) shows flux ropes observed within 60 minutes of the EDR and (c) shows flux ropes observed within 15 minutes of the EDR. The line plots show the X, Y and Z GSE components of the EDR observation location. We find that we observe mostly topology 0 flux ropes when the EDR Y GSE coordinate is positive (for EDRs 0 - 7 and 13 - 24). When the EDR Y GSE coordinate becomes negative, we find that we observe a greater mixture of topologies, with a greater proportion of topology 1 flux ropes. This is reinforced in Figure 5.6, where we plot the observed EDR location with the points colour-coded according to the fraction of topology 0 flux ropes surrounding the given EDR (red is all topology 0, blue is all topology 1) and the size of the points are proportional to the number of flux ropes observed surrounding the EDR; (a) is for all flux ropes, (b) shows flux ropes observed within 60 minutes of the EDR and (c) shows flux ropes observed within 15 minutes of the EDR. In these plots, it is clear that the red points are mostly observed in the bottom right quadrant when Y GSE is positive and Z GSE is negative.

This topology observation location dependence suggests that topology 0 flux ropes are most likely to be formed by an EDR observed in the positive Y GSE, negative Z GSE quadrant of the magnetopause, and elsewhere more varied flux rope topologies are observed. As discussed in Section 4.4.1, we cannot directly comment on the solar wind conditions, however, this is where we would expect to observe the reconnection X-line when the IMF has a significant negative B_Y component. This could indicate that topology 0 flux ropes are more likely to be produced by an EDR under negative IMF B_Y, and that more varied flux rope topologies are observed under other conditions.

5.4 Topology Variations with Flux Rope Properties

In this section, we investigate if the properties of the flux ropes vary with their topology. As in Chapter 3, extreme outliers are omitted from this analysis. Figure 5.7 compares the flux rope radius distributions for the most abundant observed topologies: topology 0

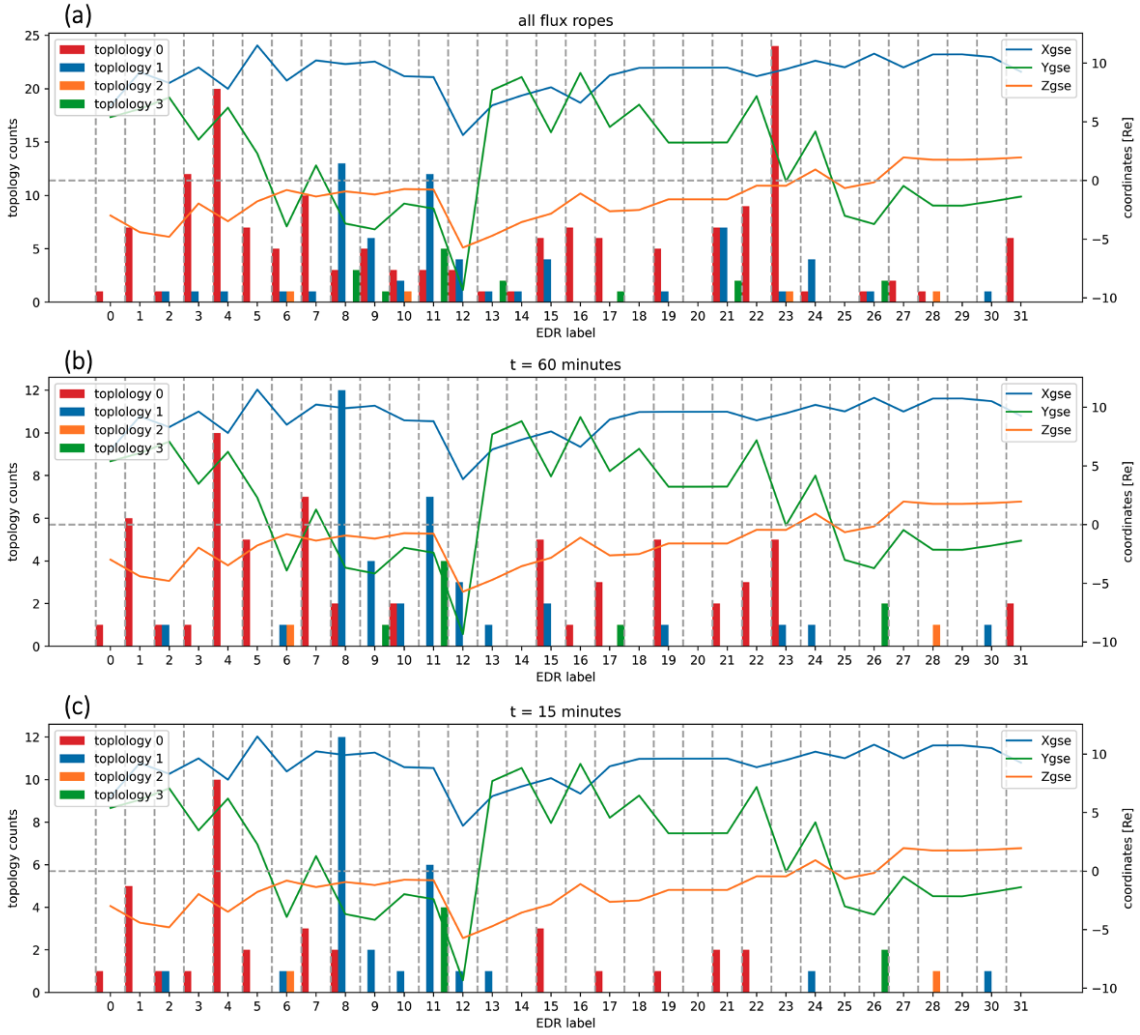

Figure 5.5: Bar plots showing the number of topology 0 (red), 1 (blue), 2 (orange) and 3 (green) flux ropes observed for each EDR encounter for (a) all flux ropes, (b) flux ropes observed within 60 minutes of an EDR encounter, and (c) within 15 minutes of an EDR encounter. The EDR observation location is included as a line plot with the blue line showing the X GSE component, the green line showing the Y GSE component and the orange line showing the Z GSE component.

and 1. Figure 5.7 (a) shows that the radius distributions are comparable when all flux ropes are considered, with the average radii being 257 km and 250 km for topology 0 and 1, respectively. Figure 5.7 (b) and (c) limit the distributions to flux ropes observed within 60 and 15 minutes of the EDR. These plots suggest that topology 0 flux ropes have greater radii closer to the EDR, with the average radii being 298 km and 234 km for topology 0 and 1, respectively, when flux ropes are limited to within 60 minutes of an EDR observation, and 296 km and 237 km for topology 0 and 1, respectively, when flux

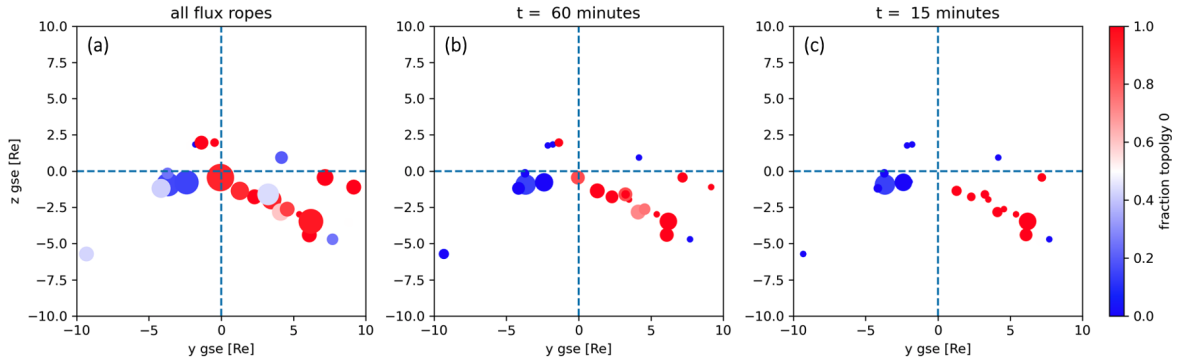

Figure 5.6: Location of EDRs and their corresponding observed flux rope topologies. Points are coloured according to the fraction of flux ropes with topology 0, where red = 1 means all flux ropes have topology 0 and blue = 0 means all flux ropes have topology 1, 2, or 3. The size of the points is proportional to the number of flux ropes observed surrounding each EDR, with (a) showing all flux ropes, (b) showing flux ropes observed within 60 minutes of the EDR, and (c) showing flux ropes observed within 15 minutes of the EDR.

ropes are limited to within 15 minutes of an EDR observation

Figures 5.8 and 5.9 compare the axial magnetic field strength and flux content distributions of topology 0 and 1 flux ropes. In Figure 5.8 all topology 0 distributions are shifted to smaller values than the topology 1 distributions, with differences in mean values of 7.4 nT, 8.0 nT and 10.7 nT for (a), (b) and (c), respectively, with the topology 1 average values being 42.7 nT, 44.5 nT and 45.5 nT, respectively. This suggests that topology 0 flux ropes generally have smaller axial magnetic fields compared to topology 1 flux ropes, with the average axial magnetic field strength of topology 0 flux ropes potentially getting larger as flux ropes are limited to being closer to the EDR. In Figure 5.9 we see that the flux content distributions for topology 0 and 1 flux ropes are comparable for all flux ropes (see (a)). When flux ropes are limited to within 60 and 15 minutes of the EDR ((b) and (c), respectively), we potentially observe more low flux content topology 0 flux ropes.

These distribution comparisons suggest that topology 0 flux ropes generally have smaller axial magnetic fields than topology 1 flux ropes. Closer to the EDR, we potentially see more smaller radii topology 0 flux ropes. These observations combine to suggest lower flux content topology 0 flux ropes closer to the EDR. This could reinforce the observations

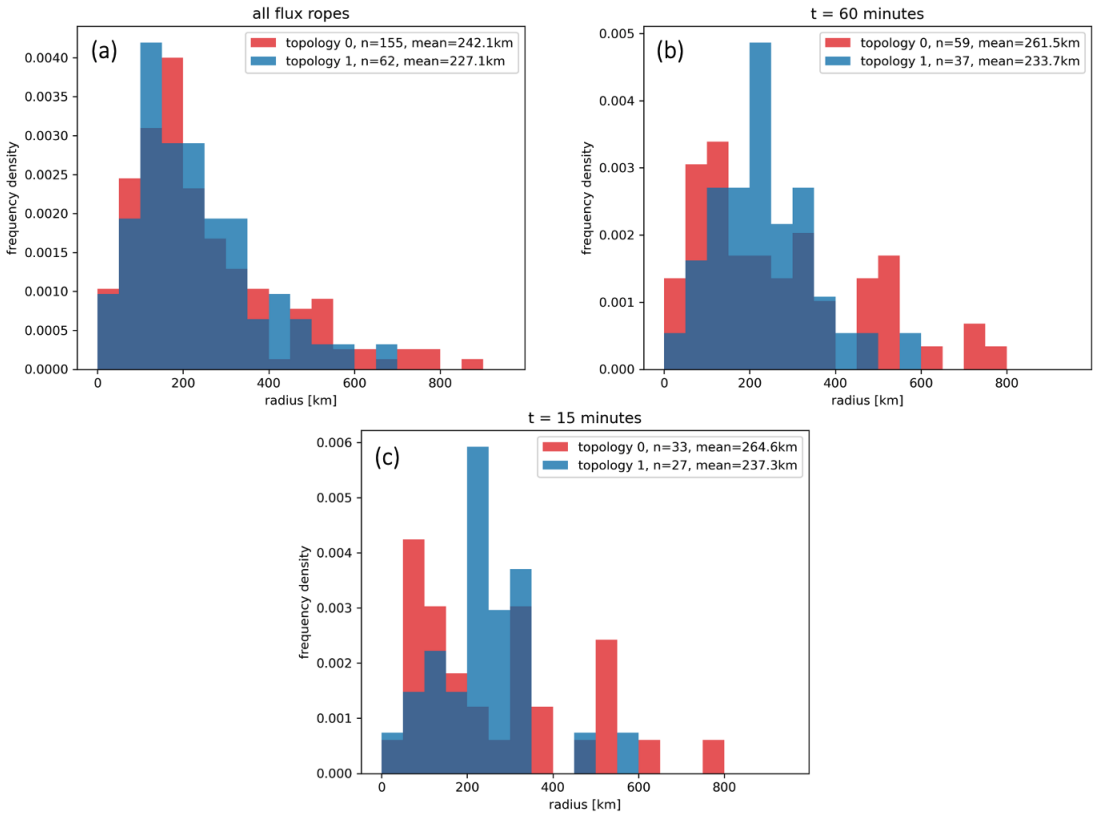

Figure 5.7: Radius distribution comparisons for flux ropes with topology 0 and 1 for (a) all flux ropes, (b) flux ropes observed within 60 minutes of an EDR, and (c) flux ropes observed within 15 minutes of an EDR.

of Chapter 3, where we observed flux ropes with stronger axial fields closer to the EDR, by suggesting that if flux ropes are formed with open topologies (topologies 1 and 2, as suggested by the Lee and Fu (1985) multiple X-line formation mechanism) they have stronger axial fields closer to the EDR.

5.5 Conclusions

In this chapter, we have presented an investigation into the topology of the EDR-associated flux ropes presented in Chapter 3. The flux rope pitch angle distributions were investigated to classify the topology of the flux ropes. Four topology classifications were used: closed topologies where the flux rope is connected to the magnetosheath (topology 0) or magnetosphere (topology 4) at both ends, and open topologies where the flux rope

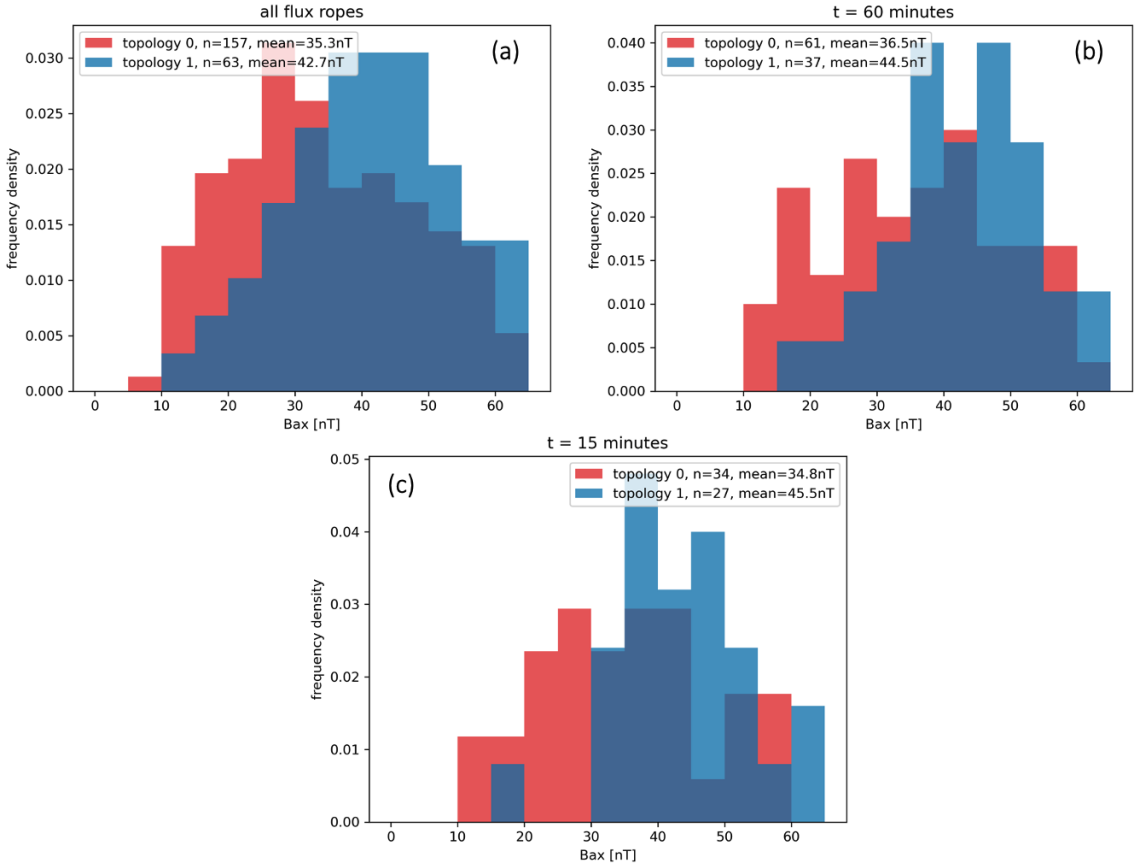

Figure 5.8: Axial field strength distribution comparisons for flux ropes with topology 0 and 1 for (a) all flux ropes, (b) flux ropes observed within 60 minutes of an EDR, and (c) flux ropes observed within 15 minutes of an EDR.

is connected to the magnetosheath at one end and the southern (topology 1) or northern (topology 2) magnetosphere at the other. Of the 245 flux ropes, we found 64.1% to have topology 0, 25.7% to have topology 1, 1.6% to have topology 2 and 6.5% to have topology 3.

These topology observations could have consequences for flux rope formation mechanisms and interactions. Topology 1 flux ropes are consistent with flux ropes embedded in a southward directed reconnection jet, as proposed by the Lee and Fu (1985) multiple X-line flux rope formation mechanism. MMS magnetopause crossings tend to be south of the reconnection X-line (Paschmann et al., 2018), which could suggest these observations of topology 1 dominating over topology 2 are consistent with this flux rope formation mechanism. Closed topology flux rope observations (topologies 0 and 3) have been postu-

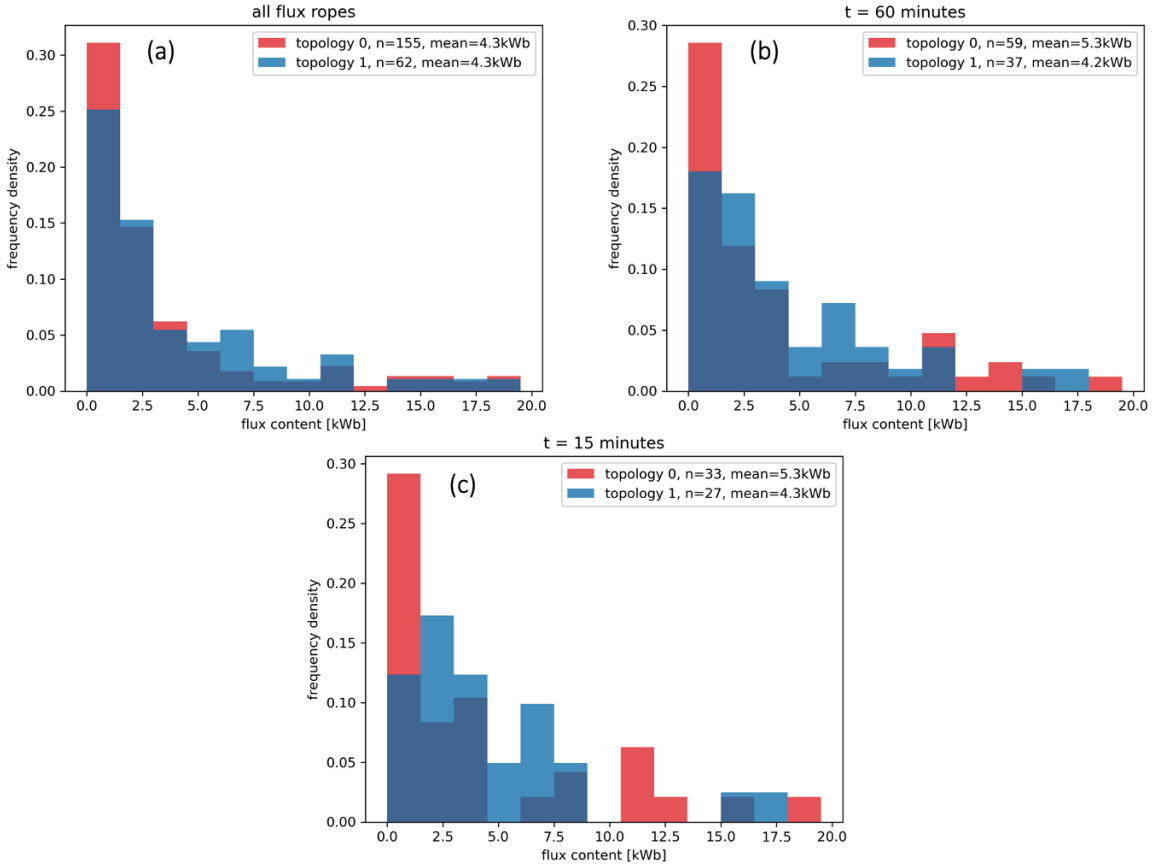

Figure 5.9: Flux content distribution comparisons for flux ropes with topology 0 & 1 for (a) all flux ropes, (b) flux ropes observed within 60 minutes of an EDR, and (c) flux ropes observed within 15 minutes of an EDR.

lated to be produced through interactions between open topology flux ropes (topologies 1 and 2) (Russell and Qi, 2020). These mechanisms suggest we would expect to observe equal numbers of closed magnetosheath (topology 0) and magnetospheric (topology 3) flux ropes, which is not the case in our observations, where closed magnetosheath topology flux ropes dominate. This suggests that there may be more complexity to flux rope interaction than previously reported.

The relationship between the flux rope topology and the EDR was also investigated. It was found that topology 0 flux ropes were more likely to be observed closer to the EDR, suggesting that flux ropes could be formed as topology 0, contrary to what is suggested by flux rope formation mechanisms. It was also observed that topology 0 flux ropes were most likely to be observed surrounding an EDR identified in the positive

Y GSE, negative Z GSE quadrant of the magnetopause. This quadrant is where the reconnection X-line would be expected to be located for IMF with a significant negative B_Y component, suggesting that such conditions could be favourable for the formation of topology 0 flux ropes. This relationship could be investigated further by identifying the expected magnetopause reconnection location using solar wind data from spacecraft located at the first Lagrange point (L1), which is located upstream of the subsolar region.

Finally, the relationships between the topology and other properties of the flux ropes were investigated. The flux rope radius, axial field strength and flux content distributions were compared for topology 0 and 1 flux ropes, and it was found that topology 0 flux ropes generally have smaller axial field strengths. We discussed how this could be paired with the findings of Chapter 3 to suggest that open topology (topologies 1 and 2) flux ropes could be formed by the EDR.

Overall, we have conflicting observations that do not obviously agree with any previously presented theories involving flux rope topology. We observed a majority of open topology flux ropes, suggesting that the EDR can produce flux ropes of this topology. We also observe closed topology flux ropes to have stronger axial fields which we found were more likely to be observed closer to the EDR. These results imply that the EDR could have the potential to produce both open and closed topology flux ropes, which is contrary to previous flux rope formation mechanisms (e.g. Lee and Fu, 1985). We also note that some of the flux ropes were identified as having 'patchy' topology, in which the pitch angle distributions showed varying topology over the duration of the flux rope observation, and highlight this as an interesting area for future research.

Chapter 6

Electron Trapping in Magnetic Mirror Structures Associated with Magnetopause Flux Ropes

The work presented in this chapter has been published in a peer-reviewed journal article: Robertson, S. L., Eastwood, J. P., Stawarz, J. E., Hietala, H., Phan, T. D., Lavraud, B., et al. (2021). Electron trapping in magnetic mirror structures at the edge of magnetopause flux ropes. *Journal of Geophysical Research: Space Physics*, 126, e2021JA029182. https://doi.org/10.1029/2021JA029182

6.1 Introduction

Magnetic reconnection has been observed to be a source of energetic particles (Oka et al., 2018). For example, in solar flares magnetic reconnection is thought to play a key role in the large amounts of energy released with a significant fraction of this energy found in the non-thermal electron population (Lin, 2006). In the Earth's magnetosphere, energetic particles are often observed; accelerated particles have been observed near the

reconnection diffusion region (Øieroset et al., 2002; Chen et al., 2016) and in magnetotail reconnection exhausts (Fu et al., 2013; Khotyaintsev et al., 2011; Liu et al., 2019).

As discussed in Chapter 1 Section 1.2.5, there are many mechanisms for particle acceleration during magnetic reconnection which rely on a variety of different mechanisms, such as Fermi and betatron acceleration (Fu et al., 2011), electron 'surfing' near current sheets (Hoshino, 2005), electron trapping in magnetic islands (Drake et al., 2006a), and particle mirroring (Zhu et al., 2019). Many of these processes are associated with the complex substructure that is formed close to the reconnection site and in reconnection outflows. For example, many mechanisms involve flux ropes; Chen et al. (2007) presented observations of energetic electrons and magnetic islands produced during reconnection in the magnetotail. Drake et al. (2006a) proposed an electron acceleration mechanism in which electrons that are trapped on magnetic island field lines are accelerated in a Fermi-like process as the island contracts. Drake et al. (2012) furthers this argument, suggesting multiple such magnetic islands can merge, resulting in an energetic electron spectra which has an $E^{\frac{1}{2}}$ dependence, which is consistent with plasma observations throughout the heliosphere. It has also been suggested that the electric fields produced during magnetic reconnection and associated magnetic minima could trap and accelerate particles (Egedal et al., 2005; Hoshino, 2005; Lavraud et al., 2016). Fu et al. (2011) proposed that particle trapping and a combination of Fermi and betatron acceleration could be responsible for the energetic particles observed in magnetotail reconnection outflow jets.

Recent observations of Zhu et al. (2019) demonstrate that particle reflection can occur against the flux pile up region at the edge of a magnetopause flux rope, energizing the plasma, and suggests the possibility of magnetic mirror structures playing a role in magnetic reconnection particle acceleration. A magnetic mirror is formed by the conservation of the magnetic moment which is an adiabatic invariant of the plasma associated with a particle's gyromotion. The magnetic moment, μ, is given by

$$\mu = \frac{m{v_\perp}^2}{2B}, \tag{6.1}$$

where $v_\perp$ is the particle's velocity perpendicular to the magnetic field, or its gyration velocity, which can be expressed as $v_\perp = v \sin \alpha$, where v is the particle velocity and α is the pitch angle of the particle, i.e. the angle between the particle's velocity vector and the magnetic field vector. As the particle's energy is conserved, we find that conservation of the magnetic moment leads to the relationship

$$\frac{\sin^2 \alpha_1}{\sin^2 \alpha_0} = \frac{B_1}{B_0}, \tag{6.2}$$

where α_0 and B_0 are the particle pitch angle and the magnetic field strength it is experiencing at some initial time, and α_1 and B_1 are the particle pitch angle and the magnetic field strength at some later time. This relationship means that if we know the pitch angle at one location, we know how it will vary as the particle moves into areas of different field strengths. As the magnetic field strength increases, there becomes a point at which the particle's pitch angle reaches 90° and the particle is reflected. This process is known as magnetic mirroring. If a particle is moving along a field line with a magnetic field strength minima surrounded by regions of stronger field strength, it can become trapped in the magnetic minima and bounce between the regions of stronger field.

Particle trapping is a common feature of may of these acceleration mechanisms. Although Zhu et al. (2019) did not observe particle trapping, the trapping of particles in magnetic mirror structures is commonly observed in space plasmas. Magnetic holes, often observed in the Earth's magnetosheath, are small-scale depressions in the ambient magnetic field strength which form magnetic mirror structures that can trap particles, resulting in anticorrelation between magnetic field strength and plasma pressure (Horbury et al., 2004; Ahmadi et al., 2017). Yao et al. (2018) investigated mirror mode structures observed in the magnetosheath and found them to exhibit particle acceleration features consistent with a mirror instability formation mechanism (Southwood and Kivelson, 1993). Kinetic-scale magnetic holes (KSMH) have also been observed and characterised throughout the magnetosphere (Gershman et al., 2016; Goodrich et al., 2016; Yao et al., 2017).

A statistical study of 66 KSMHs in the magnetosheath by Huang et al. (2017) concluded that an electron-vortex formation mechanism is the most likely candidate and KSMHs have been observed in the vicinity of a magnetopause reconnection site and flux rope (Zhong et al., 2019).

Magnetic mirror structures associated with reconnection could have the potential to produce the particle trapping required to accelerate particles during reconnection. However, the link between such mirror structures and reconnection is yet to be established. In this chapter, we present unique Magnetospheric Multiscale (MMS) mission observations of mirror structures associated with magnetopause reconnection; we observe two case studies of ion-scale flux ropes produced by reconnection at the magnetopause, on the edge of which we observe electron trapping in magnetic mirror structures. The mirror structures are found to extend along the body of the flux ropes. In one case study, we observe a second electron trapping feature identified as a KSMH. We discuss the possible formation mechanisms of the magnetic mirrors, as well as how the structures could evolve and produce particle acceleration. The chapter is organized as follows; Section 6.2 presents observations of the two case studies, observed on 2 January 2017 and 9 December 2015. Sections 6.3, 6.4 and 6.5 further discuss the observations, examining instabilities, pressure and force balance, and considering other acceleration mechanisms which could be associated with the structures, respectively. Our conclusions are then presented in Section 6.6.

6.2 Electron Trapping Case Studies

In this section, we introduce two case studies of electron trapping events in magnetic mirror structures on the edge of ion-scale magnetopause flux ropes. These structures were identified when investigating the topology of the flux ropes, as presented in Chapter 5. Investigating the topology of the flux ropes required the investigation of the particle pitch angle distributions of the flux ropes, as detailed in Section 5.2. When looking at the

electron pitch angle distributions, an interesting doughnut-shaped feature was identified on the edge of the flux rope observed on 2 January 2017 at 03:18 UT, presented in Section 6.2.1 as Case Study 1. Further investigation identified one other comparable event observed on 9 December 2015 at 00:52 UT, presented in Section 6.2.2 as Case Study 2. The identification of these two trapping features from a subset of 90 magnetopause flux ropes suggests an observation rate of $\sim$ 2.2%.

In the following subsections, we discuss the observations for the two case studies, first discussing the context of the overall magnetopause crossings and conditions before detailing the flux rope and trapping observations and presenting a diagram of the unique magnetic field arrangement for the observations.

6.2.1 Case Study 1 - 2 January 2017

Figure 6.1 presents a 1 hour overview plot of MMS 2 survey-mode data giving the context for the observations of the first electron trapping case study observed on 2 January 2017. During this interval, MMS is moving outboud from the magnetosphere into the magnetosheath at $\sim$ [9.5, -3, 0] R_e GSE, and crosses the magnetopause multiple times due to the motion of the magnetopause over the spacecraft. The magnetopause crossings are identified by rotations of the magnetic field and corresponding changes in particle energies. A complete magnetopause crossing at $\sim$ 03:07 UT (marked with the solid vertical line in Figure 6.1), is used to rotate the data from the original GSE coordinates into the presented magnetopause coordinate system using minimum variance analysis (Section 2.2). Here, L = [-0.07, -0.57, 0.82] GSE, M = [-0.18, 0.80, 0.58] GSE, and N = [-0.98, 0.19, 0.05] GSE. The magnetopause coordinate system is therefore closely aligned with GSE.

During the initial crossings of the magnetopause just before 03:00 UT, there is little evidence of a well-developed V_L reconnection exhausts, however, at the 03:07 UT encounter, where MMS moves from the magnetosphere (indicated by + B_L oriented mag-

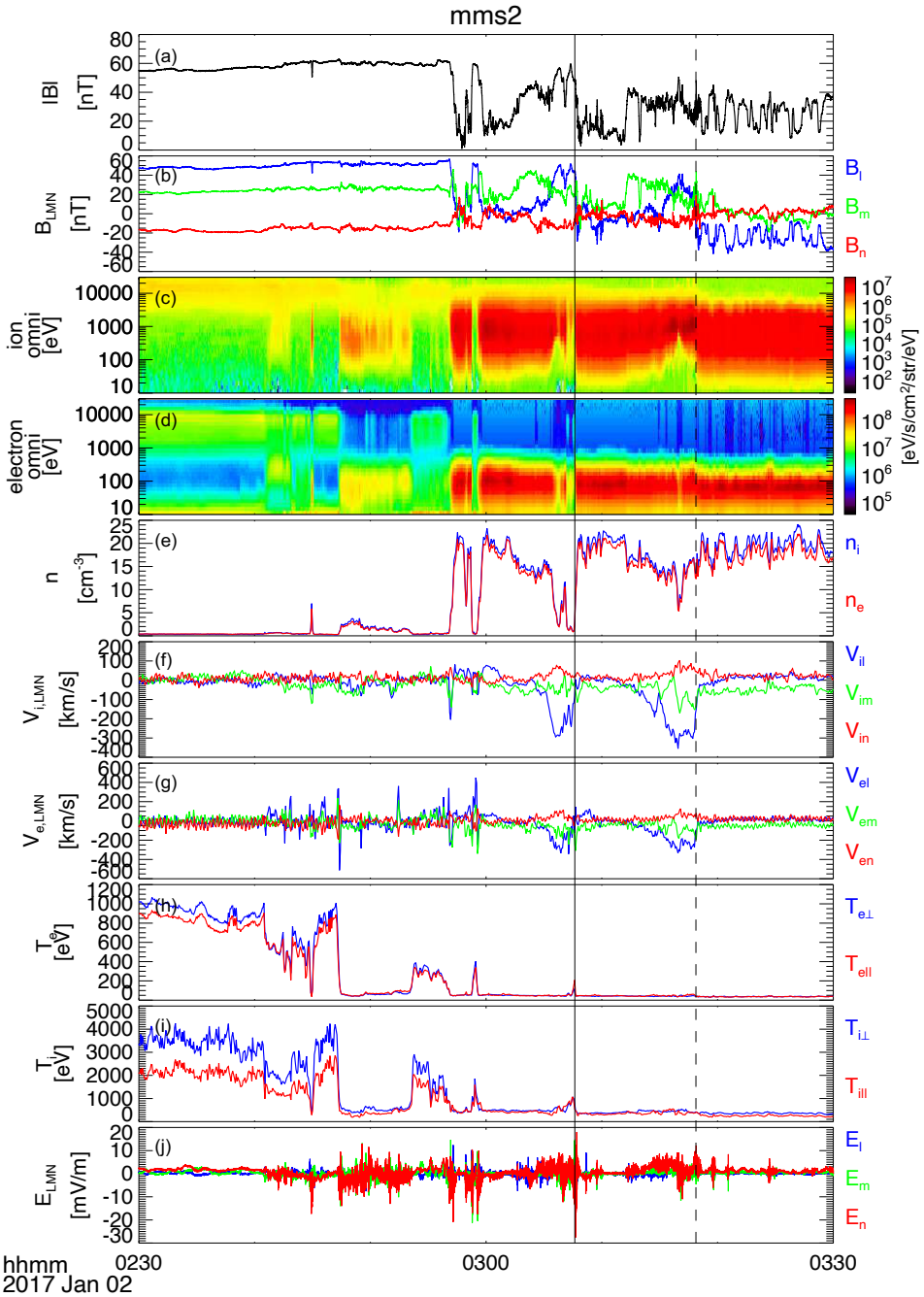

Figure 6.1: MMS 2 survey-mode observations of an outbound magnetopause crossing on 2 January 2017. The panels show: (a) & (b) magnetic field strength and components in a magnetopause boundary coordinate system [LMN]; (c) & (d) ion and electron omnidirectional energy spectra; (e) ion and electron number density; (f) & (g) ion and electron bulk velocity in LMN coordinates; (h) & (i) ion and electron temperature; (j) electric field in LMN coordinates. The solid vertical line indicates the magnetopause crossing used to determine the LMN coordinate system and the dashed vertical line indicates the flux rope observation.

netic field, low densities, and higher energy particles) to the magnetosheath (indicated by $-$ B_L magnetic field, higher densities and corresponding energy spectra), a reconnection exhaust is observed in the $-$ L direction ($\sim$ $-$ z GSE direction). A significant + B_M guide field ($\sim$ 20 nT) is observed.

Over the next few minutes between 03:12 - 03:18 UT, a decrease in particle density, a reversal in B_L, and an increasing low-energy cut off in the ion energy spectrum is observed. This occurs at the same time as observations of the reconnection exhaust, and so is identified as a re-encounter of the magnetopause from the magnetosheath side caused by the magnetopause moving Sunwards. During this magnetopause encounter, a flux rope is observed at 03:18 UT, as indicated by the dashed vertical line in Figure 6.1, just before MMS exits the exhaust and moves into the magnetosheath.

The flux rope observations from MMS 2 are shown in greater detail in Figure 6.2. The flux rope was initially identified by a peak in the magnetic field strength and a corresponding bipolar signature in the B_X GSE magnetic field component ($\sim$ normal to the magnetopause), accompanied by a peak in the B_Y GSE component of the magnetic field, confirming a helical flux rope structure (e.g. Xiao et al., 2004). In the magnetopause coordinate system, the flux rope is identified by a bipolar signature in the magnetopause normal component, B_N, and a corresponding peak in magnetic field strength. The axis of the flux rope is identified as being predominantly in the M-direction and therefore extends the structure along the magnetopause forming a flux rope. The sign of the B_L component of the magnetic field indicates whether the spacecraft is on the magnetosheath or magnetospheric side of the magnetopause. At the start of the flux rope encounter, $B_L \approx 0$, indicating that MMS is close to the magnetopause field reversal. Through the body of the flux rope, the B_L component is negative, but approaches zero at the end of the flux rope encounter, indicating that the spacecraft traverses the flux rope on the magnetosheath side and exits closer to the magnetopause current sheet. The normal component to the magnetopause (B_N) is initially negative, becomes positive in the first part of the flux rope and then reverses sign again. Together with the fact that the overall

flow is in the − L direction, this is consistent with a flux rope moving in the same direction as the reconnection outflow, as illustrated in Figure 6.3.

The size of the flux rope can be estimated using the observation duration ($\sim$ 2.5 s) and the average ion v_L flow speed through the flux rope ($\sim$ 500 kms^{-1}) to calculate the length of the spacecraft path through the flux rope. We estimate that the flux rope size is $\sim$ 500 km, or $\sim$ 6.9 d_i, where $d_i \approx 72$ km is the ion inertial length. This makes the flux rope comparable to the ion-scale flux ropes reported by Eastwood et al. (2016) and Hwang et al. (2018).

Between 03:18:07.9 UT and 03:18:08.7 UT, just before the spacecraft enters the body of the flux rope, there is a dip in the magnetic field strength of $\sim$ 10 nT. Over this feature, we observe a corresponding peak in the number density of $\sim$ 5 cm^{-3} (Figure 6.2 (d)). An unexpected feature associated with this dip in magnetic field strength is a population of electrons visible as a doughnut-shaped feature in the electron pitch angle distributions, as shown in Figure 6.2 (i) – (n), where the distributions are split over the energy ranges 0 - 50 eV, 50 - 100 eV, 100 - 200 eV, 200 - 400 eV, 400 - 600 eV and 600 - 800 eV, respectively. Over-plotted on these distributions are the magnetic mirror loss cone angles for different magnetic mirror strengths (20 nT, 30 nT and 40 nT). This is the minimum pitch angle above which we would expect particles to be trapped by a magnetic mirror of given magnetic field strength and is given by

$$\alpha = \sin^{-1}\left(\sqrt{\frac{B}{B_0}}\right), \tag{6.3}$$

where B is the observed magnetic field strength and B_0 is the magnetic mirror strength. For parallel electrons we have that $0° \leq \alpha \leq 90°$, and for antiparallel electrons we have $\alpha' = 180° - \alpha$. The increase in energy flux confined by the 20 nT and 30 nT curves suggests the electrons are trapped within a magnetic mirror with a maximum field strength of $\sim$ 30 nT.

More specifically, at 03:18:07.9 UT, we observe electrons with dominant perpen-

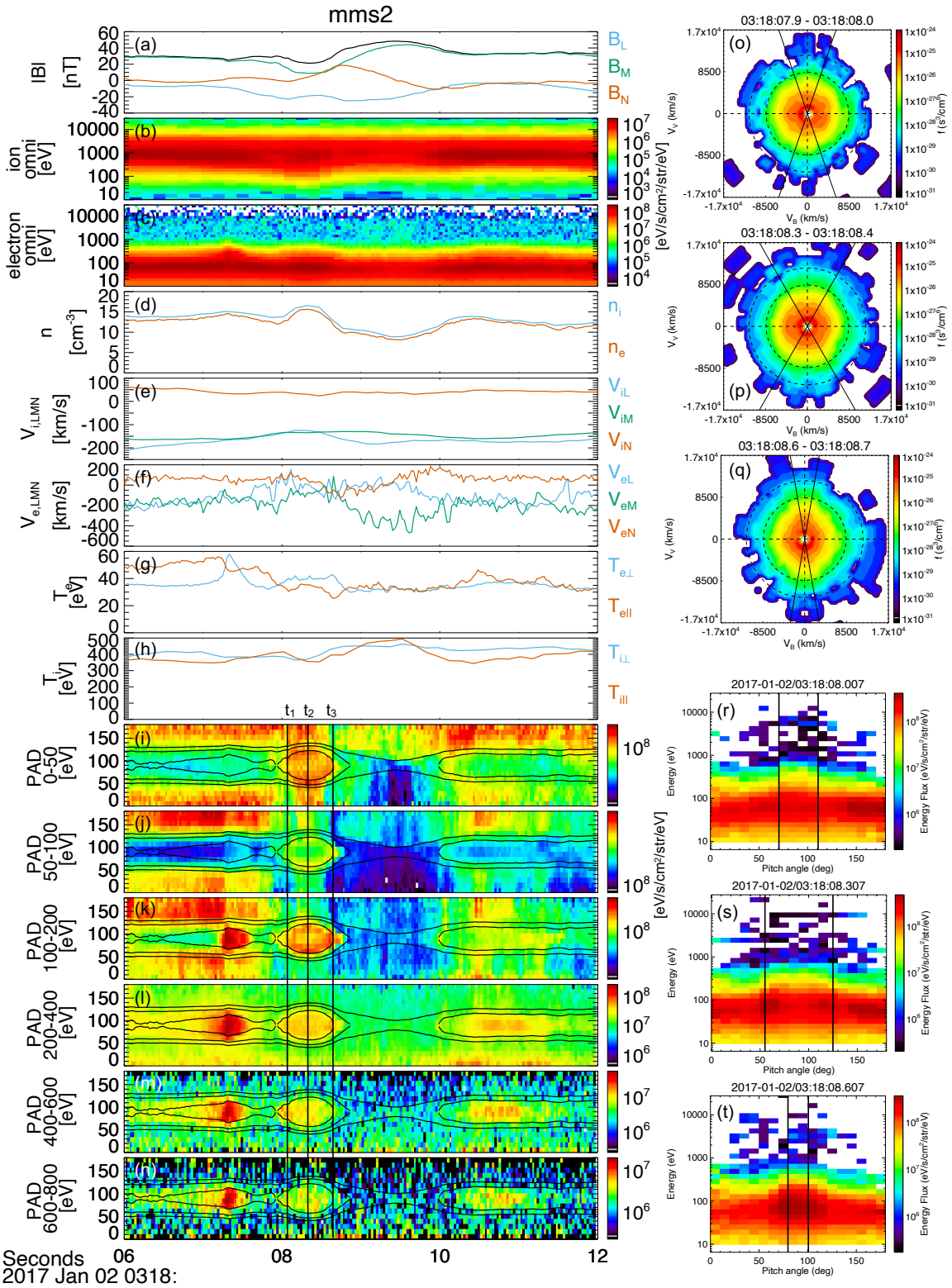

Figure 6.2: MMS 1 observations of a magnetopause flux rope observed on 2 January 2017 between 03:18:06 UT and 03:18:12 UT. *Caption continued on next page.*

Figure 6.2: *Caption continued from previous page.* The panels show: (a) magnetic field strength and components in a magnetopause boundary coordinate system (LMN); (b) & (c) ion and electron omnidirectional energy spectra; (d) ion and electron number density; (e) & (f) ion and electron bulk velocity in LMN coordinates; (g) & (h) ion and electron temperature; (i) – (n) electron pitch angle distributions over energy ranges 0 - 50 eV, 50 - 100 eV, 100 - 200 eV, 200 - 400 eV, 400 - 600 eV and 600 - 800 eV, respectively, with over plots of magnetic mirror loss cone angles for 20 nT, 30 nT and 40 nT magnetic mirrors; (o) – (q) electron energy distributions at times 03:18:07.9 - 08.0 UT, 03:18:08.3 - 08.4 UT, 03:18:08.6 - 08.7 UT, respectively, and approximately corresponding to times t_1, t_2 and t_3, as indicated on pitch angle distribution time series plots; (r) - (t) pitch angle energy plots at times 03:18:08.007 UT, 03:18:08.307 UT, 03:18:08.607UT, respectively, and approximately corresponding to times t_1, t_2 and t_3. Radial lines in plots (o) – (q) and vertical lines in plots (r) – (t) show the corresponding loss cone angles for a 30 nT magnetic mirror.

dicular velocity component which are being reflected at the $\sim$ 30 nT mirror point, corresponding to the peak magnetic field strength observed on the leading edge of the field depression. Figure 6.2 (r) shows the pitch angle-energy plot at 03:18:08.007 UT where an increase in energy of the electrons at 90° is seen. Figure 6.2 (o) shows a 2D projection of the 3D electron distribution and we observe a corresponding increase in the radius of the contours in the perpendicular direction between the radial lines showing the 30 nT mirror loss cone angles at that time. Referring to Figure 6.2 (i) – (n), the pitch angles of these electrons then spread as the field strength decreases, continuing to be confined by the $\sim$ 30 nT mirror contour until 03:18:08.3 UT where the loss cone angles are $\sim$ 60° and $\sim$ 120°. Figure 6.2 (s) shows the associated increase in energy flux of $\sim$ 60° and $\sim$ 120° electrons in the pitch angle-energy plot. In the energy distribution (Figure 6.2 (p)) we observe an increase in the radius of the energy contours at $\sim$ 60° and $\sim$ 120° and a flattening at intermediate angles. The pitch angles of the trapped electron populations then converge towards 90° and, at 03:18:08.7 UT, we again observe electrons with dominant perpendicular velocity component being reflected at the opposing $\sim$ 30 nT mirror point. Figure 6.2 (q) and (t) show the corresponding pitch angle-energy plot and energy distribution function cut.

The shape of the trapped electron signature in the pitch angle distribution varies

over the different energy ranges presented in Figure 6.2 . In Figure 6.2 (i) we observe 0 - 50 eV trapped electrons and electrons with dominant parallel velocity component, which fill the 30 nT mirror region. In Figure 6.2 (k) we observe 50 - 100 eV electrons forming a very thin doughnut-shaped feature, as well as a brief period of electrons with dominant parallel velocity component between 03:18:08.2 UT - 03:18:08.4 UT. In Figure 6.2 (k) we observe 100 - 200 eV electrons forming a thicker doughnut-shaped feature and have lost the parallel electron signature. In Figure 6.2 (l), (m) and (n) for 200 - 400 eV, 400 - 600 eV and 600 - 800 eV, respectively, we observe filled-in trapped populations. For energies greater than 800 eV there is no distinguishable trapped electron population. These pitch angle distribution features are consistent with mirror-mode instability observations (e.g. Yao et al., 2018); this is discussed further in Section 6.3.

Using the average ion V_L flow speed through the trapped population and the ion inertial length calculated for the duration of the flux rope ($d_i \approx 72$ km), we find that the trapped electron population has an observed size of ~ 120 km ($\sim 1.7\ d_i$) in the GSE L direction. Throughout the flux rope observation, we also observe a B_M guide field of ~ 20 nT. When passing through the mirror-trapped electron populations, we observe a dip in this component of the magnetic field which provides most of the overall magnetic field strength decrease which traps the electrons. The presence of the guide field also extends the structure of the mirror-trapped electron population into three dimensions. The field lines on which the electrons are trapped must extend along the body of the flux rope in the M-direction. MMS observes two 90° mirror points as it traverses the mirror structure. Based on the orientation of the of the field in the L-M plane, an estimated lower limit for the extent of the mirror structure in the M direction can be obtained. This is illustrated in Figure 6.3, where the mirror-trapping magnetic field depression extends along the body of the flux rope. This however assumes that the structure does not significantly evolve over the time of the observations which is reasonable given the duration of the observations. We observe that the average values of the B_M and B_L components are approximately equal over the trapped population, allowing us to geometrically set a minimum value on

the M-extent of the trapped population of $\sim 3.4\ d_i$.

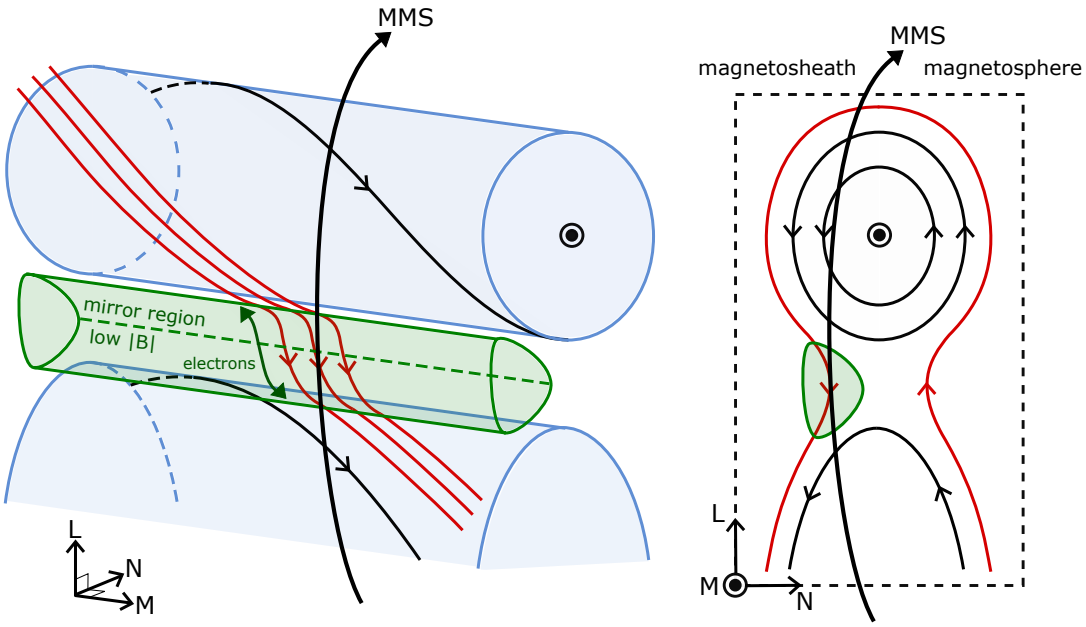

Figure 6.3: 3-dimensional interpretation for the structure of the flux ropes observed on 2 January 2017 and 9 December 2015. Magnetic field lines are shown in black and red, with the red field lines indicated those on which electrons become trapped in the magnetic mirror structure.

For completeness, we note that there is a second electron population observed between 03:18:07.2 UT and 03:18:07.5 UT at energies above 100eV, which exhibits a corresponding electron perpendicular temperature ($T_{e\perp}$) increase of ~ 20 eV (Figure 6.2 (g)). This feature is also confined by the 30 nT mirror over plot; however, it is focused to 90° electrons and does not exhibit any doughnut-like shape (Figure 6.2 (i) – (m)). There is also a slight increase in electron density (Figure 6.2 (d)). Using the average ion V_L flow speed through the trapped population and the ion inertial length calculated for the duration of the flux rope ($d_i \approx 72$ km), we find that the trapped electron population has an observed size of ~ 60 km ($\sim 0.8\ d_i$) in the GSE L direction. We, therefore, identify this structure as a kinetic-scale magnetic hole (KSMH) (Huang et al., 2017). Both the KSMH and the mirror trapped electron structure on the edge of the flux rope show evidence of bipolar perpendicular currents over the structures, consistent with electron vortices (Gershman et al., 2016; Stawarz et al., 2018). These similarities may suggest a relationship

between the structures, which could be an interesting area for further investigation.

6.2.2 Case Study 2 – 9 December 2015

The second case study was observed on 9 December 2015. Figure 6.4 shows 1 hour of survey-mode observations from MMS 2 for context. During this interval, MMS was again moving outbound from the magnetosphere into the magnetosheath, at $\sim$ [10, -3.5, -0.5] R_e GSE, and crossed the magnetopause multiple times. The data are again shown in a magnetopause coordinate system based on minimum variance analysis (Section 2.2) applied to the complete magnetopause crossing at 00:51 - 00:54 UT. Here, L = [0.11, -0.58, 0.80] GSE, M = [0.42, 0.76, 0.49] GSE, and N = [-0.90, 0.28, 0.33] GSE. After this magnetopause crossing, MMS remained in the magnetosheath until 01:03 UT when the spacecraft crossed the magnetopause and return to the magnetosphere. During this magnetosheath interval, intermittent peaks in the L component of the ion velocity ($v_{i,L}$) indicate the presence of reconnection exhausts.

Shortly after the magnetopause crossing at 00:51 UT, a flux rope was observed at 00:52:37 UT. The flux rope observations from MMS 2 can be seen in greater detail in Figure 6.5, where the data is presented in magnetopause LMN coordinates, as in Figure 6.1. The flux rope was again identified by a peak in the magnetic field strength and a corresponding positive/negative bipolar signature in the B_N component, accompanied by a peak in the B_M component of the magnetic field. The bipolar signature in B_N and large $-$ v_{iL} speed are consistent with a flux rope moving in the same direction as the reconnection outflow. The flux rope has a duration of $\sim$ 2.5 s and, based on the average v_{iL} speed through the flux rope, the length of the spacecraft path through the flux rope in the L direction is $\sim$ 563 km or $\sim$ 6.5 d_i, where $d_i \approx 86$ km, making this an ion-scale flux rope.

Between 00:52:36.7 UT and 00:52:37.4 UT, again on the magnetosheath edge of the flux rope, there is a dip in the magnetic field strength of $\sim$ 12 nT and a corresponding peak

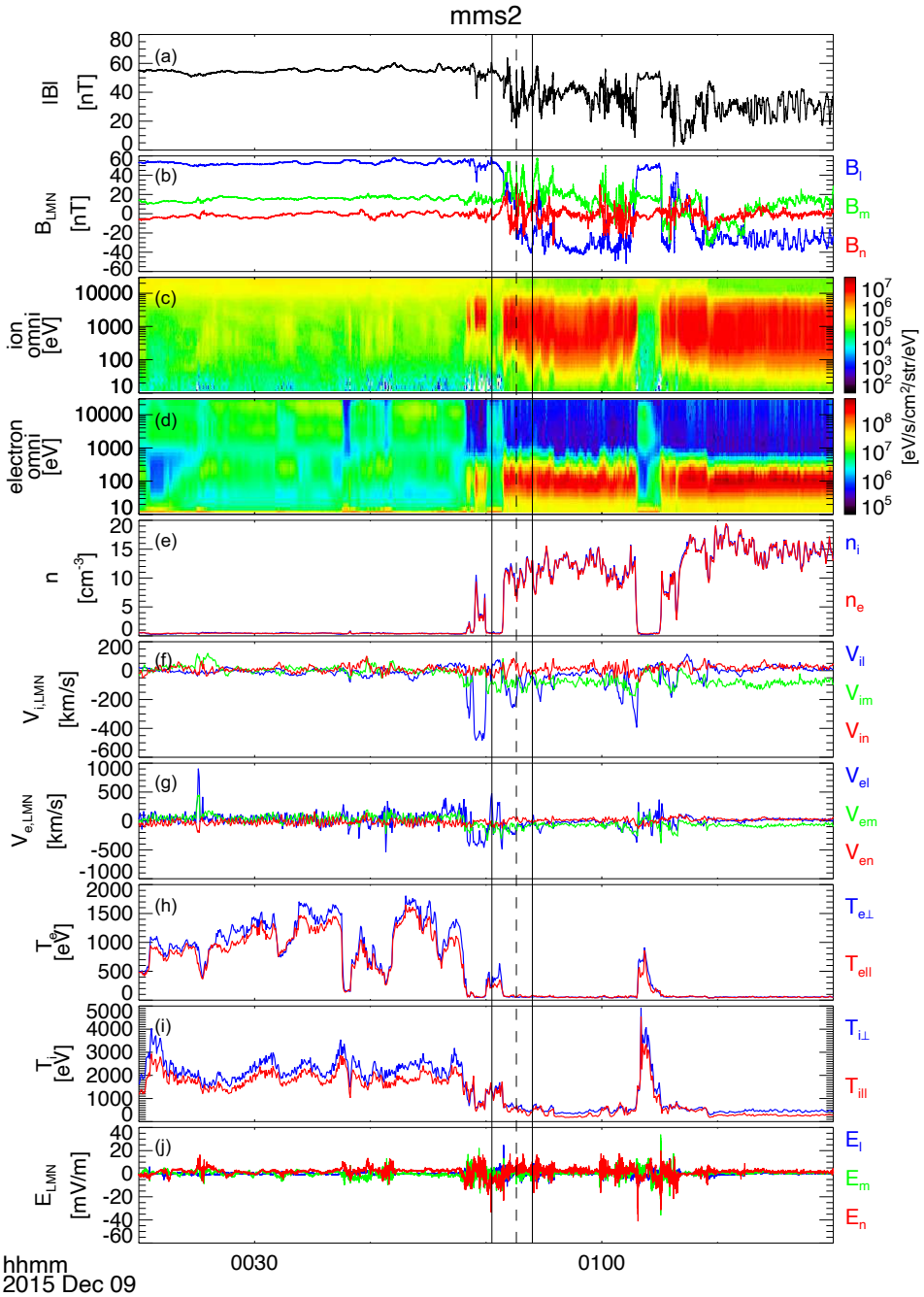

Figure 6.4: MMS 2 survey-mode observations of an outbound magnetopause crossing on 9 December 2015. The panels show: (a) & (b) magnetic field strength and components in a magnetopause boundary coordinate system [LMN]; (c) & (d) ion and electron omnidirectional energy spectra; (e) ion and electron number density; (f) & (g) ion and electron bulk velocity in LMN coordinates; (h) & (i) ion and electron temperature; (j) electric field in LMN coordinates. The solid vertical lines indicate the magnetopause crossing used to determine the LMN coordinate system and the dashed vertical line indicates the flux rope observation.

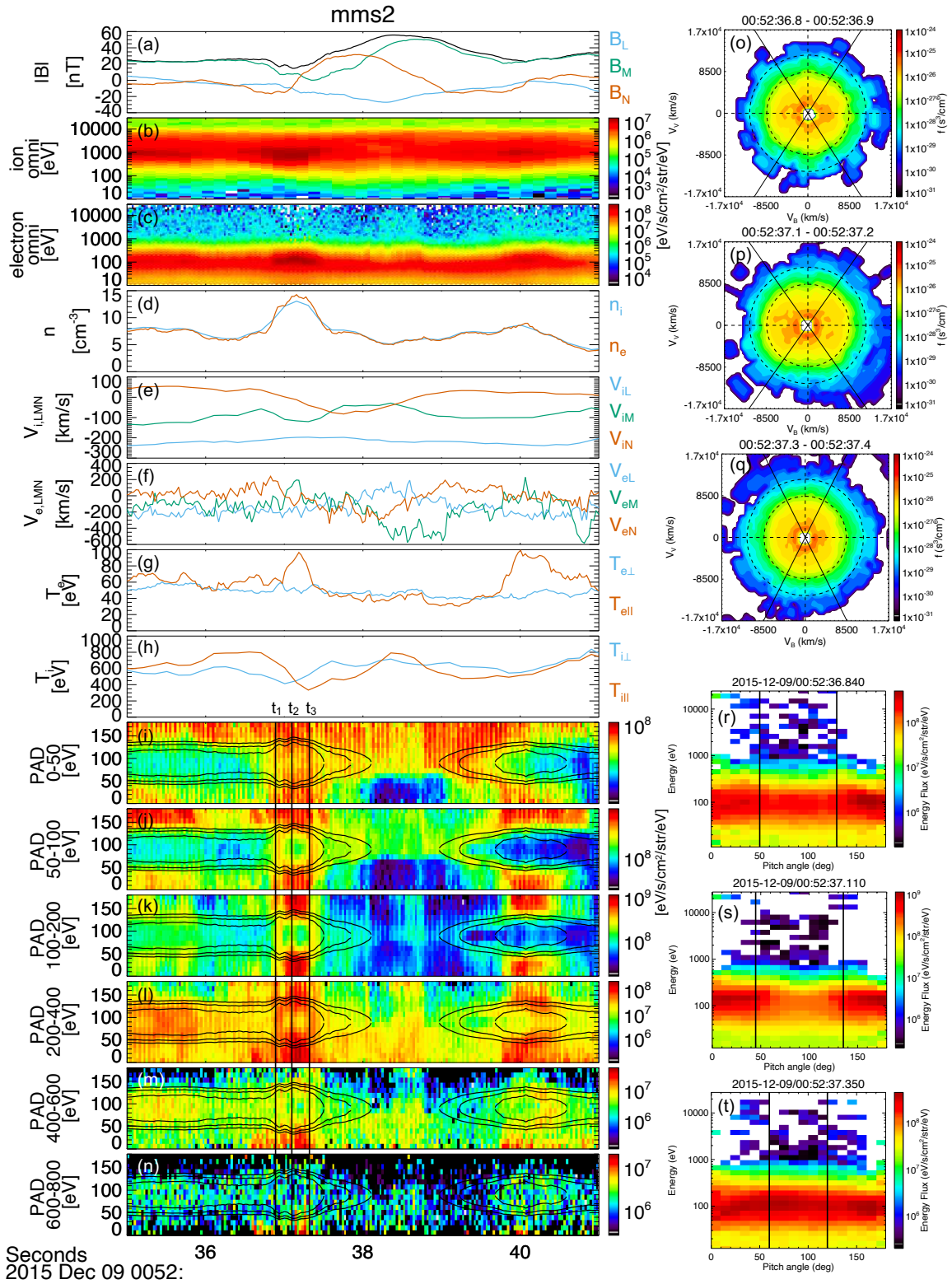

Figure 6.5: MMS 1 observations of a magnetopause flux rope observed on 9 December 2015 between 00:52:35 UT and 00:52:41 UT. *Caption continued on next page.*

Figure 6.5: *Caption continued from previous page.* The panels show: (a) magnetic field strength and components in a magnetopause boundary coordinate system (LMN); (b) & (c) ion and electron omnidirectional energy spectra; (d) ion and electron number density; (e) & (f) ion and electron bulk velocity in LMN coordinates; (g) & (h) ion and electron temperature; (i) – (n) electron pitch angle distributions over energy ranges 0 - 50 eV, 50 - 100 eV, 100 - 200 eV, 200 - 400 eV, 400 - 600 eV and 600 - 800 eV, respectively, with over plots of magnetic mirror loss cone angles for 20 nT, 30 nT and 40 nT magnetic mirrors; (o) – (q) electron energy distributions at times 03:18:07.9 - 08.0 UT, 03:18:08.3 - 08.4 UT, 03:18:08.6 - 08.7 UT, respectively, and approximately corresponding to times t_1, t_2 and t_3, as indicated on pitch angle distribution time series plots; (r) - (t) pitch angle energy plots at times 03:18:08.007 UT, 03:18:08.307 UT, 03:18:08.607UT, respectively, and approximately corresponding to times t_1, t_2 and t_3. Radial lines in plots (o) – (q) and vertical lines in plots (r) – (t) show the corresponding loss cone angles for a 30 nT magnetic mirror.

in the number density of both ions and electrons of ~ 5 cm^{-3} (Figure 6.5 (d)). Over this period, we also observe doughnut-like features in the electron pitch angle distributions, signifying mirror-trapped electrons, as discussed in detail in the previous section. The trajectory through the event is very similar to the first event, and so the cartoon in Figure 6.3 also illustrates the structure of the trapping region in this event. In contrast to the first case study, a significant parallel electron population is observed at the same time as the mirror-trapped electrons.

Using the average v_{iL} speed through the trapped population and ion inertial length calculated for the duration of the flux rope ($d_i \approx 86$ km), we find that the trapped electron population has an observed size of ~ 158 km or $\sim 1.8\ d_i$ in the L direction. The presence of the guide field also extends the structure of the mirror-trapped electron population into three-dimensions. As detailed in the previous section, we can geometrically set a minimum value on the M-extent of the trapped population of $\sim 3.6\ d_i$.

6.3 Instability Analysis

Magnetic holes with similar doughnut-shaped pitch angle features have previously been observed in the magnetosheath (Yao et al., 2018) and their formation has been attributed

to the ion magnetic mirror instability (Southwood and Kivelson, 1993). The growth of the instability is invoked to explain the characteristic doughnut-shaped pitch angle distributions (Kivelson and Southwood, 1996). Figure 6.6 shows a figure from Kivelson and Southwood (1996) which illustrates how the process works. As the instability grows, the amplitude of the peaks and troughs in the magnetic field strength grow (Figure 6.6 (a)). Electrons trapped between the peaks (in a magnetic mirror of greater magnetic field strength) are Fermi accelerated as the mirror structure grows in amplitude, and their mirror points move closer together; see how the upper solid arrowed line in Figure 6.6 (b), representing this particle bounce motion, shortens in (c). Electrons trapped deeper in the trough, in a magnetic mirror of smaller magnetic field strength, are Fermi decelerated as the trough deepens and the mirror points move further apart; see how the lower dashed arrowed line in Figure 6.6 (b) lengthens in (c). This is shown in the pitch angle distribution as a lower flux of particles at the centre of the doughnut shape and a higher flux at the edges. Furthermore, a betatron acceleration process as the magnetic field strength increases at the peaks, and deceleration as the magnetic field strength decreases in the trough, will enhance this doughnut-shaped pitch angle feature.

The magnetic mirror instability is driven by a temperature anisotropy with greater perpendicular temperature. In this study, we do not observe significant ion temperature anisotropy. This could suggest that any initial ion temperature anisotropy which could have led to the formation of the mirror-trapped electron populations has since decreased. The trapping region itself is ion-scale, suggesting an instability involving both ions and electrons could play a role in its dynamics (e.g. Kuznetsov et al., 2012). To this extent, we investigate the electron magnetic mirror instability as we do observe a significant temperature anisotropy in the electrons over the trapped population. This instability has a linear theory anisotropy threshold of the form:

$$\frac{T_{e\perp}}{T_{e\parallel}} = 1 + \frac{S_e}{{\beta_{e\parallel}}^{\alpha_e}} \tag{6.4}$$

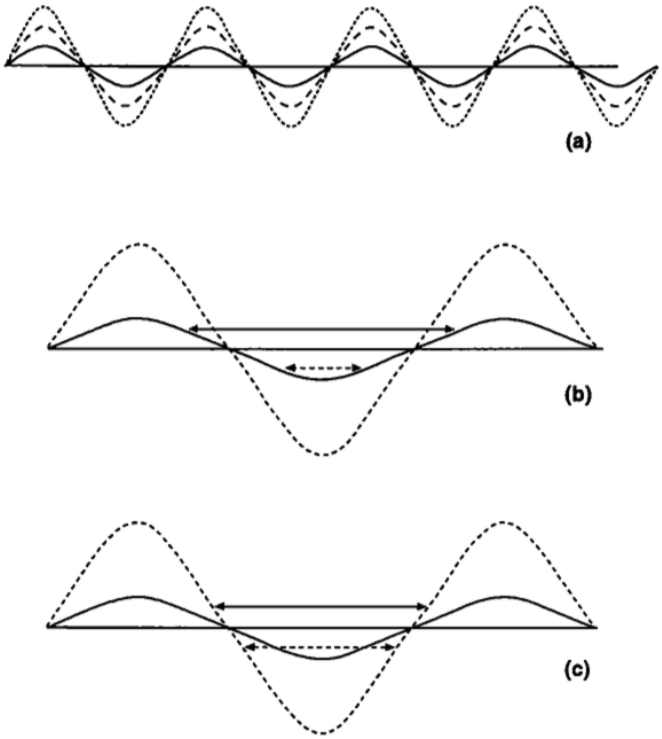

Figure 6.6: Diagram of Fermi acceleration in a growing magnetic mirror structure. (a) shows how the magnitude of the structure grows over time. In (b) arrowed lines show the bounce motion of electrons trapped in the magnetic mirror of lower field strength, shown by the solid curve. (c) shows how this bounce motion changes as the amplitude of the mirror structure increases to that of the dashed curve. *Figure from Figure 1 of Kivelson and Southwood (1996).*

where $T_{e\perp}$ and $T_{e\parallel}$ are the perpendicular and parallel electron temperatures, respectively, $\beta_{e\parallel}$ is the parallel electron plasma beta and S_e and α_e are fitting parameters determined by the chosen maximum growth rate of the instability (Gary and Wang, 1996). If a plasma of a given $\beta_{e\parallel}$ has $T_{e\perp}/T_{e\parallel}$ greater than defined by this threshold equation it suggests that the plasma is unstable to this instability. The whistler anisotropic instability has been shown to follow the same form of linear threshold when $0 \leq \beta_{e\parallel} \leq 1000$, however with unique fitting parameters for each given growth rate, $\gamma = \gamma_m/|\omega_{ge}|$ (the maximum growth rate normalized by the electron gyrofrequency). The whistler instability has a greater linear growth rate over a wider range of parameters (Gary and Karimabadi, 2006), however recent PIC simulations have suggested that the mirror mode may become dominant after non-linear saturation (Hellinger and Štěpán Štverák, 2018).

We also investigate the electron firehose instability, which is similarly driven by a temperature anisotropy, however with greater parallel temperature (Gary and Nishimura, 2003). This instability has a threshold of the form

$$\frac{T_{e\perp}}{T_{e\parallel}} = 1 - \frac{S_e}{{\beta_{e\parallel}}^{\alpha_e}} \tag{6.5}$$

where the terms have the same definitions as for the mirror and whistler instabilities.

In Figures 6.7 and 6.8 (k) we plot the electron temperature anisotropy $T_{e\perp}/T_{e\parallel}$ as a function of $\beta_{e\parallel}$ to investigate the proximity of the flux rope observations to these three instability thresholds; such plots are known as Brazil plots and are commonly used to investigate plasma stability in the solar wind (e.g. Štverák et al., 2008). The thresholds are plotted as solid line curves and data points for the flux rope observation intervals are colour-coded according to observation time. The green curve shows the mirror instability threshold, the red curve shows the whistler instability threshold, and the black curve shows the firehose instability threshold. These thresholds are all for instability growth rates $\gamma = 0.001$, approximating the marginal stability threshold of the instability. This corresponds to fitting parameters $S_e = 0.53$ and $\alpha_e = 0.64$ for the mirror instability, $S_e = 0.15$ and $\alpha = 0.56$ for the whistler instability (Gary and Karimabadi, 2006), and $S_e = 1.29$ and $\alpha = 0.97$ for the firehose instability (Gary and Nishimura, 2003). For the firehose instability, we have also included the other growth rates given in Table 1 of Gary and Nishimura (2003) as shown by the blue curves. In Figures 6.7 and 6.8 (f), (g), (h), and (i) we plot this same data as a times series, where the instability thresholds are shown by the red lines. In these plots we have used the $\gamma = 0.001$ threshold for all instabilities.

The observations for both flux ropes exhibit some similarities; as we move through the body of the flux ropes (between $\sim$ 00:52:37 UT and $\sim$ 00:52:40 UT for the 2015 case study and between $\sim$ 03:18:09 UT and $\sim$ 03:18:10.5 UT for the 2017 case study), the electrons tend to move away from both the mirror and firehose instabilities compared to the ambient conditions. This can be observed most clearly on the time series plots (Fig-

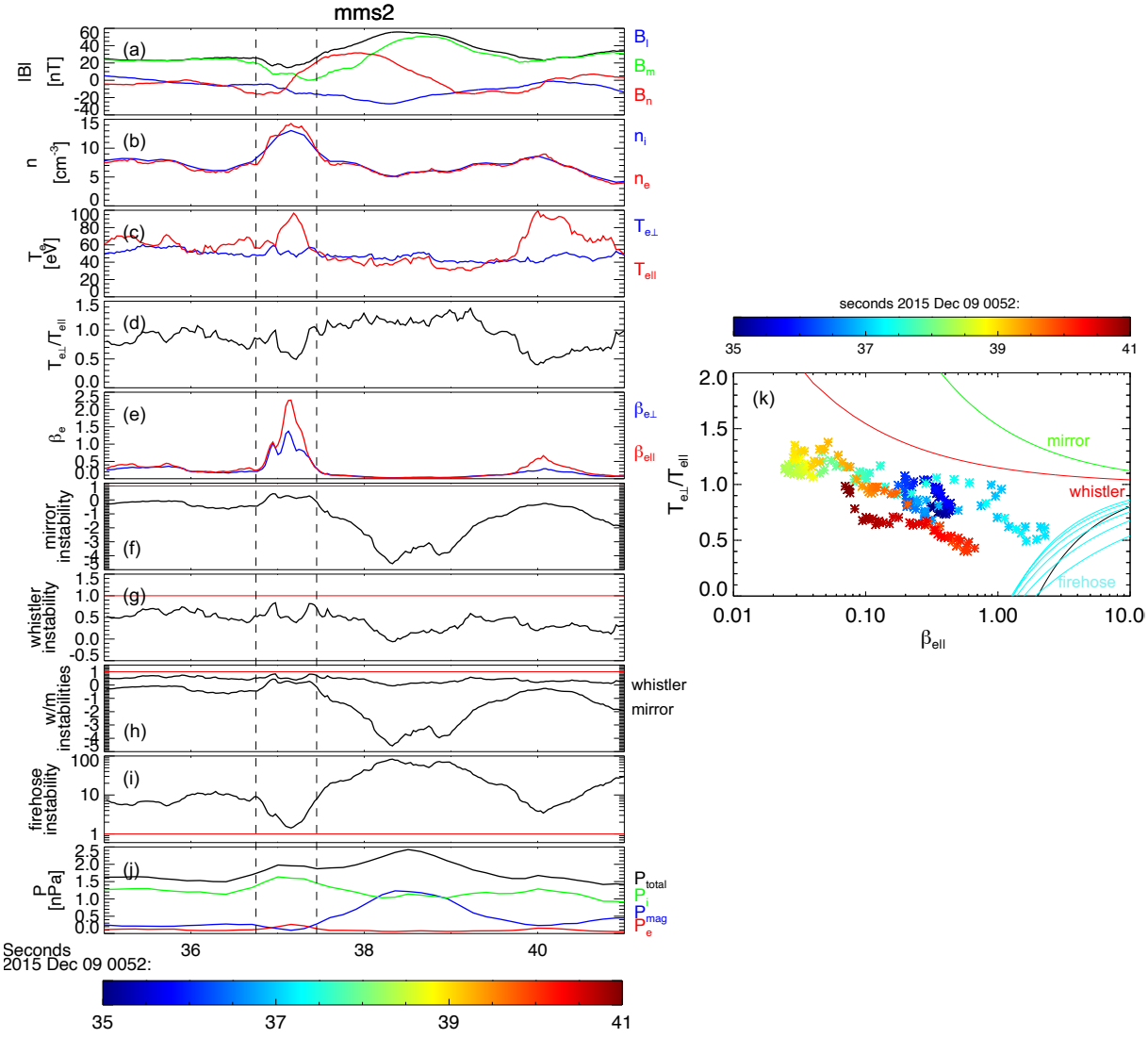

Figure 6.7: MMS 2 observations of the Case Study 1 flux rope observed on 9 December 2015. Panels show: (a) magnetic field components and magnitude in magnetopause coordinate system (LMN); (b) ion and electron number density; (c) electron parallel and perpendicular temperatures; (d) electron temperature anisotropy; (e) parallel and perpendicular electron plasma beta; (f) electron mirror instability, where threshold is shown by red line; (g) electron anisotropic whistler instability, where threshold is shown by red line; (h) combined plots of the electron mirror and anisotropic whistler instabilities; (i) electron firehose instability, where threshold is shown by red line; (j) ion, electron, plasma and total pressure. The dashed vertical lines indicate the electron trapping regions. (k) shows the electron instability analysis scatter plot for corresponding observation window. The electron mirror instability threshold is shown by the green curve, the anisotropic electron whistler instability is shown by the red curve, and the electron firehose instability threshold is shown by black and blue curves.

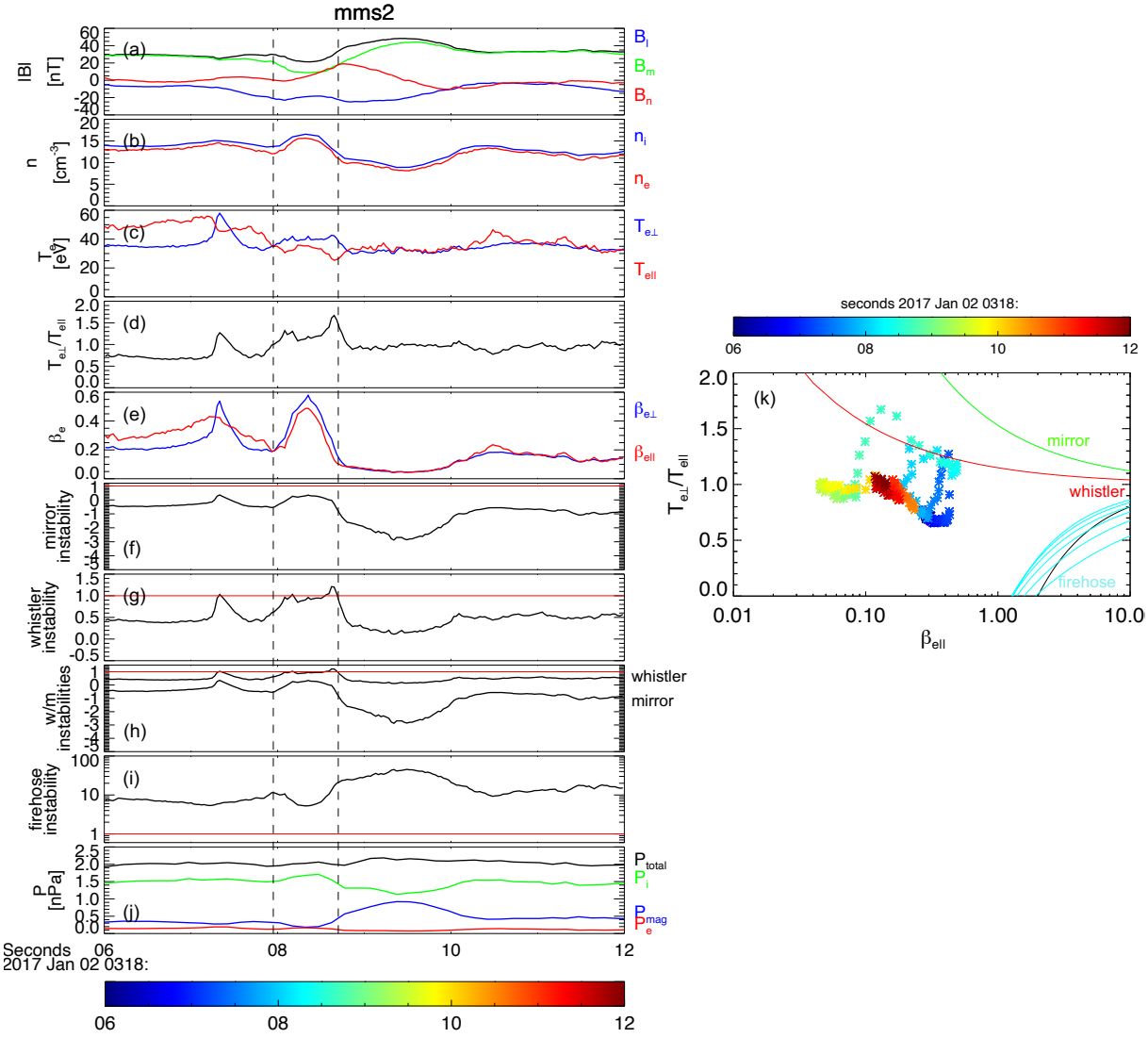

Figure 6.8: MMS 2 observations of the Case Study 2 flux rope observed on 02 January 2017. Panels show: (a) magnetic field components and magnitude in magnetopause coordinate system (LMN); (b) ion and electron number density; (c) electron parallel and perpendicular temperatures; (d) electron temperature anisotropy; (e) parallel and perpendicular electron plasma beta; (f) electron mirror instability, where threshold is shown by red line; (g) electron anisotropic whistler instability, where threshold is shown by red line; (h) combined plots of the electron mirror and anisotropic whistler instabilities; (i) electron firehose instability, where threshold is shown by red line; (j) ion, electron, plasma and total pressure. The dashed vertical lines indicate the electron trapping regions. (k) shows the electron instability analysis scatter plot for corresponding observation window. The electron mirror instability threshold is shown by the green curve, the anisotropic electron whistler instability is shown by the red curve, and the electron firehose instability threshold is shown by black and blue curves.

ures 6.7 and 6.8 (f) and (i)) by the line plots moving away from the red lines which show the instability thresholds. This trend is also potentially observed for the whistler instability (Figures 6.7 and 6.8 (g)), however it is less pronounced. When the mirror-trapped electron populations are observed (between 00:52:36.7 UT and 00:52:37.4 UT for the 2015 case study and between 03:18:07.9 UT and 03:18:08.7 UT for the 2017 case study) the trace for both observations moves towards both the mirror and firehose instabilities, however to slightly different extents, and we observe differences in the whistler stability. For the 2017 flux rope, we observe that the electrons cross the whistler instability threshold and move towards marginal mirror stability. For the 2015 flux rope, we observe enhancements in the whistler and mirror instability at the edges of the trapped population, where the particles are being reflected at the magnetic mirror point and therefore have high perpendicular velocity, and potentially marginal firehose stability at the centre of the trapped population.

6.3.1 Discussion

The whistler instability observed during the 2017 trapped population suggests that there could be whistler waves present in that event. Despite not observing the electron mirror instability over the observation, this does not rule out the electron/ion mirror instability as the original formation mechanism of the structure. The instability could have triggered the formation of the structure and any temperature anisotropy may have since diminished. As magnetic mirror modes grow, the temperature anisotropies formed at the centre of the structures creates favourable conditions for the formation of whistler waves (Ahmadi et al., 2018), which is consistent with our observations of whistler instability in the 2017 case study.

The 2015 trapped population lies near marginal firehose stability instead of marginal mirror stability, which is likely related to the presence of field aligned electrons on the field lines associated with the mirror structure, which drives up the parallel electron temper-

ature relative to the perpendicular temperature. The presence of field aligned electrons may be attributed to a change in the connectivity of the field (Pu et al., 2013).

The differences in instability observations between the two mirror structures remains an intriguing open question and may represent differences in the ongoing evolution of the two events. For example, the ion mirror instability may be responsible for the initial formation of the mirror structures, with different electron instabilities present over the evolution of the structures. In the 2017 event, a subsequent change in topology of the structure may lead to the presence of the firehose instability. Furthermore, scattering or non-adiabatic deceleration of these field-aligned electrons may lead to their trapping within the mirror structure.

6.4 Pressure and Force Analysis

The above analysis of the formation of the doughnut-shaped pitch angle distribution discusses the growth of the mirror instability in terms of the wave amplitudes, where the peaks and troughs grow. However, the two observed peaks could also be expanding (contracting) away from (towards) each other, changing the spatial extent of the structure. If the structure were to expand (contract), we would expect to see corresponding Fermi deceleration (acceleration) of the tapped particles. We can investigate the evolution of the structures by examining the pressure profiles and through the use of multi-spacecraft analysis techniques (see Section 2.3).

Figure Figures 6.7 and 6.8 (j) show the ion, electron, plasma and total pressures over the flux rope observations. Through the body of both flux ropes, we observe an increase in magnetic pressure and decrease in ion pressure. In the 2017 case study, these changes are approximately balanced ($\sim$ 0.7 nPa) and the total pressure remains approximately constant. However, for the 2015 case study, the increase in the plasma pressure ($\sim$ 1 nPa) is greater than the decrease in the magnetic pressure ($\sim$ 0.3 nPa), resulting in an increase in the total pressure of value of $\sim$ 0.7 nPa.

We also observe differences in the relative pressure profiles for the ions and electrons across the trapped populations in the two case studies. For the 2017 case study, an increase in ion and electron pressures ($\sim$ 0.3 nPa and $\sim$ 0.1 nPa, respectively) approximately balances a decrease in magnetic pressure ($\sim$ 0.2 nPa), leading to a small increase ($\sim$ 0.2 nPa) in total pressure through trapped population (Figure 6.7 (j)). For the 2015 case study, an increase in electron pressure ($\sim$ 0.2 nPa) balances a decrease in magnetic pressure ($\sim$ 0.2 nPa) and an increase in ion pressure ($\sim$ 0.4 nPa) results in overall pressure enhancement ($\sim$ 0.4 nPa) through trapped population (Figure 6.8 (j)).

For the 2017 case study, any changes in the pressure contributions approximately balance and we observe an approximately constant total pressure. However, in the 2015 case study, we observe imbalances in the pressure contributions and overall pressure enhancements over the trapped population and through the body of the flux rope. The differences in the pressure profiles could indicate different evolutionary states of the phenomena and differences in the roles of the ions and electrons within the two events.

To better understand the structure's dynamics, Figure 6.9 shows the results of a four-spacecraft force analysis on the 2015 flux rope observations, presented in magnetopause coordinates. The data from MMS 3 in the 2017 event is incomplete so precludes the use of this analysis for Case Study 2. Multi-spacecraft gradient techniques are used to calculate the required divergences and the results are presented at the barycenter of the 4 MMS spacecraft. The ion and electron data are collected at different resolutions, therefore the panels containing ion measurements (Figure 6.9 (e) and (f)) are presented on the ion time-series.

The two vertical lines in Figure 6.9 at 00:52:36.75 UT and 00:52:37.45 UT represent the boundaries of the mirror-trapped electron population. Over the trapped population, we observe signatures in the electron force components. In the $\mathbf{J} \times \mathbf{B}$ force (Figure 6.9 (b)) we observe a negative N component, a positive to negative bipolar signature in the L component and a positive to negative bipolar signature of smaller magnitude in the M component. In the electron pressure gradient force ($-\nabla \mathbf{P}_e$, Figure 6.9 (c)) we observe

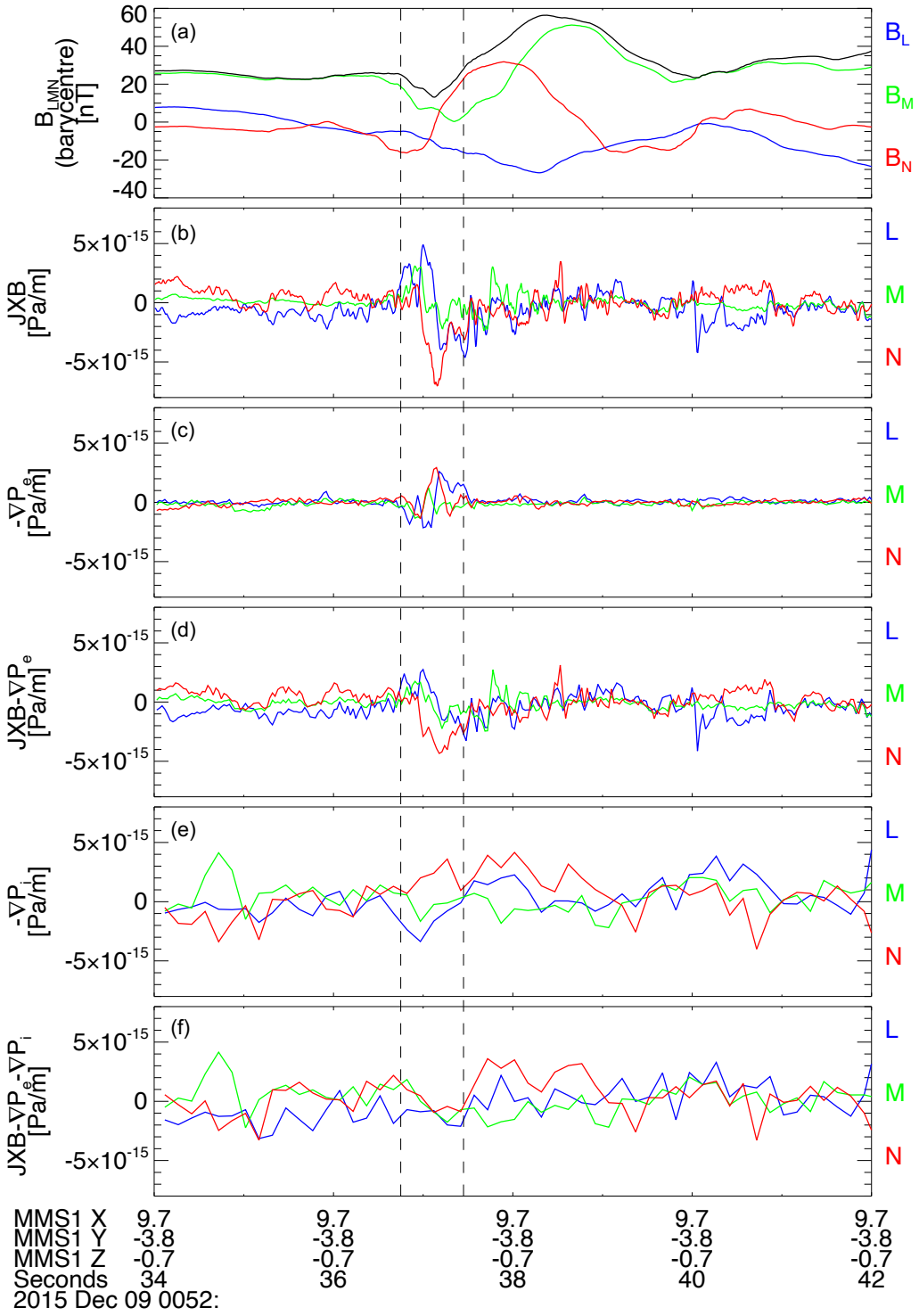

Figure 6.9: Force analysis of MMS observations of a flux rope observed on December 9 December 2015. the panels show; (a) magnetic field magnitude and components at the MMS spacecraft barycenter in magnetopause coordinates; (b) $\mathbf{J} \times \mathbf{B}$ calculated using the curlometer technique; (c) – $\nabla\ P_e$; (d) $\mathbf{J} \times \mathbf{B}$ – $\nabla\ P_e$; (e) – $\nabla\ P_i$; (f) $\mathbf{J} \times \mathbf{B}$ – $\nabla\ P_e$ – $\nabla\ P_i$. The dashed vertical lines indicate the electron trapping region.

enhancements in components through the trapped population with respect to the surrounding plasma, but of a smaller magnitude than the $\mathbf{J} \times \mathbf{B}$ components. The sum of these two force components can be seen in Figure 6.9 (d), where we observe the signatures from the $\mathbf{J} \times \mathbf{B}$ force to persist. To interpret these electron forces, we refer to Figure 6.3; the negative force in the N direction is directed away from the magnetic null point and the bipolar L force would act to decrease the L-extent of the structure. If the null point was undergoing magnetic reconnection, the force in the − N direction could be overcome by the ram pressure of the inflowing plasma.

Figure 6.9 (e) shows the ion pressure gradient force (– ∇ $\mathbf{P}_i$) where we observe a negative L component and positive N component over the trapped population which could be acting to oppose the forces observed in the electron force panels. Figure 6.9 (f) shows the sum of all force components on the ion time series. Here we observe no obvious signatures over the trapped population, which would be consistent with the ions acting to balance the electron force components. Furthermore, if the structure has previously contracted, this could show the ion force required to balance the increase in plasma pressure of the collapsed structure. However, the low resolution of the ion measurements means that significance of these observations is unclear. It is also important to note that the observed size of the trapped population ($\sim 1.8\ d_i$ in the L direction) means it is an ion-scale structure, suggesting that the gradients we observe are sub-ion scale. Comparison of the measured electric field with the calculated $-\mathbf{v} \times \mathbf{B}$ electric field over this period suggest that the ions are not frozen-in to the magnetic field. Further force analysis is required to determine how the ion dynamics couple into the electron dynamics, specifically through the electric field in the momentum equation, and therefore to determine the precise nature of the dynamics.

6.5 Acceleration Mechanisms

As discussed in the previous sections, the potential magnetic mirror instability formation mechanism and the following evolution of the structures facilitates electron acceleration. However, the presence of the flux rope could also play a role in the dynamics of these structures. As well as providing the field enhancement required to trap the particles, the location of the trapped population at the edge of the flux rope near to a null point could produce particle acceleration. If the null point is undergoing magnetic reconnection, the mirror-trapping region would be located in the reconnection inflow region, with the flux rope being located in one of the exhausts. As the electrons trapped in the magnetic mirror structure flow towards the X-point, their mirror points would move closer together as the reconnection inflow converges towards the reconnection site. This converging mirroring of particles would result in a Fermi acceleration process. This inflow scenario is potentially consistent with the force analysis discussed in Section 6.4, where a Lorentz force is observed in the $-$ N direction, which would be opposed by the ram pressure of the inflowing plasma.

This potential flux rope electron acceleration mechanism invokes the same electron trapping and Fermi acceleration as the Drake et al. (2006b) mechanism. However, rather than electron trapping within the body of the flux rope, we have electron trapping in the reconnection inflow region at the edge of the flux rope. This may also impact the magnetic reconnection acceleration mechanism proposed by Egedal et al. (2005) in which electrons are trapped by a parallel electric fields and reconnection-associated magnetic minima.

6.6 Conclusions

We have shown evidence for electron trapping in magnetic mirror structures on the magnetosheath edge of magnetopause flux ropes. Both case studies have magnetic mirror

features consistent with observations of magnetic holes formed via the magnetic mirror instability (e.g. Yao et al., 2018). These magnetic mirror features are located near a magnetic null point next to the flux rope. Both flux ropes have a guide field present which extends the mirror structures along the body of the flux rope.

The results show that magnetic field enhancements associated with flux ropes in magnetic reconnection exhausts can contribute to electron trapping. Unlike other previously proposed trapping mechanisms associated with magnetic islands in which electrons are trapped within the closed (or highly twisted) magnetic topology (Drake et al., 2006a), in this study the electrons are trapped within magnetic mirror structures at the boundary of the flux rope.

Such magnetic mirror structures could prove to be an important feature for particle acceleration at flux ropes and for magnetic reconnection more generally, as they are able to provide the particle trapping required to accelerate particles via Fermi and betatron processes. We have shown that there are electron force signatures present over the trapped populations which could facilitate such acceleration. Further investigation of the evolution of the structures is required to determine the extent of the potential acceleration and to assess the interplay between different energisation mechanisms.

Further open questions include how common such structures may be. Here we identified 2 clear examples from a survey of $\sim$ 90 magnetopause flux ropes. It is important to consider the structures' small size relative to the flux ropes, meaning spacecraft trajectories through the flux ropes and their surroundings are important for encountering the structures. Future studies should plan to investigate such flux rope substructure on statistical scales, addressing how it is influenced by the large-scale dynamics of the reconnection outflows in which it is embedded, and the topology and connectivity of the magnetic field.

Chapter 7

Conclusions

In this thesis, we have investigated flux ropes on the Earth's magnetopause. Flux ropes are a common feature of magnetic reconnection, highlighting the time-dependent nature of the process. Previously, flux ropes have been identified as important in magnetic flux transfer from the the magnetopause into the magnetotail as part of the Dungey cycle and have been proposed as a potential site for particle acceleration in magnetic reconnection. Therefore, understanding their their properties, formation mechanisms and evolution is a key component of forming a full understanding of the reconnection process itself and its impacts on magnetospheric dynamics.

Chapter 3 introduces a survey of 245 flux ropes associated with magnetopause electron diffusion region (EDR) encounters. We use data collected by the Magnetospheric Multiscale (MMS) mission, the first mission of its kind that is able to resolve the electron-scale dynamics of reconnection in the magnetosphere, therefore allowing the investigation of the EDR and its associated processes. Previous work has suggested that flux ropes could be produced by the EDR. In this work, we present the first statistical investigation into EDR-associated flux ropes, with the aim of establishing the relationship between flux ropes and the EDR.

This survey found that the flux ropes examined tended to have smaller radii and smaller flux contents than reported by previous studies, suggesting that we may have

identified a distinct subset of EDR-associated flux ropes. Skewed distributions were fit to the flux rope radius distributions, and were found to have cut-offs at $\sim 1\ d_i$. As MMS is able to resolve electron scales, this could suggest that flux ropes are formed as ion-scale features. However, it was also observed that the flux ropes were more likely to be observed closer to the EDR, reinforcing that they could be produced on electron scales by the EDR itself. It was also found that flux ropes observed closer to the EDR had greater axial field strengths and therefore greater flux contents. Finally, the number of flux ropes observed surrounding an EDR was found to be limited by the maximum electron gyroradius and plasma beta observed at the EDR, and more flux ropes were observed surrounding EDRs with larger minimum observed magnetic field strengths.

Chapter 4 investigated the force-free nature of the flux ropes. The flux ropes were found to generally have good agreement with the force-free flux rope model fit, and smaller RMS errors to the model fit were observed for flux ropes with a greater radius and stronger axial field. Combining this with the findings of Chapter 3, this could suggest that flux ropes observed closer to the EDR are more force-free, potentially suggesting that the EDR can produce force-free flux ropes. It was also found that the force-free model gave smaller flux rope radii and stronger axial field strengths than calculated in Chapter 3; the radii estimates being smaller with the force-free model is not expected as the model factors in the impact parameter of the spacecraft trajectory through the flux rope. The force-free model outputs were also used to investigate the helicity of the flux ropes; it was found that the majority of the flux ropes had positive helicity, with negative helicity flux ropes generally being restricted to the positive y GSE, negative z GSE quadrant of the magnetopasue, suggesting that their formation could be favoured by negative IMF B_Y, as this is where we would expect the reconnection X-line to be for these conditions. However, many positive helicity flux ropes were also observed in this quadrant, suggesting a more complex EDR-helicity relationship.

The topology of the flux ropes was investigated in Chapter 5. The majority of the flux ropes were found to have an open topology with one end connected to the southern

hemisphere and the other to the magnetosheath. This observation is consistent with the multiple X-line formation mechanism which predicts this topology for crossing south of the reconnection X-line, which is generally where MMS crosses the magnetopause. We found that closed flux rope topologoies were more likely to be observed closer to the EDR, which could suggest that they can be formed as closed topologies, contrary to the suggestion of previous formation theories. Furthermore, closed flux rope topologies were more likely to be observed in the positive Y GSE, negative Z GSE quadrant of the magnetopause, again suggesting negative IMF B_Y is favourable for their formation. Closed topology flux ropes were found to have larger radii and smaller axial field strength. Overall, the topology investigation results were generally conflicting with previous studies, suggesting that this is an interesting area for future research.

Chapter 6 presented two case studies of electron trapping in magnetic mirror structures on the edge of magnetopause flux ropes. These unique observations provide a link between magnetic mirror structures and magnetic reconnection substructure. Instability analysis performed on the events suggested that the mirror structures could be formed by the mirror instability and the associated temperature anisotropies. The potential for acceleration in these structures was investigated, with the magnetic mirror structures providing the required particle trapping for subsequent acceleration. Potential force signatures were observed over the trapping regions suggesting that they could provide a mechanism for particle acceleration in magnetic reconnection.

7.1 Future Work

There are many outstanding questions regarding magnetopause flux ropes; particularly regarding how they are formed and their subsequent evolution. MMS has allowed us to probe flux ropes down to electron-scales, however, a mechanism for flux rope formation within the EDR has not been determined. This thesis has shown that small-scale flux ropes can be associated with an EDR, with their properties varying with proximity to an

EDR and the properties of the EDR itself.

This thesis has identified relationships between the properties of flux ropes and their location on the magnetopause; in Chapter 5 we observed that closed topology flux ropes were more likely to be observed in the positive Y GSE, negative Z GSE quadrant. This highlights the need for further investigation into the relationship between flux ropes and the incoming solar wind conditions. The maximum magnetic shear model (Trattner et al., 2012) predicts the location of the reconnection X-line for different solar wind conditions. This model, along with the measured solar wind conditions at L1, could be used to predict the location of the reconnection which is producing the observed flux ropes. How the location of the flux ropes relative to the X-line affects their properties, such as their topology, could then be investigated. As well as this, the variability of the incoming solar wind conditions could be quantified, and the effect of this on the observed flux ropes could be investigated.

In-situ measurements are limited by the spacecraft trajectory through the observed event. Performing simulations of phenomena of interest can help to form a full picture of the processes taking place. As such, one of the next avenues for investigation is simulating the production of flux ropes by the EDR. However, such an investigation challenges the limits of simulations; to fully model flux ropes 3D kinetic simulations are required which are highly computationally expensive (e.g. Daughton et al., 2011a). Furthermore, determining initial conditions for such simulations is not a trivial task; the results of this thesis will be helpful in determining the EDR and plasma properties which are favourable for the production of flux ropes, hopefully informing boundary conditions for simulations. Such simulation studies could help to determine a mechanism for flux rope production by the EDR. Furthermore, such simulations could be useful for further study of the electron trapping case studies presented in Chapter 6. Magnetic holes have previously been investigated in simulations, with ambient conditions comparable to the magnetosheath (Ahmadi et al., 2017). Our observations suggest that the next challenge should be investigating if such magnetic holes could be produced in simulation reconnection exhausts, or

be associated with reconnection exhaust substructure, such as flux ropes.

Future planned missions also provide an interesting prospect for the study of flux ropes, FTEs and reconnection on the magnetopause. The SMILE mission (Solar-wind Magnetosphere Ionosphere Link Explorer, Raab et al., 2016), which is scheduled for launch at the end of 2024, will investigate the magnetosphere on a global scale via imaging with X-ray and ultraviolet cameras from a highly-inclined elliptical orbit. Used in conjunction with global magnetospheric simulations (e.g. Mejnertsen et al., 2021), this mission will be able to shed further light on the global process and conditions favourable for flux rope formation, as well as potentially being able to inform us on how flux ropes evolve and interact.

This thesis has highlighted the importance of magnetic flux ropes and their potential for particle acceleration during magnetopause reconnection. Magnetic reconnection also takes place in other solar system plasma environments such as at the Sun, in the solar wind and in other planetary magnetospheres; the phenomena studied in this thesis can inform observations of reconnection in these environments and in astrophysical domains beyond.

Bibliography

Ahmadi, N., Germaschewski, K., and Raeder, J. (2017). Simulation of magnetic holes formation in the magnetosheath. *Physics of Plasmas*, 24:122121.

Ahmadi, N., Wilder, F. D., Ergun, R. E., Argall, M., Usanova, M. E., Breuillard, H., Malaspina, D., Paulson, K., Germaschewski, K., Eriksson, S., Goodrich, K., Torbert, R., Contel, O. L., Strangeway, R. J., Russell, C. T., Burch, J., and Giles, B. (2018). Generation of electron whistler waves at the mirror mode magnetic holes: Mms observations and pic simulation. *Journal of Geophysical Research: Space Physics*, 123:6383–6393.

Akhavan-Tafti, M., Slavin, J. A., Le, G., Eastwood, J. P., Strangeway, R. J., Russell, C. T., Nakamura, R., Baumjohann, W., Torbert, R. B., Giles, B. L., Gershman, D. J., and Burch, J. L. (2018). Mms examination of ftes at the earth's subsolar magnetopause. *Journal of Geophysical Research: Space Physics*, 123(2):1224–1241.

Alfvén, H. (1942). Existence of electromagnetic-hydrodynamic waves. *Nature*, 150(3805):405–406.

Angelopoulos, V. (2009). The themis mission. In *The THEMIS mission*, pages 5–34. Springer.

Baumjohann, W. and Treumann, R. A. (1996). *Basic Space Plasma Physics*. PUBLISHED BY IMPERIAL COLLEGE PRESS AND DISTRIBUTED BY WORLD SCIENTIFIC PUBLISHING CO.

Berchem, J. and Russell, C. (1984). Flux transfer events on the magnetopause: Spatial

distribution and controlling factors. *Journal of Geophysical Research: Space Physics*, 89(A8):6689–6703.

Blandford, R. D. and Ostriker, J. P. (1978). Particle acceleration by astrophysical shocks. *The Astrophysical Journal*, 221:L29–L32.

Briggs, J., Brain, D., Cartwright, M., Eastwood, J., and Halekas, J. (2011). A statistical study of flux ropes in the martian magnetosphere. *Planetary and Space Science*, 59(13):1498–1505. Exploring Phobos.

Burch, J. L., Moore, T. E., Torbert, R. B., and Giles, B. L. (2016a). Magnetospheric multiscale overview and science objectives. *Space Science Reviews*, 199(1):5–21.

Burch, J. L., Torbert, R. B., Phan, T. D., Chen, L.-J., Moore, T. E., Ergun, R. E., Eastwood, J. P., Gershman, D. J., Cassak, P. A., Argall, M. R., Wang, S., Hesse, M., Pollock, C. J., Giles, B. L., Nakamura, R., Mauk, B. H., Fuselier, S. A., Russell, C. T., Strangeway, R. J., Drake, J. F., Shay, M. A., Khotyaintsev, Y. V., Lindqvist, P.-A., Marklund, G., Wilder, F. D., Young, D. T., Torkar, K., Goldstein, J., Dorelli, J. C., Avanov, L. A., Oka, M., Baker, D. N., Jaynes, A. N., Goodrich, K. A., Cohen, I. J., Turner, D. L., Fennell, J. F., Blake, J. B., Clemmons, J., Goldman, M., Newman, D., Petrinec, S. M., Trattner, K. J., Lavraud, B., Reiff, P. H., Baumjohann, W., Magnes, W., Steller, M., Lewis, W., Saito, Y., Coffey, V., and Chandler, M. (2016b). Electron-scale measurements of magnetic reconnection in space. *Science*, 352(6290).

Burlaga, L. F. (1988). Magnetic clouds and force-free fields with constant alpha. *Journal of Geophysical Research: Space Physics*, 93(A7):7217–7224.

Chen, L.-J., Bessho, N., Lefebvre, B., Vaith, H., Fazakerley, A., Bhattacharjee, A., Puhl-Quinn, P. A., Runov, A., Khotyaintsev, Y., Vaivads, A., Georgescu, E., and Torbert, R. (2008). Evidence of an extended electron current sheet and its neighboring magnetic island during magnetotail reconnection. *Journal of Geophysical Research: Space Physics*, 113(A12).

Chen, L. J., Bhattacharjee, A., Puhl-Quinn, P. A., Yang, H., Bessho, N., Imada, S., Mühlbachler, S., Daly, P. W., Lefebvre, B., Khotyaintsev, Y., Vaivads, A., Fazakerley, A., and Georgescu, E. (2007). Observation of energetic electrons within magnetic islands. *Nature Physics*, 4:19 EP –.

Chen, L.-J., Hesse, M., Wang, S., Gershman, D., Ergun, R., Pollock, C., Torbert, R., Bessho, N., Daughton, W., Dorelli, J., Giles, B., Strangeway, R., Russell, C., Khotyaintsev, Y., Burch, J., Moore, T., Lavraud, B., Phan, T., and Avanov, L. (2016). Electron energization and mixing observed by mms in the vicinity of an electron diffusion region during magnetopause reconnection. *Geophysical Research Letters*, 43:6036–6043.

Chen, Z. Z., Fu, H. S., Wang, Z., Guo, Z. Z., Xu, Y., and Liu, C. M. (2021). First observation of magnetic flux rope inside electron diffusion region. *Geophysical Research Letters*, 48(7):e2020GL089722. e2020GL089722 2020GL089722.

Crooker, N. (1979). Dayside merging and cusp geometry. *Journal of Geophysical Research: Space Physics*, 84(A3):951–959.

Daughton, W., Roytershteyn, V., Karimabadi, H., Yin, L., Albright, B. J., Bergen, B., and Bowers, K. J. (2011a). Role of electron physics in the development of turbulent magnetic reconnection in collisionless plasmas. *Nature Physics*, 7:539 EP –.

Daughton, W., Roytershteyn, V., Karimabadi, H., Yin, L., Albright, B. J., Gary, S. P., and Bowers, K. J. (2011b). Secondary island formation in collisional and collisionless kinetic simulations of magnetic reconnection. *AIP Conference Proceedings*, 1320(1):144–159.

Daughton, W., Roytershteyn, V., Karimabadi, H., Yin, L., Albright, B. J., Gary, S. P., and Bowers, K. J. (2011c). Secondary island formation in collisional and collisionless kinetic simulations of magnetic reconnection. *AIP Conference Proceedings*, 1320:144–159.

DiBraccio, G. A., Slavin, J. A., Imber, S. M., Gershman, D. J., Raines, J. M., Jackman, C. M., Boardsen, S. A., Anderson, B. J., Korth, H., Zurbuchen, T. H., McNutt, R. L.,

and Solomon, S. C. (2015). Messenger observations of flux ropes in mercury's magnetotail. *Planetary and Space Science*, 115:77–89. Solar wind interaction with the terrestrial planets.

Drake, J., Swisdak, M., and Fermo, R. (2012). The power-law spectra of energetic particles during multi-island magnetic reconnection. *The Astrophysical Journal Letters*, 763(1):L5.

Drake, J. F., Swisdak, M., Che, H., and Shay, M. A. (2006a). Electron acceleration from contracting magnetic islands during reconnection. *Nature*, 443(7111):553–556.

Drake, J. F., Swisdak, M., Schoeffler, K. M., Rogers, B. N., and Kobayashi, S. (2006b). Formation of secondary islands during magnetic reconnection. *Geophysical Research Letters*, 33(13).

Dungey, J. (1953). Lxxvi. conditions for the occurrence of electrical discharges in astrophysical systems. *The London, Edinburgh, and Dublin Philosophical Magazine and Journal of Science*, 44(354):725–738.

Dungey, J. W. (1961). Interplanetary magnetic field and the auroral zones. *Phys. Rev. Lett.*, 6:47–48.

Dunlop, M. W., Dong, X.-C., Wang, T.-Y., Eastwood, J. P., Robert, P., Haaland, S., Yang, Y.-Y., Escoubet, P., Rong, Z.-J., Shen, C., Fu, H.-S., and De Keyser, J. (2021). Curlometer technique and applications. *Journal of Geophysical Research: Space Physics*, 126(11):e2021JA029538. e2021JA029538 2021JA029538.

Dunlop, M. W., Taylor, M. G. G. T., Davies, J. A., Owen, C. J., Pitout, F., Fazakerley, A. N., Pu, Z., Laakso, H., Bogdanova, Y. V., Zong, Q.-G., Shen, C., Nykyri, K., Lavraud, B., Milan, S. E., Phan, T. D., Rème, H., Escoubet, C. P., Carr, C. M., Cargill, P., Lockwood, M., and Sonnerup, B. (2005). Coordinated cluster/double star observations of dayside reconnection signatures. *Annales Geophysicae*, 23(8):2867–2875.

Eastwood, J. P., Hietala, H., Toth, G., Phan, T. D., and Fujimoto, M. (2015). What controls the structure and dynamics of earth's magnetosphere? *Space Science Reviews*, 188(1):251–286.

Eastwood, J. P., Phan, T. D., Cassak, P. A., Gershman, D. J., Haggerty, C., Malakit, K., Shay, M. A., Mistry, R., Øieroset, M., Russell, C. T., Slavin, J. A., Argall, M. R., Avanov, L. A., Burch, J. L., Chen, L. J., Dorelli, J. C., Ergun, R. E., Giles, B. L., Khotyaintsev, Y., Lavraud, B., Lindqvist, P. A., Moore, T. E., Nakamura, R., Paterson, W., Pollock, C., Strangeway, R. J., Torbert, R. B., and Wang, S. (2016). Ion-scale secondary flux ropes generated by magnetopause reconnection as resolved by mms. *Geophysical Research Letters*, 43(10):4716–4724.

Eastwood, J. P., Phan, T. D., Fear, R. C., Sibeck, D. G., Angelopoulos, V., Øieroset, M., and Shay, M. A. (2012a). Survival of flux transfer event (fte) flux ropes far along the tail magnetopause. *Journal of Geophysical Research: Space Physics*, 117(A8).

Eastwood, J. P., Phan, T. D., Fear, R. C., Sibeck, D. G., Angelopoulos, V., Øieroset, M., and Shay, M. A. (2012b). Survival of flux transfer event (fte) flux ropes far along the tail magnetopause. *Journal of Geophysical Research: Space Physics*, 117(A8).

Eastwood, J. P., Phan, T. D., Øieroset, M., Shay, M. A., Malakit, K., Swisdak, M., Drake, J. F., and Masters, A. (2013). Influence of asymmetries and guide fields on the magnetic reconnection diffusion region in collisionless space plasmas. *Plasma Physics and Controlled Fusion*, 55(12):124001.

Egedal, J., Øieroset, M., Fox, W., and Lin, R. P. (2005). In situ discovery of an electrostatic potential, trapping electrons and mediating fast reconnection in the earth's magnetotail. *Phys. Rev. Lett.*, 94:025006.

Escoubet, C., Fehringer, M., and Goldstein, M. (2001a). Introduction the cluster mission. In *Annales Geophysicae*, volume 19, pages 1197–1200. Copernicus GmbH.

Escoubet, C. P., Fehringer, M., and Goldstein, M. (2001b). Introductionthe cluster mission. *Annales Geophysicae*, 19(10/12):1197–1200.

Fargette, N., Lavraud, B., Øieroset, M., Phan, T. D., Toledo-Redondo, S., Kieokaew, R., Jacquey, C., Fuselier, S. A., Trattner, K. J., Petrinec, S., Hasegawa, H., Garnier, P., Génot, V., Lenouvel, Q., Fadanelli, S., Penou, E., Sauvaud, J.-A., Avanov, D. L. A., Burch, J., Chandler, M. O., Coffey, V. N., Dorelli, J., Eastwood, J. P., Farrugia, C. J., Gershman, D. J., Giles, B. L., Grigorenko, E., Moore, T. E., Paterson, W. R., Pollock, C., Saito, Y., Schiff, C., and Smith, S. E. (2020). On the ubiquity of magnetic reconnection inside flux transfer event-like structures at the earth's magnetopause. *Geophysical Research Letters*, 47(6):e2019GL086726. e2019GL086726 2019GL086726.

Fear, R. C., Milan, S. E., Fazakerley, A. N., Lucek, E. A., Cowley, S. W. H., and Dandouras, I. (2008). The azimuthal extent of three flux transfer events. *Annales Geophysicae*, 26(8):2353–2369.

Fear, R. C., Trenchi, L., Coxon, J. C., and Milan, S. E. (2017). How much flux does a flux transfer event transfer? *Journal of Geophysical Research: Space Physics*, 122(12):12,310–12,327.

Fermo, R. L., Drake, J. F., Swisdak, M., and Hwang, K.-J. (2011). Comparison of a statistical model for magnetic islands in large current layers with hall mhd simulations and cluster fte observations. *Journal of Geophysical Research: Space Physics*, 116(A9).

Fu, H. S., Khotyaintsev, Y. V., André, M., and Vaivads, A. (2011). Fermi and betatron acceleration of suprathermal electrons behind dipolarization fronts. *Geophysical Research Letters*, 38(16).

Fu, H. S., Khotyaintsev, Y. V., Vaivads, A., Retinò, A., and André, M. (2013). Energetic electron acceleration by unsteady magnetic reconnection. *Nature Physics*, 9:426 EP –.

Furth, H. P., Killeen, J., and Rosenbluth, M. N. (1963). Finite-resistivity instabilities of a sheet pinch. *The Physics of Fluids*, 6(4):459–484.

Fuselier, S. A., Lewis, W. S., Schiff, C., Ergun, R., Burch, J. L., Petrinec, S. M., and Trattner, K. J. (2016). Magnetospheric multiscale science mission profile and operations. *Space Science Reviews*, 199(1):77–103.

Fuselier, S. A., Vines, S. K., Burch, J. L., Petrinec, S. M., Trattner, K. J., Cassak, P. A., Chen, L.-J., Ergun, R. E., Eriksson, S., Giles, B. L., Graham, D. B., Khotyaintsev, Y. V., Lavraud, B., Lewis, W. S., Mukherjee, J., Norgren, C., Phan, T.-D., Russell, C. T., Strangeway, R. J., Torbert, R. B., and Webster, J. M. (2017). Large-scale characteristics of reconnection diffusion regions and associated magnetopause crossings observed by mms. *Journal of Geophysical Research: Space Physics*, 122(5):5466–5486.

Gary, S. P. and Karimabadi, H. (2006). Linear theory of electron temperature anisotropy instabilities: Whistler, mirror, and weibel. *Journal of Geophysical Research: Space Physics*, 111.

Gary, S. P. and Nishimura, K. (2003). Resonant electron firehose instability: Particle-in-cell simulations. *Physics of Plasmas*, 10:3571–3576.

Gary, S. P. and Wang, J. (1996). Whistler instability: Electron anisotropy upper bound. *Journal of Geophysical Research: Space Physics*, 101:10749–10754.

Gershman, D. J., Dorelli, J. C., Viñas, A. F., Avanov, L. A., Gliese, U., Barrie, A. C., Coffey, V., Chandler, M., Dickson, C., MacDonald, E. A., Salo, C., Holland, M., Saito, Y., Sauvaud, J.-A., Lavraud, B., Paterson, W. R., Torbert, R., Chen, L.-J., Goodrich, K., Russell, C. T., Strangeway, R. J., Giles, B. L., Pollock, C. J., Moore, T. E., and Burch, J. L. (2016). Electron dynamics in a subproton-gyroscale magnetic hole. *Geophysical Research Letters*, 43:4112–4118.

Giovanelli, R. G. (1947). Magnetic and Electric Phenomena in the Sun's Atmosphere associated with Sunspots. , 107:338.

Goodrich, K. A., Ergun, R. E., Wilder, F. D., Burch, J., Torbert, R., Khotyaintsev, Y., Lindqvist, P.-A., Russell, C., Strangeway, R., Magnes, W., Gershman, D., Giles, B.,

Nakamura, R., Stawarz, J., Holmes, J., Sturner, A., and Malaspina, D. M. (2016). Mms multipoint electric field observations of small-scale magnetic holes. *Geophysical Research Letters*, 43:5953–5959.

Harvey, C. C. (1998). Spatial Gradients and the Volumetric Tensor. *ISSI Scientific Reports Series*, 1:307–322.

Hasegawa, H., Wang, J., Dunlop, M. W., Pu, Z. Y., Zhang, Q.-H., Lavraud, B., Taylor, M. G. G. T., Constantinescu, O. D., Berchem, J., Angelopoulos, V., McFadden, J. P., Frey, H. U., Panov, E. V., Volwerk, M., and Bogdanova, Y. V. (2010). Evidence for a flux transfer event generated by multiple x-line reconnection at the magnetopause. *Geophysical Research Letters*, 37(16).

Hellinger, P. and Štěpán Štverák (2018). Electron mirror instability: particle-in-cell simulations. *Journal of Plasma Physics*, 84:905840402.

Henderson, P., Owen, C., Alexeev, I., Slavin, J., Fazakerley, A., Lucek, E., and Rème, H. (2006). Cluster observations of flux rope structures in the near-tail. *Annales Geophysicae*, 24.

Hesse, M., Aunai, N., Sibeck, D., and Birn, J. (2014). On the electron diffusion region in planar, asymmetric, systems. *Geophysical Research Letters*, 41(24):8673–8680.

Hones Jr., E. W. (1984). *Plasma Sheet Behavior During Substorms*, pages 178–184. American Geophysical Union (AGU).

Horbury, T. S., Lucek, E. A., Balogh, A., Dandouras, I., and Rème, H. (2004). Motion and orientation of magnetic field dips and peaks in the terrestrial magnetosheath. *Journal of Geophysical Research: Space Physics*, 109.

Hoshino, M. (2005). Electron surfing acceleration in magnetic reconnection. *Journal of Geophysical Research: Space Physics*, 110(A10).

Huang, S. Y., Du, J. W., Sahraoui, F., Yuan, Z. G., He, J. S., Zhao, J. S., Contel, O. L., Breuillard, H., Wang, D. D., Yu, X. D., Deng, X. H., Fu, H. S., Zhou, M., Pollock, C. J., Torbert, R. B., Russell, C. T., and Burch, J. L. (2017). A statistical study of kinetic-size magnetic holes in turbulent magnetosheath: Mms observations. *Journal of Geophysical Research: Space Physics*, 122:8577–8588.

Hudson, H. and Ryan, J. (1995). High-energy particles in solar flares. *Annual Review of Astronomy and Astrophysics*, 33(1):239–282.

Hwang, K.-J., Burch, J. L., Russell, C. T., Choi, E., Dokgo, K., Fear, R. C., Fuselier, S. A., Petrinec, S. M., Sibeck, D. G., Hasegawa, H., Fu, H., Øieroset, M., Escoubet, C. P., Giles, B. L., Khotyaintsev, Y., Graham, D. B., Gershman, D. J., Pollock, C. J., Ergun, R. E., Torbert, R. B., and Broll, J. (2021). Microscale processes determining macroscale evolution of magnetic flux tubes along earth's magnetopause. *The Astrophysical Journal*, 914(1):26.

Hwang, K.-J., Sibeck, D. G., Burch, J. L., Choi, E., Fear, R. C., Lavraud, B., Giles, B. L., Gershman, D., Pollock, C. J., Eastwood, J. P., Khotyaintsev, Y., Escoubet, P., Fu, H., Toledo-Redondo, S., Torbert, R. B., Ergun, R. E., Paterson, W. R., Dorelli, J. C., Avanov, L., Russell, C. T., and Strangeway, R. J. (2018). Small-scale flux transfer events formed in the reconnection exhaust region between two x lines. *Journal of Geophysical Research: Space Physics*, 123(10):8473–8488.

Jasinski, J. M., Slavin, J. A., Arridge, C. S., Poh, G., Jia, X., Sergis, N., Coates, A. J., Jones, G. H., and Waite Jr., J. H. (2016). Flux transfer event observation at saturn's dayside magnetopause by the cassini spacecraft. *Geophysical Research Letters*, 43(13):6713–6723.

Karimabadi, H., Krauss-Varban, D., Omidi, N., and Vu, H. X. (1999). Magnetic structure of the reconnection layer and core field generation in plasmoids. *Journal of Geophysical Research: Space Physics*, 104(A6):12313–12326.

Khotyaintsev, Y. V., Cully, C. M., Vaivads, A., André, M., and Owen, C. J. (2011). Plasma jet braking: Energy dissipation and nonadiabatic electrons. *Phys. Rev. Lett.*, 106:165001.

Kieokaew, R., Lavraud, B., Fargette, N., Marchaudon, A., Génot, V., Jacquey, C., Gershman, D., Giles, B., Torbert, R., and Burch, J. (2020). Statistical relationship between interplanetary magnetic field conditions and the helicity sign of flux transfer event flux ropes. *Earth and Space Science Open Archive*, page 13.

Kivelson, M. G. and Southwood, D. J. (1996). Mirror instability ii: The mechanism of nonlinear saturation. *Journal of Geophysical Research: Space Physics*, 101:17365–17371.

Kuznetsov, E. A., Passot, T., and Sulem, P. L. (2012). On the mirror instability in the presence of electron temperature anisotropy. *Physics of Plasmas*, 19:90701.

Lapenta, G., Berchem, J., Zhou, M., Walker, R. J., El-Alaoui, M., Goldstein, M. L., Paterson, W. R., Giles, B. L., Pollock, C. J., Russell, C. T., Strangeway, R. J., Ergun, R. E., Khotyaintsev, Y. V., Torbert, R. B., and Burch, J. L. (2017). On the origin of the crescent-shaped distributions observed by mms at the magnetopause. *Journal of Geophysical Research: Space Physics*, 122(2):2024–2039.

Lavraud, B., Zhang, Y. C., Vernisse, Y., Gershman, D. J., Dorelli, J., Cassak, P. A., Dargent, J., Pollock, C., Giles, B., Aunai, N., Argall, M., Avanov, L., Barrie, A., Burch, J., Chandler, M., Chen, L.-J., Clark, G., Cohen, I., Coffey, V., Eastwood, J. P., Egedal, J., Eriksson, S., Ergun, R., Farrugia, C. J., Fuselier, S. A., Génot, V., Graham, D., Grigorenko, E., Hasegawa, H., Jacquey, C., Kacem, I., Khotyaintsev, Y., MacDonald, E., Magnes, W., Marchaudon, A., Mauk, B., Moore, T. E., Mukai, T., Nakamura, R., Paterson, W., Penou, E., Phan, T. D., Rager, A., Retino, A., Rong, Z. J., Russell, C. T., Saito, Y., Sauvaud, J.-A., Schwartz, S. J., Shen, C., Smith, S., Strangeway, R., Toledo-Redondo, S., Torbert, R., Turner, D. L., Wang, S., and Yokota, S. (2016).

Currents and associated electron scattering and bouncing near the diffusion region at earth's magnetopause. *Geophysical Research Letters*, 43:3042–3050.

Lee, L. C. and Fu, Z. F. (1985). A theory of magnetic flux transfer at the earth's magnetopause. *Geophysical Research Letters*, 12(2):105–108.

Lin, R. P. (2006). Particle acceleration by the sun: Electrons, hard x-rays/gamma-rays. *Space Science Reviews*, 124:233–248.

Liu, H., Zong, Q.-G., Zhang, H., Xiao, C. J., Shi, Q. Q., Yao, S. T., He, J. S., Zhou, X.-Z., Pollock, C., Sun, W. J., Le, G., Burch, J. L., and Rankin, R. (2019). Mms observations of electron scale magnetic cavity embedded in proton scale magnetic cavity. *Nature Communications*, 10:1040.

Liu, R., Zhang, J., Wang, Y., and Song, H. (2020). *Magnetic Flux Ropes: From the Sun to the Earth and Beyond*. Frontiers Research Topics. Frontiers Media SA.

Lundquist, S. (1950). Magnetohydrostatic fields. *Ark. Fys.*, 2:361–365.

Malyshkin, L. M., Linde, T., and Kulsrud, R. M. (2005). Magnetic reconnection with anomalous resistivity in two-and-a-half dimensions. i. quasistationary case. *Physics of plasmas*, 12(10):102902.

Mandt, M. E., Denton, R. E., and Drake, J. F. (1994). Transition to whistler mediated magnetic reconnection. *Geophysical Research Letters*, 21(1):73–76.

Martin, C. J., Arridge, C. S., Badman, S. V., Russell, C. T., and Wei, H. (2020). Distribution and properties of magnetic flux ropes in titan's ionosphere. *Journal of Geophysical Research: Space Physics*, 125(4):e2019JA027570. e2019JA027570 10.1029/2019JA027570.

Massey, F. J. (1951). The kolmogorov-smirnov test for goodness of fit. *Journal of the American Statistical Association*, 46(253):68–78.

Mauk, B. H., Blake, J. B., Baker, D. N., Clemmons, J. H., Reeves, G. D., Spence, H. E., Jaskulek, S. E., Schlemm, C. E., Brown, L. E., Cooper, S. A., Craft, J. V., Fennell, J. F., Gurnee, R. S., Hammock, C. M., Hayes, J. R., Hill, P. A., Ho, G. C., Hutcheson, J. C., Jacques, A. D., Kerem, S., Mitchell, D. G., Nelson, K. S., Paschalidis, N. P., Rossano, E., Stokes, M. R., and Westlake, J. H. (2016). The energetic particle detector (epd) investigation and the energetic ion spectrometer (eis) for the magnetospheric multiscale (mms) mission. *Space Science Reviews*, 199(1):471–514.

Mejnertsen, L., Eastwood, J. P., and Chittenden, J. P. (2021). Control of magnetopause flux rope topology by non-local reconnection. *Frontiers in Astronomy and Space Sciences*, 8.

Milan, S. E., Lester, M., Cowley, S. W. H., and Brittnacher, M. (2000). Convection and auroral response to a southward turning of the imf: Polar uvi, cutlass, and image signatures of transient magnetic flux transfer at the magnetopause. *Journal of Geophysical Research: Space Physics*, 105(A7):15741–15755.

Modena, A., Najmudin, Z., Dangor, A. E., Clayton, C. E., Marsh, K. A., Joshi, C., Malka, V., Darrow, C. B., Danson, C., Neely, D., and Walsh, F. N. (1995). Electron acceleration from the breaking of relativistic plasma waves. *Nature*, 377(6550):606–608.

Mozer, F. S., Bale, S. D., and Phan, T. D. (2002). Evidence of diffusion regions at a subsolar magnetopause crossing. *Phys. Rev. Lett.*, 89:015002.

Nagai, T., Shinohara, I., Fujimoto, M., Matsuoka, A., Saito, Y., and Mukai, T. (2011). Construction of magnetic reconnection in the near-earth magnetotail with geotail. *Journal of Geophysical Research: Space Physics*, 116(A4).

NASA, Garner, R., and Dunbar, B. (2021). Instruments aboard mms. https://www.nasa.gov/mission$_p ages/mms/spacecraft/mms - instruments.htmlafg. Accessed : 2022 - 03 - 01$.

Øieroset, M., Lin, R. P., Phan, T. D., Larson, D. E., and Bale, S. D. (2002). Evidence for electron acceleration up to ~ 300 keV in the magnetic reconnection diffusion region of earth's magnetotail. *Phys. Rev. Lett.*, 89:195001.

Øieroset, M., Phan, T. D., Eastwood, J. P., Fujimoto, M., Daughton, W., Shay, M. A., Angelopoulos, V., Mozer, F. S., McFadden, J. P., Larson, D. E., and Glassmeier, K.-H. (2011). Direct evidence for a three-dimensional magnetic flux rope flanked by two active magnetic reconnection x lines at earth's magnetopause. *Phys. Rev. Lett.*, 107:165007.

Øieroset, M., Phan, T. D., Fujimoto, M., Lin, R. P., and Lepping, R. P. (2001). In situ detection of collisionless reconnection in the earth's magnetotail. *Nature*, 412(6845):414–417.

Øieroset, M., Phan, T. D., Haggerty, C., Shay, M. A., Eastwood, J. P., Gershman, D. J., Drake, J. F., Fujimoto, M., Ergun, R. E., Mozer, F. S., Oka, M., Torbert, R. B., Burch, J. L., Wang, S., Chen, L. J., Swisdak, M., Pollock, C., Dorelli, J. C., Fuselier, S. A., Lavraud, B., Giles, B. L., Moore, T. E., Saito, Y., Avanov, L. A., Paterson, W., Strangeway, R. J., Russell, C. T., Khotyaintsev, Y., Lindqvist, P. A., and Malakit, K. (2016). Mms observations of large guide field symmetric reconnection between colliding reconnection jets at the center of a magnetic flux rope at the magnetopause. *Geophysical Research Letters*, 43(11):5536–5544.

Oka, M., Birn, J., Battaglia, M., Chaston, C. C., Hatch, S. M., Livadiotis, G., Imada, S., Miyoshi, Y., Kuhar, M., Effenberger, F., Eriksson, E., Khotyaintsev, Y. V., and Retinò, A. (2018). Electron power-law spectra in solar and space plasmas. *Space Science Reviews*, 214:82.

Owen, C. J., Fazakerley, A. N., Carter, P. J., Coates, A. J., Krauklis, I. C., Szita, S., Taylor, M. G. G. T., Travnicek, P., Watson, G., Wilson, R. J., Balogh, A., and Dunlop, M. W. (2001). Cluster PEACE observations of electrons during magnetospheric flux transfer events. *Annales Geophysicae*, 19(10/12):1509–1522.

Owens, M. J. and Forsyth, R. J. (2013). The heliospheric magnetic field. *Living Reviews in Solar Physics*, 10(1):5.

Palmerio, E., Kilpua, E. K. J., Möstl, C., Bothmer, V., James, A. W., Green, L. M., Isavnin, A., Davies, J. A., and Harrison, R. A. (2018). Coronal magnetic structure of earthbound cmes and in situ comparison. *Space Weather*, 16(5):442–460.

Parker, E. N. (1957). Sweet's Mechanism for Merging Magnetic Fields in Conducting Fluids. *jgr*, 62:509–520.

Paschmann, G., Haaland, S. E., Phan, T. D., Sonnerup, B. U. , Burch, J. L., Torbert, R. B., Gershman, D. J., Dorelli, J. C., Giles, B. L., Pollock, C., Saito, Y., Lavraud, B., Russell, C. T., Strangeway, R. J., Baumjohann, W., and Fuselier, S. A. (2018). Large-scale survey of the structure of the dayside magnetopause by mms. *Journal of Geophysical Research: Space Physics*, 123(3):2018–2033.

Paschmann, G., Øieroset, M., and Phan, T. (2014). *In-Situ Observations of Reconnection in Space*, pages 309–341. Springer US, Boston, MA.

Paschmann, G. and Schwartz, S. J. (2000). ISSI Book on Analysis Methods for Multi-Spacecraft Data. In Harris, R. A., editor, *Cluster-II Workshop Multiscale / Multipoint Plasma Measurements*, volume 449 of *ESA Special Publication*, page 99.

Paschmann, G., Sonnerup, B. U. Ö., Papamastorakis, I., Sckopke, N., Haerendel, G., Bame, S. J., Asbridge, J. R., Gosling, J. T., Russell, C. T., and Elphic, R. C. (1979). Plasma acceleration at the earth's magnetopause: evidence for reconnection. *Nature*, 282(5736):243–246.

Petschek, H. E. (1964). Magnetic Field Annihilation. *NASA Special Publication*, 50:425.

Phan, T., Frey, H. U., Frey, S., Peticolas, L., Fuselier, S., Carlson, C., Rème, H., Bosqued, J.-M., Balogh, A., Dunlop, M., Kistler, L., Mouikis, C., Dandouras, I., Sauvaud, J.-A., Mende, S., McFadden, J., Parks, G., Moebius, E., Klecker, B., Paschmann, G.,

Fujimoto, M., Petrinec, S., Marcucci, M. F., Korth, A., and Lundin, R. (2003). Simultaneous cluster and image observations of cusp reconnection and auroral proton spot for northward imf. *Geophysical Research Letters*, 30(10).

Phan, T. D., Drake, J. F., Shay, M. A., Gosling, J. T., Paschmann, G., Eastwood, J. P., Oieroset, M., Fujimoto, M., and Angelopoulos, V. (2014). Ion bulk heating in magnetic reconnection exhausts at earth's magnetopause: Dependence on the inflow alfvén speed and magnetic shear angle. *Geophysical Research Letters*, 41(20):7002–7010.

Phan, T. D., Kistler, L. M., Klecker, B., Haerendel, G., Paschmann, G., Sonnerup, B. U. Ö., Baumjohann, W., Bavassano-Cattaneo, M. B., Carlson, C. W., DiLellis, A. M., Fornacon, K. H., Frank, L. A., Fujimoto, M., Georgescu, E., Kokubun, S., Moebius, E., Mukai, T., Øieroset, M., Paterson, W. R., and Reme, H. (2000). Extended magnetic reconnection at the earth's magnetopause from detection of bi-directional jets. *Nature*, 404(6780):848–850.

Phan, T. D., Shay, M. A., Eastwood, J. P., Angelopoulos, V., Oieroset, M., Oka, M., and Fujimoto, M. (2016). Establishing the context for reconnection diffusion region encounters and strategies for the capture and transmission of diffusion region burst data by mms. *Space Science Reviews*, 199(1):631–650.

Phan, T. D., Shay, M. A., Gosling, J. T., Fujimoto, M., Drake, J. F., Paschmann, G., Oieroset, M., Eastwood, J. P., and Angelopoulos, V. (2013). Electron bulk heating in magnetic reconnection at earth's magnetopause: Dependence on the inflow alfvén speed and magnetic shear. *Geophysical Research Letters*, 40(17):4475–4480.

Pollock, C., Moore, T., Jacques, A., Burch, J., Gliese, U., Saito, Y., Omoto, T., Avanov, L., Barrie, A., Coffey, V., Dorelli, J., Gershman, D., Giles, B., Rosnack, T., Salo, C., Yokota, S., Adrian, M., Aoustin, C., Auletti, C., Aung, S., Bigio, V., Cao, N., Chandler, M., Chornay, D., Christian, K., Clark, G., Collinson, G., Corris, T., De Los Santos, A., Devlin, R., Diaz, T., Dickerson, T., Dickson, C., Diekmann, A., Diggs, F., Duncan,

C., Figueroa-Vinas, A., Firman, C., Freeman, M., Galassi, N., Garcia, K., Goodhart, G., Guererro, D., Hageman, J., Hanley, J., Hemminger, E., Holland, M., Hutchins, M., James, T., Jones, W., Kreisler, S., Kujawski, J., Lavu, V., Lobell, J., LeCompte, E., Lukemire, A., MacDonald, E., Mariano, A., Mukai, T., Narayanan, K., Nguyan, Q., Onizuka, M., Paterson, W., Persyn, S., Piepgrass, B., Cheney, F., Rager, A., Raghuram, T., Ramil, A., Reichenthal, L., Rodriguez, H., Rouzaud, J., Rucker, A., Saito, Y., Samara, M., Sauvaud, J.-A., Schuster, D., Shappirio, M., Shelton, K., Sher, D., Smith, D., Smith, K., Smith, S., Steinfeld, D., Szymkiewicz, R., Tanimoto, K., Taylor, J., Tucker, C., Tull, K., Uhl, A., Vloet, J., Walpole, P., Weidner, S., White, D., Winkert, G., Yeh, P.-S., and Zeuch, M. (2016). Fast plasma investigation for magnetospheric multiscale. *Space Science Reviews*, 199(1):331–406.

Pu, Z. Y., Raeder, J., Zhong, J., Bogdanova, Y. V., Dunlop, M., Xiao, C. J., Wang, X. G., and Fazakerley, A. (2013). Magnetic topologies of an in vivo fte observed by double star/tc-1 at earth's magnetopause. *Geophysical Research Letters*, 40(14):3502–3506.

Raab, W., Branduardi-Raymont, G., Wang, C., Dai, L., Donovan, E., Enno, G., Escoubet, P., Holland, A., Jing, L., Kataria, D., Li, L., Read, A., Rebuffat, D., Romstedt, J., Runciman, C., Sembay, S., Spanswick, E., Sykes, J., Thornhill, J., and Zheng, J. (2016). Smile: A joint esa/cas mission to investigate the interaction between the solar wind and earth's magnetosphere. page 990503.

Raeder, J. (2006). Flux Transfer Events: 1. generation mechanism for strong southward IMF. *Annales Geophysicae*, 24(1):381–392.

Rijnbeek, R., Cowley, S., Southwood, D., and Russell, C. (1984). A survey of dayside flux transfer events observed by isee 1 and 2 magnetometers. *Journal of Geophysical Research: Space Physics*, 89(A2):786–800.

Robertson, S. L., Eastwood, J. P., Stawarz, J. E., Hietala, H., Phan, T. D., Lavraud, B., Burch, J. L., Giles, B., Gershman, D. J., Torbert, R., Lindqvist, P.-A., Ergun, R. E.,

Russell, C. T., and Strangeway, R. J. (2021). Electron trapping in magnetic mirror structures at the edge of magnetopause flux ropes. *Journal of Geophysical Research: Space Physics*, 126(4):e2021JA029182.

Russell, C. T. (1978). The ISEE 1 and 2 Fluxgate magnetometers. *IEEE Transactions on Geoscience Electronics*, 16:239–242.

Russell, C. T. and Elphic, R. C. (1978). Initial isee magnetometer results: magnetopause observations. *Space Science Reviews*, 22(6):681–715.

Russell, C. T. and Qi, Y. (2020). Flux ropes are born in pairs: An outcome of interlinked, reconnecting flux tubes. *Earth and Space Science Open Archive*, page 11.

Scholer, M. (1988). Magnetic flux transfer at the magnetopause based on single x line bursty reconnection. *Geophysical Research Letters*, 15(4):291–294.

Shay, M. A., Drake, J. F., Denton, R. E., and Biskamp, D. (1998). Structure of the dissipation region during collisionless magnetic reconnection. *Journal of Geophysical Research: Space Physics*, 103(A5):9165–9176.

Shuster, J. R., Gershman, D. J., Chen, L.-J., Wang, S., Bessho, N., Dorelli, J. C., da Silva, D. E., Giles, B. L., Paterson, W. R., Denton, R. E., Schwartz, S. J., Norgren, C., Wilder, F. D., Cassak, P. A., Swisdak, M., Uritsky, V., Schiff, C., Rager, A. C., Smith, S., Avanov, L. A., and Viñas, A. F. (2019). Mms measurements of the vlasov equation: Probing the electron pressure divergence within thin current sheets. *Geophysical Research Letters*, 46(14):7862–7872.

Sonnerup, B. t. (1979). Magnetic field reconnection. *Solar system plasma physics*, pages 45–108.

Sonnerup, B. U. (1974). The reconnecting magnetosphere. In McCormac, B., editor, *Magnetospheric Physics*, pages 23–33. vol 44, Springer, Dordrecht. **URL:** *https://doi.org/10.1007/978-94-010-2214-92*.

Sonnerup, B. U. and Scheible, M. (1998). Minimum and maximum variance analysis. *Analysis methods for multi-spacecraft data*, pages 185–220.

Sonnerup, B. U. Ö., Hasegawa, H., and Paschmann, G. (2004). Anatomy of a flux transfer event seen by cluster. *Geophysical Research Letters*, 31(11).

Southwood, D., Farrugia, C., and Saunders, M. (1988). What are flux transfer events? *Planetary and Space Science*, 36(5):503 – 508.

Southwood, D. J. and Kivelson, M. G. (1993). Mirror instability: 1. physical mechanism of linear instability. *Journal of Geophysical Research: Space Physics*, 98:9181–9187.

Stawarz, J. E., Eastwood, J. P., Genestreti, K. J., Nakamura, R., Ergun, R. E., Burgess, D., Burch, J. L., Fuselier, S. A., Gershman, D. J., Giles, B. L., Le Contel, O., Lindqvist, P.-A., Russell, C. T., and Torbert, R. B. (2018). Intense electric fields and electron-scale substructure within magnetotail flux ropes as revealed by the magnetospheric multiscale mission. *Geophysical Research Letters*, 45(17):8783–8792.

Sweet, P. A. (1958). The Neutral Point Theory of Solar Flares. In Lehnert, B., editor, *Electromagnetic Phenomena in Cosmical Physics*, volume 6 of *IAU Symposium*, page 123.

Taylor, M. G. G. T., Reeves, G. D., Friedel, R. H. W., Thomsen, M. F., Elphic, R. C., Davies, J. A., Dunlop, M. W., Laakso, H., Lavraud, B., Baker, D. N., Slavin, J. A., Perry, C. H., Escoubet, C. P., Masson, A., Opgenoorth, H. J., Vallat, C., Daly, P. W., Fazakerley, A. N., and Lucek, E. A. (2006). Cluster encounter with an energetic electron beam during a substorm. *Journal of Geophysical Research: Space Physics*, 111(A11).

Teh, W.-L., Denton, R. E., Sonnerup, B. U. Ö., and Pollock, C. (2017). Mms observations of oblique small-scale magnetopause flux ropes near the ion diffusion region during weak guide-field reconnection. *Geophysical Research Letters*, 44(13):6517–6524.

Thomsen, M. F., Stansberry, J. A., Bame, S. J., Fuselier, S. A., and Gosling, J. T. (1987). Ion and electron velocity distributions within flux transfer events. *Journal of Geophysical Research: Space Physics*, 92(A11):12127–12136.

Torbert, R. B., Russell, C. T., Magnes, W., Ergun, R. E., Lindqvist, P.-A., LeContel, O., Vaith, H., Macri, J., Myers, S., Rau, D., Needell, J., King, B., Granoff, M., Chutter, M., Dors, I., Olsson, G., Khotyaintsev, Y. V., Eriksson, A., Kletzing, C. A., Bounds, S., Anderson, B., Baumjohann, W., Steller, M., Bromund, K., Le, G., Nakamura, R., Strangeway, R. J., Leinweber, H. K., Tucker, S., Westfall, J., Fischer, D., Plaschke, F., Porter, J., and Lappalainen, K. (2016). The fields instrument suite on mms: Scientific objectives, measurements, and data products. *Space Science Reviews*, 199(1):105–135.

Trattner, K., Mulcock, J., Petrinec, S., and Fuselier, S. (2007a). Probing the boundary between antiparallel and component reconnection during southward interplanetary magnetic field conditions. *Journal of Geophysical Research: Space Physics*, 112(A8).

Trattner, K. J., Mulcock, J. S., Petrinec, S. M., and Fuselier, S. A. (2007b). Location of the reconnection line at the magnetopause during southward imf conditions. *Geophysical Research Letters*, 34(3).

Trattner, K. J., Petrinec, S. M., Fuselier, S. A., and Phan, T. D. (2012). The location of reconnection at the magnetopause: Testing the maximum magnetic shear model with themis observations. *Journal of Geophysical Research: Space Physics*, 117(A1).

Vaivads, A., Khotyaintsev, Y., André, M., Retinò, A., Buchert, S. C., Rogers, B. N., Décréau, P., Paschmann, G., and Phan, T. D. (2004). Structure of the magnetic reconnection diffusion region from four-spacecraft observations. *Phys. Rev. Lett.*, 93:105001.

Varsani, A., Owen, C. J., Fazakerley, A. N., Forsyth, C., Walsh, A. P., André, M., Dandouras, I., and Carr, C. M. (2014). Cluster observations of the substructure of a flux transfer event: analysis of high-time-resolution particle data. *Annales Geophysicae*, 32(9):1093–1117.

Wang, Y. L., Elphic, R. C., Lavraud, B., Taylor, M. G. G. T., Birn, J., Raeder, J., Russell, C. T., Kawano, H., Zong, Q.-G., Zhang, H., Zhang, X. X., and Friedel, R. H. (2005). Initial results of high-latitude magnetopause and low-latitude flank flux transfer events from 3 years of cluster observations. *Journal of Geophysical Research: Space Physics*, 110(A11).

Webster, J. M., Burch, J. L., Reiff, P. H., Daou, A. G., Genestreti, K. J., Graham, D. B., Torbert, R. B., Ergun, R. E., Sazykin, S. Y., Marshall, A., Allen, R. C., Chen, L.-J., Wang, S., Phan, T. D., Giles, B. L., Moore, T. E., Fuselier, S. A., Cozzani, G., Russell, C. T., Eriksson, S., Rager, A. C., Broll, J. M., Goodrich, K., and Wilder, F. (2018). Magnetospheric multiscale dayside reconnection electron diffusion region events. *Journal of Geophysical Research: Space Physics*, 123(6):4858–4878.

Xiao, C. J., Pu, Z. Y., Ma, Z. W., Fu, S. Y., Huang, Z. Y., and Zong, Q. G. (2004). Inferring of flux rope orientation with the minimum variance analysis technique. *Journal of Geophysical Research: Space Physics*, 109(A11).

Yamada, M., Chen, L. J., Yoo, J., Wang, S., Fox, W., Jara-Almonte, J., Ji, H., Daughton, W., Le, A., Burch, J., Giles, B., Hesse, M., Moore, T., and Torbert, R. (2018). The two-fluid dynamics and energetics of the asymmetric magnetic reconnection in laboratory and space plasmas. *Nature Communications*, 9(1):5223.

Yao, S. T., Shi, Q. Q., Liu, J., Yao, Z. H., Guo, R. L., Ahmadi, N., Degeling, A. W., Zong, Q. G., Wang, X. G., Tian, A. M., Russell, C. T., Fu, H. S., Pu, Z. Y., Fu, S. Y., Zhang, H., Sun, W. J., Li, L., Xiao, C. J., Feng, Y. Y., and Giles, B. L. (2018). Electron dynamics in magnetosheath mirror-mode structures. *Journal of Geophysical Research: Space Physics*, 123:5561–5570.

Yao, S. T., Wang, X. G., Shi, Q. Q., Pitkänen, T., Hamrin, M., Yao, Z. H., Li, Z. Y., Ji, X. F., Spiegeleer, A. D., Xiao, Y. C., Tian, A. M., Pu, Z. Y., Zong, Q. G., Xiao, C. J., Fu, S. Y., Zhang, H., Russell, C. T., Giles, B. L., Guo, R. L., Sun, W. J., Li, W. Y.,

Zhou, X. Z., Huang, S. Y., Vaverka, J., Nowada, M., Bai, S. C., Wang, M. M., and Liu, J. (2017). Observations of kinetic-size magnetic holes in the magnetosheath. *Journal of Geophysical Research: Space Physics*, 122:1990–2000.

Young, D. T., Burch, J. L., Gomez, R. G., De Los Santos, A., Miller, G. P., Wilson, P., Paschalidis, N., Fuselier, S. A., Pickens, K., Hertzberg, E., Pollock, C. J., Scherrer, J., Wood, P. B., Donald, E. T., Aaron, D., Furman, J., George, D., Gurnee, R. S., Hourani, R. S., Jacques, A., Johnson, T., Orr, T., Pan, K. S., Persyn, S., Pope, S., Roberts, J., Stokes, M. R., Trattner, K. J., and Webster, J. M. (2016). Hot plasma composition analyzer for the magnetospheric multiscale mission. *Space Science Reviews*, 199(1):407–470.

Zenitani, S., Hesse, M., Klimas, A., and Kuznetsova, M. (2011). New measure of the dissipation region in collisionless magnetic reconnection. *Phys. Rev. Lett.*, 106:195003.

Zhao, C., Russell, C. T., Strangeway, R. J., Petrinec, S. M., Paterson, W. R., Zhou, M., Anderson, B. J., Baumjohann, W., Bromund, K. R., Chutter, M., Fischer, D., Le, G., Nakamura, R., Plaschke, F., Slavin, J. A., Torbert, R. B., and Wei, H. Y. (2016). Force balance at the magnetopause determined with mms: Application to flux transfer events. *Geophysical Research Letters*, 43(23):11,941–11,947.

Zhong, Z. H., Zhou, M., Huang, S. Y., Tang, R. X., Deng, X. H., Pang, Y., and Chen, H. T. (2019). Observations of a kinetic-scale magnetic hole in a reconnection diffusion region. *Geophysical Research Letters*, 46:6248–6257.

Zhu, C., Zhang, H., Fu, S., Ni, B., Strangeway, R. J., Giles, B. L., Wan, W., Liu, L., Chen, Y., and Le, H. (2019). Trapped and accelerated electrons within a magnetic mirror behind a flux rope on the magnetopause. *Journal of Geophysical Research: Space Physics*, 124:3993–4008.

Øieroset, M., Phan, T. D., Drake, J. F., Eastwood, J. P., Fuselier, S. A., Strangeway, R. J., Haggerty, C., Shay, M. A., Oka, M., Wang, S., Chen, L.-J., Kacem, I., Lavraud,

B., Angelopoulos, V., Burch, J. L., Torbert, R. B., Ergun, R. E., Khotyaintsev, Y., Lindqvist, P. A., Gershman, D. J., Giles, B. L., Pollock, C., Moore, T. E., Russell, C. T., Saito, Y., Avanov, L. A., and Paterson, W. (2019). Reconnection with magnetic flux pileup at the interface of converging jets at the magnetopause. *Geophysical Research Letters*, 46(4):1937–1946.

Štverák, , Trávníček, P., Maksimovic, M., Marsch, E., Fazakerley, A. N., and Scime, E. E. (2008). Electron temperature anisotropy constraints in the solar wind. *Journal of Geophysical Research: Space Physics*, 113.

Appendix A

Flux Rope Data

Below we list the flux rope data from the 245 flux ropes analysed in this thesis, including:

- The index of the flux rope from the original 491 identified flux rope candidates, sometimes noted at the top of plots in this thesis.
- The start and end times of the observed flux ropes as IDL strings.
- The start and end times in seconds from epoch.
- Time to the closest observed EDR in seconds.
- The calculated axial magnetic field component and ion velocity used for the simple estimates for the flux rope radius.
- The identified topology of the flux ropes.
- The calculated force-free fit parameters, noted with the subscript ff, including: axial magnetic field strength, radius, RMS error, impact parameter and helicity.

	index	start	end	start [seconds]	end [seconds]
0	4	2015-9-19/7:43:0	2015-9-19/7:43:3	1442648580.65899	1442648580.65899
1	9	2015-10-16/9:44:11	2015-10-16/9:44:20	1444988652.31999	1444988652.31999
2	10	2015-10-16/10:26:11	2015-10-16/10:26:14	1444991171.473	1444991171.473
3	11	2015-10-16/10:30:15	2015-10-16/10:30:24	1444991415.43	1444991415.43
4	13	2015-10-16/10:33:29	2015-10-16/10:33:32	1444991609.496	1444991609.496
5	14	2015-10-16/10:33:46	2015-10-16/10:33:51	1444991627.477	1444991627.477
6	16	2015-10-16/10:34:37	2015-10-16/10:34:39	1444991677.96	1444991677.96
7	22	2015-10-16/11:38:56	2015-10-16/11:39:3	1444995536.963	1444995536.963
8	24	2015-10-16/13:4:32	2015-10-16/13:4:37	1445000672.404	1445000672.404
9	25	2015-10-16/13:7:28	2015-10-16/13:7:31	1445000848.10599	1445000848.10599
10	30	2015-10-22/6:6:0	2015-10-22/6:6:5	1445493961.14299	1445493961.14299
11	31	2015-10-22/14:45:8	2015-10-22/14:45:12	1445525109.803	1445525109.803
12	32	2015-10-22/15:7:11	2015-10-22/15:7:14	1445526431.68899	1445526431.68899
13	33	2015-10-22/15:7:55	2015-10-22/15:7:59	1445526475.056	1445526475.056
14	37	2015-10-22/15:9:41	2015-10-22/15:9:45	1445526582.21199	1445526582.21199
15	39	2015-10-22/15:10:23	2015-10-22/15:10:27	1445526624.03	1445526624.03
16	40	2015-10-22/15:11:16	2015-10-22/15:11:20	1445526677.253	1445526677.253
17	42	2015-10-22/15:17:24	2015-10-22/15:17:29	1445527045.38299	1445527045.38299
18	47	2015-10-22/15:25:56	2015-10-22/15:25:59	1445527556.56399	1445527556.56399
19	48	2015-10-22/15:26:0	2015-10-22/15:26:6	1445527560.25799	1445527560.25799
20	51	2015-10-22/15:40:35	2015-10-22/15:40:44	1445528435.97	1445528435.97
21	53	2015-10-22/15:46:35	2015-10-22/15:46:37	1445528795.47199	1445528795.47199
22	54	2015-10-22/15:50:1	2015-10-22/15:50:3	1445529001.586	1445529001.586
23	56	2015-11-1/3:35:53	2015-11-1/3:35:55	1446348953.63899	1446348953.63899
24	57	2015-11-1/3:36:18	2015-11-1/3:36:23	1446348980.184	1446348980.184
25	58	2015-11-1/3:36:21	2015-11-1/3:36:25	1446348982.13599	1446348982.13599
26	59	2015-11-1/3:37:30	2015-11-1/3:37:39	1446349051.81999	1446349051.81999
27	60	2015-11-1/3:37:50	2015-11-1/3:37:54	1446349071.19199	1446349071.19199
28	61	2015-11-1/3:37:55	2015-11-1/3:37:59	1446349076.303	1446349076.303
29	63	2015-11-1/3:39:22	2015-11-1/3:39:25	1446349162.549	1446349162.549
30	64	2015-11-1/3:39:36	2015-11-1/3:39:41	1446349176.24	1446349176.24
31	66	2015-11-1/3:40:30	2015-11-1/3:40:44	1446349234.60999	1446349234.60999
32	67	2015-11-1/3:40:45	2015-11-1/3:40:50	1446349246.982	1446349246.982
33	69	2015-11-1/8:41:13	2015-11-1/8:41:20	1446367275.404	1446367275.404
34	71	2015-11-1/14:57:10	2015-11-1/14:57:14	1446389830.84299	1446389830.84299
35	73	2015-11-1/15:2:0	2015-11-1/15:2:5	1446390120.20199	1446390120.20199
36	74	2015-11-1/15:2:50	2015-11-1/15:2:54	1446390171.035	1446390171.035
37	78	2015-11-1/15:6:6	2015-11-1/15:6:14	1446390366.9	1446390366.9
38	79	2015-11-1/15:6:53	2015-11-1/15:6:55	1446390414.068	1446390414.068
39	89	2015-11-1/15:15:54	2015-11-1/15:15:56	1446390954.59299	1446390954.59299
40	91	2015-11-1/15:16:37	2015-11-1/15:16:43	1446390998.48499	1446390998.48499
41	93	2015-11-1/15:17:18	2015-11-1/15:17:27	1446391039.23	1446391039.23
42	94	2015-11-1/15:17:53	2015-11-1/15:17:55	1446391074.068	1446391074.068
43	97	2015-11-1/15:18:25	2015-11-1/15:18:29	1446391106.545	1446391106.545
44	104	2015-11-12/6:6:17	2015-11-12/6:6:24	1447308377.362	1447308377.362
45	105	2015-11-12/6:7:48	2015-11-12/6:7:57	1447308470.74	1447308470.74
46	107	2015-11-12/6:33:4	2015-11-12/6:33:13	1447309985.02	1447309985.02
47	109	2015-11-12/6:40:56	2015-11-12/6:41:3	1447310456.80399	1447310456.80399
48	110	2015-11-12/6:41:5	2015-11-12/6:41:13	1447310465.60999	1447310465.60999
49	112	2015-11-12/7:6:1	2015-11-12/7:6:7	1447311962.40899	1447311962.40899

	index	start	end	start [seconds]	end [seconds]
50	113	2015-11-12/7:20:18	2015-11-12/7:20:35	1447312820.35999	1447312820.35999
51	114	2015-12-6/0:25:1	2015-12-6/0:25:5	1449361502.152	1449361502.152
52	115	2015-12-6/0:25:8	2015-12-6/0:25:12	1449361509.62599	1449361509.62599
53	130	2015-12-6/4:14:57	2015-12-6/4:15:0	1449375297.72	1449375297.72
54	133	2015-12-6/4:20:25	2015-12-6/4:20:29	1449375626.14599	1449375626.14599
55	134	2015-12-6/4:57:14	2015-12-6/4:57:20	1449377835.152	1449377835.152
56	136	2015-12-6/23:38:27	2015-12-6/23:38:33	1449445108.90899	1449445108.90899
57	139	2015-12-6/23:47:47	2015-12-6/23:47:53	1449445668.08299	1449445668.08299
58	142	2015-12-8/0:8:9	2015-12-8/0:8:14	1449533290.408	1449533290.408
59	143	2015-12-8/1:24:40	2015-12-8/1:25:0	1449537885.57999	1449537885.57999
60	145	2015-12-8/8:2:57	2015-12-8/8:3:15	1449561777.95	1449561777.95
61	151	2015-12-8/9:56:40	2015-12-8/9:56:45	1449568600.562	1449568600.562
62	153	2015-12-8/10:21:13	2015-12-8/10:21:30	1449570075.88	1449570075.88
63	154	2015-12-8/10:30:7	2015-12-8/10:30:19	1449570608.34999	1449570608.34999
64	157	2015-12-8/11:2:56	2015-12-8/11:3:0	1449572578.39899	1449572578.39899
65	160	2015-12-8/11:20:15	2015-12-8/11:20:24	1449573616.10999	1449573616.10999
66	161	2015-12-8/11:20:31	2015-12-8/11:20:38	1449573632.237	1449573632.237
67	166	2015-12-8/11:34:5	2015-12-8/11:34:10	1449574446.559	1449574446.559
68	170	2015-12-8/11:47:15	2015-12-8/11:47:20	1449575236.14299	1449575236.14299
69	172	2015-12-9/0:52:36	2015-12-9/0:52:41	1449622357.288	1449622357.288
70	174	2015-12-9/0:53:6	2015-12-9/0:53:10	1449622387.227	1449622387.227
71	175	2015-12-9/0:53:15	2015-12-9/0:53:19	1449622395.66199	1449622395.66199
72	176	2015-12-9/0:53:52	2015-12-9/0:53:56	1449622433.747	1449622433.747
73	177	2015-12-9/0:53:56	2015-12-9/0:54:0	1449622437.848	1449622437.848
74	178	2015-12-9/1:0:14	2015-12-9/1:0:24	1449622816.92	1449622816.92
75	179	2015-12-9/1:0:26	2015-12-9/1:0:35	1449622828.57999	1449622828.57999
76	180	2015-12-9/1:1:27	2015-12-9/1:1:32	1449622888.84999	1449622888.84999
77	181	2015-12-9/1:1:35	2015-12-9/1:1:40	1449622897.039	1449622897.039
78	182	2015-12-9/1:1:40	2015-12-9/1:1:44	1449622900.60599	1449622900.60599
79	183	2015-12-9/1:1:42	2015-12-9/1:1:49	1449622903.025	1449622903.025
80	184	2015-12-9/1:1:47	2015-12-9/1:1:52	1449622908.604	1449622908.604
81	185	2015-12-9/1:2:3	2015-12-9/1:2:9	1449622923.848	1449622923.848
82	186	2015-12-9/1:6:13	2015-12-9/1:6:19	1449623173.848	1449623173.848
83	191	2015-12-9/10:48:50	2015-12-9/10:48:58	1449658132.3	1449658132.3
84	195	2015-12-9/23:51:40	2015-12-9/23:51:49	1449705100.2	1449705100.2
85	196	2015-12-9/23:51:48	2015-12-9/23:14:52	1449705109.301	1449705109.301
86	197	2015-12-9/23:52:3	2015-12-9/23:52:9	1449705123.576	1449705123.576
87	198	2015-12-9/23:53:27	2015-12-9/23:53:35	1449705209.57999	1449705209.57999
88	199	2015-12-14/0:58:36	2015-12-14/0:58:40	1450054718.677	1450054718.677
89	200	2015-12-14/0:58:48	2015-12-14/0:58:52	1450054729.773	1450054729.773
90	201	2015-12-14/0:58:56	2015-12-14/0:59:4	1450054737.2	1450054737.2
91	205	2015-12-14/1:20:27	2015-12-14/1:20:33	1450056028.83299	1450056028.83299
92	206	2015-12-14/1:20:37	2015-12-14/1:29:43	1450056038.515	1450056038.515
93	208	2015-12-14/5:32:45	2015-12-14/5:33:0	1450071166.56999	1450071166.56999
94	211	2015-12-14/6:1:20	2015-12-14/6:1:26	1450072881.492	1450072881.492
95	213	2015-12-14/7:56:41	2015-12-14/7:56:47	1450079802.37899	1450079802.37899
96	214	2015-12-14/7:59:26	2015-12-14/7:59:36	1450079967.69	1450079967.69
97	218	2015-12-14/10:9:5	2015-12-14/10:9:14	1450087747.13	1450087747.13
98	219	2015-12-14/12:9:25	2015-12-14/12:9:30	1450094967.361	1450094967.361
99	220	2015-12-14/12:9:28	2015-12-14/12:9:34	1450094969.924	1450094969.924

	index	start	end	start [seconds]	end [seconds]
100	221	2016-1-7/6:13:23	2016-1-7/6:13:28	1452147203.99099	1452147203.99099
101	224	2016-1-7/8:59:57	2016-1-7/9:0:3	1452157198.87899	1452157198.87899
102	225	2016-1-7/9:3:20	2016-1-7/9:3:27	1452157402.457	1452157402.457
103	227	2016-1-7/9:13:16	2016-1-7/9:13:23	1452157997.927	1452157997.927
104	228	2016-1-7/9:23:5	2016-1-7/9:23:8	1452158586.15899	1452158586.15899
105	231	2016-1-7/22:11:38	2016-1-7/22:11:44	1452204699.697	1452204699.697
106	241	2016-1-10/1:25:41	2016-1-10/1:25:46	1452389141.802	1452389141.802
107	242	2016-1-10/1:38:51	2016-1-10/1:38:53	1452389931.79	1452389931.79
108	243	2016-1-10/1:39:5	2016-1-10/1:39:9	1452389946.424	1452389946.424
109	244	2016-1-10/8:57:3	2016-1-10/8:57:8	1452416224.092	1452416224.092
110	245	2016-1-10/8:59:12	2016-1-10/8:59:17	1452416353.14299	1452416353.14299
111	246	2016-1-10/8:59:49	2016-1-10/8:59:53	1452416390.03	1452416390.03
112	247	2016-1-10/9:0:35	2016-1-10/9:0:44	1452416437.64	1452416437.64
113	248	2016-1-10/9:1:3	2016-1-10/9:1:7	1452416464.596	1452416464.596
114	249	2016-1-10/9:1:13	2016-1-10/9:1:24	1452416475.89	1452416475.89
115	250	2016-1-10/9:5:2	2016-1-10/9:5:17	1452416703.23	1452416703.23
116	251	2016-1-10/9:8:43	2016-1-10/9:8:50	1452416925.033	1452416925.033
117	252	2016-1-10/9:9:39	2016-1-10/9:9:43	1452416979.72199	1452416979.72199
118	254	2016-1-10/9:9:45	2016-1-10/9:9:49	1452416985.753	1452416985.753
119	257	2016-1-10/9:13:31	2016-1-10/9:13:34	1452417212.515	1452417212.515
120	260	2016-1-10/20:58:24	2016-1-10/20:58:27	1452459505.121	1452459505.121
121	261	2016-1-10/20:58:33	2016-1-10/20:58:35	1452459514.043	1452459514.043
122	264	2016-1-10/22:8:56	2016-1-10/22:9:3	1452463737.061	1452463737.061
123	265	2016-1-10/22:9:54	2016-1-10/22:9:56	1452463794.828	1452463794.828
124	266	2016-1-10/22:16:53	2016-1-10/22:16:56	1452464213.98499	1452464213.98499
125	267	2016-1-10/22:16:55	2016-1-10/22:16:58	1452464216.28399	1452464216.28399
126	270	2016-2-7/1:4:23	2016-2-7/1:4:28	1454807064.16199	1454807064.16199
127	271	2016-2-7/1:4:26	2016-2-7/1:4:37	1454807067.34999	1454807067.34999
128	273	2016-2-7/3:43:19	2016-2-7/3:43:27	1454816600.54	1454816600.54
129	274	2016-2-7/19:26:20	2016-2-7/19:26:27	1454873181.821	1454873181.821
130	275	2016-2-7/19:26:26	2016-2-7/19:26:31	1454873186.802	1454873186.802
131	277	2016-2-7/20:32:5	2016-2-7/20:32:10	1454877126.282	1454877126.282
132	279	2016-2-7/21:52:34	2016-2-7/21:35:38	1454881955.49499	1454881955.49499
133	280	2016-10-22/10:9:35	2016-10-22/10:9:39	1477130976.12599	1477130976.12599
134	282	2016-10-22/13:11:6	2016-10-22/13:11:14	1477141868.98	1477141868.98
135	284	2016-10-22/17:41:40	2016-10-22/17:41:48	1477158101.53	1477158101.53
136	285	2016-10-22/17:52:12	2016-10-22/17:52:17	1477158732.75099	1477158732.75099
137	291	2016-11-2/11:22:34	2016-11-2/11:22:39	1478085755.578	1478085755.578
138	292	2016-11-2/11:28:21	2016-11-2/11:28:26	1478086102.77399	1478086102.77399
139	294	2016-11-6/8:43:4	2016-11-6/8:43:11	1478421786.289	1478421786.289
140	295	2016-11-6/8:44:4	2016-11-6/8:44:8	1478421844.596	1478421844.596
141	297	2016-11-6/8:45:52	2016-11-6/8:46:4	1478421954.41	1478421954.41
142	299	2016-11-6/9:6:39	2016-11-6/9:6:34	1478423200.66	1478423200.66
143	300	2016-11-6/9:6:44	2016-11-6/9:6:47	1478423204.742	1478423204.742
144	301	2016-11-6/9:6:49	2016-11-6/9:6:53	1478423210.177	1478423210.177
145	303	2016-11-6/9:15:9	2016-11-6/9:15:13	1478423709.97499	1478423709.97499
146	308	2016-11-6/14:21:57	2016-11-6/14:22:0	1478442118.13599	1478442118.13599
147	309	2016-11-6/16:18:15	2016-11-6/16:18:20	1478449096.83699	1478449096.83699
148	312	2016-11-6/16:34:36	2016-11-6/16:34:42	1478450077.614	1478450077.614
149	314	2016-11-12/9:12:12	2016-11-12/9:12:15	1478941933.045	1478941933.045

	index	start	end	start [seconds]	end [seconds]
150	315	2016-11-12/9:12:37	2016-11-12/9:12:40	1478941958.08699	1478941958.08699
151	317	2016-11-12/9:14:19	2016-11-12/9:14:23	1478942060.26799	1478942060.26799
152	318	2016-11-12/11:41:40	2016-11-12/11:41:46	1478950902.848	1478950902.848
153	320	2016-11-12/15:58:54	2016-11-12/15:59:0	1478966335.492	1478966335.492
154	321	2016-11-12/15:59:20	2016-11-12/15:59:25	1478966360.227	1478966360.227
155	324	2016-11-12/18:14:4	2016-11-12/18:14:9	1478974445.572	1478974445.572
156	329	2016-11-13/8:21:38	2016-11-13/8:21:50	1479025300.39	1479025300.39
157	330	2016-11-13/9:3:28	2016-11-13/9:3:32	1479027809.237	1479027809.237
158	331	2016-11-13/9:35:46	2016-11-13/9:35:50	1479029748.611	1479029748.611
159	332	2016-11-13/9:36:37	2016-11-13/9:36:42	1479029799.229	1479029799.229
160	333	2016-11-13/13:43:31	2016-11-13/13:43:37	1479044612.523	1479044612.523
161	334	2016-11-13/13:48:46	2016-11-13/13:48:51	1479044928.216	1479044928.216
162	337	2016-11-13/14:55:2	2016-11-13/14:55:13	1479048905.78	1479048905.78
163	340	2016-11-23/7:9:17	2016-11-23/7:9:22	1479884958.99499	1479884958.99499
164	341	2016-11-23/7:13:46	2016-11-23/7:13:52	1479885228.144	1479885228.144
165	342	2016-11-23/7:13:57	2016-11-23/7:14:1	1479885238.535	1479885238.535
166	343	2016-11-23/7:15:52	2016-11-23/7:15:57	1479885353.52099	1479885353.52099
167	344	2016-11-23/7:16:1	2016-11-23/7:16:4	1479885361.826	1479885361.826
168	350	2016-11-23/7:49:2	2016-11-23/7:49:6	1479887343.19199	1479887343.19199
169	351	2016-11-23/7:49:33	2016-11-23/7:49:40	1479887377.08299	1479887377.08299
170	352	2016-11-23/7:50:34	2016-11-23/7:50:37	1479887435.443	1479887435.443
171	356	2016-11-23/9:40:38	2016-11-23/9:40:43	1479894039.54699	1479894039.54699
172	357	2016-11-23/9:43:21	2016-11-23/9:43:27	1479894202.644	1479894202.644
173	358	2016-11-23/9:43:27	2016-11-23/9:43:35	1479894209.24	1479894209.24
174	359	2016-11-23/9:43:36	2016-11-23/9:43:44	1479894219.13	1479894219.13
175	361	2016-11-23/16:34:53	2016-11-23/16:34:59	1479918895.18199	1479918895.18199
176	362	2016-11-23/16:35:32	2016-11-23/16:35:38	1479918933.348	1479918933.348
177	363	2016-11-23/16:46:44	2016-11-23/16:46:54	1479919605.96	1479919605.96
178	364	2016-11-23/17:11:17	2016-11-23/17:11:20	1479921078.26099	1479921078.26099
179	365	2016-11-23/17:11:27	2016-11-23/17:11:37	1479921088.93	1479921088.93
180	366	2016-11-23/17:13:11	2016-11-23/17:13:17	1479921193.25	1479921193.25
181	367	2016-11-23/17:13:31	2016-11-23/17:13:40	1479921213.09999	1479921213.09999
182	368	2016-11-23/17:14:15	2016-11-23/17:14:22	1479921257.263	1479921257.263
183	370	2016-11-23/17:20:57	2016-11-23/17:21:3	1479921658.318	1479921658.318
184	372	2016-11-23/17:29:26	2016-11-23/17:29:33	1479922168.61599	1479922168.61599
185	377	2016-11-28/7:31:7	2016-11-28/7:31:13	1480318268.902	1480318268.902
186	380	2016-11-28/9:32:20	2016-11-28/9:32:28	1480325542.71	1480325542.71
187	381	2016-11-28/9:32:45	2016-11-28/9:32:53	1480325567.66	1480325567.66
188	382	2016-11-28/10:33:23	2016-11-28/10:33:53	1480329223.98	1480329223.98
189	384	2016-11-28/10:44:42	2016-11-28/10:44:48	1480329882.72	1480329882.72
190	386	2016-11-28/11:33:41	2016-11-28/11:33:46	1480332822.433	1480332822.433
191	389	2016-11-28/14:55:13	2016-11-28/14:55:21	1480344915.72	1480344915.72
192	390	2016-11-28/15:46:55	2016-11-28/15:46:53	1480348015.71199	1480348015.71199
193	391	2016-11-28/15:46:56	2016-11-28/15:46:59	1480348016.951	1480348016.951
194	392	2016-12-11/4:18:3	2016-12-11/4:18:8	1481429884.67899	1481429884.67899
195	393	2016-12-11/4:18:53	2016-12-11/4:18:58	1481429934.667	1481429934.667
196	395	2016-12-11/4:19:0	2016-12-11/4:19:5	1481429940.76399	1481429940.76399
197	396	2016-12-11/4:22:2	2016-12-11/4:22:6	1481430122.93899	1481430122.93899
198	398	2016-12-11/5:9:6	2016-12-11/5:9:11	1481432947.42	1481432947.42
199	399	2016-12-11/5:9:46	2016-12-11/5:9:54	1481432988.8	1481432988.8

	index	start	end	start [seconds]	end [seconds]
200	404	2016-12-11/8:30:32	2016-12-11/8:30:35	1481445032.82999	1481445032.82999
201	405	2016-12-11/8:31:0	2016-12-11/8:31:6	1481445061.977	1481445061.977
202	411	2016-12-11/8:41:55	2016-12-11/8:41:59	1481445715.798	1481445715.798
203	412	2016-12-11/8:42:7	2016-12-11/8:42:12	1481445729.02	1481445729.02
204	414	2016-12-11/8:42:40	2016-12-11/8:42:45	1481445761.07999	1481445761.07999
205	421	2016-12-11/8:53:14	2016-12-11/8:53:20	1481446396.23499	1481446396.23499
206	423	2016-12-11/9:38:15	2016-12-11/9:38:20	1481449096.29399	1481449096.29399
207	424	2016-12-11/9:38:35	2016-12-11/9:38:38	1481449115.97	1481449115.97
208	425	2016-12-11/9:38:40	2016-12-11/9:38:45	1481449121.989	1481449121.989
209	427	2016-12-11/11:13:2	2016-12-11/11:13:6	1481454783.44899	1481454783.44899
210	428	2016-12-11/11:14:10	2016-12-11/11:14:18	1481454852.93	1481454852.93
211	429	2016-12-11/12:30:27	2016-12-11/12:30:33	1481459429.045	1481459429.045
212	430	2016-12-11/12:30:34	2016-12-11/12:30:39	1481459435.667	1481459435.667
213	431	2016-12-11/12:31:13	2016-12-11/12:31:18	1481459474.818	1481459474.818
214	432	2016-12-11/13:33:42	2016-12-11/13:33:47	1481463223.963	1481463223.963
215	433	2016-12-11/13:33:56	2016-12-11/13:34:2	1481463238.15899	1481463238.15899
216	434	2016-12-11/13:34:0	2016-12-11/13:34:4	1481463240.747	1481463240.747
217	436	2016-12-11/15:24:32	2016-12-11/15:24:38	1481469873.93199	1481469873.93199
218	437	2016-12-11/15:24:45	2016-12-11/15:24:50	1481469886.174	1481469886.174
219	439	2016-12-11/15:29:51	2016-12-11/15:29:58	1481470193.051	1481470193.051
220	442	2016-12-19/3:27:41	2016-12-19/3:27:44	1482118061.917	1482118061.917
221	443	2016-12-19/3:27:56	2016-12-19/3:28:0	1482118077.066	1482118077.066
222	444	2016-12-19/3:28:6	2016-12-19/3:28:11	1482118087.313	1482118087.313
223	445	2016-12-19/6:1:45	2016-12-19/6:1:54	1482127306.89	1482127306.89
224	446	2016-12-19/14:16:21	2016-12-19/14:16:29	1482156984.32999	1482156984.32999
225	449	2017-1-2/3:8:1	2017-1-2/3:8:5	1483326482.111	1483326482.111
226	450	2017-1-2/3:18:6	2017-1-2/3:18:12	1483327088.667	1483327088.667
227	451	2017-1-2/3:18:14	2017-1-2/3:18:19	1483327096.809	1483327096.809
228	455	2017-1-2/14:2:38	2017-1-2/14:2:47	1483365761.76	1483365761.76
229	456	2017-1-2/14:2:53	2017-1-2/14:2:59	1483365775.265	1483365775.265
230	457	2017-1-11/1:41:55	2017-1-11/1:42:1	1484098917.053	1484098917.053
231	463	2017-1-11/4:21:19	2017-1-11/4:21:23	1484108480.111	1484108480.111
232	464	2017-1-11/4:22:46	2017-1-11/4:22:59	1484108570.32999	1484108570.32999
233	466	2017-1-11/5:57:58	2017-1-11/5:58:4	1484114280.20499	1484114280.20499
234	469	2017-1-20/3:27:23	2017-1-20/3:27:27	1484882844.611	1484882844.611
235	471	2017-1-20/9:11:4	2017-1-20/9:11:8	1484903465.303	1484903465.303
236	473	2017-1-22/7:59:55	2017-1-22/8:0:0	1485071997.519	1485071997.519
237	474	2017-1-22/10:15:46	2017-1-22/10:15:50	1485080147.101	1485080147.101
238	477	2017-1-22/10:47:28	2017-1-22/10:47:34	1485082050.038	1485082050.038
239	478	2017-1-27/0:38:57	2017-1-27/0:39:1	1485477538.596	1485477538.596
240	479	2017-1-27/0:46:52	2017-1-27/0:46:56	1485478012.96499	1485478012.96499
241	482	2017-1-27/6:28:35	2017-1-27/6:28:44	1485498517.01	1485498517.01
242	484	2017-1-27/6:32:20	2017-1-27/6:32:24	1485498741.253	1485498741.253
243	488	2017-1-27/11:11:19	2017-1-27/11:11:21	1485515480.043	1485515480.043
244	489	2017-1-27/11:11:25	2017-1-27/11:11:28	1485515485.913	1485515485.913

	index	t to EDR [s]	B_{ax} [nT]	V_i [kms^{-1}]	top-ology	$B_{ax,ff}$ [nT]	R$_{ff}$ [km]	RMS [nT]	IP	hel-icity
0	4	1	44.02280921	294.179	0.0	37.4662	66.0	18.80781271	0.3	-1
1	9	2928	19.80454616	142.466	0.0	19.2263	410.0	11.53894312	0.1	-1
2	10	409	-26.94938746	179.42	0.0	21.9352	50.0	16.56048233	0	-1
3	11	165	23.69324378	162.322	0.0	18.8942	495.5	5.950504703	-0.05	1
4	13	29	14.80151492	175.939	0.0	13.1948	106.5	6.947708029	-0.25	-1
5	14	47	-23.68693741	185.983	0.0	21.0565	171.5	13.13024138	0.2	1
6	16	98	-20.48499669	202.561	0.0	11.0976	41.5	15.21357495	-0.25	1
7	22	3957	-19.1891972	135.928	0.0	16.4513	366.0	6.892971213	0.05	-1
8	24	148	60.07607658	287.081	1.0	51.6399	205.0	12.73653552	-0.05	1
9	25	28	-26.82960606	260.983	0.0	30.2896	154.0	12.73573087	0.3	1
10	30	61	-35.83471937	160.107	0.0	33.3176	116.0	16.5562249	-0.1	-1
11	31	31210	33.08480766	173.414	1.0	29.9442	84.0	17.80648742	0.05	1
12	32	32532	-25.97551847	262.607	0.0	21.6797	127.0	10.36875292	-0.05	1
13	33	32575	31.1002593	279.9	0.0	33.4846	178.0	8.226858941	0.2	1
14	37	32682	25.03230437	364.836	0.0	24.053	94.0	13.14431414	-0.15	1
15	39	32724	-41.19773615	259.247	0.0	40.692	141.0	19.71604945	0	1
16	40	32777	36.24450602	279.392	0.0	39.2057	88.0	17.91361574	0.15	1
17	42	33145	-29.19361787	223.591	0.0	27.6513	160.0	12.1877148	0.1	1
18	47	33657	11.40230261	227.992	0.0	10.418	128.0	9.747958055	0.15	-1
19	48	33660	42.72166351	216.739	0.0	48.2669	328.0	14.55863116	0.2	1
20	51	34536	-48.25645729	186.074	0.0	43.057	369.5	17.24429328	-0.05	1
21	53	34895	-35.00709627	275.927	0.0	36.9873	92.5	16.95202603	0.2	1
22	54	35102	-38.31981132	211.252	0.0	34.647	54.0	21.40764577	0.15	1
23	56	41526	62.60674068	220.588	0.0	65.8652	56.0	28.61277289	0.2	1
24	57	41500	66.08325722	252.607	0.0	63.0988	108.0	27.19985736	0	-1
25	58	41498	-54.39632948	236.881	0.0	67.828	111.0	32.25881298	-0.35	-1
26	59	41428	-75.6141647	224.037	0.0	74.6243	390.0	32.95652493	-0.25	-1
27	60	41409	-53.69316545	270.662	0.0	62.0069	133.5	35.15340143	-0.2	-1
28	61	41404	66.00364202	190.661	0.0	64.5712	119.5	30.85681258	-0.15	1
29	63	41317	61.25058285	101.451	0.0	59.7737	112.0	29.07098084	0	1
30	64	41304	-60.93351257	78.6735	1.0	60.8226	238.5	31.51804696	0.15	1
31	66	41245	-62.94568339	96.164	0.0	74.3784	484.5	32.67472294	0.35	1
32	67	41233	-47.29923605	92.678	0.0	56.8237	139.0	29.19625943	0.45	1
33	69	23205	-29.15454689	126.426	0.0	26.9678	211.5	14.88951109	0	1
34	71	649	-13.77305428	218.372	0.0	10.8157	176.0	4.634280315	0.1	1
35	73	360	-30.34047024	277.441	0.0	29.1751	248.0	10.47255921	-0.15	1
36	74	309	-21.76580336	341.445	0.0	19.82	145.5	7.421433068	0	1
37	78	113	-44.13030257	221.18	0.0	35.9478	297.5	12.37485517	0.05	1
38	79	66	-30.37046576	248.726	0.0	35.3439	27.0	14.42749574	0.3	1
39	89	475	-18.27898705	289.966	0.0	18.2357	31.0	9.118964375	-0.25	-1
40	91	518	-27.61438235	189.723	0.0	24.8693	213.5	5.691992501	-0.15	-1
41	93	559	27.73360863	210.939	0.0	23.6959	323.0	9.536763725	-0.1	-1
42	94	594	18.91005444	251.281	0.0	13.145	39.5	7.74795597	-0.15	1
43	97	627	-35.12975413	297.345	0.0	33.7257	83.0	16.56815031	-0.15	1
44	104	4363	-28.08966141	120.571	0.0	23.1272	336.5	11.4658297	0.05	1
45	105	4269	33.32496496	81.7287	0.0	32.5289	298.0	13.88142604	-0.15	1
46	107	2755	38.67546884	233.478	0.0	32.7445	390.5	8.926070212	0	-1
47	109	2283	-34.9266632	299.08	0.0	35.1227	232.5	15.42949477	-0.2	-1
48	110	2274	-29.04257599	310.851	0.0	30.5725	306.0	11.31073233	-0.15	1
49	112	778	37.75062774	300.314	0.0	37.9279	196.0	6.477700198	0.3	-1

	index	t to EDR [s]	B_{ax} [nT]	V_i [kms^{-1}]	topology	$B_{ax,ff}$ [nT]	R_{ff} [km]	RMS [nT]	IP	helicity
50	113	80	-36.27020231	191.284	0.0	30.9857	883.0	19.81807936	-0.05	-1
51	114	83578	25.68868917	96.7939	0.0	42.494	111.5	17.97058738	0.45	1
52	115	83570	-48.34370985	98.6354	0.0	46.4016	63.5	25.37929529	0.05	-1
53	130	69782	-10.12307001	125.821	0.0	13.4146	114.0	28.32963957	-0.5	-1
54	133	69454	46.59266879	168.57	0.0	43.0608	87.0	7.87792416	-0.1	1
55	134	67245	-21.04833599	334.074	0.0	19.6581	157.0	5.877911778	-0.1	1
56	136	29	45.90939659	152.04	1.0	45.7497	136.0	18.82374848	0.05	1
57	139	588	56.95879606	228.546	2.0	51.5252	241.5	28.1570254	0.05	1
58	142	40310	33.3243661	159.616	0.0	28.5444	149.0	12.75719958	0	1
59	143	35714	45.167727	234.07	1.0	47.0771	897.5	18.86787732	-0.2	1
60	145	11822	-24.23868328	110.886	0.0	20.7612	986.5	5.647971217	0.05	1
61	151	4999	24.13532438	235.883	0.0	17.073	198.5	7.515263665	-0.25	-1
62	153	3524	40.26274925	74.2413	0.0	34.6266	788.5	18.07559092	0.25	-1
63	154	2992	-47.60456837	289.488	0.0	41.1374	632.5	16.75237342	-0.2	1
64	157	1022	19.37639338	177.022	0.0	19.3003	73.0	8.949174346	-0.1	1
65	160	16	47.18212863	254.105	0.0	40.9505	388.5	15.24126702	-0.1	1
66	161	32	-55.55435032	247.982	0.0	47.325	261.0	9.966910324	0	1
67	166	847	-50.32345782	220.621	0.0	45.4083	104.0	27.66993693	0	1
68	170	1636	-42.82421924	173.253	0.0	29.6619	191.5	26.1895569	-0.15	1
69	172	803	-55.19011556	229.45	0.0	50.7868	174.5	11.04347592	-0.1	1
70	174	773	-53.31469982	168.561	1.0	58.1099	110.0	26.89047107	0.3	1
71	175	764	-47.8397003	181.021	1.0	46.3939	167.0	16.63327063	0.1	1
72	176	726	-43.55580858	97.5546	1.0	44.5304	89.0	23.98168027	-0.25	1
73	177	722	-36.32241313	60.6189	1.0	37.4909	70.0	23.27297307	0.2	-1
74	178	343	-55.75670851	184.903	1.0	53.6981	195.5	19.57310272	0.1	1
75	179	331	42.50185429	131.939	1.0	40.0457	329.5	15.67524586	-0.05	1
76	180	271	48.23939787	213.945	1.0	33.9839	110.0	31.70875495	-0.05	1
77	181	263	-38.58574836	271.625	1.0	45.8881	145.0	16.71844288	-0.35	1
78	182	259	32.11900972	249.378	1.0	35.148	143.0	14.84454507	-0.15	1
79	183	257	33.65456978	237.699	1.0	32.0134	311.0	12.98919252	-0.25	1
80	184	251	-38.99000909	296.041	1.0	31.7047	116.0	14.60086624	0	1
81	185	236	-52.06965182	146.008	1.0	48.2171	287.0	12.82025628	-0.15	1
82	186	14	-42.55486892	187.662	0.0	30.3486	254.0	12.56813229	0	1
83	191	34972	-41.56333709	157.403	0.0	37.7898	173.5	19.56936552	0.05	-1
84	195	81940	94.45429256	131.21	3.0	74.12	402.5	42.75216831	-0.1	1
85	196	81949	-46.30692283	188.282	3.0	41.7701	64.0	19.73566387	0.05	1
86	197	81964	71.23708142	184.499	1.0	71.768	302.0	18.46186484	-0.15	1
87	198	82050	-63.04121389	59.6661	3.0	60.5271	334.0	25.91971357	0	1
88	199	1101	28.23954433	195.711	3.0	28.447	61.0	11.37186777	-0.15	1
89	200	1090	-29.46197374	178.045	1.0	27.3377	113.5	13.46425775	0.05	1
90	201	1083	-46.72311742	246.829	1.0	47.7356	217.5	17.06429815	-0.1	1
91	205	209	47.56013981	191.533	1.0	45.5023	143.5	9.78635446	-0.05	1
92	206	219	-40.37386511	207.509	1.0	39.9047	205.0	11.83013753	-0.2	1
93	208	15347	31.35686667	19.1623	1.0	31.5219	771.5	13.49001769	0	1
94	211	17061	-24.75409036	97.9739	0.0	25.1642	215.5	10.48522341	-0.1	-1
95	213	23982	17.72254393	90.3605	0.0	18.4135	203.5	7.085740844	0.15	-1
96	214	24148	-25.68367552	192.511	0.0	21.151	428.5	11.72766133	0	1
97	218	31927	-42.04761329	132.518	0.0	39.543	275.0	20.11143464	0	1
98	219	39147	-66.69400806	181.164	1.0	61.7208	83.0	30.9980889	-0.2	1
99	220	39150	-53.37199494	187.205	0.0	10.9863	172.5	39.75358701	0.2	1

	index	t to EDR [s]	B_{ax} [nT]	V_i [kms^{-1}]	topology	$B_{ax,ff}$ [nT]	R$_{ff}$ [km]	RMS [nT]	IP	helicity
100	221	12156	57.29125966	427.035	2.0	53.5781	173.0	18.40328572	0.25	-1
101	224	2161	-34.7488363	329.385	0.0	30.1289	175.0	14.07218038	0.15	-1
102	225	1958	-56.94873033	214.201	1.0	54.6578	223.5	24.61385645	0.05	1
103	227	1362	66.12290568	251.756	0.0	65.9818	199.5	30.28459891	-0.1	-1
104	228	774	16.8854874	169.024	1.0	12.7805	94.0	5.69526209	0.05	1
105	231	45340	33.50751064	120.364	0.0	20.692	185.0	18.55565842	0.45	1
106	241	28038	-19.48265943	237.601	0.0	19.2112	167.5	7.07378883	-0.15	-1
107	242	27248	25.54446988	197.707	0.0	21.7614	46.0	14.59023134	0.05	1
108	243	27234	-33.95992901	205.303	0.0	34.2282	114.5	10.62717894	0.25	-1
109	244	956	-47.67543527	262.207	1.0	41.4448	188.5	23.43934937	-0.1	1
110	245	827	72.79381153	184.816	1.0	61.9088	192.0	13.07025183	-0.1	1
111	246	790	62.99941184	171.395	1.0	58.2113	150.0	22.37100771	-0.3	1
112	247	742	-65.70026709	220.55	3.0	56.8958	286.5	29.2573237	-0.1	1
113	248	715	62.69197841	140.94	3.0	68.9721	92.5	25.69036189	-0.1	1
114	249	704	75.05459426	83.5868	1.0	89.3541	380.5	29.82256074	-0.3	1
115	250	477	59.79042674	264.821	3.0	60.0179	792.5	28.06276673	0.1	1
116	251	255	53.38391406	128.34	1.0	56.667	206.0	29.24704812	0.05	1
117	252	200	47.4952391	178.968	1.0	40.461	59.0	27.04340181	0.15	1
118	254	194	38.51032377	162.156	1.0	35.7288	161.0	9.571933729	0.15	1
119	257	33	49.67465809	126.099	3.0	28.0485	60.5	29.39270022	0	1
120	260	42325	-26.64131834	299.583	1.0	24.3734	70.0	18.47862004	0.1	1
121	261	42334	11.07975178	328.045	1.0	11.0687	19.0	5.617944081	-0.05	-1
122	264	46557	26.21762978	178.504	1.0	26.9767	289.5	14.1693772	-0.2	1
123	265	46615	25.6881827	133.791	3.0	21.5785	35.0	18.11199487	-0.1	-1
124	266	47034	20.04044816	162.151	1.0	6.76535	72.5	15.28995483	0.35	-1
125	267	47036	17.75649186	186.915	1.0	10.4583	22.0	11.16572435	-0.5	1
126	270	69516	-14.51611855	155.207	0.0	14.3942	142.0	3.833802518	-0.1	1
127	271	69513	-20.23468755	183.068	0.0	16.4108	117.5	8.21712786	0.05	-1
128	273	59979	30.49500723	133.387	0.0	31.6434	367.0	15.63631076	-0.45	-1
129	274	3398	27.46506121	147.22	1.0	27.6093	202.5	8.683932144	-0.05	1
130	275	3393	23.04032968	127.868	1.0	21.2156	180.5	5.469276768	0	1
131	277	546	40.27644147	206.476	1.0	34.6273	125.0	7.174060851	-0.1	1
132	279	5375	31.90662675	219.881	1.0	33.4603	57.5	15.13084371	-0.2	1
133	280	10104	41.53289582	168.747	3.0	42.1208	54.0	24.97836662	-0.2	1
134	282	789	36.45640437	202.921	1.0	31.7301	205.0	12.07820749	-0.05	-1
135	284	17022	-43.01492274	216.572	3.0	45.3819	376.0	12.29214333	-0.15	-1
136	285	17653	-12.76220097	215.798	0.0	15.0048	193.0	10.48510217	-0.4	-1
137	291	12204	37.60861363	564.203	0.0	40.0409	130.0	18.06533594	0.4	1
138	292	11857	37.45239176	440.54	1.0	36.9925	134.5	13.85518945	-0.1	1
139	294	186	56.15687453	168.237	0.0	51.2219	152.5	21.39068282	-0.1	1
140	295	245	-32.66477469	124.735	0.0	29.3323	123.5	17.59675031	-0.1	1
141	297	354	-51.86851286	144.391	0.0	53.334	300.5	25.47486004	0.2	1
142	299	1601	-53.05933714	170.887	1.0	48.0161	92.0	26.26550141	0.1	1
143	300	1605	36.11087893	147.079	1.0	44.253	102.5	21.40758924	0.35	1
144	301	1610	-41.33845738	176.121	0.0	38.2267	55.0	23.87573123	-0.1	1
145	303	2110	-51.21942154	222.734	0.0	49.783	74.5	21.84495216	0.2	1
146	308	20518	29.71159458	207.009	0.0	28.5757	82.0	12.74875056	-0.1	1
147	309	27497	-28.99521896	173.433	1.0	27.7056	110.0	11.22394905	0.05	1
148	312	28478	42.5668347	223.588	1.0	41.4862	106.5	21.66088514	-0.15	-1
149	314	30947	-33.42572025	413.933	0.0	32.7565	59.5	12.8987434	0	1

	index	t to EDR [s]	B_{ax} [nT]	V_i [kms^{-1}]	topology	$B_{ax,ff}$ [nT]	R$_{ff}$ [km]	RMS [nT]	IP	helicity
150	315	30922	-52.65083746	395.264	0.0	40.9696	40.0	17.68211306	-0.15	1
151	317	30820	50.45451511	401.979	0.0	43.6894	56.0	20.96567576	-0.15	-1
152	318	21977	-49.2119005	246.595	0.0	49.8105	95.0	22.96457216	0.3	-1
153	320	6545	-47.30086226	280.664	0.0	41.4802	222.0	16.25296075	-0.15	1
154	321	6520	-28.6463549	349.838	0.0	25.366	39.5	13.7426381	-0.25	1
155	324	1566	51.77249203	357.697	0.0	54.4796	70.5	28.43133033	0.15	1
156	329	2900	-45.97862494	137.834	3.0	45.0889	340.0	23.33546573	-0.05	-1
157	330	391	30.00336193	296.125	0.0	30.627	118.5	14.13057754	-0.15	-1
158	331	1549	56.62795905	323.344	0.0	42.8465	40.5	18.44989812	0.05	-1
159	332	1599	-48.20012513	179.55	0.0	43.8793	94.0	25.93869042	0	-1
160	333	16413	-53.47196936	243.723	0.0	57.6114	142.0	13.55363099	0.3	-1
161	334	16728	-45.2657049	287.572	0.0	44.0097	94.0	20.3969842	0.1	-1
162	337	20706	-23.15927747	368.776	0.0	21.0271	267.5	7.292852705	0.05	1
163	340	2381	-42.05609314	171.753	1.0	44.1755	67.0	9.330549811	-0.15	1
164	341	2112	-35.03049854	90.325	0.0	34.7163	128.5	15.52498867	-0.25	1
165	342	2101	-27.29953814	20.1944	0.0	25.3881	61.5	14.09269507	0.1	-1
166	343	1986	-42.97575842	272.169	0.0	42.2655	95.0	21.59446034	0.2	1
167	344	1978	-49.67645275	286.935	0.0	45.9592	63.5	27.07507599	0	1
168	350	3	-42.06781643	194.534	0.0	38.9352	89.0	19.66182632	0	1
169	351	23	53.94340857	248.93	0.0	52.7886	64.5	28.45078696	-0.15	1
170	352	35	28.29307479	139.046	0.0	6.36179	15.0	16.51542614	0.45	1
171	356	6640	18.62001989	149.682	0.0	14.0787	110.5	7.181643137	-0.15	1
172	357	6803	30.29149687	162.159	1.0	30.4187	200.5	12.11496236	-0.1	-1
173	358	6809	36.75411114	225.518	1.0	31.2369	299.5	9.259546041	0.05	-1
174	359	6819	24.04942393	191.564	1.0	22.8393	83.0	12.7203904	-0.1	1
175	361	31495	17.12761083	172.611	0.0	13.9942	149.0	5.09566236	0	-1
176	362	31533	-8.710321576	171.671	0.0	8.77052	214.0	3.132344968	0.3	1
177	363	32206	29.96113162	180.156	3.0	31.7235	226.0	14.34975137	0.15	-1
178	364	33678	-28.87609036	209.148	0.0	28.6652	63.5	11.21883764	-0.1	1
179	365	33689	-46.30159199	216.496	1.0	39.5043	407.5	20.56756583	-0.15	1
180	366	33793	41.43342605	267.087	1.0	41.1881	160.0	18.4857042	0.1	1
181	367	33813	44.76574763	233.665	1.0	45.4511	155.0	21.2087325	0.2	-1
182	368	33857	42.74625851	162.734	1.0	37.4666	145.5	20.93158487	-0.1	-1
183	370	34258	-42.0244412	224.603	3.0	43.1866	147.0	11.28606958	0.15	1
184	372	34769	34.91597836	210.604	0.0	32.9286	99.0	14.67970835	0.25	1
185	377	29751	-35.59358332	245.318	0.0	34.1421	81.0	17.32279206	0.25	1
186	380	22477	-14.87585717	134.793	0.0	13.9562	204.0	6.163511524	-0.15	-1
187	381	22452	22.83611569	177.109	0.0	21.4796	134.0	13.31638593	0.15	1
188	382	18796	24.29058066	160.427	0.0	20.5311	427.0	11.03573328	0	-1
189	384	18137	-27.79890496	173.903	0.0	25.611	110.5	10.0310148	-0.2	-1
190	386	15198	43.24119663	194.521	0.0	44.3954	99.0	13.87907418	-0.1	1
191	389	3104	-29.21383186	224.25	0.0	29.0138	118.0	16.04843926	-0.1	1
192	390	4	-40.7295795	182.878	0.0	42.7664	58.0	19.30739548	0.25	1
193	391	3	-37.24873268	192.045	0.0	36.1685	55.5	19.66179296	-0.15	1
194	392	1375	-61.72878873	390.792	0.0	61.8624	90.5	26.97294355	-0.05	1
195	393	1325	-53.18871043	164.035	1.0	55.9073	125.5	24.02033671	-0.2	1
196	395	1319	-55.32869863	204.7	0.0	52.0999	150.0	27.85607981	-0.15	1
197	396	1137	-48.1226242	197.404	0.0	46.8873	100.5	23.37992371	0.1	1
198	398	1687	-18.91072981	236.21	0.0	18.1593	142.5	5.255952242	-0.05	-1
199	399	1729	-19.84206986	291.632	0.0	18.6867	138.0	8.034577754	0.25	1

	index	t to EDR [s]	B_{ax} [nT]	V_i [kms^{-1}]	top-ology	$B_{ax,ff}$ [nT]	R$_{ff}$ [km]	RMS [nT]	IP	hel-icity
200	404	13773	-59.01521154	229.307	0.0	57.5883	14.0	25.55660655	0	1
201	405	13802	13.2625235	168.773	0.0	10.8911	97.5	7.460787395	-0.15	-1
202	411	14456	23.54289036	158.298	0.0	22.0091	87.5	9.72348768	-0.35	-1
203	412	14469	-13.14261212	157.951	0.0	12.8274	88.0	5.655356985	0.05	-1
204	414	14501	-25.53491882	93.1818	0.0	23.4146	117.0	8.342216413	-0.05	1
205	421	15136	30.20704643	199.674	0.0	27.9738	128.0	6.974197337	-0.05	-1
206	423	17836	55.94944428	249.798	0.0	50.5925	89.0	16.81639523	0	-1
207	424	17856	-21.81983955	207.724	0.0	24.3794	27.0	10.06605683	-0.35	1
208	425	17862	17.07664924	225.767	0.0	18.1358	51.0	9.47834022	0.15	1
209	427	23523	59.45808669	259.502	0.0	60.9833	104.5	16.06543343	-0.2	1
210	428	23593	-29.6160528	195.299	2.0	29.7373	141.5	17.2767748	0.05	-1
211	429	28169	30.58414615	225.953	0.0	26.8574	105.0	8.143850742	-0.05	-1
212	430	28176	33.40491295	222.327	0.0	32.0534	89.0	7.820019455	0	1
213	431	28215	28.32885822	242.061	0.0	27.1892	81.0	6.048748376	0	1
214	432	31964	37.5338872	332.255	0.0	29.7579	76.0	20.22823861	0	-1
215	433	31978	34.65959786	314.611	0.0	32.2194	129.5	8.847974198	-0.1	-1
216	434	31981	-18.17339012	302.25	0.0	26.863	96.0	8.303127812	-0.45	1
217	436	38614	-29.7540078	259.84	0.0	31.8074	104.5	17.07860912	0.3	-1
218	437	38626	-21.90445163	235.766	0.0	21.1034	64.0	5.567689409	0.1	-1
219	439	38933	31.72999203	195.137	0.0	30.6751	140.0	5.769999457	-0.2	1
220	442	38838	-53.51323266	137.068	1.0	54.4899	67.0	23.68907305	0.05	1
221	443	38823	-55.14343625	122.485	1.0	52.2598	161.0	13.40083442	0.05	1
222	444	38813	-59.82504166	132.715	1.0	62.8795	131.0	27.68823406	0.2	1
223	445	29593	-16.53868899	86.2689	0.0	13.4635	298.0	5.57544149	-0.05	-1
224	446	84	-32.69625839	126.772	1.0	36.0741	210.0	17.50883088	-0.25	1
225	449	602	-14.92220992	94.7098	n/a	13.7433	109.5	9.663332695	0.05	-1
226	450	1209	46.7043108	224.472	n/a	48.1918	87.0	19.84175558	-0.05	1
227	451	1217	-24.06914653	167.624	n/a	33.7678	34.5	19.50399379	0.45	1
228	455	39882	40.84811961	186.945	n/a	42.0588	239.0	18.61496524	-0.25	1
229	456	39895	34.56730145	204.236	n/a	36.7744	135.5	16.26165053	0.1	-1
230	457	9603	60.47842502	89.7991	1.0	57.572	148.0	29.32585007	-0.05	-1
231	463	40	42.96859842	226.21	3.0	33.5739	62.0	15.77714594	-0.05	-1
232	464	50	-57.73879629	81.2841	3.0	52.4065	329.0	15.29638366	0.05	1
233	466	5760	28.91866309	169.353	0.0	27.14	84.0	13.75761743	-0.1	1
234	469	32675	35.91658438	186.328	0.0	39.1169	55.0	16.79312421	0	-1
235	471	12055	23.14112212	118.814	0.0	22.0928	38.5	10.43263163	-0.15	1
236	473	8102	59.3611667	147.981	0.0	56.7201	143.5	9.018883777	0.1	-1
237	474	47	46.93699888	187.849	2.0	44.8669	84.0	10.27802604	0.15	1
238	477	30	35.73056896	74.1842	1.0	35.4827	196.5	13.20288105	-0.05	1
239	478	41161	47.63098275	185.391	0.0	43.8142	49.0	24.76684406	-0.15	-1
240	479	40687	44.47775439	225.199	0.0	47.4323	92.5	7.910074725	0.2	-1
241	482	20183	56.35942046	245.464	0.0	54.1807	241.0	27.0416578	0.1	-1
242	484	19959	-31.9037673	159.783	0.0	32.4087	68.5	5.242881159	0.1	1
243	488	3220	18.44486435	215.504	0.0	13.4434	16.0	9.201882581	-0.05	-1
244	489	3214	12.84872862	239.39	0.0	9.00451	10.0	4.849568114	0.05	1

Appendix B

Permissions

Webster et al. (2018) - EDR data, Chapter 3

Robertson et al. (2021) - Chapter 6